ISSN 1451 - 9372(Print)
ISSN 2217 - 7434(Online)
APRIL-JUNE 2017
Vol.23, Number 2, 151-289

Chemical Industry & Chemical Engineering Quarterly

SERBIA
Belgrade
AChE

The AChE Journal for Chemical Engineering,
Biochemical Engineering, Chemical Technology,
New Materials, Renewable Energy and Chemistry

www.ache.org.rs/ciceq

Journal of the
Association of Chemical Engineers of
Serbia, Belgrade, Serbia

Chemical Industry &
Chemical Engineering
CI&CE Quarterly

EDITOR-In-Chief
Vlada B. Veljković
Faculty of Technology, University of Niš, Leskovac, Serbia
E-mail: veljkovicvb@yahoo.com

ASSOCIATE EDITORS

Jonjaua Ranogajec
Faculty of Technology, University of Novi Sad, Novi Sad, Serbia

Srđan Pejanović
Department of Chemical Engineering, Faculty of Technology and Metallurgy, University of Belgrade, Belgrade, Serbia

Milan Jakšić
ICEHT/FORTH, University of Patras, Patras, Greece

EDITORIAL BOARD (Serbia)
Đorđe Janaćković, Sanja Podunavac-Kuzmanović, Viktor Nedović, Sandra Konstantinović, Ivanka Popović
Siniša Dodić, Zoran Todorović, Olivera Stamenković, Marija Tasić, Jelena Avramović

ADVISORY BOARD (International)

Dragomir Bukur
Texas A&M University,
College Station, TX, USA
Milorad Dudukovic
Washington University,
St. Luis, MO, USA
Jiri Hanika
Institute of Chemical Process Fundamentals, Academy of Sciences
of the Czech Republic, Prague, Czech Republic
Maria Jose Cocero
University of Valladolid,
Valladolid, Spain
Tajalli Keshavarz
University of Westminster,
London, UK
Zeljko Knez
University of Maribor,
Maribor, Slovenia
Igor Lacik
Polymer Intitute of the Slovak Academy of Sciences,
Bratislava, Slovakia
Denis Poncelet
ENITIAA, Nantes, France

Ljubisa Radovic
Pen State University,
PA, USA
Peter Raspor
University of Ljubljana,
Ljubljana, Slovenia
Constantinos Vayenas
University of Patras,
Patras, Greece
Xenophon Verykios
University of Patras,
Patras, Greece
Ronnie Willaert
Vrije Universiteit,
Brussel, Belgium
Gordana Vunjak Novakovic
Columbia University,
New York, USA
Dimitrios P. Tassios
National Technical University of Athens,
Athens, Greece
Hui Liu
China University of Geosciences, Wuhan, China

FORMER EDITOR (2005-2007)
Professor Dejan Skala
University of Belgrade, Faculty of Technology and Metallurgy, Belgrade, Serbia

Journal of the
Association of Chemical Engineers of
Serbia, Belgrade, Serbia

Chemical Industry & Chemical Engineering
CI&CE Quarterly

Vol. 23 Belgrade, April-June 2017 No. 2

Chemical Industry & Chemical Engineering Quarterly (ISSN 1451-9372) is published quarterly by the Association of Chemical Engineers of Serbia, Kneza Miloša 9/I, 11000 Belgrade, Serbia

Editor:
Vlada B. Veljković
veljkovic@yahoo.com

Editorial Office:
Kneza Miloša 9/I, 11000 Belgrade, Serbia
Phone/Fax: +381 (0)11 3240 018
E-mail: shi@yubc.net
www.ache.org.rs

For publisher:
Tatijana Duduković

Secretary of the Editorial Office:
Slavica Desnica

Marketing and advertising:
AChE Marketing Office
Kneza Miloša 9/I, 11000 Belgrade, Serbia
Phone/Fax: +381 (0)11 3240 018

Publication of this Journal is supported by the Ministry of Education, Science and Technological Development of the Republic of Serbia

Subscription and advertisements make payable to the account of the Association of Chemical Engineers of Serbia, Belgrade, No. 205-2172-71, Komercijalna banka a.d., Beograd

Computer typeface and paging:
Vladimir Panić

Printed by:
Faculty of Technology and Metallurgy, Research and Development Centre of Printing Technology, Karnegijeva 4, P.O. Box 3503, 11120 Belgrade, Serbia

Abstracting/Indexing:
Articles published in this Journal are indexed in *Thompson Reuters* products: *Science Citation Index - Expanded*^{TM} - access *via Web of Science*$^{®}$, part of *ISI Web of Knowledge*^{SM}

CONTENTS

CONTENTS Continued

Activities of the Association of Chemical Engineers of Serbia are supported by:

- Ministry of Education, Science and Technological Development, Republic of Serbia
- Hemofarm Koncern AD, Vršac, Serbia
- Faculty of Technology and Metallurgy, University of Belgrade, Belgrade, Serbia
- Faculty of Technology, University of Novi Sad, Novi Sad, Serbia
- Faculty of Technology, University of Niš, Leskovac, Serbia
- Institute of Chemistry, Technology and Metallurgy, University of Belgrade, Belgrade, Serbia

CI&CEQ
Chemical Industry & Chemical Engineering Quarterly

Available on line at
Association of the Chemical Engineers of Serbia *AChE*
www.ache.org.rs/CICEQ

Chem. Ind. Chem. Eng. Q. 23 (2) 151–160 (2017) CI&CEQ

BOHUŠ KYSELA[1]
JIŘÍ KONFRŠT[1]
ZDENĚK CHÁRA[1]
IVAN FOŘT[2]

[1]Institute of Hydrodynamics, AS CR, v.v.i., Prague, Czech Republic.
[2]Department of Process Engineering, Faculty of Mechanical Engineering, CTU in Prague, Prague, Czech Republic

SCIENTIFIC PAPER

UDC 621.646.7:66

STRUCTURE OF TURBULENT VELOCITY FIELD IN THE DISCHARGE STREAM FROM A STANDARD RUSHTON TURBINE IMPELLER

Article Highlights

- The discharged stream velocity field from Rushton turbine impeller is mapped by LDA measurements
- Mean ensemble-averaged velocities and fluctuations of all three velocity components are presented
- Results treated by frequency analysis are presented at different radial positions
- Results of velocity decomposition into mean, periodic and random component are shown

Abstract

The radial discharge jet from a standard Rushton turbine was investigated by the Laser Doppler Anemometry (LDA) method. Several distances from the impeller blades (in the radial direction) were chosen for the measurement of axial profiles: all three velocity components (radial, tangential and axial) were measured at each point of the axial profile. The obtained velocity time records were analysed and averaged results were decomposed into three parts: mean ensemble-average, random and periodic. The ratio of the derived periodic part of the velocity was evaluated in each measurement point and for all velocity components. The obtained results indicate the regions where the periodic part of the velocity has significant effect and where the contribution of this part is almost negligible. Although the values of the periodic part of all velocity components have a rather similar range, the spatial distributions are different in the investigated region.

Keywords: Rushton turbine, LDA, discharge stream, agitated vessel.

The hydrodynamic properties of fluid flow inside agitated vessels are important parameters for their design. Deeper knowledge of turbulent flow inside the vessels is necessary for better understanding of the mixing process. The basic hydrodynamic investigations are proven in cylindrical vessel with Rushton turbine impeller [1-12]. The advantage of radial Rushton turbine impeller is the similarity of the radial discharge jet flow and the immersed jet, which allows using simplified models to determine velocity field and to derive turbulent properties. The distribution of dissipation rate of turbulent kinetic energy is required for the description of the mixing process [13,14] namely micro-mixing, gas or aggregates dispersion, and scale-up modelling. For this case, compartment models with several zones have been established [12,15-17]. The proposed zones correspond to volumes where the turbulent kinetic energy is dominant. The basic mixing zone (impeller zone) is a region where the trailing vortices disintegrate. The trailing vortices, which play a crucial role in radially agitated systems, have been observed and described by many research studies [4,13,18-21]. The agitated system with radial impeller was also investigated by CFD simulations [4,8,22-25,37] where similar results were obtained, but validated namely only in impeller blade vicinity, where the discharged stream analogy was established. As mentioned above, the dissipation of turbulent kinetic energy in this region is a very intensive process caused by the fast kinetic energy transfers over turbulent scales. This is considered to be

---

Correspondence: B. Kysela, Institute of Hydrodynamics, AS CR, v.v.i., Pod Paťankou 30/5,166 12 Prague 6, Czech Republic.
E-mail: kysela@ih.cas.cz
Paper received: 2 October, 2015
Paper revised: 23 February, 2016
Paper accepted: 26 April, 2016

https://doi.org/10.2298/CICEQ151002025K

the main mixing process, which is driven by the decomposition of the trailing vortex structures.

Discharge stream

The implementation of theoretical form of the immersed turbulent jet projected onto discharged stream originated from development of analytic solution of the mean flow. It is sufficiently accurate and derived namely in the form for the radial and tangential velocity [12,26-30]. The velocity profiles in the discharge stream were compared with theoretical curves derived namely form the basic analytical solution [28]. The turbulent flow in fully turbulent regime ($Re > 10^4$) in discharge stream could be divided into three regions where:

- The potential core flow is generated by the impeller blade.
- The jet axial-distribution of the mean radial velocity and root mean square (*RMS*) values of fluctuations are not evolved.
- Both profiles of the mean radial velocity and RMS values of fluctuations are in their final self-similar axial-distribution profiles.

The boundary between zone of flow establishment (ZFE) and zone of established flow (ZEF) regions was established in a distance $r/R = 1.6$ from the blades [12].

Velocity decomposition

The flow in the discharge stream is induced by periodic passing of the impeller blades. Hence, the resulting flow contains also the velocity component with periodic behaviour. So, the discharge flow velocity could be separated into three parts: mean U_i, periodic $u_i^{(\mathrm{per})}$ and random $u_i^{(\mathrm{rand})}$ [31]:

$$u_i = U_i + u_i^{(\mathrm{per})} + u_i^{(\mathrm{rand})} \tag{1}$$

where the kinetic energy transfers are between:

- mean and turbulent motion,
- mean and organized (periodic) motion and
- organized (periodic) and turbulent motion.

The transfer of kinetic energy from the mean flow to turbulence is commonly known as the production term of turbulence in the classic Reynolds decomposition and that exchange of kinetic energy is the main characteristic of the discharge stream. The kinetic energy transferred from the mean to the organized motion is clearly positive in the impeller jet. The organized kinetic energy is significant in the impeller vicinity and decreases as the radial distance from the impeller increases. The main energy exchange takes place in the impeller area, due to the development of the trailing vortices that are much more coherent near the impeller blade. The transfers of the kinetic energy between the organized and turbulent flows are located in the region close to the trailing vortices. The organized velocity component is narrowly bonded with the trailing vortices volume and with the region where they are broken-up. In the break-up region of the trailing vortices most of the kinetic energy of the organized motion is transferred to the turbulent one.

Different decomposing methods have been used to separate each velocity component, namely periodic and random. The first is a temporal analysis of velocity data record in terms of velocity correlation functions, where the periodic component is separated from the temporal data records [1]. The second way is to synchronize the acquisitions of velocity data with blade position and to obtain the phase-averaged velocity components [31]. Nowadays, new decomposition techniques of coherent structures are under development and they are also applied in the mixing processes [32,33].

Trailing vortices region

The compartment models divide the volume of mixing vessel into sections where the local kinetic energy takes ordinarily similar values, *e.g.*, bulk region, wall impact stream region or region around the impeller [15], commonly presented as the main working volume, where the trailing vortices play a key role for the transfer and dissipation of kinetic energy. The trailing vortices generated by Rushton turbine impeller have been experimentally investigated by several methods [4,30,34,35]. The published data originated mostly from the phase-averaging, and it should be noted that the structures obtained from that data are more symmetric, stable and homogeneous than the instantaneous ones [35]. Although the vortex structures are broken up during the movement and the velocity magnitudes of periodic component decrease, they are finally destroyed on the vessel wall and baffles. The observed length of resulting trailing vortex primarily depends on the identification technique setup [18,20,35] and whether the velocity data are phase-averaged or instantaneous [30].

In this paper, laser Doppler anemometry (LDA) measurements in the discharge stream from a standard Rushton turbine impeller were performed. The temporal analysis [10] of the data records including ensemble-averaging was applied, as well as the velocity decomposition based on separation from autocorrelation function (ACF) [1]. The distribution of the organized and turbulent motion was evaluated in the impeller discharge stream.

A future improvement of the mixing tank modelling depends mainly on CFD calculations. The prediction of the mean flow is reasonably good [37], but more accurate results of the turbulent characteristic are still required. The disintegration of the trailing vortices with coupled kinetic energy transfers is predicted with low accuracy, and the dissipation rate of the turbulent kinetic energy is mostly under-predicted by the CFD [37]. It was found that the kinetic energy was rapidly transferred in the discharged stream region to r^* = 1.6 or 1.8 [12,31]. Hence, we decided to map the wider region from impeller tip to r^* = 2.2 and obtain mean ensemble-averaged results and evaluate kinetic energy distribution desirable for validation of CFD results. The anisotropy behaviour in that region [4] enforced the investigation of all the three components [31] as well as comparison of their behaviour with the change of the impeller speed. Several experimental methods were compared [1,5,14,31]. Two main methods were used for non-invasive measurement. The first was LDA and second one was particle image velocimetry (PIV). The advantage of the LDA system is that the velocity values are physically given (by laser wave length, used lens, etc.) and no calibration is needed, while the images in PIV are necessary for spatial calibration and to make corrections of optical deformations. Although the advantage of PIV is a wider field of velocity values at the same time and equally spaced sampling, the measurement of all the three components needs a very sophisticated approach [31]. The stereoscopic PIV or the other three dimensional PIV measurements are also based on the deformation recalculations and employment of some interpolation techniques. Hence, we decided to use simple LDA method with minimal optical disturbances. The measurement through the flat bottom [5] allows obtaining very accurate results of radial and tangential component, with only a correction of axial position multiplied by refractive index 1.33 required. Moreover, the symmetrically placed impeller and the lid used to cover the vessel allow simple control of results by their symmetricity.

EXPERIMENTAL

Measurements of the velocity profiles were carried out in a pilot plant flat bottomed mixing vessel with four baffles at its wall (Figure 1), with water as the working liquid (density, 1000 kg·m^{-3}, dynamic viscosity, 1 mPa·s) for two impeller speeds 200 and 400 rpm (impeller Reynolds number Re_M = 3.3×10^4 and 6.6×10^4). A standard Rushton turbine impeller was used for the investigation (Figure 1).

LDA equipment and settings

Two component LDA system set-up consisted of Coherent INNOVA 305 Ion-Argon laser supply with power 5 W in a multiline regime; fiber flow transmitter, where the beam was separated into components, two separated wavelengths were used for two component measurement: 514.5 and 488 nm, respectively; Dantec fiber flow transmitting optics; 57N35 and 57N20 Dantec BSA processors. The optic parameters were: focal length 310 mm, diameter of the beam 1.2 mm, fringe spacing 2.135 μm (514.5 nm) and 2.025 μm (488 nm), number of fringes 40, and the measured volume was ellipsoid with sizes of the axes 0.086 mm×0.085 mm×0.709 mm (514.5 nm) for first wavelength and 0.082 mm×0.081 mm×0.673 mm (488 nm) for the second wavelength. The frequency shift was 40 MHz, and velocity span up 8.4 m·s^{-1}. Silver-coated hollow glass spheres (S-HGS) with mean diameter 10 μm and density 1.1 g·cm^{-3} were used as trace particles.

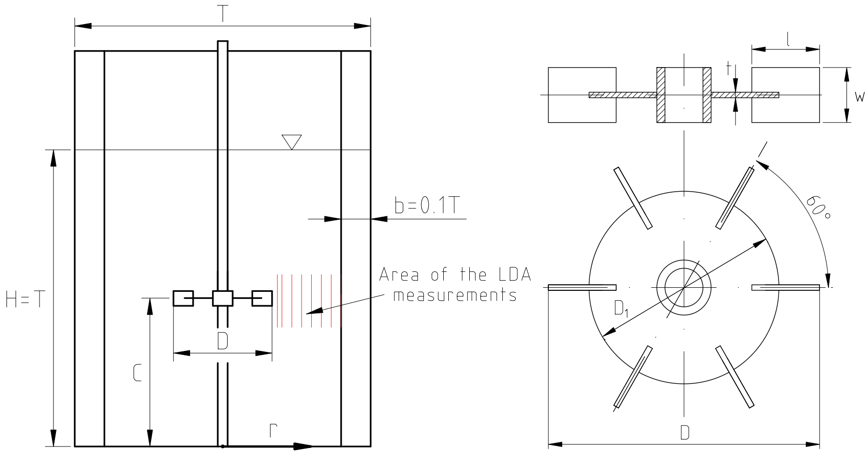

Figure 1. Mixing vessel setup (T = 300 mm; H/T = 1; D/T = 1/3; C/T = 1/2; b/T = 1/10; four baffles) and standard Rushton turbine impeller (w/D = 1/5; D_1/D = 3/4; l/D = 1/4; t/D = 1/50; six blades).

LDA measurements

The LDA measurements of all the three velocity components (radial, tangential, axial) were performed in the impeller discharge stream. In this case the radial and tangential velocity components were measured simultaneously by 2D LDA system through the vessel flat bottom. Consecutively, the measurement of the axial velocity was carried out through the vessel wall using optical box around the cylindrical vessel filled with water. Radial, tangential and axial instantaneous velocities were measured in vertical planes between two adjacent baffles (in radial non-dimensional coordinates $r^* = 2r/D$: 1.05; 1.1; 1.2; 1.4; 1.6; 1.8; 2.0; 2.2, Figure 1). In each position, 21 points were measured.

RESULTS

The data from LDA measurements were treated by ensemble-averaging. The ensemble-averaged mean velocities are shown in Figure 2, where the radial, tangential and axial velocity components are depicted separately. The root mean square values (*RMS*) of ensemble-averaged velocity fluctuations are depicted in Figure 3. Since the LDA data were taken in a burst-mode the measured velocities were biased. To eliminate the bias effect, we used a residence time weighting procedure based on a burst length (L_B), for each velocity component (radial, tangential, axial) the ensemble-averaged mean was evaluated from:

$$U = \sum_j u_j (L_B)_j / \sum_j (L_B)_j \,, \tag{2}$$

and *RMS* value:

$$u' = \sqrt{\sum_j (u_j - U)^2 (LE)_j / \sum_j (L_B)_j} \,. \tag{3}$$

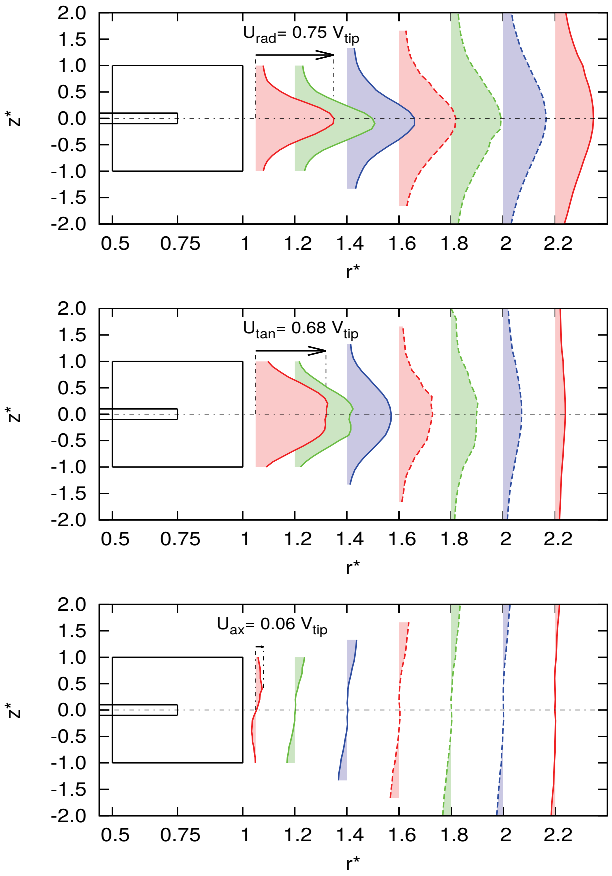

Figure 2. Mean ensemble-averaged velocity profiles (impeller speed 400 rpm): radial (top), tangential (middle) and axial (bottom).

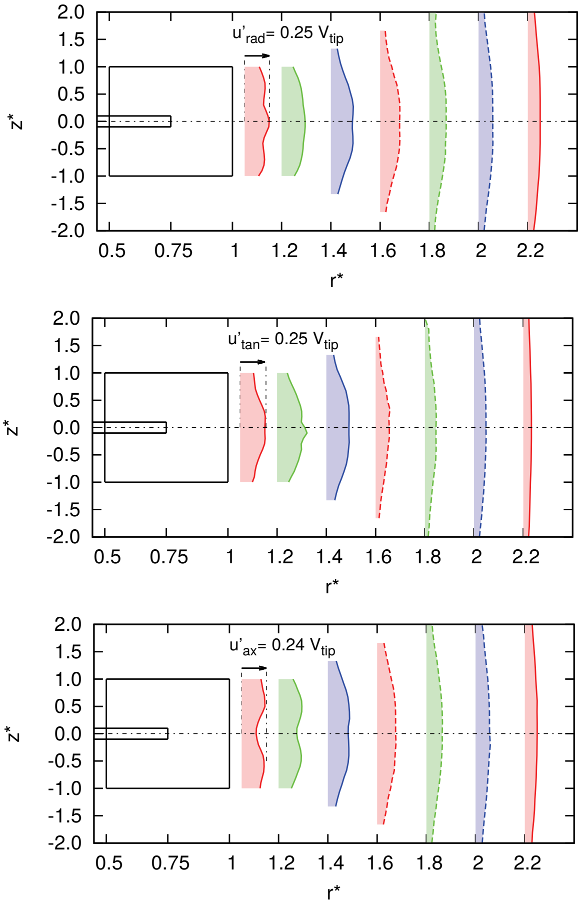

Figure 3. Velocity profiles of RMS values of the fluctuation velocities (impeller speed 400 rpm): radial (top), tangential (middle) and axial (bottom).

The index j is the number of the burst record. The variable $(L_B)_j$ indicates time length of the burst (5--500 μs) and u_j is the evaluated instantaneous velocity. The typical number of the burst records was around 80000 samples with the data rate of approximately 500 samples per second. The minimal measurement time length was 120 s and maximal 180 s. The final number of samples and the data rate were affected by the measured velocities at each point. Hence, in the main flow, the data rate was doubled on approximately 1000 samples per second and 130000 samples, while for some points outside the flow or for points with very low velocities (namely for axial velocity component) the data rate was very low, around 250 samples per second and number of samples around 30000.

From the time data series the temporal velocity analysis in each measured point was carried out autocorrelation function (ACF) and power spectrum. The periodic and random parts were segregated using the ACF separation approach [1].

Averaged velocity results

Axial profiles of radial, tangential, axial mean ensemble-averaged velocity components are shown in Figure 2 in dimensionless form:

$$U_i^* = U_i / V_{\mathrm{tip}} \tag{4}$$

where V_{tip} is the impeller tip speed and i denotes the axial, tangential or axial velocity component. Corresponding profiles of the ensemble-averaged dimensionless *RMS* of the radial, tangential, axial velocity fluctuations in the discharge stream from a standard Rushton turbine impeller were calculated likewise:

$$u'_i = u'_i / V_{\mathrm{tip}} \tag{5}$$

The obtained results are shown in Figure 3. The dimensionless coordinates in Figures 2 and 3 are defined as:

$$z^* = 2z/w \text{ and } r^* = 2r/D = \text{const.} \tag{6}$$

where w is the height of the impeller blade and D is the impeller diameter.

The obtained results of mean ensemble-averaged values were compared with other published ones (Figure 5). It is obvious that the "mean and *RMS*" are sensitive to the averaging process. The data rate, averaging time and spatial resolution of the measurement method are important parameters namely in zone of flow establishment (ZFE) [12]. The ensemble-averaged mean flow is influenced by intensive kinetic energy transfer in this zone reach onto r^* = 1.8. This phenomenon is caused by the effect of trilling vortices and their disintegration. This is in accordance with results obtained by other researchers [30,31,37].

Power spectrum analysis

The power spectrum at each measurement point was estimated by the slot correlation method [10]. Data of all three velocity components were analysed. As expected, the velocity data in the impeller (blade) vicinity contained significant periodic part, the frequencies of which corresponded to frequencies of the blade passing nN_B and their multiples. The harmonic signal slowly disappeared with increasing remoteness from the impeller blade due to decomposition of trailing vortices. The damping of periodic component along radial axis at the impeller disk level is shown in Figure 4. It is obvious that periodicity also appears behind the interface between the ZFE and ZEF at r^* = 1.6 [12], but the periodic component becomes negligible in comparison with the random one. It is also shown that the periodic behaviour is not equal for all velocity components.

Comparison with other results

The mean ensemble-averaged velocities were compared with the data from [1,31,36]. The axial profiles of radial, tangential and axial component is shown in Figure 5 (top), in which the results from dimensionless radius r^* = 1.07 from literature are compared with the present measurements from r^* = = 1.05. There is very good agreement with the data obtained by Escudie and Line [31] by the PIV method. The profiles were only shifted to axis of symmetry. The shape and magnitudes were almost the same.

The kinetic energy represented by the periodic and random part of the velocity fluctuations for each velocity component was compared with the results obtained by Escudie and Line [31]. Their results were compared with the results obtained by Wu and Patterson [1] and they concluded in a good agreement. The comparison of our results with Escudie and Line [31], shown in Figure 5 (bottom), was also in a good agreement, where the values of both periodic and random were almost the same. The discrepancy was only in symmetricity, where our results were quite symmetric.

Distribution of decomposed velocity components

The dimensionless *RMS* values from all 168 measurement points were included in the contour plots to map the distribution of the velocity fluctuations in the impeller discharge stream. The results at 200 rpm are shown in Fig. 6 (the first column); the derived periodic components (the second column); the derived random components (the third column). The top figure represents radial velocity component, the middle one tangential and the bottom one axial component. The results of 400 rpm are depicted in Fig. 7. Results from both impeller speeds are similar in shape, but the results from higher impeller speed have slightly longer operating range. It should be in accordance with the operation of higher inertial

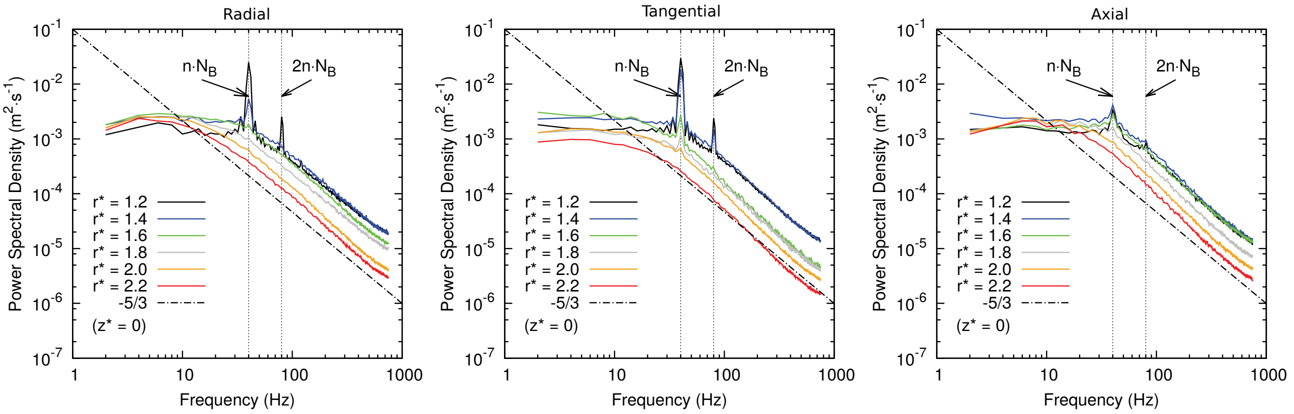

Figure 4. Comparison of the power spectra of radial, tangential and axial velocity component (400 rpm) along the discharge stream in the level of horizontal plane of the turbine disc (n - impeller speed, N_B - number of blades).

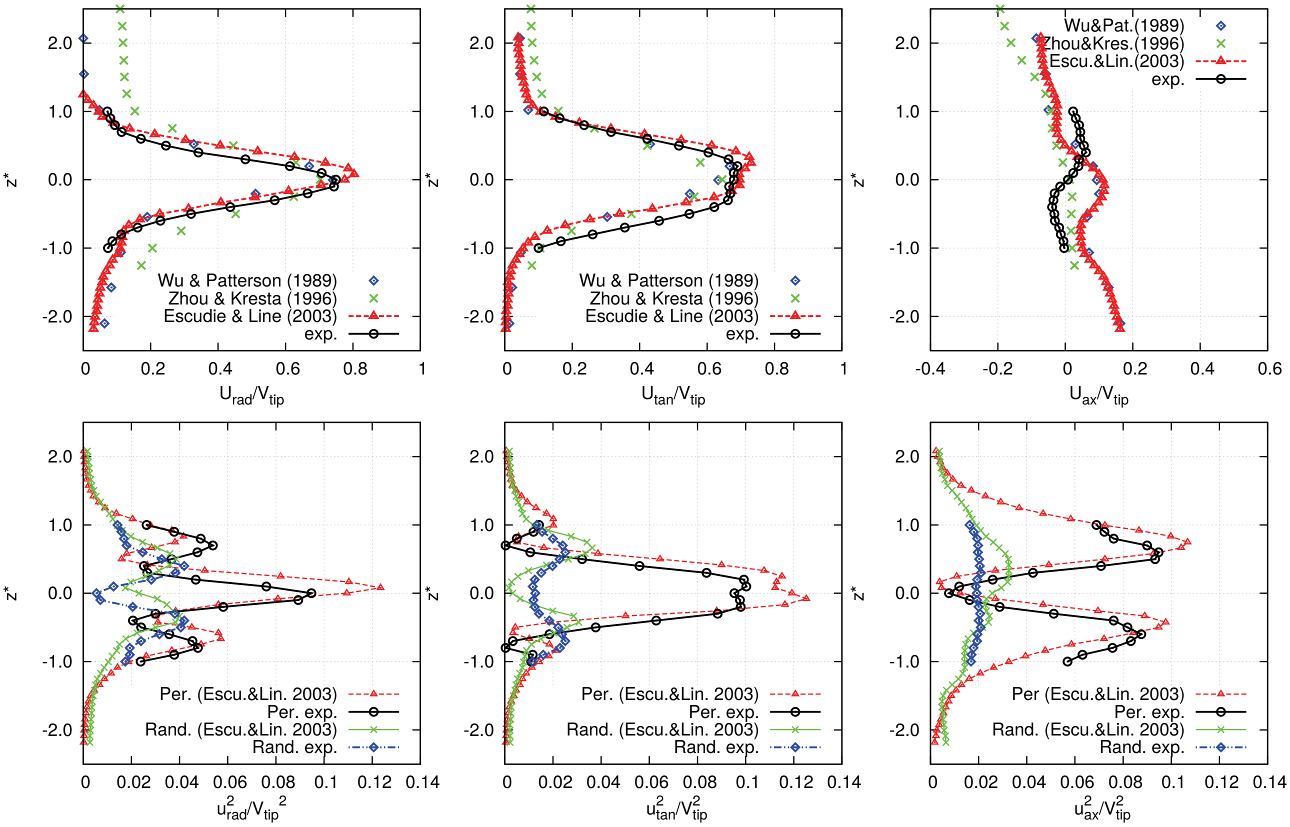

Figure 5. Comparison of the mean ensemble-averaged velocity profiles of the radial, tangential and axial velocity component obtained at r = 1.07 [1,31,36] with the present measurements at r* = 1.05, and comparison of the periodic and random (turbulent) kinetic energy [31] (below).*

forces. The direct measurements of trailing vortices indicate similar trend. The contour plots of evaluated *RMS* dimensionless values u_i'/V_{tip} indicate:

i) The operating radius of the radial velocity fluctuations is longer than for tangential ones.

ii) The axial velocity fluctuations show similar trend as radial ones.

iii) The diagram of the axial fluctuations indicates a distribution onto upper and lower part according to the mean axial velocity maximums.

The decomposed periodic components $u^{(per)}/V_{tip}$ depicted in Figures 6 and 7 (middle) show:

i) Radial periodic component contains three significant peaks, while the tangential contains only one and axial contains two.

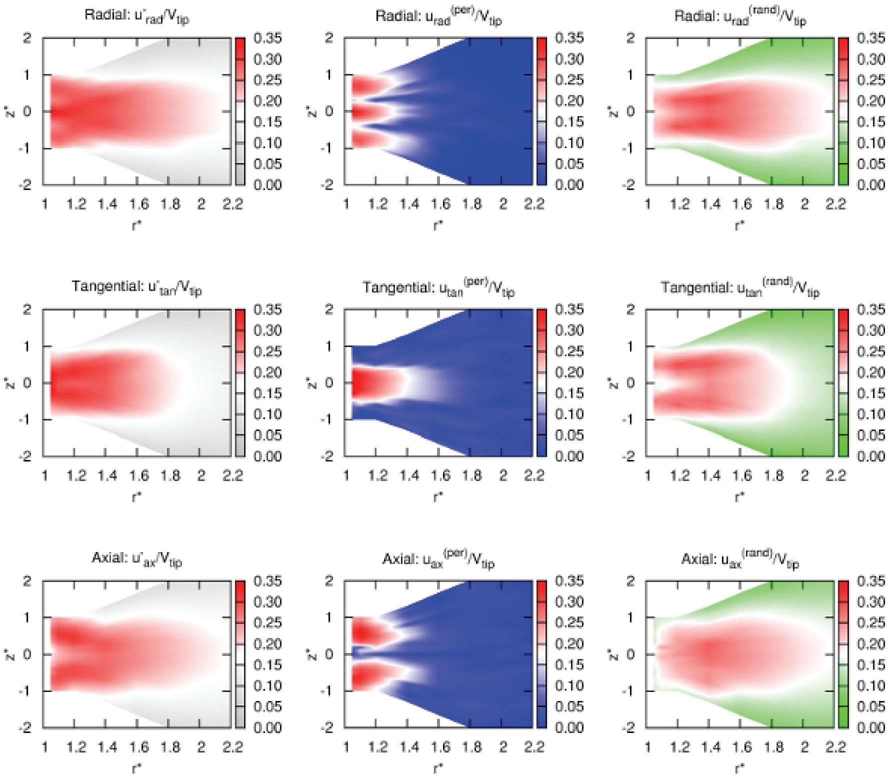

Figure 6. Dimensionless RMS values (first column), derived periodic components (second column) and derived random components (third column) of fluctuation velocity. The top figure represents radial velocity component, the middle one tangential and the bottom one axial (impeller speed 200 rpm).

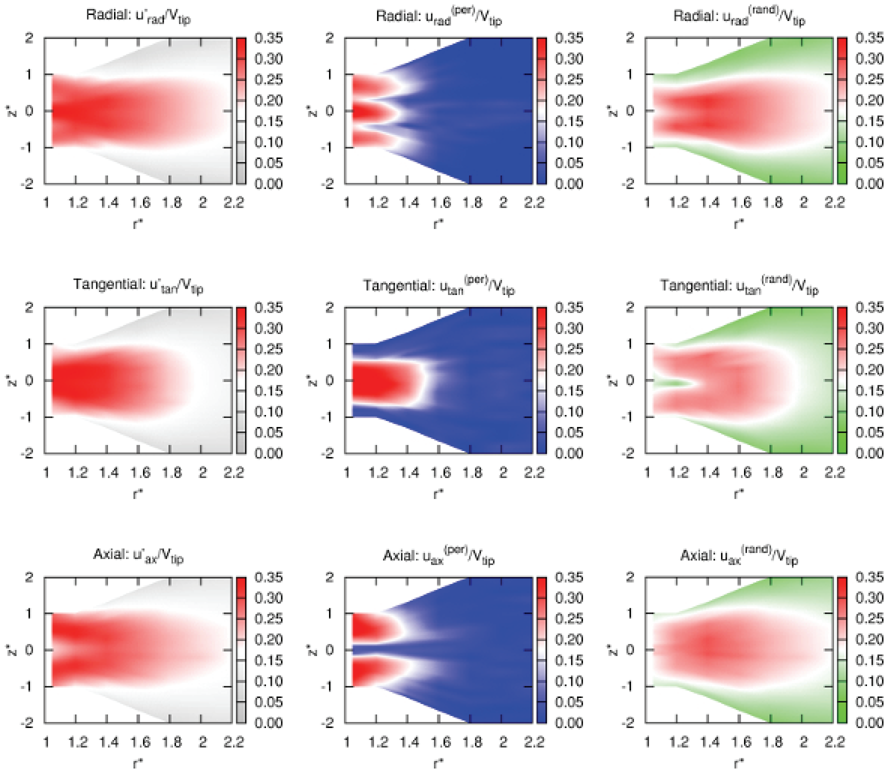

Figure 7. Dimensionless RMS values (first column), derived periodic components (second column) and derived random components (third column) of the fluctuation velocity. The top figure represents radial velocity component, the middle one tangential and the bottom one axial (impeller speed 400 rpm).

ii) The peaks headed in parallel with upper and lower blade edge which appeared in radial and axial periodic components are probably caused by trailing vortices movement.

iii) The peaks in the middle of the blade appeared only in radial and tangential components are obviously generated by potential flow jet induced after blade passing.

The dimensionless random velocity component $u^{(\mathrm{rand})}/V_{\mathrm{tip}}$ which should be proportional to real turbulent kinetic energy is shown in Figures 6 and 7 (right). It could be found that:

i) In the vicinity of the blade there are two regions of different behaviour of both the tangential and the radial random components. On the horizontal axis of the impeller the values of the tangential and radial random components are lower that indicates a region of the potential core. With increasing axial distance the values of the random components increase that indicates a formation of the trailing vortices.

ii) The removal of the periodic velocity component reduces the magnitude of the axial random component, which could indicate that the periodic component is the main part of the axial flow.

Turbulent kinetic energy

Turbulent kinetic energy is described as the energy dissipated by vortices in small scales. That is why the periodic velocity component, which only transports kinetic energy, is removed from the measured data. The total kinetic energy is calculated from:

$$k = \frac{1}{2}\left(u'^2_{\mathrm{rad}} + u'^2_{\mathrm{tan}} + u'^2_{\mathrm{ax}}\right) \tag{7}$$

where u'_{rad}, u'_{tan} and u'_{ax} are obtained *RMS* values for radial, tangential, axial velocity component, respectively. The results are depicted in Figure 8, where the kinetic energy was calculated for *RMS* values (top figure), periodic (middle figure), and random ones (bottom figure). The kinetic energy component distributions are well described in region between $r^* = 1.05$ and 2.2. The kinetic energy distributions are in agreement with results obtained from the PIV measurements published by Escudie and Line [31]. The maximum values of random (turbulent) kinetic energy are approximately at dimensionless radius $r^* = 1.4$, where the kinetic energy, which is proportional to the periodic velocity component, becomes indifferent. Nevertheless, it is necessary to mention that the results are obtained as ensemble-averaged ones and it is very disputable to use them for prediction of the real time distribution in an agitated tank, moreover, the values of the turbulent kinetic energy are evaluated only for limited spatial and temporal resolution and the corrections for the resolution to Kolmogorov scales should be demanded. However, the obtained kinetic energy distributions are very useful for validations of the turbulent models and kinetic energy transfer equations used in the CFD modelling [37].

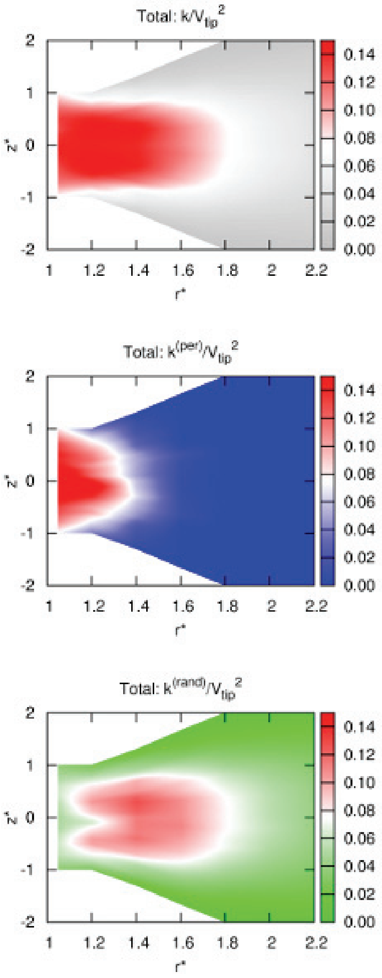

Figure 8. Calculated kinetic energy (Eq. (7)) from all the measured RMS velocity components (top), derived periodic (middle) and random (bottom) components of the fluctuation velocity in the impeller discharge stream (impeller speed 400 rpm).

CONCLUSIONS

Results from LDA measurements in ensemble-averaged mode are usable for detection of periodic phenomena in the impeller discharge stream of the Rushton turbine impeller. The temporal analysis of the measured data verifies the presence of three zones in the impeller discharge stream: the potential core, where the periodic component is dominant, the second zone (called the zone of flow establishment), where both periodic and random components are taking place, and the third zone (called the zone of established flow), where the random component is dominant and the periodic component of flow is negligible. The periodic component in the impeller disk plane seems to be negligible approximately at the dimensionless radius $r^* = 1.7$. The profiles of periodic component show different shape for each (radial, tangential, axial) velocity component. Profiles of the radial velocity component have three significant peaks, while for the tangential one peak and for axial two peaks were observed. Comparison of two impeller speeds (200 and 400 rpm) in the dimensionless form shows little discrepancy, where the higher impeller speed has longer operating range than the lower one. It should be in accord with acting of the higher inertial forces, but the measurements accuracy has not allowed identifying such a phenomenon completely up to now.

Symbols

b	Baffle width, m
C	Off-bottom clearance, m
D	Impeller diameter, m
f	Frequency, s^{-1}
H	Total liquid depth, m
L_B	Burst length, s
n	Impeller speed, s^{-1}
N_B	Number of blades
r^*	Dimensionless radius of agitated vessel
Re_M	Impeller Reynolds number
t	Time, s
T	Vessel diameter, m
V_{tip}	Impeller tip speed, $m \cdot s^{-1}$
U	Mean ensemble-averaged velocity, $m \cdot s^{-1}$
u'	Root mean square of measured velocity fluctuations, $m \cdot s^{-1}$
$u^{(per)}$	Periodic velocity component, $m \cdot s^{-1}$
$u^{(rand)}$	Random velocity component, $m \cdot s^{-1}$
z^*	Dimensionless height of agitated vessel

Greek Letters

μ	Kinematic viscosity of agitated liquid, $m^2 \cdot s^{-1}$
ρ	Density of agitated liquid, $kg \cdot m^{-3}$

Acknowledgements

This research has been subsidized by the research project No. GA CR 16-20175S and RVO: 67985874.

REFERENCES

[1] H. Wu, G.K. Patterson, Chem. Eng. Sci. **44** (1989) 2207-2221

[2] M. Schafer, M. Hofken, F. Durst, Chem. Eng. Res. Des. **75** (1997) 729-736

[3] A. Bakker, R.D. Laroche, M.H. Wang, R.V. Calabrese, Chem. Eng. Res. Des. **75** (1997) 42-44

[4] J. Derksen, H.E.A. Van den Akker, AICHE J. **45** (1999) 209-221

[5] K.V. Sharp, R.J. Adrian, AIChE J. **47** (2001) 766-778

[6] S.M. Kresta, K.J. Bittorf, D.J. Wilson, AIChE J. **47** (2001) 2390-2401

[7] A. Delafosse, A. Line, J. Morchain, P. Guiraud, Chem. Eng. Res. Des. **86** (2008) 1322-1330

[8] J.J.J. Gillissen, H.E.A. Van den Akker, AIChE J. **58** (2012) 3878-3890

[9] B. Kysela, J. Konfrst, I. Fort, Z. Chara, Int. J. Chem. Eng. **2014** (2014) 1-7

[10] B. Kysela, J. Konfrst, Z. Chara, EPJ Web Conf. **45** (2013) 1-6

[11] B. Kysela, J. Konfrst, I. Fort, M. Kotek, Z. Chara, Chem. Process Eng. **35** (2014) 137-147

[12] R. Ben-Nun, M. Sheintuch, B. Kysela, J. Konfrst, I. Fort, AIChE J. **61** (2015) 1413-1426

[13] K.C. Lee, M. Yianneskis, AIChE J. **44** (1998) 13-24

[14] S. Baldi, A. Ducci, M. Yianneskis, Chem. Eng. Technol. **27** (2004) 275-281

[15] M.H. Vakili, M.N. Esfahany, Chem. Eng. Sci. **64** (2009) 351-362

[16] A.H. Alexopoulos, D. Maggioris, C. Kiparissides, Chem. Eng. Sci. **57** (2002) 1735-1752

[17] H. Bashiri, M. Heniche, F. Bertrand, J. Chaouki, Can. J. Chem. Eng. **92** (2014) 1070-1081

[18] [18] J. J. Derksen, M. S. Doelman, H. E. A. Van den Akker, Exp. Fluids 27 (1999) 522-532.

[19] R. Escudie, D. Bouyer, A. Line, AIChE J. **50** (2004) 75-86

[20] R. Escudie, A. Line, AIChE J. **53** (2007) 523-526

[21] J. Zhao, Z. Gao, Y. Bao, Chin. J. Chem. Eng. **19** (2011) 232

[22] A. Bakker and L. M. Oshinowo, Chem. Eng. Res. Des. **82** (2004) 1169-1178

[23] A. Kukukova, M. Mostek, M. Jahoda, V. Machon, Chem. Eng. Technol. **28** (2005) 1125-1133

[24] M. Jahoda, M. Mostek, A. Kukukova, V. Machon, Chem. Eng. Res. Des. **85** (2007) 616-625

[25] J.B. Joshi, N.K. Nere, C.V. Rane, B.N. Murthy, C.S. Mathpati, A.W. Patwardhan, V.V. Ranade, Can. J. Chem. Eng. **89** (2011) 23-82

[26] I. Fort, M. Hrach, H.O. Mockel, J. Drbohlav, Collect. Czech. Chem. Commun. **44** (1979) 700-710

[27] V. Kolar, P. Filip, A. G. Curev, Appl. Sci. Res. **39** (1982) 329-335

[28] V. Kolar, P. Filip, A. G. Curev, Chem. Eng. Commun. **27** (1984) 313-326

[29] J. Talaga, I. Fort, in Proceedings of 14th Eur. Conf. Mixing, Warszava, Poland, 2012

[30] Z. Chara, B. Kysela, J. Konfrst, I. Fort, Appl. Math. Comput. **272** (2016) 614-628

[31] R. Escudie, A. Line, AIChE J. **49** (2003) 585-603

[32] A. Line, J.-C. Gabelle, J. Morchain, D. Anne-Archard, F. Augier, Chem. Eng. Res. Des. **91** (2013) 2073-2083

[33] D. Jasikova, M. Kotek, V. Kopecky, Act. Mater. Adapt. Struct., Proc. SPIE Conf. **9442** (2015) 1-7

[34] V.V. Ranade, M. Perrard, N.L. Sauze, C. Xuereb, J. Bertrand, Chem. Eng. Res. Des. **79** (2001) 3-12

[35] K.V. Sharp, D. Hill, D. Troolin, G. Walters, W. Lai, Exp. Fluids **48** (2009) 167-183

[36] G. Zhou, S. M. Kresta, Trans. Inst. Chem. Eng. **76** (1996) 379-389

[37] H. Singh, D.F. Fletcher, J.J. Nijdam, Chem. Eng. Sci. **64** (2011) 5976-5988.

BOHUŠ KYSELA[1]
JIŘÍ KONFRŠT[1]
ZDENĚK CHÁRA[1]
IVAN FOŘT[2]

[1]Institute of Hydrodynamics, AS CR, v.v.i., Prague, Czech Republic.
[2]Department of Process Engineering, Faculty of Mechanical Engineering, CTU in Prague, Prague, Czech Republic

NAUČNI RAD

STRUKTURA TURBULENTNOG POLJA BRZINE POTISNE STRUJE STANDARDNE RUŠTONOVE TURBINSKE MEŠALICE

Radijalni mlaz standardne Ruštonov turbinske mešalice je proučavan metodom laserske Doplerove anemometrije (LDA). Za merenje aksijalnog profila odabrano je nekoliko rastojanja od lopatica mešalice (u radijalnom smeru), pri čemu su sve tri komponente brzine (radijalna, ugaona i aksijalna) merene sa vremenom u svakoj tački aksijalnog profila. Zabeležene brzine su analizirane, a usrednjene vrednosti su razložene na tri dela: srednji (ensemble-average), slučajni i periodični. Veličina periodičnog dela brzine je procenjena na svakom mernom mestu i za sve komponente brzine. Dobijeni rezultati ukazuju na oblasti gde periodični deo brzine ima značajan uticaj i gde je njegov doprinos gotovo zanemarljiv. Iako su vrednosti periodičnog dela svih komponenti brzine slične, prostorne raspodele se razlikuju u ispitivanoj oblasti.

Ključne reči: Ruštonova turbinska memšalica, laserska Doplerova anemometrija, potisna struja, sud sa mešanjem.

CI&CEQ
Chemical Industry & Chemical Engineering Quarterly

Available on line at
Association of the Chemical Engineers of Serbia *AChE*
www.ache.org.rs/CICEQ

Chem. Ind. Chem. Eng. Q. 23 (2) 161–167 (2017) CI&CEQ

LINA LV[1]
RUI GAO[1]
JIANBIN YANG[2]
ZHIGANG SHEN[2]
YANBO ZHOU[1]
JUN LU[1]

[1]Key Laboratory of Coal Gasification and Energy Chemical Engineering of Ministry of Education, East China University of Science and Technology, Shanghai, China
[2]R&D Center, Shanghai Oriental Enviro-Industry Co., Ltd., Shanghai, China

SCIENTIFIC PAPER

UDC 666.9.022.6:54:66

INVESTIGATION OF ORGANIC DESULFURIZATION ADDITIVES AFFECTING THE CALCIUM SULFATE CRYSTALS FORMATION

Article Highlights

- The optimal experimental conditions for calcium sulfate crystals formation were found
- Mg^{2+}, Al^{3+} and Fe^{3+} inhibit calcium sulfate formation, Fe^{3+} being the strongest inhibitor
- Induction time, moisture content, particle size distribution, and crystal morphology were analyzed
- The influence of organic desulphurization additives on calcium sulfate formation was studied
- Citric acid and sodium citrate can improve the removal of SO_2 and quality of calcium sulfate

Abstract

In the study, the optimal experimental conditions for gypsum crystals formation were 323 K, 300 rpm stirring speed. The major impurities of Mg^{2+}*,* Al^{3+} *and* Fe^{3+} *were found to inhibit calcium sulfate crystals formation.* Fe^{3+} *caused the strongest inhibition, followed by* Mg^{2+} *and* Al^{3+}*. The influence of desulfurization additives on the gypsum crystals formation was explored with the properties of moisture content, particle size distribution and crystal morphology. The organic desulfurization additives of adipic acid, citric acid, sodium citrate and benzoic acid were investigated. Citric acid and sodium citrate were found to improve the quality of gypsum. Moisture contents were reduced by more than 50%, gypsum particle sizes were respectively enlarged by 9.1 and 22.8%, induction time extended from 4.3 (blank) to 5.3 and 7.8 min, and crystal morphology trended to be thicker.*

Keywords: calcium sulfate crystals, desulfurization additives, impurities, wet flue gas desulfurization.

The limestone-gypsum wet flue gas desulfurization (WFGD) process is the most widely used desulfurization technology in Chinese coal-power plants, for removing acidic compounds (SO_2, HCl and HF) from flue gases [1-3]. In WFGD system, SO_2 gases are absorbed by the limestone slurry, and SO_2 combines with H_2O to produce HSO_3^- ions. In the slurry holding tank, HSO_3^- are oxidized to SO_4^{2-} by injected oxygen. Finally, SO_4^{2-} combine with the Ca^{2+} to produce calcium sulfate dihydrate crystals, which is an unsolvable chemical. Gypsum can be refined for commercial applications. The quality of formatted gypsum crystals is related to process conditions, including temperature, stirring speed, impurities and so on [4-6]:

$$CaCO_3(s)+SO_2(g)+2H_2O(l)+0.5O_2(g)\rightarrow$$
$$\rightarrow CaSO_4\cdot 2H_2O(s)+CO_2(g) \qquad (1)$$

Mg^{2+}, Al^{3+} and Fe^{3+} are three common impurity ions in wet FGD slurry. The effects of Mg^{2+} and Al^{3+} on gypsum crystallization in a $CaCl_2$-Na_2SO_4-H_2O system have been investigated by many authors. In the presence of Mg^{2+}, the growth rate of gypsum crystal was reduced and the crystals were elongated,

---

Correspondence: J. Lu, Key Laboratory of Coal Gasification and Energy Chemical Engineering of Ministry of Education, East China University of Science and Technology, No. 130, Meilong Road, Shanghai 200237, People's Republic of China.
E-mail: lujun@ecust.edu.cn; mail: lln224@126.com
Paper received: 23 November, 2015
Paper revised: 31 March, 2016
Paper accepted: 26 April, 2016

https://doi.org/10.2298/CICEQ151123027L

while the growth rate of gypsum crystal increased in the presence of Al^{3+}.

As the emission standard of SO_2 reduced to 50 mg/m^3, the existing WFGD techniques were required to improve. Adding organic desulfurization additive has been proven to be the most efficient and economical means to enhance SO_2 removal from power plants [3]. Organic desulfurization additives have been developed to significantly improve SO_2 removal in WFGD systems in the past decade, such as formic acid, adipic acid, maleic acid, acetic acid, citric acid, sodium citrate and benzoic acid [7-9]. However, there is concern that addition of desulfurization additives may undermine the quality of produced calcium sulfate crystals [10].

Purity, moisture content and particle size distribution (PSD) were usually considered as end use characteristics of gypsum. Gypsum with low quality cannot meet the standard for commercial applications and is considered as solid waste. Many organic acids have been reported to change the crystallinity and affect calcium sulfate crystal morphology (both size and shape), such as citric acid [11,12].

In this study, besides the influence of experimental conditions on the calcium sulfate crystals, the effect of four common desulfurization additives (adipic acid, citric acid, sodium citrate and benzoic acid) were also investigated.

MATERIALS AND METHODS

Chemicals and materials

Analytically pure adipic acid, citric acid, sodium citrate, benzoic acid, $CaCl_2$, HCl, Na_2SO_4 and $Ca(OH)_2$ were supplied by Sinopharm Chemical Reagent Co., Ltd. (Shanghai, China). The initial pH of $CaCl_2$ solution was adjusted by the addition of HCl and $Ca(OH)_2$ solution; the initial pH of solution was adjusted to 5.4±0.2. The metal ions, Mg^{2+}, Al^{3+} and Fe^{3+} were added as the form of $MgCl_2$, $AlCl_3$ and $FeCl_3$, which were also supplied by Sinopharm Chemical Reagent Co., Ltd. (Shanghai, China).

The pH of solution was monitored by using a Bante 901b pH meter, and solution conductivity was measured by using a Bante 901b conductivity meter. The PSD analysis was performed using an LS-POP (VI) laser particle size analyzer, and the crystal morphology structure was observed by using an SEM Quanta 250 scanning electron microscope.

The induction time was determined by the solution conductivity. In the conductivity curve, the time of peak is the induction time. At the same time, initial precipitation was observed visually and the solutions became turbid [13].

Experimental procedure

The experimental setup was a thermostatic crystallization reactor. Thermostatic water baths were used to maintain the temperature of Na_2SO_4 solution storage tank and crystallization reactor at 323 K.

The first step was the addition of 250 mL 0.5 mol/L $CaCl_2$ solution and additives or metal ions (if need) to the crystallization reactor. The concentration of additive was 2 mmol/L, and the content of metal ions was 300 mg/L. The concentrations were set to be similar to the FGD system in coal-power plants. Then, 0.5 mol/L Na_2SO_4 solution was slowly feed to the crystallization reactor by a peristaltic pump with a flow rate of 7 mL/min.

Conductivity of the reaction solution was monitored throughout the 30-min experiment. Besides, all slurry samples were taken for analyses of moisture content, PSD, and crystal morphology.

Analyses of calcium sulfate crystals properties

The quality of formatted calcium sulfate crystals was analyzed. Moisture content, particle size distribution (PSD), and crystal morphology were three targeted properties for calcium sulfate crystals.

The moisture content was analyzed with the help of a vacuum pump. A 100 mL slurry sample was compressed by suction filter at 0.1 MPa for 10 min. Then, the moisture content was obtained by measuring the reduction of water at 313 K after 24 h. The dried samples were stored in a dryer.

The PSD was analyzed by using a laser particle size analyzer and the crystal morphology was analyzed by using a scanning electron microscope. A total of 0.5 to 1.0 mg dried samples was needed for PSD analysis and crystal morphology structure analysis, respectively.

RESULTS AND DISCUSSION

The experimental conditions, such as temperature, stirring speed, impurities and so on, were investigated in this part [14,15], and the optimal experimental conditions for calcium sulfate crystals formatting were determined. The particle size distributions (PSD) of calcium sulfate crystals were determined as the quality property of calcium sulfate crystal.

Effect of temperature

The formation of calcium sulfate crystal includes two steps: nucleation and growth. The temperature during crystallization process was found to have great influence on both crystal nucleation and growth [4,10,16]. On the one hand, increasing temperature causes lower viscosity and less strong surface tension of slurry, which will improve the ion diffusion and the nucleation rate. As a result, the initial nucleation time is reduced, while crystal growth time is increased. On the other hand, the solubility of calcium sulfate dehydrate is also decreased with increased temperature, which results in the reduction of further nucleation driving force and crystal growth rate [8]. Hence, there is an optimal temperature for calcium sulfate crystal formatting.

The PSD of calcium sulfate crystals at different temperatures are shown in Figure 1. There were three peaks in the differential distribution curves, and the grain diameters of three peaks were about 9, 20 and 75 μm. At the peak of 20 μm, the peak value of 323 K was lower than others, while at the peak of 75 μm the value was higher than others. So at 323 K, there were fewer small diameter crystals than others, and the rise of nucleation rate is greater than the decrease of growth rate.

At 323 K, the gypsum crystal particle size was the largest (D_{50} = 57.43 μm, where D_{50} is the diameter value as the percentage of cumulative distribution reaches 50%). 323 K was chosen as the optimal experimental temperature for calcium sulfate crystal formation.

Effect of stirring speed

The stirring speed during calcium sulfate crystal formation process was also found to affect crystal nucleation and crystal growth.

On one hand, increasing stirring speed is helpful for ion diffusion, which can reduce the possibility of high local ion concentration and obtain a uniform super-saturation of solution. On the other hand, increasing stirring speed is beneficial for the acceleration of the nucleation rate and crystal growth rate. However, dissolution is in a dynamic balance with crystallization. The increasing stirring speed is also helpful for dissolving the formed crystal nucleus. Faster stirring speed also leads to a higher possibility of breaking of formed crystals and grain refinement.

The result of stirring speed experiments is shown in Figure 2. There were also three peaks in the differential distribution curves, with grain diameters about 9, 20 and 75 μm. Obviously, the peak values of 300 rpm were lower than others at 9 and 20 μm, and the peak values of 300, 400 and 500 rpm were higher than others at 75 μm. Thus, the particle size of crystals at 300 rpm had a more concentrated ditribution and the D_{50} was also bigger, so the stirring speed of 300 rpm was a good choice for the experiments.

Effect of impurities

Mg^{2+}, Al^{3+} and Fe^{3+} are three common impurity ions in wet FGD slurries [17-19] that undermine calcium sulfate crystallization. Mg^{2+}, Al^{3+} or Fe^{3+} affect the gypsum crystallization in a similar way, by adsorb-

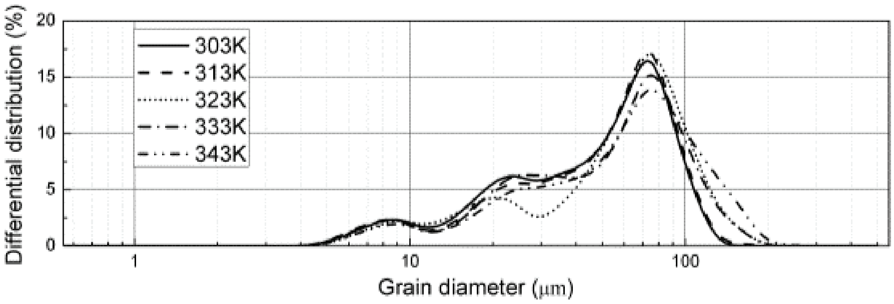

Figure 1. PSD of calcium sulfate crystals at different temperature.

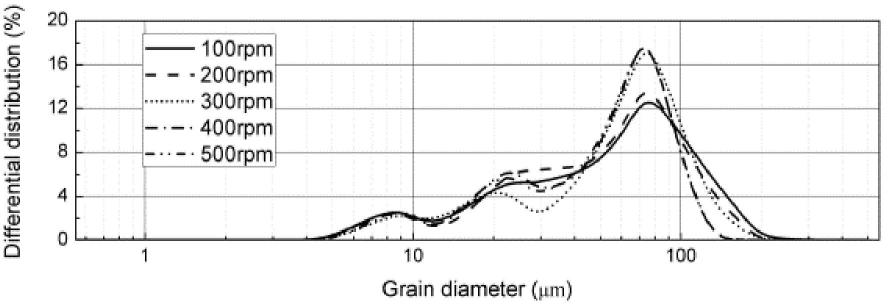

Figure 2. PSD of calcium sulfate crystals at different stirring speed.

ing on the crystal faces, occupying combining sites, and changing the super-saturation of solution. During the calcium sulfate crystals crystallization, Mg^{2+} will retard the nucleation phase by improving the surface tension and reducing super-saturation of solution [20].

PSD of calcium sulfate crystals formed in the presence of Mg^{2+}, Al^{3+} or Fe^{3+} are shown in Figure 3. At the peaks of 9 and 20 μm, the values of Fe^{3+} were higher than Mg^{2+} and Al^{3+}. In the presence of Mg^{2+}, Al^{3+} and Fe^{3+}, the peak values of 75 μm were all lower than the blank group.

The conclusion can be obtained that the Mg^{2+}, Al^{3+} and Fe^{3+} will inhibit the calcium sulfate crystal growth. At the present of 300 mg/L Mg^{2+}, Al^{3+} and Fe^{3+}, the calcium sulfate crystals particle size (D_{50}) decreased from 57.43±0.02 to 50.38±0.02, 51.41± ±0.02 and 46.19±0.02 μm, respectively. The inhibiting effect of Fe^{3+} on the gypsum crystallization was stronger than Mg^{2+}, which was also stronger than Al^{3+}.

Effect of desulfurization additives

At the experimental conditions of 323 K, 300 rpm, and no ion impurities, the effect of four common desulfurization additives (adipic acid, citric acid, sodium citrate and benzoic acid) on calcium sulfate crystals formation were studied. The induction time, moisture content, PSD and morphology of produced gypsum were all determined.

Comparison of induction time

Induction time is one of the most important dynamic features of crystallization processes. It is defined as the time when a constant super-saturation is created and crystals are detected [4]. The effects of each additive on the induction time of calcium sulfate crystals are shown in Figure 4. In the presence of citric acid and sodium citrate, the induction time increased from 4.3 (blank) to 5.3 and 7.8 min, respectively. Citrates can complex with Ca^{2+}, then decrease the initial super-saturation degree and increase the induction time. Therefore, there was enough time and space for calcium sulfate crystals to grow up in the present of citric acid and sodium citrate, and the crystal size became much larger.

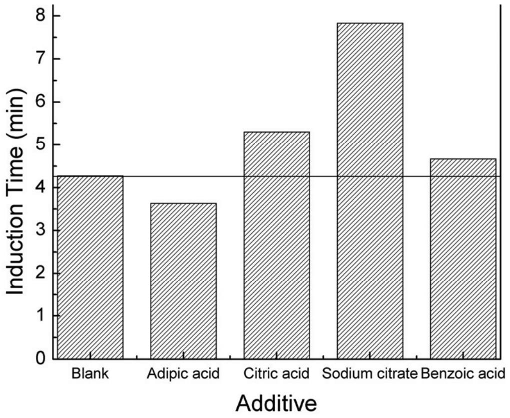

Figure 4. The induction time of calcium sulfate crystals.

Comparison of moisture content

Moisture content is a macroscopic property, which is associated with particle size distribution and crystal morphology.

The moisture content of calcium sulfate dihydrate determines the cost of gypsum dehydration. In the presence of adipic acid, citric acid, sodium citrate or benzoic acid, the moisture content of produced gypsum is shown in Figure 5. The values were 38.66, 39.82, 15.5, 17.94 and 37.91%, respectively.

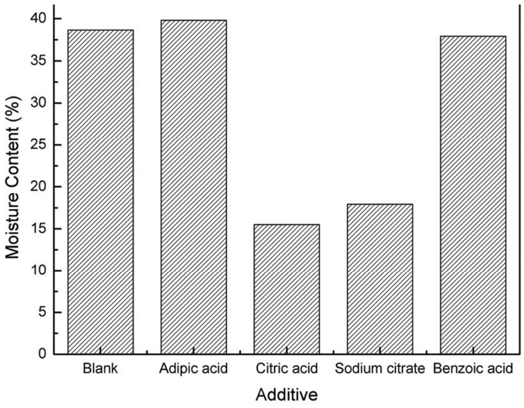

Figure 5. Gypsum moisture content of calcium sulfate crystals.

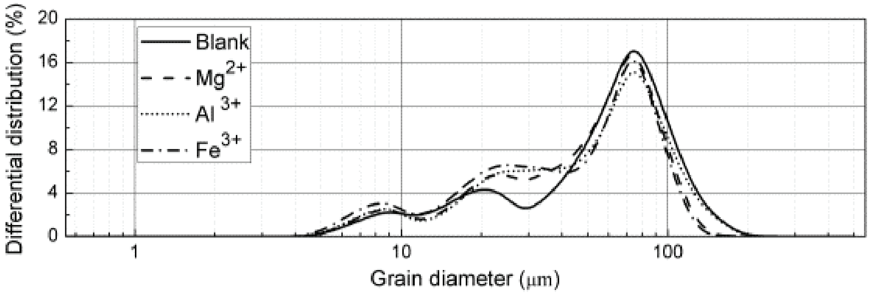

Figure 3. PSD of calcium sulfate crystals formed with Mg^{2+}, Al^{3+} or Fe^{3+} added.

The moisture content was relevant to the calcium sulfate dihydrate crystal shape and size. Low moisture content meant large and concentrated distributed particle size [11]. High moisture content always meant acicular and undersized crystals. the consequence of the citric acid and sodium citrate reducing the moisture content more than 50% can be observed in Figure 5.

Comparison of calcium sulfate crystal PSD

Particle size is the major property of calcium sulfate crystals, and D_{50} is the diameter value as the percentage of cumulative distribution reaches 50%. Obviously, in Figure 6a, in the presence of citric acid and sodium citrate, the particle sizes of calcium sulfate dihydrate crystals were bigger than others. In the group of differential distribution curves, there was only one peak for citric acid and sodium citrate experimental groups, the peaks of 9 and 25 μm were gone. Furthermore, the peak value of sodium citrate rose from 75 to 90 μm. The complexation between citrate and Ca^{2+} decreases the initial super-saturation degree and correspondingly increases the growth time and space [21]. As a result, the crystal size became much larger in the presence of sodium citrate. In Figure 6b, the cumulative distribution curves of citric acid and sodium citrate were on the right of the blank group.

Comparison of calcium sulfate crystal morphology

Calcium sulfate dihydrate crystals formed without any additive, showed needle-like shapes, with flat cross sections and smooth surface (Figure 7). In the presence of adipic acid or benzoic acid, there were no obvious effects on crystal morphology. However, the effects of citric acid and sodium citrate on crystals morphology were significant (Figure 8). Citric acid was found preferably to adsorb on c-axis that had the fastest growth rate [21]. In Figure 8a, calcium sulfate crystals transformed to irregular and thick flaky, with flat cross section, and non-smooth surfaces. Obviously, there was a trace of flaky growth on the formed crystals surface, which made the crystals thicker and greater. In Figure 8b, with the help of sodium citrate, the citrate concentration was higher than the citric acid, leading to a higher growth rate.

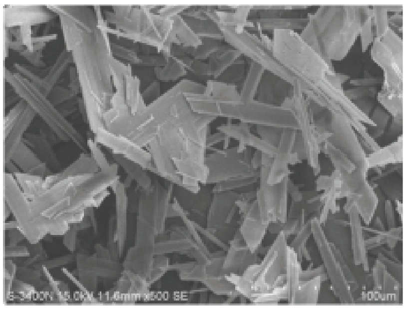

Figure 7. SEM image of calcium sulfate crystals without any additive.

Citric acid and sodium citrate had significant impacts on calcium sulfate dihydrate crystals morphology, which led to a non-flat crystal surface. And citric acid and sodium citrate changed the gypsum crystals morphology from needle-like shape to thick slab-like and columnar shape.

CONCLUSIONS

The investigation of experimental conditions, including temperature, stirring speed, and impurities,

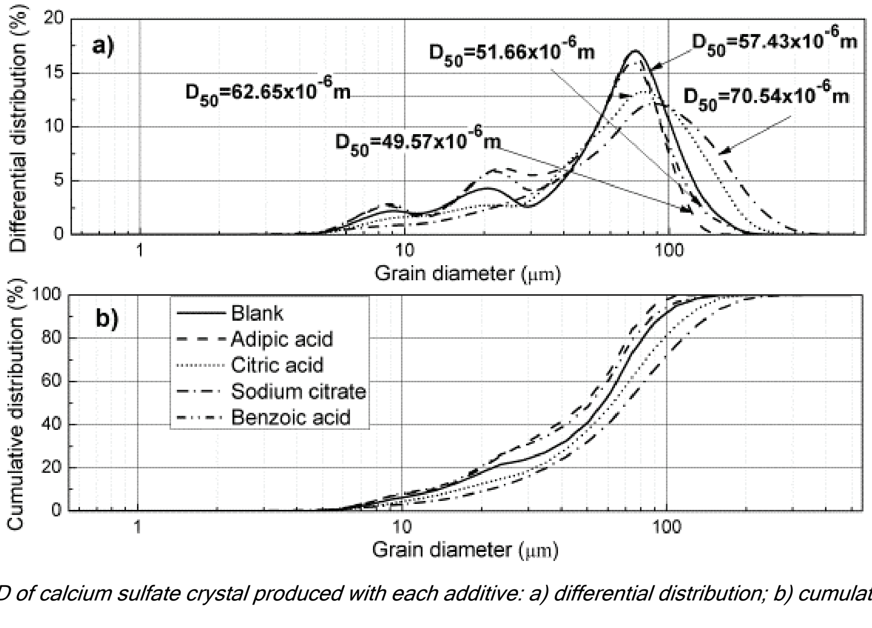

Figure 6. PSD of calcium sulfate crystal produced with each additive: a) differential distribution; b) cumulative distribution.

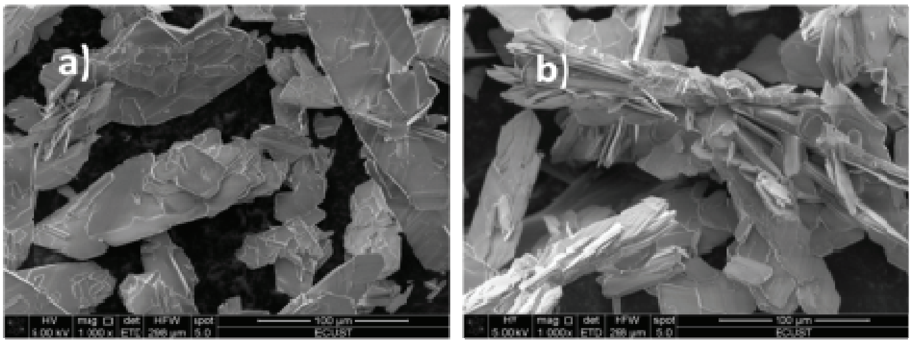

Figure 8. SEM images of calcium sulfate crystals: a) with citric acid added; b) with sodium citrate added.

showed that the optimal experimental temperature was 323 K, optimal stirring speed was 300 rpm, and Mg^{2+}, Al^{3+} and Fe^{3+} were the major impurities that should be considered. Those impurities inhibited the gypsum crystals formation, and Fe^{3+} ions caused the strongest inhibition, followed by Mg^{2+} and Al^{3+}.

The moisture content, particle size distribution and crystal morphology were the investigated properties of calcium sulfate crystals. Four common organic desulfurization additives – adipic acid, citric acid, sodium citrate and benzoic acid – were selected to research the influence of desulfurization additives on the calcium sulfate dihydrate crystals formation. Citric acid and sodium citrate were found to improve the quality of gypsum. Moisture contents were reduced by more than 50%, calcium sulfate particle sizes were respectively enlarged by about 9.1 and 22.8%, induction time extended from 4.3 (blank) to 5.3 and 7.8 min, and crystal morphology trended to be thicker, especially in the presence of sodium citrate.

Acknowledgements

The authors would like to express their sincere gratitude to Shanghai Oriental Enviro-Industry Co., Ltd., China, for their financial support of this study.

REFERENCES

[1] C. Feng, X. Gao, Y. Tang, J. Clean. Prod. **68** (2014) 81--92

[2] F. Yu, J. Chen, F. Sun, Energy Policy **39** (2011) 1586--1599

[3] H. Qi, B. Zhao, Cleaner Combustion and Sustainable World, Springer-Verlag, Berlin, 2013, p. 207

[4] S.A. Kulkarni, S.S. Kadam, H. Meekes, A. I. Stankiewicz, J. H. Horst, Cryst. Growth Des. **13** (2013) 2435-2440

[5] K. Luo, C. Li, L. Xiang, Particuology **8** (2010) 240-244

[6] Y.O. Rosenberg, I.J. Reznik, S. Zmora-Nahum, J. Ganor, Desalination **284** (2012) 207-220

[7] H. Barna, H. Melanie, S. Gunter, Appl. Energ. **114** (2014) 485-491

[8] S. Li, Progress in Environmental Science and Technology, Science Press, Beijing, 2009, p, 156

[9] S. Liu, W. Xiao, Chem. Eng. Technol. **29** (2006) 1167--1173

[10] S. Titiz-Sargut, P. Sayan, B. Avci, Cryst. Res. Technol. **42** (2007) 119-126

[11] T.S. Sibel, S. Perviz, K. Bercem, Chem. Eng. Technol. **33** (2010) 804-811

[12] M.M. Rashad, H.M. Baioumy, E.A. Abdel-Aal, Cryst. Res. Technol. **38** (2003) 433-439

[13] F. Rahman, Desalination **319** (2013) 79-84

[14] N. Thibaut, L.M. Yann, Ind. Eng. Chem. Res. **50** (2011) 7579-7592

[15] B.B. Hansen, F. Fogh, N.O. Knudsen, S. Kiil, Ind. Eng. Chem. Res. **50** (2011) 4238-4244

[16] B. Guo, L. Yang, Z. Wu, Z. Shen, X. Ma, Q. Ye, Fuel **88** (2009) 1286-1293

[17] S.K. Hamdona, U.A. AlHadad, J. Cryst. Growth **299** (2007) 146-152

[18] B.B. Hansen, S. Kiil, J.E. Johnsson, Fuel **90** (2011) 2965--2973

[19] F. Thomas, D.P. George, Ind. Eng. Chem. Res. **52** (2013) 6540-6549

[20] B. Guan, L. Yang, Z. Wu, Ind. Eng. Chem. Res. **49** (2010) 5569-5574

[21] J. Qu, J. Peng, B. Li, Adv. Mater. Res. **250-253** (2011) 321-326.

LINA LV[1]
RUI GAO[1]
JIANBIN YANG[2]
ZHIGANG SHEN[2]
YANBO ZHOU[1]
JUN LU[1]

[1]Key Laboratory of Coal Gasification and Energy Chemical Engineering of Ministry of Education, East China University of Science and Technology, Shanghai, China
[2]R&D Center, Shanghai Oriental Enviro-Industry Co., Ltd., Shanghai, China

NAUČNI RAD

UTICAJ ORGANSKIH ADITIVA ZA DESULFURIZACIJU NA FORMIRANJE KRISTALA KALCIJUM-SULFATA

Rezultati dobijeni u ovom radu pokazuju da su optimalni uslovi za formiranje kristala gipsa temperatura od 323 K i brzina mešanja 300 min^{-1}*. Joni* Mg^{2+}, Al^{3+} *i* Fe^{3+}*, koji su glavne nečistoće, inhibiraju formiranje kristala kalcijum sulfata.* Fe^{3+} *jon pokazuje najjače inhibitorno dejstvo. Uticaj aditiva desulfurizacije na formiranje kristala gipsa je praćen preko sadržaja vlage, distribucije veličine čestice i morfologije kristala. Pri tome je praćen uticaj organskih aditiva poput adipinske kiseline, limunske kiseline, natrijum citrata i benzoeve kiseline. Istraživanje pokazuje da limunska kiselina i natrijum citrat poboljšavaju kvalitet gipsa, Sadržaj vlage je redukovan više od 50%, dok je veličina čestica gipsa uvečana 9,1 i 22,8%, redom, vreme indukcije je povećano sa 4,3 (slepa proba) na 5,3 i 7,8 min, dok morfologija pokazuje tendenciju povećanja kristala.*

Ključne reči: kristali kalcijum sulfata, aditivi desulfurizacije, nečistoće, vlažna desulfurizacija dimnog gasa.

CI&CEQ
Chemical Industry & Chemical Engineering Quarterly
Available on line at
Association of the Chemical Engineers of Serbia AChE
www.ache.org.rs/CICEQ
Chem. Ind. Chem. Eng. Q. 23 (2) 169–175 (2017) CI&CEQ

BESHEIR AHMED A. ABD-EL-NABEY[1]
SHERIF EL-HOUSSEINY[1]
ESSAM KHAMIS[1]
ASHRAF MOUSTAFA ABDEL-GABER[1,2]

[1]Alexandria University, Faculty of Science, Chemistry Department, Ibrahimia, Alexandria, Egypt
[2]Department of Chemistry, Faculty of Science, Beirut Arab University, Lebanon

SCIENTIFIC PAPER

UDC 620.19:620.197.6:667.6

CORROSION PROTECTION AND ANTIFOULING PROPERTIES OF VARNISH-COATED STEEL CONTAINING NATURAL ADDITIVE

Article Highlights

- Testing of alternative use for cannabis extracts to control corrosion and fouling
- The amount of fouling organisms becomes less in the presence of 1.0 to 3.0 ppm
- Deterioration tendency of the varnish decrease with cannabis extract concentration
- Rusting along the scribe mark for varnish disappeared in presence of 3.0 ppm
- Cannabis extract offers good antifouling properties and good corrosion protection

Abstract

The corrosion protection and antifouling properties of varnish-coated steel panels containing different amounts of cannabis extracts were investigated using electrochemical impedance spectroscopy (EIS), salt spray and immersion tests in 0.5 M NaCl solution and subjected to a field test in seawater. Analysis of the experimental data showed that the presence of cannabis extract resisted the deterioration (peeling off) tendency of the varnish-coated steel panels exposed to aggressive environments. Visual inspection showed that the cannabis extract also provided good antifouling properties.

Keywords: corrosion, varnish, antifouling, salt spray, field test.

Corrosion protection by polymeric coatings is considered one of the best methods to protect metals exposed to corrosive marine environments. Salt-water immersion, partial immersion, and spray followed by drying winds are tests used to investigate and develop paints that protect the steel of a ship's hull. In addition to the problems of corrosion, the fouling of ships' bottoms with marine organisms leads to increased drag, which raises fuel consumption and affects maneuverability. The availability of effective anticorrosive and antifouling compositions is clearly of major interest to ship owners [1]. Previous studies on preventing the corrosion of steel by seawater used electrochemical impedance spectroscopy (EIS) and a salt spray cabinet to perform accelerated ageing tests and evaluate green algae and lupine seed extracts as natural additives for paint based on a vinyl chloride-vinyl acetate copolymer (VYHH) [2-4]. The results indicated that the addition of algae extract blocked unfilled spaces in the microstructure of the varnish, giving a more uniform distribution pattern. VYHH varnish containing 0.025 g/L lupine extract was found to provide the optimum corrosion protection efficiency. The addition of lupine extract also had a slight effect on the degree of surface coverage by fouling organisms.

Cannabis plant extracts were shown to be efficient corrosion inhibitors for copper and nickel in acidic aqueous solutions [5,6]. The main goals of this work are to test and evaluate the anticorrosive and antifouling property of the cannabis plant as a natural additive for varnish- coated steel immersed in marine environments.

EXPERIMENTAL

Preparation of Cannabis extract

100 g of dry cannabis (the flowering tops) plants, which was obtained by permission from the public

---

Correspondence: A.M. Abdel-Gaber, Alexandria University, Faculty of Science, Chemistry Department, Ibrahimia, P.O. Box 426, Alexandria 21321, Egypt.
E-mail: ashrafmoustafa@yahoo.com
Paper received: 20 November, 2015
Paper revised: 20 April, 2016
Paper accepted: 13 May, 2016

https://doi.org/10.2298/CICEQ151120028A

prosecutor, was minced into very small pieces. The minced plant was boiled in water for 5 min to extract chlorophyll and water-soluble compounds. The boiled minced plant was filtered, and the water was discarded. The process was repeated several times until the filtered water was transparent [7]. The residue of the filtrate was air-dried at room temperature, then refluxed with 100 mL of ethyl alcohol and filtered using a Whatman No. 1 filter paper. The alcohol was allowed to evaporate from the extract to obtain Cannabis residue [8]. A stock solution of cannabis extract was prepared by dissolving 1.7 g of the cannabis residue in 100 mL of benzene.

Varnish preparation

Varnish was prepared by dissolving 20 g vinyl chloride-vinyl acetate copolymer, VYHH (Dow Chemical Company) in analytical grade solvent-mixture consisting of 40 g methyl isobutyl ketone (MIBK), 20 g toluene, and 20 g benzene.

Preparation of varnish containing cannabis extract

A certain amount of the previously prepared stock solution of cannabis extract was diluted by benzene to obtain the required weight of cannabis extract solution. Then, 20 g of this solution was mixed with 40 g MIBK, 20 g toluene and 20 g VYHH.

Preparation of varnish-coated steel samples

Commercial steel panels analyzed by optical emission spectrophotometer (OES) were used. The composition of the steel samples are (wt.%): 0.21 C, 0.35 Si, 2.5 Mn, 0.04 P and 0.04 S, with the remaining percentage consisting of Fe. Steel panels of dimensions 5 cm×2 cm×0.2 cm were polished with a series of graded emery papers (320, 600, 800 and 1000), starting with the coarsest grit and proceeding step-wise to finer grades. Steel panels were degreased with *m*-xylene, sequentially washed with distilled water and ethanol, and finally, dried with filter paper. Different coatings were applied to steel panels by immersion in a 500 mL tank containing the required varnish. If present, excess varnish that collected at the panel edges was removed. The coated steel panels were hung perpendicular to the ground and allowed to dry at room temperature (25-30 °C) until a visibly dry surface was obtained (~30 min). The process of dipping and drying was repeated for each sample (three to five times) to obtain a constant thickness of 120±5 μm while the varnish layer was monitored using a coating thickness gauge (Minitest 300FN, Elektrophysik, Erichsen Testing Equipment).

Electrochemical tests

EIS of varnish-coated steel panels was achieved by connecting an electrochemical cell to a Parstat 2263 transfer function analyzer (TFA) that was controlled by a computer for data logging and analysis. The frequency range for EIS measurements was 100 kHz to 0.01 Hz with an applied potential signal amplitude of 10 mV around the rest potential. Data were obtained from a three-electrode configuration: a platinum sheet, saturated calomel electrode (SCE), and varnish-coated steel panel were used as the counter, reference and working electrodes, respectively. All measurements were carried out using air saturated 0.5 M NaCl solutions without stirring.

Salt spray test

Cyclic corrosion tests correlate well to realistic, naturally occurring conditions and thus provide significantly improved predictive ability. The test was carried out using an Equilam cabinet (Equilam North America) for the cyclic salt spray that work under prohesion type testing as described by ASTM G85 A5. Varnish-coated steel specimens, containing different concentrations of cannabis extracts, were exposed to a two-phase programme using an Equilam cabinet for the cyclic salt spray. The sequence consisted of four hours of salt spray (SS) at 25 °C, followed by one hour of drying at 35 °C. This two-phase programme was repeated continuously for 1000 h. Photographs of coated samples were taken before and after exposure at different time intervals to document extended changes to the surfaces [9].

Immersion test

The varnish-coated steel and cross-cut panels were immersed in 100 mL 0.5 M NaCl solution for 28 days. Photographs were taken before and after exposure to the test solution, which allowed qualitative comparisons between samples. The concentration of ferric ions released from cross-cut panels and into the test solution was measured spectrophotometrically using a Beckman DU640 UV/Vis spectrophotometer at wavelengths (λ) 580-600 nm.

Field test

Steel panels with dimension of 10 cm×10 cm×0.2 cm were coated with varnish containing different concentrations of Cannabis extract. The coated panels were hung in frames and immersed in Western Harbour seawater, Alexandria, Egypt, to test the anticorrosion and antifouling properties of these coatings. The surfaces were carefully inspected visually and photographically permitting qualitative comparisons of the coats.

Chemical structure of the constituents of the Cannabis extract

ElSohly [10] detected sixty-six phytocannabinoids, mainly belonging to one of 10 subclasses or types, consisting of the cannabigerol type, cannabichromene type, cannabidiol type, cannabicyclol type, cannabielsoin type, cannabinol type, cannabinodiol type, or to the cannabitriol type. Quantitatively, the most important cannabinoids present in the plant are the cannabinoid acids, cannabidiol, cannabichromene and cannabigerol, Figure 1. Their relative concentrations vary, and plants have been described that mainly contain one of these cannabinoid types.

RESULTS AND DISCUSSION

EIS measurements

The impedance spectra of varnish-coated steel panels containing different concentrations of cannabis extract for different exposure times were analyzed by fitting to an equivalent circuit model, as shown in Figure 2.

A detailed description of this model is described in the literature [4]. Computer fitting of the spectra allowed for evaluation of the different elements of the analogue circuit. An equivalent circuit includes the solution resistance element, R_s, and the film constant phase element CPE_f that is shorted by a resistive element, R_f. Additional components include the double-layer constant phase element CPE_{dl} and the charge transfer resistance element, R_{ct}. To compensate for non-homogeneity in the system, the capacitances were implemented as constant phase elements (CPE), each defined by two values, a non-ideal capacitance Q and a constant n.

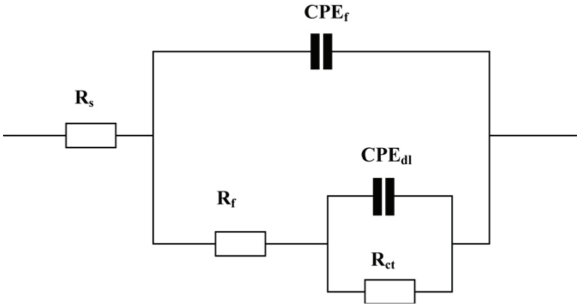

Figure 2. Schematic for the equivalent circuit.

Varnish-coated steel

Typical computerized fit of the Nyquist impedance data for varnish-coated steel after 6 days of immersion in 0.5 M NaCl solution are shown in Figure 3. As shown, fitting EIS data to the model corresponded well with the measured spectra.

Computer fits of the electrochemical impedance spectroscopy results of steel coated by varnish after different times of immersion in 0.5 M NaCl are provided in Table 1. It is clear that the non-ideal film capacitance, Q_f, increased with exposure time, which may be attributed to the uptake of water. A decrease in R_f can be explained in terms of penetration of the coating by ionic species from the surrounding environment [4], while the decrease in R_{ct} indicated a continuing deterioration tendency of the varnish-coated steel. It is clear that the values for the modulus of impedance at minimum frequency, R_{min} exhibit the same trend as that shown by R_f and R_{ct}. For this reason, the modulus of impedance at low frequency (R_{min}) was used as a measure of: 1) the system's tendency to retard the penetration of aqueous ionic species within the coat and 2) the deterioration tendency for coat with time.

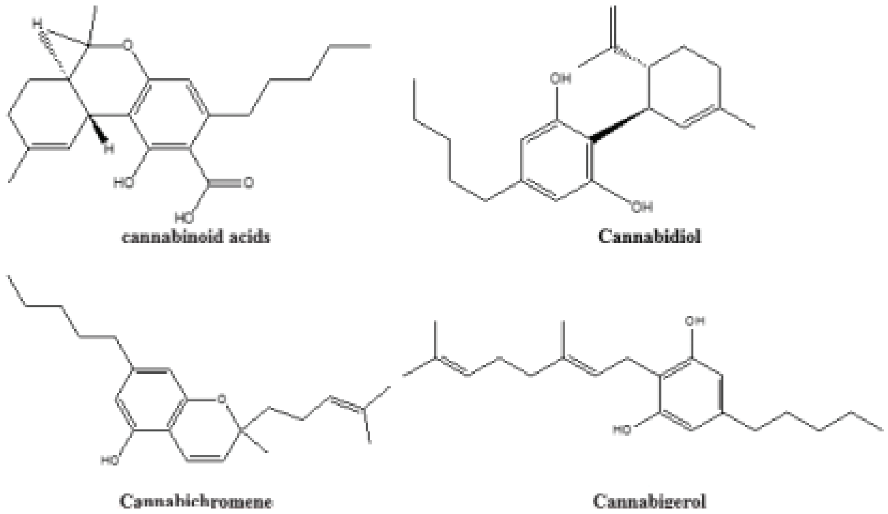

Figure 1. Major quantitative chemical constituents of cannabis extract.

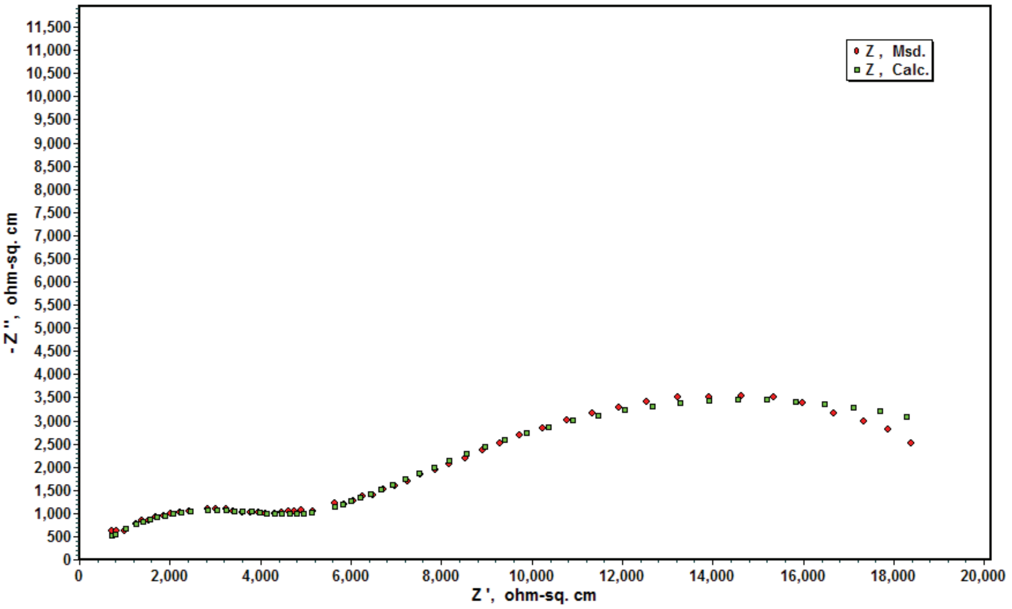

Figure 3. The experimental and computer-fit results of Nyquist impedance plot for varnish coated-steel panels after 6 days of immersion in 0.5 M NaCl.

Varnish containing cannabis extract coated-steel

The variations of R_{min} for steel panels coated with varnish containing different concentrations of Cannabis extract at 10 or 28 days of exposure in 0.5 M NaCl are shown in Figure 4. It is clear that the deterioration of the varnish-coated steel panels decreased with increasing the cannabis extract concentration and increased with increasing the immersion time.

Salt spray test

The photographs of varnish-coated steel panels containing different cannabis extract concentrations after exposure to the salt spray test for 28 days are shown in Figure 5a. Visual inspection verified the effective corrosion protection for varnish coatings containing cannabis extract compared to the unmodified varnish. The degree of rusting underneath the coating was observed to decrease with an increase in extract concentration, and no film blisters were observed during the exposure period. This indicates that cannabis extract had a physical role in improving the barrier properties of the coating by separating the metallic substrate from the corrosive medium [9,11].

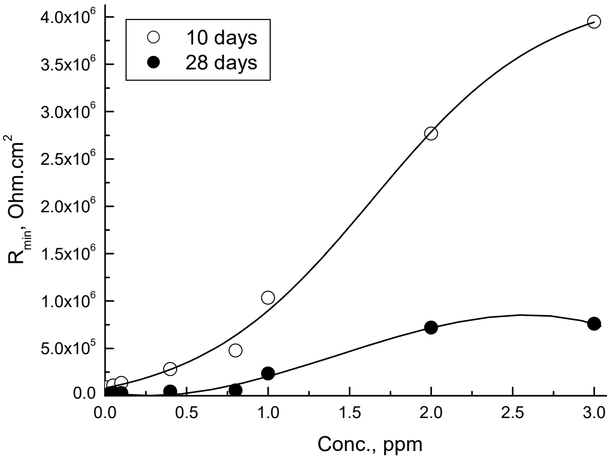

Figure 4. Variation of Rmin of the varnish coated-steel panels with the cannabis extract concentration after 10 and 28 day of exposure in 0.5 M NaCl.

Table 1. Computer-fit results of steel coated by varnish-after different times of immersion in 0.5 M NaCl

Exposure time, day	Q_{dl} / μF	R_{ct} / Ω cm^2	Q_f / μF	R_f / Ω cm^2	R_{min} / Ω cm^2
6	1.90	5188	75	19000	18550
10	2.10	3424	82	14280	15070
15	0.02	3150	50	12790	11230
20	0.01	577	57	9960	9529
23	0.22	468	173	7587	5806
26	0.20	406	248	6018	4466
28	0.02	391	201	5833	4374

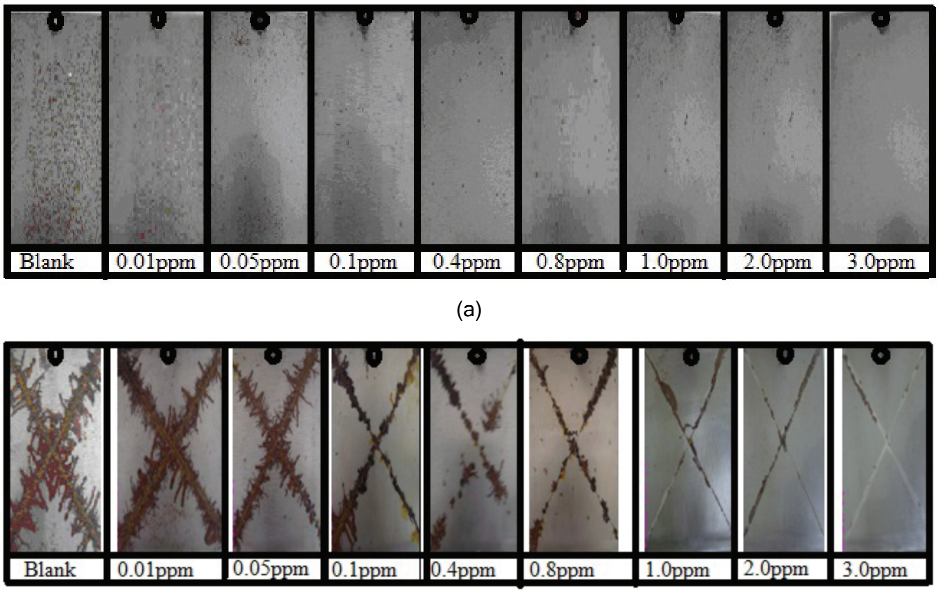

(a)

(b)

Figure 5. a) Photographs of varnish coated-steel panels containing different cannabis extract concentrations after exposure to salt spry test for 28 days. b) Photographs of the cross cut varnish coated-steel panels containing different cannabis extract concentrations after exposure to salt spry test for 28 days.

This may be attributed to the adsorption molecules of the chemical constituents of cannabis extract (Figure 1) that contains oxygen atoms and п-electrons at the steel/coat interface. The adsorption could take place *via*: *i*) dipole-type interaction between unshared electron pairs in the molecules of the extract with the metal and *ii*) the π-electrons bonds interaction with the metal [12].

Photographs of the cross-cut varnish-coated steel panels containing different cannabis extract concentrations after exposure to the salt spray test for 28 days are shown in Figure 5b. The figures show the existence of severe rusting along the scribe mark of the varnish-coated samples. An increase in the concentration of the cannabis extract led to a decrease in the degree of rust observed at the scribe mark boundaries; for panels coated with varnish containing 3.0 ppm of extract, the corrosion that extended along the scribe mark was almost non-existent. The minimized deterioration and rust can be related to the water-repellent quality and/or the chemical activity of cannabis extract. The chemical activity may be related to: *i*) a decrease in the rate of the anodic reaction by binding metal ions produced by corrosion reactions and consequently forming coordination compounds near the anode; *ii*) a decrease in the rate of both anodic and cathodic processes by adsorption of the molecules of the chemical constituents of the extract at the cathodic and anodic areas of the steel surface; *iii*) a reaction between the chemical constituents of the extract and the copolymer resin, giving rise to an enhanced mechanical integrity and a reduction in the degradation of the coating under corrosive conditions [3,13].

Immersion test

The immersion of cross-cut varnish-coated steel panels containing different cannabis extract concentrations in 0.5 M NaCl solution for 28 days turns the colour of the test solution into brown. This brown colour is the result of the dissolution of steel initiated at the scribe mark. The intensity of the brown colour, which is related to the concentration of ferric ions, was observed to decrease with increasing cannabis content.

The concentrations of ferric ions released from the cross-cut varnish-coated steel panels were determined spectrophotometrically, as shown in Figure 6. It is evident that the level of absorbance decreased with cannabis content, which indicated that the extract enhanced the corrosion protection of the varnish. Since, the coat system could be seen as a simple three-part system consisting of the coat film, the interface between the film and the steel surface, and the steel itself. Therefore, the adsorption of the chemical constituents of the extract at the interface between the steel and the coat film provide a barrier that retards the attack of the steel by the aggressive ions in the seawater.

Field test

Figure 7 shows photographs of the varnish-coated steel panels containing different Cannabis extract concentrations after immersion in seawater for 100 days. For varnish lacking the cannabis extract, the coated steel panel was completely covered by fouling organisms. The addition of 0.01-0.1 ppm cannabis extract had a minimal effect, while fouling was noticeably reduced in the presence of 1.0 to 3.0 ppm extract. This demonstrated that cannabis extract could also impart antifouling attributes to the coating.

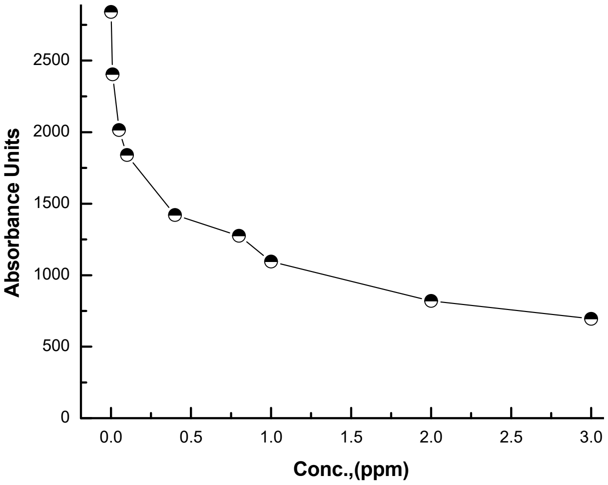

Figure 6. Variation of the absorbance with the cannabis concentration in varnish coated-steel panels.

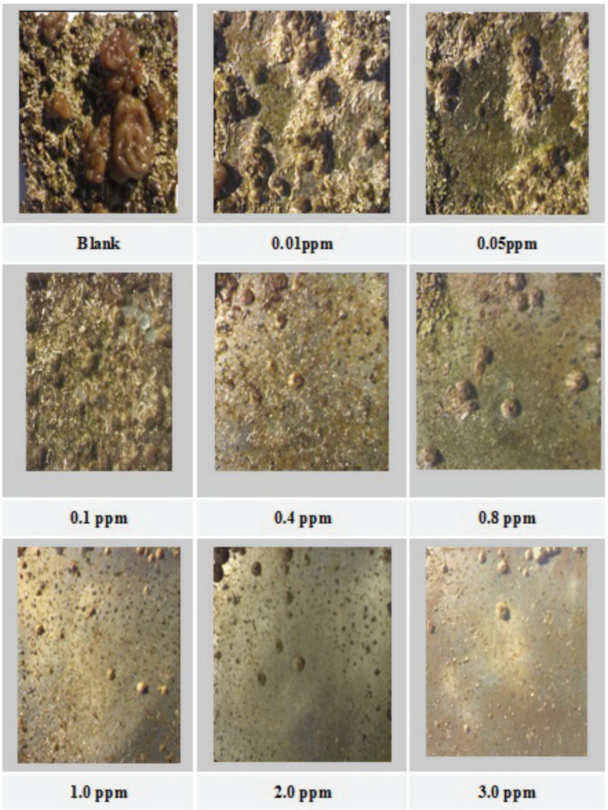

Figure 7. Photographic photos for the varnish coated-steel panels containing different cannabis extract concentrations after immersion in seawater for 100 days.

CONCLUSIONS

The results in this paper can be summarized as follows:

1. EIS measurements indicated that the deterioration tendency of the coat decreases with increasing the concentration of the cannabis extract.
2. The inspection of the photographs of the cross-cut samples indicated that the degree of rusting at the scribe mark decrease with increasing the concentration of the cannabis extract in coat.
3. The field test results indicated that the inclusion of the cannabis extract in the coat improved its protection against corrosion and antifouling properties.

REFERENCES

[1] R. Lambourne, in: Paint and Surface Coatings, Theory and Practice, R. Lambourne, T.A. Strivens (Eds.), 2nd ed., Woodhead Publishing Ltd., New York, 1999, p. 530

[2] E.M.E. Mansour, A.M. Abdel-Gaber, B.A. Abd-El Nabey, A. Tadros, H. Aglan, Corrosion **58** (2002) 113-118

[3] E.M.E. Mansour, A.M. Abdel-Gaber, B.A. Abd-El Nabey, N. Khalil, E. Khamis, A. Tadros, H. Aglan, A. Ludwick, Corrosion **59** (2003) 242-249

[4] A.M. Abdel-Gaber, B.A. Abd-El Nabey, E. Khamis, O.A. Abdelattef, H. Aglan, A. Ludwick, Prog. Org. Coat. **69** (2010) 402-409

[5] B.A. Abd-El-Nabey, A.M. Abdel-Gaber, M. El. Said Ali, E. Khamis, S. El-Housseiny, Int. J. Electrochem. Sci **7** (2012) 11811-11826

[6] B.A. Abd-El-Nabey, A.M. Abdel-Gaber, M. El. Said Ali, E. Khamis, S. El-Housseiny, Int. J. Electrochem. Sci **8** (2013) 5851-5865

[7] A.B. Segelman, R.D. Sofia, F.P. Segelman, J.J. Harakal, LC. Knobloch, J. Pharm. Sci. **63** (1974) 962-964

[8] D.H. Gieringer, J. Cannabis Ther. **3** (2001) 153-170

[9] E. Armelin, R. Pla, F. Liesa, X. Ramis, I. J. Iribarren, C. Aleman, Corros. Sci. **50** (2008) 721-728

[10] M.A. ElSohly, Chemical constituents of cannabis, in: Cannabis and Cannabinoids Pharmacology, Toxicology, and Therapeutic Potential, F. Grotenhermen, E. Russo (Eds.), The Haworth Press, Inc., Binghamton, NY, 2002

[11] M. Bethencourt, F.J. Botana, M. Marcos, R.M. Osuna, J.M. Sánchez-Amaya, Prog. Org. Coat. **46** (2003) 280--287

[12] A.M. Abdel-Gaber, B.A. Abd-El-Nabey, M. Saadawy, Corros. Sci. **51** (2009) 1038

[13] G. Adrian, A. Bittner, J. Coat. Technol. **58** (1986) 59-65.

BESHEIR AHMED A. ABD-EL-NABEY[1]
SHERIF EL-HOUSSEINY[1]
ESSAM KHAMIS[1]
ASHRAF MOUSTAFA ABDEL-GABER[1,2]

[1]Alexandria University, Faculty of Science, Chemistry Department, Ibrahimia, Alexandria, Egypt
[2]Department of Chemistry, Faculty of Science, Beirut Arab University, Lebanon

NAUČNI RAD

ZAŠTITA OD KOROZIJE I RAZGRADNJE LAKOM ZAŠTIĆENOG ČELIKA KOJI SADRŽI PRIRODNE ADITIVE

Zaštita od korozije i razgradnje lakom zaštićenih čeličnih panela koji sadrže različite akstrakte kanabisa proučavani su korišćenjem spektroskopije elektrohemijske impedancije (EIS), slanog naprskavanja i testa uranjanja u 0,5 M rastvoru natrijum-hlorida i morsku vodu. Analiza eksperimentalnih rezultata ukazuje na to da se prisustvom ekstrakta kanabisa smanjuje razgradnja (ljuštenje) lakom zaštićenih čeličnih panela izloženih agresivnom delovanju okoline. Uočeno je da ekstrakt kanabisa obezbeđuje dobru zaštitu od razgradnje.

Ključne reči: korozija, lak, razgradnja, slano naprskavanje, testovi u realnim uslovima.

CI&CEQ
Chemical Industry & Chemical Engineering Quarterly

Available on line at
Association of the Chemical Engineers of Serbia *AChE*
www.ache.org.rs/CICEQ
Chem. Ind. Chem. Eng. Q. 23 (2) 177–186 (2017) CI&CEQ

GAMZE DALGIC
F. ILTER TURKDOGAN
KAAN YETILMEZSOY
EMEL KOCAK

Department of Environmental Engineering, Faculty of Civil Engineering, Yildiz Technical University, Davutpasa, Esenler, Istanbul, Turkey

SCIENTIFIC PAPER

UDC 628.3.034.2:615:66

TREATMENT OF REAL PARACETAMOL WASTEWATER BY FENTON PROCESS

Article Highlights

- Real paracetamol (PCT) wastewater was pre-treated by Fenton process
- Best experimental conditions of Fenton process were determined
- Mass balance calculations were studied to show the mass distributions
- Fenton process was found as a promising method for the treatment of PCT wastewater

Abstract

The study investigated the pretreatment of real paracetamol (PCT) wastewater of a pharmaceutical industry by Fenton process. At the best experimental conditions (COD/H_2O_2 = 1/1, Fe^{+2}/H_2O_2 = 1/70, settling method:centrifuging, pH 6 at settling step), 92.7, 92.7, 95.5, 99.1, 99.9 and 99.4% of chemical oxygen demand (COD), total organic carbon (TOC), 5-day biological oxygen demand (BOD_5), PCT, para-amino phenol (PAP) and aniline were removed, respectively. Changes in the concentrations of these parameters were also investigated for both oxidation and settling steps of Fenton process. It was found that COD and TOC were removed at the settling step (precipitation) whereas PCT, PAP and aniline were removed at the oxidation step. Mass balance calculations were also studied to show the mass distributions of COD in different phases (gas + foam, effluent and sludge). Fenton process was found as an effective method for the pretreatment of real PCT wastewater for discharging in a determined collective treatment plant.

Keywords: chemical oxygen demand, Fenton process, mass balance, real paracetamol wastewater, total organic carbon.

Over the last two decades, a large variety of pharmaceutical drugs including analgesics, anti-inflammatory, beta-blockers, antimicrobials, blood lipid regulators and so on, has been detected at low contents of micrograms per liter in soils, surface waters, ground waters and even in drinking waters [1-9]. Pharmaceutical drugs can reach aquatic environment from domestic waste or industrial wastewater, hospitals and health centers [10].

Unused drugs, manufacturing waste and sewage sludge can also be introduced into the environment by way of landfill leachates [11]. Pharmaceuticals can reach sewage treatment plants by way of domestic and hospital wastewater without being completely metabolized and changed. Although they are treated in these plants, they can be present in the aquatic environment [11] or they are discharged directly without any treatment [12]. Classical biological treatment plants do not have enough efficieny to remove this kind of compounds [12,13] as they are designed to treat only urban and industrial wastewater. Removal efficienies of this kind of plants are usually evaluated by parameters as particulate matter, phosphate, metal ions, pathogens and nitrogen, but not pharmaceuticals [12]. Thus, low cost and easily applied methods must be developed beyond the conventional ones for removing these substances.

Paracetamol (PCT), a common analgesic and antipyretic drug [14], has a widespread usage as the raw material of many drugs. Pharmaceutically ineffective main metabolites of PCT are glucuronide

---

Correspondence: F.I. Turkdogan, Department of Environmental Engineering, Faculty of Civil Engineering, Yildiz Technical University, 34220, Davutpasa, Esenler, Istanbul, Turkey.
E-mail: ilter@yildiz.edu.tr; ilterturkdogan@gmail.com
Paper received: 31 August, 2015
Paper revised: 4 February, 2016
Paper accepted: 18 May, 2016

https://doi.org/10.2298/CICEQ150831029D

(55%) and sulphate (35%) [15]. About 1-3% of PCT is excreted without being changed by the uretic system. Besides being a good pain reliever, a certain amount of PCT can also be used for controlling brown tree snakes and cause hepetotoxicity in humans. As there are lots of organisms in the environment and each organism has different sensitivities, pharmaceuticals can be qualified as risk factors for the environment [14].

Recent studies show that in addition to advanced oxidation processes (AOPs) [16-26], adsorption [10], pure bacterial cultures [27], active sludge [28], subsurface flow constructed wetlands [29] and anaerobic treatment [20] can be used for PCT removal from wastewater. In the traditional environmental engineering technologies, wastewater treatments are usually realized by the parameters: chemical oxygen demand (*COD*), 5-day biological oxygen demand (*BOD*$_5$), and total organic carbon (*TOC*).

Over the past few years, AOPs have been used to reduce the contamination based on the presence of stable pharmaceuticals [30,31]. Complex organic chemicals are formed during the production of pharmaceuticals and it is not easy to remove these compounds biologically. As a result, AOPs are more appropriate than conventional methods for treatment of pharmaceutical wastewater [32]. AOPs comprises Fenton, photo-Fenton, ozonation combined with UV-light and/or H_2O_2, mainly TiO_2-mediated photocatalysis [30], electrolysis, wet air oxidation, ultrasound and ionizing radiation, microwaves, pulsed plasma and the ferrate reagent [31].

The Fenton system is one of the most promising methods among all AOPs for removal of organic pollutants [33], while also cost-effective and easily operated [32], although it has some disadvantages, such as the necessity to be operated in a limited pH range [31] and the formation of sluge that has to be separated by an additional operation [34]. Advanced oxidation with Fenton's reagent is based on ferrous ions, hydrogen peroxide (H_2O_2) and hydroxyl radicals ($HO^\bullet$) produced by the catalytic decomposition of H_2O_2 in acidic solution [35]. The main chemicals of the Fenton reaction are hydrogen peroxide and iron, which are environmentally friendly, inexpensive and safe [36]. Formation of $HO^\bullet$ and oxidation of Fe^{2+} to Fe^{3+} explains the efficiency of this system [33]. The $HO^\bullet$, which is known as the second strongest oxidant after fluorine [37] and has the ability of oxidizing organic compounds in a short time [32], is the main oxidizing species of the Fenton system.

The main reactions of the Fenton system are shown below [38]:

$$Fe^{2+} + H_2O_2 \rightarrow Fe^{3+} + HO^\bullet + OH^- \quad (1)$$

$$Fe^{2+} + {}^\bullet OH \rightarrow Fe^{3+} + OH^- \quad (2)$$

$$HO^\bullet + H_2O_2 \rightarrow HO_2^\bullet + H_2O \quad (3)$$

$$Fe^{3+} + HO_2^\bullet \rightarrow Fe^{2+} + H^+ + O_2 \quad (4)$$

$$Fe^{3+} + O_2^{-\bullet} \rightarrow Fe^{2+} + O_2 \quad (5)$$

$$Fe^{2+} + HO_2^\bullet \rightarrow Fe^{3+} + HO_2^- \quad (6)$$

The Fenton process consists of pH adjustment, oxidation reaction, neutralization-coagulation and precipitation. The H_2O_2/Fe^{2+} ratio is the major factor affecting the coagulation and oxidation stages [39].

Efficiency of wastewater treatment is usually evaluated by the parameters of *COD*, *BOD*$_5$ and *TOC*. It has been known that pollutants such as PCT, para-amino phenol (PAP) and aniline have negative effects on both human health and the environment. A comprehensive study involving multi-parameters like *COD*, *BOD*$_5$, *TOC*, PCT, PAP and aniline has not been reported yet for the pretreatment of a high strength pharmaceutical wastewater. It is apparent from the literature that although much attention has been given to the treatment of synthetic wastewater [21-26], there are almost no systematic papers available in the literature specifically devoted to a study of real PCT wastewater. It is seen that synthetic PCT wastewaters have been used in most of the recent studies. Studying with synthetic wastewater is much easier than studying with real wastewater as the pollutant concentrations can be defined and the interferences of the involuntary substances can be prevented in synthetic wastewaters. In addition to these, synthetic wastewaters may not completely reflect the real case situation. For this reason, the present study aims at fulfilling the gap in this field by focusing upon some investigations on Fenton process as an effective method for the pretreatment of real PCT wastewater.

Considering the above-mentioned facts, the specific objectives of this study were: 1) to investigate the removal of organic matter, PCT, PAP, aniline in treatability of real PCT wastewater using Fenton process and 2) the mass balance using the removal mechanism of COD in different phases.

EXPERIMENTAL

Wastewater source and characteristics

Wastewater was obtained from a pharmaceutical factory which is in the first rank for PCT production in Marmara Region of Turkey. According to the process, main part, 80% of the produced PCT is exported to USA and Europe, 10% is sold to the other pharmaceutical factories in Turkey and the remaining 10% is used as the raw material of other drugs produced by the factory. Process flow diagram of the factory is shown in Figure 1a. As shown in Figure 1a, para-aminophenol (PAP) is synthesized as by-product for PCT production. Nitrobenzene, aniline, H_2SO_4, H_2 and H_2O are used in PCT synthesis. PCT molecule is formed after the reaction of PAP and acetic anhydride and the stage of crystallization. Figure 1b shows the molecules of nitrobenzene, aniline and PAP.

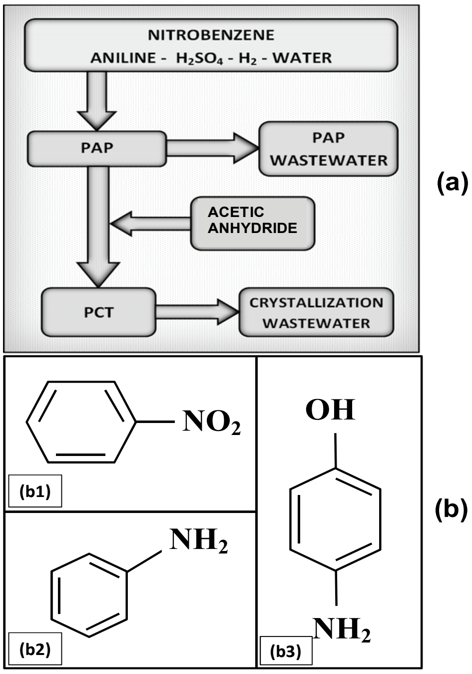

Figure 1. a) Steps of PCT and PAP synthesis; b) chemical structure of the compounds in PCT synthesis: b1) nitrobenzene, b2) aniline and b3) PAP.

The main characteristics of real PCT wastewater are shown in Table 1. High *COD* value of the wastewater is related to the high concentrations of PCT, PAP and aniline. Wastewater flow is nearly 200 m^3/day in the process. Pollutant concentrations of the wastewater can change day by day according to the process operations.

As seen in Table 1, pollutant concentrations are extremely high and the *BOD*/*COD* ratio is very low in PCT wastewater. Badawy *et al.* [33] indicated that wastewater having *BOD*/*COD* ratio between 0.25-0.30 cannot be treated biologically. Likewise, Tekin *et al.* [32] point out the resistance of pharmaceutical wastewater to biological treatment and treatability of this wastewater by AOPs instead of classical methods. It can be clearly seen that the PCT wastewater must be pretreated chemically, as conventional biological treatment methods are not appropriate for this kind of wastewater.

Table 1. Main characteristics of PCT wastewater

Parameter	Value
pH	9.0-9.5
Chemical oxygen demand, *COD* / mg L^{-1}	36,000-76,800
5-day biological oxygen demand, BOD_5 / mg L^{-1}	15,120-21,500
Total organic carbon, *TOC* / mg L^{-1}	12,000-24,312
Paracetamol, PCT, ppm	37-294
Para-amino phenol, PAP, ppm	1273-4604
Aniline, ppm	1699-2915
Total suspended solids, *TSS* / mg L^{-1}	350-380

The industries producing chemical raw materials (such as PCT) are generally located in the large-scale organized industrial zones. The wastewaters of the different industries are collected and treated in a common wastewater treatment plant. As the wastewaters of these industries have different characteristics, the *BOD*/*COD* ratio of the other wastewaters are not same as the ratio of PCT wastewater. The aim of the study is developing a system for the pretreatment of mere PCT wastewater.

Fenton process

Wastewater samples were kept in a refrigerator at 4 °C and *COD* measurements were made prior to calculate chemical dosages for each sample in Fenton experiments. Fenton experiments were performed at room temperature in a glass beaker by mixing at 300 rpm. $FeSO_4 \cdot 7H_2O$ solution (source of Fe^{+2}) was prepared in 3 M H_2SO_4 and added to the sample at the beginning of the experiment. pH was adjusted at 3.0±0.2 by using 3 M H_2SO_4, and kept at the same value by using 6 M NaOH during the reaction [33]. For that reason, H_2O_2 was dosed continuously at each minute by an automatic pipette (Brand 704782) during the reaction time. Durán *et al.* [21] indicated the enhancement in mineralization process with continuous addition of H_2O_2. After Fenton's oxidation, the pH was adjusted at 6.0 for the settling step.

Analytical procedure

Experimental analyses were performed by the procedures described in standard methods [40], *COD* (closed reflux - titrimetric method, 5220 C), *BOD* (5-day test, 5210 B), *TSS* (dried at 103-105 °C, 2540 D). *TOC* analyses were performed by TOC-TN analyzer (HACH-LANGE IL550 TOC-TN), based on combustion catalytic oxidation method, using a highly sensitive multi-channel non-dispersive infrared detector

[41]. PCT, PAP and aniline were quantified using the official chromatographic method based on high-performance liquid chromatography (HPLC) according to the procedures described in the European Pharmacopoeia 8.0 [42]. The HPLC system comprised of a Shimadzu liquid chromatograph, model 20A, coupled to an UV-visible detector (SPD-20A), auto-injector (SIL-20A) and a degasser DGU-20A5, controlled by a personal computer. Shimadzu EZstart 7.4 chromatography software was used for processing of data and peaks integration. A Shim-pack CLC-ODS C18 column (size: l = 0.25 m, Ø = 4.6 mm, stationary phase: octylsilyl silica gel for chromatography R (5 µm)) was used inside a CTO-10AS oven (Shimadzu, Kyoto, Japan) maintained at 35 °C. Mobile phase was a mixture of 375 volumes of a 17.9 g/L solution of disodium hydrogen phosphate R, 375 volumes of a 7.8 g/L solution of sodium dihydrogen phosphate R and 250 volumes of methanol R containing 4.6 g/L of a 400 g/l solution of tetrabutylammonium hydroxide R. The flow rate was 1.5 mL/min, the sample injection volume 20 mL, and the detector absorption wavelength 245 nm [42]. All analytical measurements were done in triplicate to observe the reproducibility of each test. A magnetic stirrer (RCT, 0-1500 rpm) was used during the experiments. The pH and temperature was measured with a Hanna - HI 2211 pH/ORP meter. Beckman Coulter Allegra X-12 was used for centrifuge. All analyses were performed at room temperature (24±2 °C).

RESULTS AND DISCUSSION

Investigation of the best experimental set

Each different Fenton experiment was named as "set" and in each set *COD*/H_2O_2-Fe^{+2}/H_2O_2 ratios and reaction time were used as variables of the present study. The aim of this investigation is obtaining the highest *COD* removal efficiency using the chemical dosages during the shortest reaction time. High *COD* removal efficiencies were obtained between 1/2 and 1/0.8 for *COD*/H_2O_2 ratios. Similar ratios (*COD*/H_2O_2 in range 1/4.4-1/1.1) were used in the study of Badawy *et al.* [33] and high efficiencies were obtained. The selected sets having high *COD* removal efficiencies are summarized in Table 2. As seen in Table 2, set 25 (*COD*/H_2O_2 = 1/1, Fe^{+2}/H_2O_2 = 1/70 and

Table 2. COD removal efficiencies (%) of different sets

Set	*COD*/H_2O_2	Fe^{+2}/H_2O_2	Reaction time, min	*COD* removal efficiency, %
1	1/2	1/10	60	80.9
2	1/2	1/10	45	78.7
3	1/2	1/15	75	79.7
4	1/2	1/15	60	83.3
5	1/2	1/15	45	80.2
6	1/2	1/15	30	76.9
7	1/2	1/20	75	79.6
8	1/2	1/20	60	79.6
9	1/2	1/20	45	82.9
10	1/2	1/20	30	82.2
11	1/2	1/20	15	82.2
12	1/2	1/25	75	79.8
13	1/2	1/25	60	79.8
14	1/2	1/25	45	78.7
15	1/2	1/25	30	78.7
16	1/2	1/40	45	81.1
17	1/2	1/40	30	80.7
18	1/1.4	1/15	30	78.0
19	1/1.4	1/15	15	76.0
20	1/1	1/15	30	73.3
21	1/1	1/15	15	75.0
22	1/1	1/25	30	80.5
23	1/1	1/25	15	78.9
24	1/1	1/50	15	84.2
25	**1/1**	**1/70**	**15**	**88.1**
26	1/1	1/90	15	83.5
27	1/0.8	1/70	15	82.0

reaction time of 15 min) was determined as the best experimental set.

Improvement studies for the best experimental set

Settling alternatives, different pH for the settling step and different reaction times were studied for obtaining higher removal efficiencies in the best experimental set.

Determination of settling method

In the present experiments, wastewater was kept for 1 day in a measuring cylinder for settling and thereafter, *COD* measurements were conducted with the sample taken from the supernatant of the wastewater. Su *et al.* [26] indicated that leaving the samples overnight prevented the remaining H_2O_2 from affecting *COD* measurements. The seperating point of effluent and sludge could not be determined even waiting for 1 day. So, it was determined to study different settling alternatives to separate the effluent from the sludge. Adding anionic and cationic polyelectrolytes (p.e.) and centrifuging were tested for the best experimental set (Figure 2a).

As seen in Figure 2a, 91.9 and 88.1% *COD* removal efficiencies were obtained from the effluents after 1 day and 92.7 and 89.1% after 2 days for anionic and cationic polyelectrolytes (p.e.), respectively. It could be seen that settling time had a positive effect on COD removal efficiency for both p.e. On the other hand, *COD* removal efficiency of centrifuged sample was 92.3%.

When all the results were compared, it was seen that the highest *COD* removal efficiency was obtained from the sample containing anionic p.e. after settling for 2 days. On the other hand, the second highest removal efficiency was obtained from the sample centrifuged 2 h later after oxidation. Centrifuging was

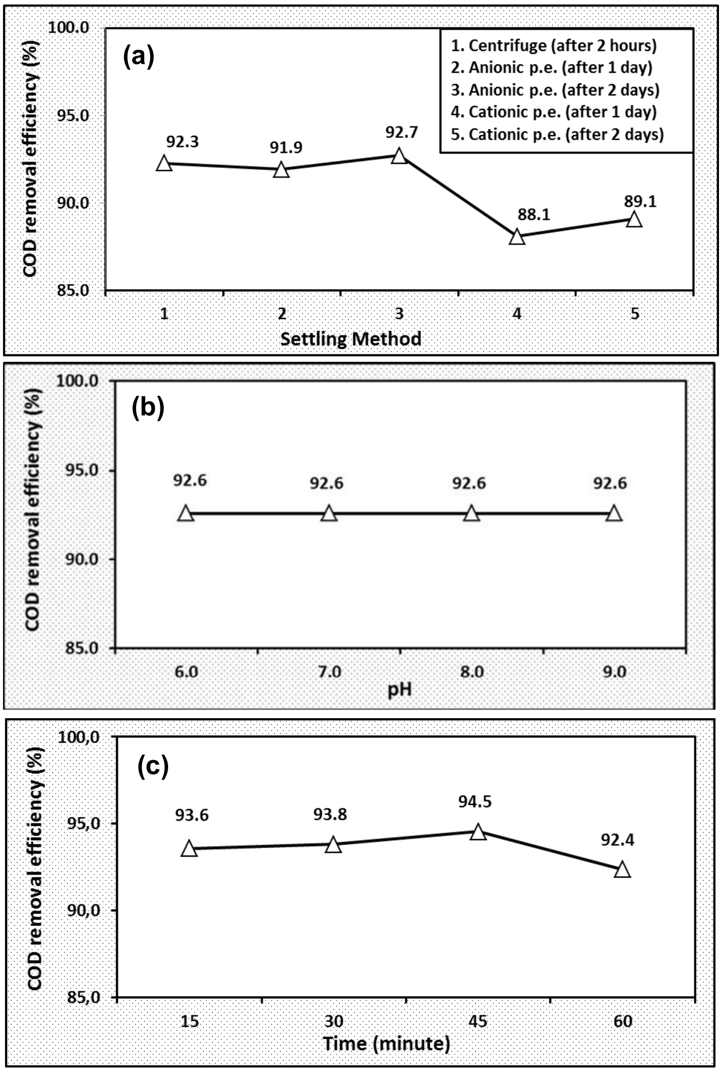

Figure 2. a) COD removal efficiencies of different settling methods; b) effect of pH on COD removal efficiency at settling step; c) effect of reaction time on COD removal efficiency.

determined as the best settling method considering the facts like settling time, sludge formation and little difference between the removal efficiencies of the methods. After various trial runs, it was decided that the mixture after oxidation was better to be centrifuged for minimum 20 min at 3750 rpm (also used in the experiments depicted in Figure 2a).

Effect of pH at settling step

According to Turkish Water Pollution Control Regulation [43], pH value of the wastewater has to be between 6-9 for discharge standards. In the experiments, pH was adjusted with centrifugation at 6.0 after oxidation step. In order to determine the effect of pH at the settling step, pH was adjusted at 6.0, 7.0, 8.0 and 9.0 after the oxidation experiments. The obtained results are depicted in Figure 2b.

As seen in Figure 2b, increase in pH for the settling step had no effect on *COD* removal efficiencies. Increasing the pH to 6.0 would be enough for the settling step after oxidation. Therefore, the pH was set to 6.0 in the other experiments.

Effect of reaction time

In the experiments investigating the best conditions, the sets with different COD/H_2O_2-Fe^{+2}/H_2O_2 ratios were studied for various reaction times. The best experimental set was studied for 15, 30, 45 and 60 min, and *COD* removal efficiencies were found for each reaction time (Figure 2c). As seen in Figure 2c, 93.6, 93.8, 94.5 and 92.4% *COD* removal efficiencies were obtained for 15, 30, 45 and 60 min reaction times, respectively. Increase in reaction time had a positive effect on the *COD* removal efficiency until 45 min. It could be easily recognized that the removal efficiencies were close to each other. Although the removal efficiency is a bit more in 45 min compared to 15 min, it is obvious that the costs are much more in 45 min by taking into consideration the factors as consumptions of chemicals for pH adjustment and electric power. Furthermore, the unpaired *t*-test concluded that there was insufficient evidence for a significant difference between *COD* removal efficiencies since the two-tailed *p*-values (0.9934-0.9987) are higher than the chosen α level of 0.05. By conventional criteria, this difference is considered to be not statistically significant. Therefore, the small difference in the removal efficiencies can be ignored. Consequently, 15 min was accepted as the best reaction time in the present Fenton process.

Removal efficiencies in terms of other parameters

All the recent experiments were based on *COD* removal efficiencies. Besides *COD*, BOD_5, *TOC*, PCT, PAP and aniline measurements were performed for the best experimental set and removal efficiencies for each parameter were shown in Figure 3a.

As mentioned before, the best experimental set was repeated for several times and *COD* removal efficiency was found as 92.7±0.6%. Removal efficiencies for the parameters BOD_5, *TOC*, PCT, PAP and aniline were found as 95.5±0.1, 92.7±0.1, 99.1±0.1, 99.9±0.2 and 99.4±0.2%, respectively.

Change in all the parameters during Fenton process

In all the experiments, pollutant measurements were only conducted in the effluent after the Fenton process. In order to determine the change in all the parameters during the Fenton process, samples were taken at each 5 min during the oxidation and after settling.

Change *COD* and *TOC*

COD and *TOC* during the oxidation and settling steps are illustrated in Figure 3b. As seen in Figure 3b, Fenton process was divided in two steps as oxidation and settling. As mentioned before, H_2O_2 was dosed every minute in the oxidation step. Samples were taken at each 5 min after dosing the required amount of H_2O_2. *COD* and *TOC* concentrations had decreased during the oxidation and settling steps. However, a sharp decrease in the concentrations of both parameters after the oxidation step could be easily seen. As a result of these, it can be commented that the parameters *COD* and *TOC* were removed in the settling step by the mechanism of precipitation [39].

Change in the concentrations of PCT, PAP and aniline

Concentrations of PCT, PAP and aniline during the oxidation and settling steps are shown in Figure 3c. As seen in Figure 3c, PCT, PAP and aniline showed a gradually decreasing trend as *COD* and *TOC* within the first 5 min of the oxidation reaction. This study focused on removing essential parameters defined in the local regulations. Therefore, the decreases in *COD* and *TOC* concentrations had more significances than the other parameters as PCT, PAP and aniline. But even so, the analysis of these parameters (PCT, PAP and aniline) were carried out besides *COD* and *TOC* by taking samples at intervals of 5 min for the aim of determining the time-dependent changes in the concentrations. When the decreases in concentrations of these three parameters (PAP, *COD* and *TOC*) were examined within the subsequent time period, it could be seen that their removal was realized by the mechanism of oxidation.

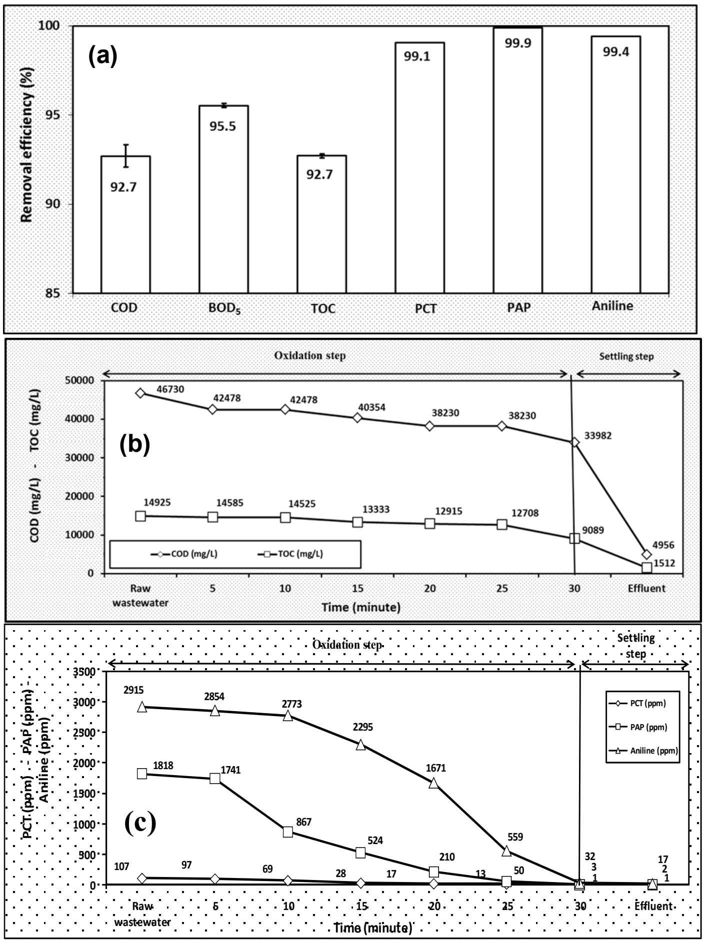

Figure 3. a) Removal efficiencies of all the parameters for the best experimental set; b) change in the concentrations of COD and TOC during Fenton process; c) change in the concentrations of PCT, PAP and aniline during Fenton process.

Consequently, *COD* and *TOC* were removed in settling step while PCT, PAP and aniline were removed in the oxidation step.

It could also be seen that the molecules PCT, PAP and aniline were almost completely degraded in the oxidation step of Fenton process. Nevertheless, *COD* and *TOC* concentrations of the mixture were still considerably high. Andreozzi *et al.* [16] also indicated the by-products synthesized in PCT degradation.

COD of different phases after Fenton process

In this study, mass balance calculations were also conducted to explain the removal mechanisms of *COD* in different phases. *COD* concentrations of the phases (gas + foam, effluent, sludge) after Fenton process are depicted in Figure 4. As seen in Figure 4, mass distribution of *COD* in gas + foam, effluent and sludge phases were calculated as 11132, 2678 and 18901 mg, respectively. In each set of Fenton experiments, gas discharge and foam formation was observed. The decrease of *COD* concentration was derived from the *COD* content of gas and foam. Sludge and effluent were formed from the mixture and it could be seen that a large quantity of *COD* passed to the sludge in the settling step. This case also verified the hypothesis that the removal of *COD* was realized by the precipitation mechanism. Studies about collection

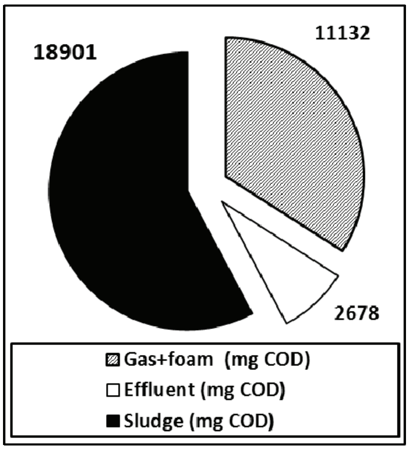

Figure 4. Mass distribution of COD in different phases in Fenton process.

of the gas and disposal of the sludge will be done in the future research.

Comparisons with literature data

Different treatment methods used for PCT removal in the literature are given in Table 3. As seen in Table 3, in addition to advanced oxidation technics, the other methods like adsorption, pure bacterial cultures, active sludge and anaerobic treatment has also been used in PCT removal. Removal efficiencies have usually been determined over the parameters PCT and *TOC*. PCT and *TOC* removal efficiencies have changed within wide ranges as 30-99.9% and 10-99%, respectively. However, these removal efficiencies were obtained by using synthetic wastewater. It can been seen that removal efficiencies in the preesent study are considerably high when compared with the literature.

CONCLUSIONS

PCT sythesis wastewater, which had high concentrations of *COD* and *TOC*, was pretreated by Fenton process used as an effective advanced oxidation process. Significant removal efficiencies were obtained at the best experimental conditions as follows: *COD*/H$_2$O$_2$ ratio 1/1, Fe^{+2}/H$_2$O$_2$ ratio 1/70, reaction time 15 min, settling by centrifuging at pH 6. Removal efficiencies as 92.7±0.628% *COD*, 95.5±0.123% *BOD*$_5$, 92.7±0.107% *TOC*, 99.1% PCT, 99.9% PAP and 99.4% aniline were obtained at these conditions. Removal mechanisms of *COD* and *TOC* were identified as precipitation, and as oxidation for PCT, PAP and aniline. The findings of this study clearly indicated that under the optimal conditions, real PCT wastewater could be effectively pretreated with the contribution of the Fenton process used as a feasible and promising method. Finally, it should be noted that this work has only focused on a local problem of a specific industry that produces paracet-

Table 3. Different treatment methods used for PCT removal in the literature

Type of wastewater	Treatment method	Removal efficiency	Reference
Synthetic PCT wastewater	Ozonation	30% *TOD*	[16]
Synthetic PCT wastewater	H$_2$O$_2$ photolysis	40% *TOD*	[16]
Synthetic PCT wastewater	Advanced electrochemical oxidation	100% *TOD*	[19]
Real PCT wastewater	Fenton	75% *COD*	[20]
Real PCT wastewater	Fenton +anaerobic treatment	98% *COD*	[20]
Synthetic PCT wastewater	Ultrasonic irradiation	100% PCT, 39% *TOD*	[17]
Synthetic PCT wastewater	Subsurface flow constructed wetlands	99.9% PCT	[29]
Synthetic PCT wastewater	Adsorption (vegetable sponge)	40% PCT	[10]
Synthetic PCT wastewater	Adsorption (active carbon)	45% PCT	[10]
Synthetic PCT wastewater	Adsorption (sugar cane bagasse)	60% PCT	[10]
Synthetic municipal wastewater effluent containing PCT	Photo-Fenton	83% *COD*, 71%, *TOD*, 94% *BOD*$_5$	[21]
Synthetic PCT wastewater	Photo-Fenton	60% DOC	[22]
Synthetic PCT wastewater	A combination of three microbial strains	100% PCT, 87.1% *TOD*	[27]
Synthetic PCT wastewater	Advanced oxidation processes	80-99% *TOD*	[23]
Synthetic PCT wastewater	Activated sludge	90% PCT	[28]
Synthetic PCT wastewater	Fenton	99.6% PCT	[24]
Synthetic PCT wastewater	Sonolysis	13% *TOD*	[25]
Synthetic PCT wastewater	TiO$_2$ pho*TOD*atalysis	71% *TOD*	[25]
Synthetic PCT wastewater	Sonolysis + pho*TOD*atalysis	67% *TOD*	[25]
Synthetic PCT wastewater	Ultrasound + Fe^{+3}	10% *TOD*	[25]
Synthetic PCT wastewater	UV+ Fe^{+3}	66% *TOD*	[25]
Synthetic PCT wastewater	Fenton	99% PCT, 34%, *COD*, 14% *TOD*	[26]
Real PCT wastewater from pharmaceutical industry	**Fenton**	**92.7% *COD*, 95,5% *BOD*$_5$, 92.7% *TOD*, 99.1% PCT, 99.9% PAP, 99.4% aniline**	**Present study**

amol, and suggests the Fenton process for the aquatic wastes of the industry, but there are complex systems for the industry of other pharmaceuticals. Based on the advantages of the method described in this study, it can be concluded that additional studies are worthy of investigation by future work to explore the treatability of different types of pharmaceuticals and intermediates during the treatment.

Acknowledgments

The authors would like to thank Research Project Coordinator of Yildiz Technical University for supporting this study financially under the number 2011-05-02-KAP03, and also the factory for providing the wastewater. We also express our great sorrow for the death of dear professor and one of the members of our project group, Ferruh Erturk, on 08.24.2011. He was a great scientist and at the same time he was a great person with humanity and warm kindness to all of us. The authors have declared no conflict of interest.

REFERENCES

[1] T.A. Ternes, Water Res. **32** (1998) 3245-3260

[2] F. Tamtam, F. Mercier, B. Le Bot, J. Eurin, Q.T. Dinh, M. Clement, M. Chevreuil, Sci. Total Environ. **393** (2008) 84--95

[3] A. Alighardashi, M.N. Pons, O. Potier, Rev. Sci. Eau. **21** (2008) 413-426

[4] M. Grung, T. Kallqvist, S. Sakshaug, S. Skurtveit, K.V. Thomas, Ecotox. Environ. Safe. **371** (2008) 328-340

[5] S. Mompelat, B. Le Bot, O. Thomas, Environ. Int. **35** (2009) 803-814

[6] K.M. Onesios, J.T. Yu, E.J. Bouwer, Biodegradation **20** (2009) 441-466

[7] K. Kummerer, Chemosphere **75** (2009) 417-434

[8] C. Postigo, M.J. Lopez de Alda, D. Barcelo, Environ. Int. **36** (2009) 75-84

[9] H. Li, P.A. Helm, C.D. Metcalfe, Environ. Toxicol. Chem. **29** (2010) 751-762

[10] A.V.F.N. Ribeiro, M. Belisário, R.M. Galazzi, D.C. Balthazar, M.G. Pereira, J.N. Ribeiro, Electron. J. Biotechnol. **14** (2011) 7

[11] N. Kulik, M. Trapido, A. Goi, Y. Veressina, R. Munter, Chemosphere **70** (2008) 1525-1531

[12] I.R. Bautitz, R.F.P. Nogueira, Catalysis Today **151** (2010) 94-99

[13] L.A. Pérez-Estrada, S. Malato, W. Gernjak, A. Agüera, E.M. Thurman, I. Ferrer, A.R. Fernández-Alba, Environ. Sci. Technol. **39** (2005) 8300-8306

[14] I. Sirés-Sadornil, Ph.D. Thesis, Universitat de Barcelona, Facultat de Quimica, Barcelona, 2006

[15] H. Kabak, Ph.D. Thesis, Cukurova University, Institute of Natural and Applied Sciences, Adana, 2008

[16] R. Andreozzi, V. Caprio, R. Marotta, D. Vogna, Water Res. **37** (2003) 993-1004

[17] I. Quesada-Peñate, C. Julcour-Lebigue, U.J. Jauregui-Hazac, A.M. Wilhelm, H. Delmas, Ultrasonics Sonochem. **16** (2009) 610-616

[18] I. Quesada-Peñate, C. Julcour-Lebigue, U.J. Jauregui--Hazac, A.M. Wilhelm, H. Delmas, J. Hazard. Mater. **221--222** (2012) 131-138

[19] I. Sirés, C. Arias, P.L. Cabot, F. Centallas, R.M. Rodriguez, J.A. Garrido, E. Brillas, Environ. Chem. **1** (2004) 26-28

[20] U.D. Keris, M.Sc. Thesis, Gebze Institute of Technology, Graduate School of Engineering and Sciences, Gebze, 2008

[21] A. Durán, J.M. Monteagudo, A. Carnicer, M. Ruiz-Murillo, Desalination **270** (2011) 124-129

[22] L.S.-J. Jordá, M.M.B. Martín, E.O. Gómez, A.C. Reina, I.M.R. Sánchez, J.L.C. López, J.A.S. Pérez, J. Hazard. Mater. **186** (2011) 1924-1929

[23] H.C.A. Valdez, G.G. Jiménez, S.G. Granados, P.L. León, Chemosphere **89** (2012) 1195-1201

[24] M.D.G. Luna, R.W. Briones, C.-C. Su, M.-C. Lu, Chemosphere **90** (2013) 1444-1448

[25] M. Jagannathan, F. Grieser, M. Ashokkumar, Sep. Purif. Technol. **103** (2013) 114-118

[26] C.-C. Su, L.M. Bellotindos, A.-T. Chang, M.-C. Lu, J. Taiwan Inst. Chem. Eng. **44** (2013) 310-316

[27] L. Zhang, J. Hu, R. Zhu, Q. Zhou, J. Chen, Appl. Microbiol. Biotechnol. **97** (2012) 3687-3698

[28] B. Balci, O. Keskinkan, A. Erkus, Cukurova University, J. Fac. Eng. Archit. **27** (2012) 1-12

[29] E. Ranieri, P. Verlicchi, T.M. Young, Hydrol. **404** (2011) 130-135

[30] I. Arslan-Alaton, S. Dogruel, J. Hazard. Mater., B **112** (2004) 105-113

[31] M. Klavarioti, D. Mantzavinos, D. Kassinos, Environ. Int. **35** (2009) 402-417

[32] H. Tekin, O. Bilkay, S.S. Ataberk, T.H. Balta, I.H. Ceribasi, F.D. Sanin, F.B. Dilek, U. Yetis, J. Hazard. Mater., B **136** (2006) 258-265

[33] M.I. Badawy, R.A. Wahaab, A.S. El-Kalliny, J. Hazard. Mater. **167** (2009) 567-574

[34] C. Ratanatamskul, N. Masomboon, M-C. Lu, Pesticides in the Modern World - Pesticides Use and Management, InTech Pub., 2011, pp. 463-474.

[35] E. Chamarro, A. Marco, S. Esplugas, Water Res. **35** (2001) 1047-1051

[36] J.J. Pignatello, E. Oliveros, A. MacKay, Crit. Rev. Environ. Sci. Technol. **36** (2006) 1-84

[37] L.C. Almeida, S. Garcia-Segura, N. Bocchi, E. Brillas, Appl. Catal., B: Environ. **103** (2011) 21-30

[38] A.Y. Sychev, V.G. Isak, Russ. Chem. Rev. **64** (1995) 1105-1129

[39] R.J. Bigda, Chem. Eng. Prog. **91** (1995) 62-66

[40] APHA (American Public Health Association). Standard Methods for the Examination of Water and Wastewater, 20th ed., Washington, DC, 1998

[41] O.Ö. Sögüt, E. Yıldırım, M. Akgün, Desalin. Water Treat. **26** (2011) 1-8

[42] European Directorate for the Quality of Medicines & HealthCare: European Pharmacopoeia 8.0 (2014), https://www.edqm.eu/ (accessed 27 Aug 2015)

[43] TWPCR (Turkish Water Pollution Control Regulation). Official Gazette No. 25687 dated December 31, 2004.

GAMZE DALGIC
F. ILTER TURKDOGAN
KAAN YETILMEZSOY
EMEL KOCAK

Department of Environmental Engineering, Faculty of Civil Engineering, Yildiz Technical University, Davutpasa, Esenler, Istanbul, Turkey

NAUČNI RAD

OBRADA OTPADNE VODE SA PARACETAMOLOM FENTONOVIM PROCESOM

U ovom radu izvršen je pretretman otpadne vode zagađene paracetamolom (PCT) iz farmaceutske industrije Fentonovim procesom. Pri najboljim eksperimentalnim uslovima pretretmana (odnos HPK/H_2O_2 *= 1,1,* Fe^{2+}/H_2O_2 *= 1,70, metoda taloženja: centrifugisanje i pH 6 u fazi taloženja) procenat uklanjanja hemijske potrošnje kiseonika (HPK), ukupnog organkog ugljenika (TOC), PCT, para-aminofenola (PAP) i anilina iznose 92,7, 92,7, 95,5, 99,1, 99,9 i 99,4%, redom. Promena ovih parametara je analizirana za taložni i oksidacionu fazu Fentonovog procesa. Nađeno je da se HPK i TOC uklanjaju u taložnoj fazi, a da se PCT, PAP i anilin uklanjaju u oksidacionoj fazi. Bilansi mase su pokazali distribuciju HPK u različitim fazama (gas + pena, otpadna voda i mulj). Utvrđeno je da je Fentonov proces efikasna metoda za pretretman otpadne vode sa PCT u postrojenju za tretman otpadne vode.*

Ključne reči: hemijska potrošnja kiseonika, Fenton proces, bilans mase, otpadna voda sa paracetamolom, ukupni organski ugljenik.

CI&CEQ
Chemical Industry & Chemical Engineering Quarterly

Available on line at
Association of the Chemical Engineers of Serbia *AChE*
www.ache.org.rs/CICEQ

Chem. Ind. Chem. Eng. Q. 23 (2) 187–195 (2017) CI&CEQ

K.D. RADOSAVLJEVIĆ[1]
A.V. GOLUBOVIĆ[2]
M.M. RADIŠIĆ[3]
A.R. MLADENOVIĆ[4]
D.Ž. MIJIN[1]
S.D. PETROVIĆ[1]

[1]Faculty of Technology and Metallurgy, University of Belgrade, Belgrade, Serbia
[2]Centre for Solid State Physics and New Materials, Institute of Physics, University of Belgrade, Belgrade-Zemun, Serbia
[3]Innovation Center, Faculty of Technology and Metallurgy, University of Belgrade, Belgrade, Serbia
[4]Hemofarm A.D., STADA Company, Vršac, Serbia

SCIENTIFIC PAPER

UDC 544.526.5: 543.544:615.33:66

AMOXICILLIN PHOTODEGRADATION BY NANOCRYSTALLINE TiO_2

Article Highlights

- Nanocrystalline TiO_2 was synthesized by sol-gel route
- Nanocrystalline TiO_2 was applied in the degradation of amoxicillin
- The effect of catalyst, salt, ethanol and pH on the reaction was established
- The mineralization of amoxicillin was analyzed by IC and TOC
- The catalytic properties of nanocrystalline TiO_2 was compared to P25

Abstract

Nanocrystalline TiO_2, synthesized by sol-gel route and characterized by XRPD, BET and SEM measurements, was applied in the photocatalytic degradation of amoxicillin, using an Osram Ultra-Vitalux® lamp as the light source. Amoxicillin is a semi-synthetic penicillin type antibiotic active against a wide range of gram-positive and a limited range of gram-negative organisms. The continuous release of antibiotics and their persistence in the environment may result in serious irreversible effects on aquatic and terrestrial organisms. Heterogeneous catalysis, which uses catalysts like TiO_2, is a promising route for the degradation of organic pollutants including antibiotics. The effects of initial concentration of catalyst, initial salt concentration (NaCl and Na_2SO_4), ethanol and pH on the photocatalytic degradation of amoxicillin were studied. The mineralization of amoxicillin was analyzed by ion chromatography as well as by total organic analysis. The catalytic properties of nanocrystalline TiO_2 were compared to Evonik P25 catalyst.

Keywords: nanopowder, SEM, XRD, optimization, HPLC-MS, TOC.

From an environmental point of view, antibiotics constitute a new group of man-made chemicals of concern due to their high consumption rate worldwide. Their continuous release and persistence in the ecosystem, even at low concentrations, may result in serious irreversible effects on aquatic and terrestrial organisms. Antibiotics are an especially hazardous class of compounds, because they are potent in damaging micro-flora and fauna, they accumulate in food chains [1], and accelerate the development of resistant bacteria. Hence, antibiotics must be degraded or destroyed before discharging contingent wastewater to the environment. Central nervous system damage, mutagenic effects, nephropathy, arthropathy, light sensitivity and spermatogenesis can result from the accumulation of antibiotics in organisms [2].

Penicillin class drugs are among frequently detected antibiotics in wastewaters. However, penicillins are not usually thought to be a serious threat to the environment because of the poor stability of the β-lactam ring under pH conditions and β-lactamase activity [3]. The opening of this ring is related to the loss of microbiological activity [4,5].

Amoxicillin ($C_{16}H_{19}N_3O_5S$ (AMX), Figure 1) is a semi-synthetic penicillin type antibiotic active against a wide range of gram-positive and a limited range of gram-negative organisms. It is used in human medicine as well as in veterinary practice. The presence and fate of amoxicillin in the environment has been investigated [6,7].

Studies available in the scientific literature reported that, although usually detected in trace concen-

---

Correspondence: D.Ž. Mijin, Faculty of Technology and Metallurgy, University of Belgrade, Karnegijeva 4, 11120 Belgrade, Serbia.
E-mail: kavur@tmf.bg.ac.rs

Paper received: 22 January, 2016
Paper revised: 13 April, 2016
Paper accepted: 18 May, 2016

https://doi.org/10.2298/CICEQ160122030R

trations, amoxicillin continuous release into the environment increases the possibility of synergistic effects with other pharmaceuticals or chemicals in the aquatic effluent [8].

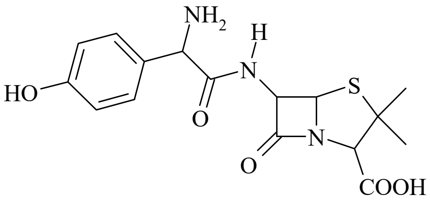

Figure 1. AMX structure.

It is useful to apply effective treatment technology to remove the amoxicillin from water. In this regard, advanced oxidation processes (AOPs), namely heterogeneous catalysis which uses catalysts like TiO_2 and ZnO, are a promising route for the degradation of organic pollutants based on the formation of hydroxyl, $^{\bullet}OH$, and other radicals and they are more suitable in comparison to other more expensive techniques, such as activated carbon adsorption, air stripping and reverse osmosis. Indeed, these techniques only transfer the pollutants from one phase to another without degrading or destroying them while AOPs radicals strongly oxidize toxic and non-biodegradable compounds to the different co-products, and, in the course of time, to innocuous end-products such as CO_2 and H_2O [9].

TiO_2 is the most commonly used photocatalyst for pollutant destruction in aqueous solution and it is very efficient – furthermore, it is inexpensive, commercially available at various crystalline forms and particle characteristics, non-toxic, stable to photocorrosion and easy to work with. The single drawback is that TiO_2 does not absorb visible light and to overcome that doping, dye sensitization, coupling and capping of TiO_2 have been studied [10].

A number of reported studies on degradation of amoxicillin by different AOPs include the treatment of amoxicillin wastewater by combination of extraction, Fenton oxidation and reverse osmosis [11]. Elmolla and Chaudhuri studied the degradation of amoxicillin, ampicillin and cloxacillin antibiotics by using Fenton [12], photo-Fenton [13] and UV/ZnO photocatalysis [14]. Degussa P-25 and other commercial as well as synthesized TiO_2 were used in the study of degradation of amoxicillin [15,16]. So, Klauson *et al.* [15] showed that aqueous photocatalytic oxidation of amoxicillin by applying TiO_2 Degussa P25 and visible light-sensitive sol-gel synthesized carbon-and iron-doped titania as photocatalysts proceeds with maximum efficiency in neutral solutions. Doped catalysts were close in efficiency to Degussa catalyst under solar radiation. Dimitrakopoulou *et al.* [16] found out that among studied photocatalysts Degussa P25 was highly active with complete AMX degradation and 93% mineralization using 10 mg dm^{-3} AMX and 250 mg dm^{-3} TiO_2 in a laboratory scale photoreactor. In general, mineralization was slower than degradation.

The aim of this work is to study the potency of sol-gel route synthesized nanocrystalline TiO_2, previously applied in the degradation of azo dye, phenol and pesticide [17], in the photocatalytic amoxicillin degradation, using an Osram Ultra-Vitalux® lamp as the light source. The catalytic property of nanocrystalline TiO_2 was compared to commercial Evonik P25 in AMX degradation. The effect of the parameters such as initial concentration of catalyst, initial salt concentration (NaCl and Na_2SO_4), ethanol and pH was analyzed. The mineralization of amoxicillin was analyzed by TOC and ion analysis.

EXPERIMENTAL

Materials

Amoxicillin trihydrate was obtained from Hemofarm-Stada. Methanol and sodium hydroxide were purchased from J.T. Baker, while acetic acid was produced by Lachner. Tetrabutyl titanate $Ti(OBu)_4$ was produced by Acros Organics, hydrochloric acid by Zorka, and ethanol by Carlo Erba. Sodium chloride was obtained from Zdravlje, and sodium sulfate from Centrochem. P25 titanium dioxide was supplied by Aldrich. All chemical used were of analytical grade or higher. All chemicals were used without further purifications. Deionized water was obtained from a Millipore water purification system.

Preparation of nanocrystalline TiO_2

The TiO_2 nanocrystals were prepared by a sol-gel method [17]. The precursor was tetrabutyl titanate and the mole ratio between reagents was $Ti(OBu)_4$:HCl:EtOH:H_2O = 1:0.3:15:4. The synthesis was carried out at the temperature of ice, where hydrochloric acid (36.2%, Zorka, Serbia), ethanol (96%, denatured, Carlo Erba, Italy), and at the end, distilled water were slowly added to tetrabutyl titanate (99%, Acros Organics, Belgium). The hydrolysis and polycondensation reactions of $Ti(OBu)_4$ were carried out at the temperature of ice. After the gelation, the wet gels were dried at 80 °C, and then the dry gels were calcined at 500 °C for 2.5 h to obtain TiO_2 nanocrystals. The heating rate and the cooling rate were the same (135 °C h^{-1}).

Photocatalytic experiment

The photodegradation of AMX was investigated in deionised water in an open reactor (100 cm³), thermostated at 25 °C [18]. For the irradiation an Osram Ultra Vitalux® 300 W lamp was used, with ratio of UV-A and UV-B lights of 13.6:3. The position of the lamp was 40 cm from the surface of the reaction mixture, containing in general AMX and TiO_2. The temperature of the reaction mixture changed for 2.5 °C during 210 min of irradiation. For every experimental cycle, 25 cm³ of the reaction mixture was placed into the reactor and stirred, using magnetic stirrer (Heidolph) for 30 min in the dark in order to reach adsorption/desorption equilibrium. Then the lamp was switched on while the continuous stirring was maintained. The aliquots were taken at defined time intervals. All the aliquots were filtrated by 0.45 µm Cronus 13 mm nylon syringe filters, in order to remove the suspended TiO_2 particles before the analysis. All the experiments were done in triplicate.

Analytical procedures

XRD

Structural analysis of prepared samples was done by XRPD on Ital Structures APD2000 diffractometer, using CuKα radiation (λ = 1.5406 Å), angular range: $20° < 2\theta < 90°$. Data were collected at every 0.01° in the 20-90° 2θ using a counting time of 80 s/step. MDI Jade 5.0 software was used for calculation of the structural and microstructural parameters. The Williamson-Hall method was applied for the determination of average microstrain and the mean crystallite sizes, $<D>$, of the prepared samples. The obtained values are compared to the mean crystallite sizes calculated by Scherrer formula. The Scherrer formula is an estimate crystallite size calculated from FWHM of all diffractions collected during measurement.

SEM

The morphology of the prepared TiO_2 nanopowder was analyzed by scanning electron microscope (SEM). The measurements were carried out on a Tescan MIRA3 field emission gun SEM, at 10 kV in high vacuum. SEM working distance was about 4 mm. The powder was sonicated in ethanol for 15 min. Immediately afterwards, a drop of solution was casted onto a freshly cleaved kish graphite crystal embedded with a silver paste into a sample holder. Access material was removed in a stream of argon gas and the sample was left to degas in low vacuum for 1 h, before the measurements on a scanning electron microscope. The sample plane was 40° tilted relative to the plane perpendicular to the SEM column axis.

BET

The porous structure of anatase samples is evaluated from adsorption/desorption isotherms of N_2 at -196 °C, using the gravimetric McBain method. The main parameters of the porosity, such as specific surface area and pore volume, have been estimated by BET method from α_s-plot. The pore size distribution has been estimated from hysteresis sorption data by Barret-Joyner-Halenda method.

UV and HPLC analysis

The concentration of the antibiotic was monitored by Shimadzu 1700 UV-Vis spectrophotometer at 228 nm and checked by HPLC analysis. The HPLC determinations were carried out using an HPLC instrument Agilent 1100 Series equipped with Zorbax Eclipse XDB-C18 column (Agilent). The analyses were performed in isocratic mode using water/methanol/acetic acid (200:300:5 volume ratio). The mobile phase had the flow rate of 0.8 cm³ min⁻¹ and the column temperature was 258 °C. The injection volume was 5 µL and UV detection was carried out at 228 nm.

pH Measurement

The pH value of the samples was adjusted by the addition of 0.1 mol dm⁻³ NaOH or HCl and the determination of pH was performed on a Hanna HI 2210 pH meter.

Ion chromatographic analysis

Ion chromatographic analysis was performed on a Dionex DX 300 ion chromatograph at ambient temperature 25 °C with suppressed conductivity detector. The ion chromatograph was equipped with a Dionex IonPac AS14 column.

Total organic carbon analysis

Total organic carbon was measured using a Zellweger LabTOC 2100 instrument.

RESULTS AND DISCUSSION

Synthesis of TiO_2 catalyst

The TiO_2 nanocrystals can be usually obtained by a sol-gel method where titanium tetrachloride, isopropoxide titanate and tetrabutyl titanate are used as precursors [19,20]. In our study, tetrabutyl titanate ($Ti(OBu)_4$) was used as a precursor and the mole ratio between reagents were $Ti(OBu)_4$:HCl:EtOH:H_2O = 1:0.3:15:4, where hydrochloride acid was used as the catalyst, ethanol as the solvent, and water for hydrolysis. Measured pH value of the colloidal suspension was 7. Many experiments of TiO_2 synthesis were done in order to find the optimal combination of reagents with different acids (HCl and CH_3COOH) and their various molar ratios, or different alcohols (EtOH, AmylOH), but the best combination was the mentioned one, which is in accordance to the ratio from the literature [21].

Photocatalytic properties of obtained TiO_2 were previously checked in photodegradation of textile dye C.I. Reactive Orange 16 [17] and compared to Evonik P25. The recorded activity was similar to the activity of P25 catalyst.

Characterization methods

XRPD

The most intensive diffraction peaks in the XRPD patterns of sol-gel produced sample can be ascribed to the anatase crystal structure (JCPDS card 21-1272) and it is presented, together with corresponding Miller indices, in Figure 2. There is no evidence of neither rutile nor brookite phase. Structure characteristics of our TiO_2 were: lattice parameters, a = 3.784(3) Å, c = 9.53(0) Å, V = 136.4 Å^3. Average primary particle size of 15 nm was obtained by Scherrer analyses, or 24 nm with microstrain of 0.301% obtained by Williamson-Hall method, while for Degussa P25 it was found to be 31 [22] or 20 nm [23] calculated by Scherrer equations. BET analysis revealed specific surface area (BET) of 52 m^2 g^{-1} for our sample with pore volumes 0.1063 cm^3 g^{-1} and pore diameter 5.3 nm, while data for Degussa P25 were specific surface area of 52 m^2 g^{-1} as in [22] and similar value found in the literature of 51 m^2 g^{-1} [23]. Pore volumes were 0.150 cm^3 g^{-1} and pore diameter 31.5 nm [23], where these data not cited in [22]. Therefore, it could be suggested that the specific surface area is an important parameter for the photocatalytic degradation. Degussa P25 is commercial and the most popular compound for the photocatalytic degradation. It is a combination of anatase and rutile phase (82% of anatase phase and 18% of rutile phase [22], while our sample had the pure anatase phase. One of the reasons for the synthesis of nanocrystalline TiO_2 and its comparison to Degussa P25 is the fact that one can improve the knowledge about the mechanism of photocatalytic degradation and, within the choice of offered parameters, to tailor their own process.

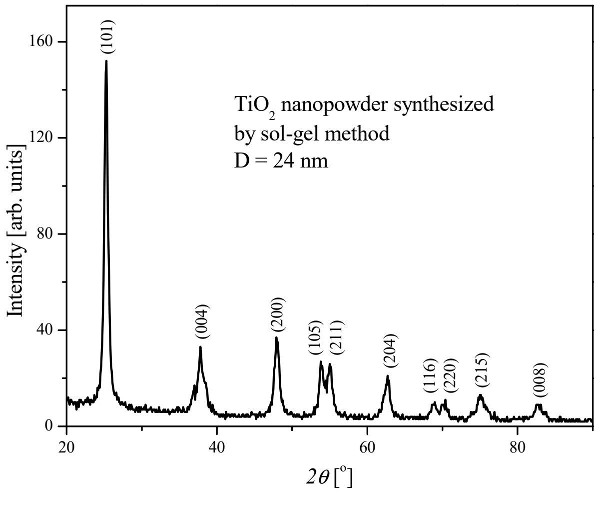

Figure 2. XRPD diffractograms of chosen TiO_2 sample together with corresponding Miller indices (JCPDS card 21-1272).

SEM

The results of SEM measurements are shown in Figure 3. Agglomerated structure could be clearly seen, which is in accordance with the fact that pH value of gel equals the point of zero charge (PZC) for TiO_2 obtained from tetrabutyl titanate [24], which promotes higher agglomeration. Values of diameters of the individual particles are in accordance with the value of the average particle size obtained by Williamson-Hall method (24 nm).

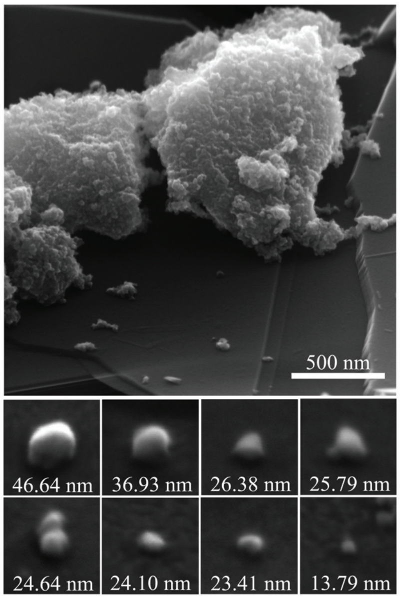

Figure 3. Top: SEM image of the conglomerated structure, also showing smaller conglomerated structures and several single particles. The top image is magnified 200×. Bottom: eight single particles. The size of each image is 100 nm×100 nm, the magnification of each bottom image is 1M×. The diameter of each particle is estimated to be within ±4 nm of the given value.

AMX photocatalytic degradation

Initial experiments

In the first experiment, the adsorption of AMX on nanocrystalline TiO_2 as well as the photolysis of AMX was investigated (Figure 4). As can be seen, the change in normalized concentration (normalized concentration c/c_0, where c is the concentration of AMX at irradiation time t and c_0 is the initial concentration of AMX) is about 5%, indicating low adsorption (experiment in dark) of AMX on nanocrystalline TiO_2 by using the catalyst at concentration of 2 g dm^{-3}. during the photolysis of 210 min using Osram Ultra-Vitalux® 300W lamp, AMX was proven to be stable. This is in agreement with previously published literature data, where it was found that AMX is relatively stable during short reaction time in the environment as well us under simulated sunlight photolysis [6,25]. Degradation under UV light at 365 nm was ascribed to the hydrolysis rather than photolysis [26]. Due to the adsorption of AMX on nanocrystalline TiO_2, the suspension was stirred for 30 minutes in the dark prior to photocatalysis process to reach the adsorption equilibrium [27]. The equilibrium AMX concentration was then used as c_0 concentration (Figure 4). The adsorption of AMX on P25 catalyst was found to be similar to that of the prepared nanocrystalline TiO_2 (about 4%).

Consequently, the degradation of the studied antibiotic was recorded when the suspension of nanocrystalline TiO_2 and AMX was irradiated. Figure 4 shows that almost complete degradation of AMX was achieved after 210 min. The inset in Figure 4 represents the influence of the initial catalyst concentration on pseudo-first reaction constant (k). It is known that the photodegradation reaction can be well described using a pseudo-first kinetic order, which is given by the following equations [28]:

$$\ln\left(\frac{c_0}{c}\right) = kt \tag{1}$$

$$c = c_0 e^{-k\,t} \tag{2}$$

Initial photocatalyst concentration was varied in the range 0.5-4.0 g dm^{-3} and AMX concentration was 100 mg dm^{-3}. It can be seen that the photodegradation rate of AMX increased with TiO_2 concentration in the range 0.5-2.0 g dm^{-3}, presumably due to the increase in $^{\bullet}OH$ production. Further increase of catalyst concentration produced a small decrease of AMX photodegradation rate. This may be due to the decreasing UV light penetration, increasing light scattering, agglomeration and sedimentation of TiO_2 at high catalyst concentration. The reaction rate may also decrease due to lessening of light density in turbid solution [29]. Based on the results, the optimum titanium dioxide concentration for degradation of AMX in aqueous suspension is 2.0 g dm^{-3}.

The catalytic property of nanocrystalline TiO_2 was compared to P25 catalyst. Figure 4 shows that in the case of AMX degradation nanocrystalline TiO_2 has similar catalytic properties as P25. This is in agreement with previously obtained results for the photocatalytic degradation of C.I. Reactive orange dye [17].

The effect of the pH value

The photodegradation of AMX was studied at five different pH values. The pH of the AMX water solution was 6. pH value of the solution was adjusted before irradiation. The adjustments of acidic (pH 3 and 5) and alkaline medium (pH 9 and 11) were made using diluted HCl or NaOH. Figure 5 reveals that

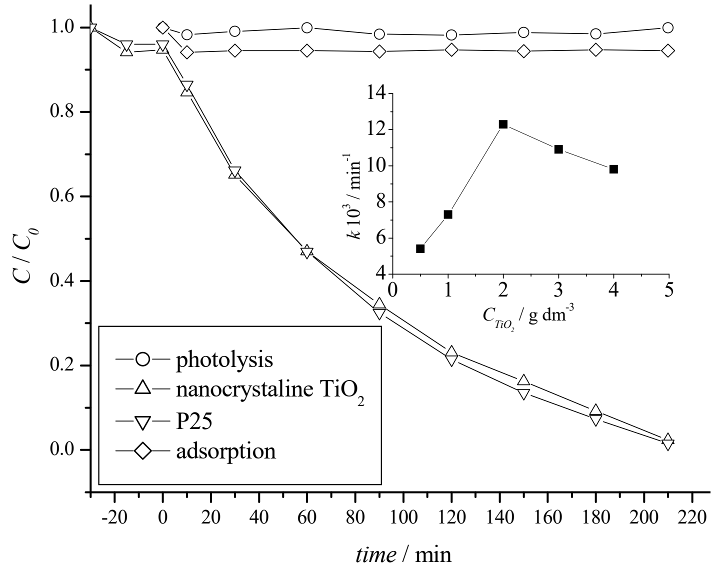

Figure 4. The effect of different experimental conditions on AMX degradation in deionised water (AMX concentration 100 mg dm^{-3}, catalyst concentration 2 g dm^{-3}). inset: influence of nanocrystalline TiO_2 concentration on the reaction rate.

increasing pH from 3 to 5/6 decreases the reaction rate. Emmola *et al.* showed that AMX is positively charged at acidic pH while at alkaline pH it is negatively charged [26]. On the other hand TiO_2 surface charge change from positive to negative. Point zero charge should be at pH 6.8 [30]. So, AMX and TiO_2 are both positively charged in acidic conditions. These should hinder the adsorption of AMX on TiO_2 surface and slow the reaction. The observed higher degradation rate (*ca.* 20%) in more acidic conditions in comparison to less acidic/neutral conditions can be explained by the hydrolysis of antibiotic as suggested earlier [31]. Increase in degradation rate (*ca.* 60%) with the increase of pH is a result of more intensive hydroxyl radical formation at higher pH on one hand, and the hydrolysis of the antibiotics, on the other. The instability of the β-lactam ring at high pH is documented in literature [32]. At alkaline pH, like in acidic, AMX and TiO_2 have the same charge (negative) so again the adsorption is hindered. The obtained results are in agreement with the previously reported effects of pH on AMX photodegradation [15,26].

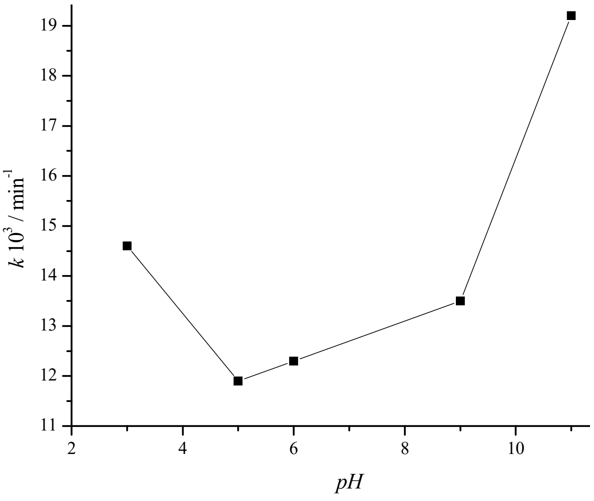

Figure 5. The effect of pH value on the photocatalytic degradation rate of AMX (100 mg dm⁻³) in deionized water (c_{cat} = 2 g dm⁻³).

Our photolytic experiment as well as the reported photolytic data [26] indicates the catalytic properties of the used catalyst in photodegradation of AMX. The higher observed degradation rates at low and high pH are the result of the photocatalytic effect of TiO_2 and the instability of AMX. Namely, it was found that the AMX hydrolysis rate constants, at pH 3 and 11 were 0.13 and 1.7 min^{-1}, respectively [7]. Our photocatalytic reaction rate constants, at pH 3 and 11, were found to be 14.6 and 19.2 min^{-1}, respectively. This proves the photocatalytic nature of the process.

The effect of the added salts

Inorganic ions that are usually present in wastewaters can affect the photocatalytic degradation of the organic pollutants. Inorganic anions such as carbonate, nitrate, chlorides and sulphates can have significant impact on the photodegradation reactions [18]. So, we choose to study the effect of chloride and sulphate ions on the photodegradation of AMX by using sodium chloride (NaCl) and sodium sulphate (Na_2SO_4). The influence of different concentrations of salts (20 and 200 mmol) on the photodegradation rate of AMX is presented in Figure 6.

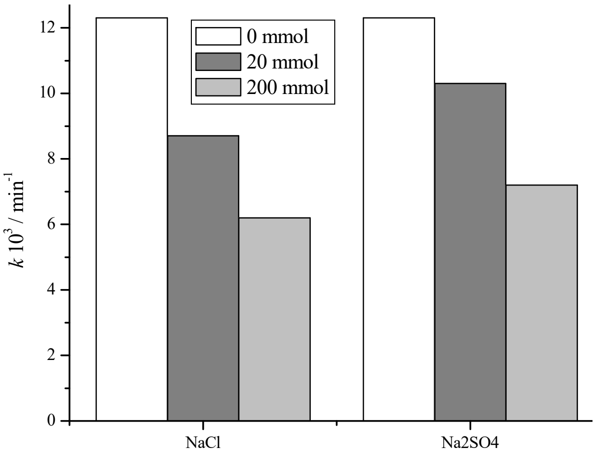

Figure 6. The effect of salts on the photocatalytic degradation rate of AMX (100 mg dm⁻³) in the presence of nanocrystalline TiO_2 (c_{cat} = 2 g dm⁻³).

These influences can be described by the Eqs. (3)-(9) [33-35] for chloride:

$$Cl^- + h^+ \rightarrow Cl^\bullet \quad (3)$$

$$Cl^- + {}^\bullet OH \rightarrow ClOH^{\bullet -} \quad (4)$$

$$ClOH^{\bullet -} + H^+ \rightarrow Cl^\bullet + H_2O \quad (5)$$

$$Cl^\bullet + Cl^- \rightarrow Cl_2^{\bullet -} \quad (6)$$

and sulfate:

$$SO_4^{2-} + h^+ \rightarrow SO_4^{\bullet 2-} \quad (7)$$

$$SO_4^{2-} + {}^\bullet OH \rightarrow SO_4^{\bullet -} + OH^- \quad (8)$$

$$SO_4^{\bullet -} + e_{CB}^- \rightarrow SO_4^{2-} \quad (9)$$

The observed inhibition of AMX photodegradation in Figure 6 is a result of hole scavenging properties of chloride and sulfate ions. Also there are reactions with hydroxyl radicals [36]. The observed decrease of photodegradation of AMX in the presence of chloride or sulfate anions can be explained by competitive adsorption [37]. The TiO_2 surface sites at which adsorption and electron transfer occurs can be blocked by anions thus making them effective inhibitors.

The obtained results (Figure 6) show that the chlorides are a more powerful inhibitor in comparison to sulphates, which is in accordance with previously reported results on salt effects [35]. The increase in salt concentration increases the inhibition of the reaction. While the pseudo-first reaction constant for lower sodium chloride concentration was 8.7×10^{-3} min^{-1}, the pseudo-first reaction constant for the same sodium sulphate concentration was 10.3×10^{-3} min^{-1} clearly indicating that the chloride anion is a stronger inhibitor than sulphate. The same was observed for higher concentrations (constants for sodium chloride and sodium sulphate were 6.2×10^{-3} and 7.2×10^{-3} min^{-1}, respectively).

The effect of $^\bullet$OH scavenger

It is known that alcohols like ethanol or methanol act as $^\bullet$OH scavengers [38,39], so we wanted to investigate whether the photodegradation of AMX takes place *via* $^\bullet$OH by adding ethanol to the reaction mixture. Ethanol was chosen because the products of the reaction are weaker oxidants (alkoxy-radicals) that react with the substrate [40].

The obtained results, given in Figure 7, clearly show that the degradation rate decreases with an increase of ethanol concentration in the reaction mixture. Addition of ethanol, in concentration of 0.69 mol dm^{-3}, decreases the reaction rate to almost half of the reaction without ethanol. This implies that $^\bullet$OH plays major role in photodegradation of AMX [39].

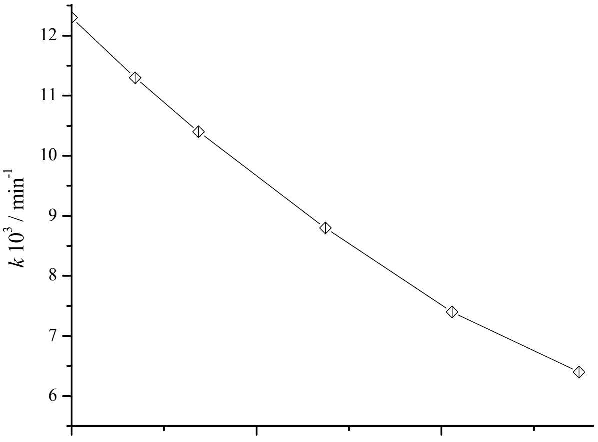

Figure 7. The effect of ethanol concentration on the photocatalytic degradation rate of AMX (100 mg dm^{-3}) in deionized water (c_{cat} = 2 g dm^{-3}).

Readings of ion chromatography and total organic carbon elimination

The mineralization of AMX was studied by ion chromatography analysis and by total organic carbon elimination. The evolutions of ionic species formed during the degradation of AMX as well as the normalized total organic carbon elimination (*TOC*/*TOC*$_0$) change are shown in Figure 8. The main goal of each photodegradation is the mineralization of organic molecule. Carbon and hydrogen atoms give CO_2 and H_2O, while heteroatoms give corresponding inorganic ions. Since AMX contains nitrogen and sulfur as heteroatoms, the formation of NH_4^+, NO_2^-/NO_3^- and SO_4^{2-} can be expected. Ion chromatography revealed the formation of NH_4^+, NO_3^- and SO_4^{2-} as the result of AMX degradation. According to the structure, AMX has three nitrogen atoms and one sulphur atom. For AMX, each molecule contains three nitrogen atoms, two of them in aliphatic bonds and the other in the β-lactam ring. The results showed that the initial NH_4^+ concentration was 1.1 mg dm^{-3} and after the photodegradation increased to 2.4 mg dm^{-3}. The NO_3^- concentration gradually increased from 0.26 to 1.50 mg dm^{-3}. This means that after 210 min of photocatalytic degradation about 11.2% of nitrogen was transformed - about 8.8% for NH_4^+ and 2.4% for NO_3^-. At the beginning of the reaction, concentration of sulphates was 0.42 mg dm^{-3}, while after 210 min it was 8.4 mg dm^{-3}. This indicates that about 30.4% of sulfur was mineralized. Klausen *et al.* [15] reported that AMX molecule is cleaved usually with the release of *p*-hydroxybenzoic acid or by the loss of the amino group, followed by the opening of β-lactam ring, giving at the end 3-methyl-2-oxo-3-sulfobutyric acid. Our results, which also indicate that the degradation of AMX involve the formation of carbon dioxide, water, nitrate, ammonia and sulphate anions, are in agreement with these findings.

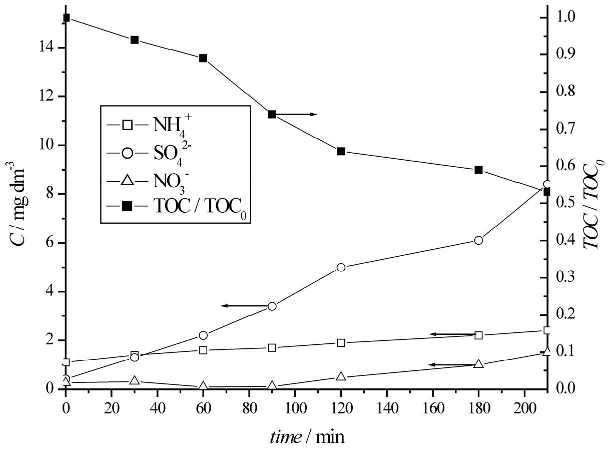

Figure 8. Time dependence of inorganic ions concentration and TOC/TOC$_0$ during the photocatalytic degradation of AMX (100 mg dm^{-3}) in deionized water (c_{cat} = 2 g dm^{-3}).

The mineralization of AMX was also studied by total organic carbon analysis. After 210 min of irradiation, TOC elimination was 47%, indicating that *TOC* elimination rate was not proportional to the rate of AMX disappearance and also confirms the formation of products that contain sulfur and/or nitrogen atoms.

CONCLUSION

The photodegradation of AMX was studied at five different pH values. The observed higher degradation rate in acidic conditions in comparison to neutral conditions can be explained by the hydrolysis of the antibiotic. Increase in degradation rate with the increase of pH is a result of more intensive hydroxyl radical formation at higher pH and the hydrolysis of the antibiotics. The salt effect on the photodegradation of AMX was studied by the addition of sodium chloride and sodium sulphate. The observed inhibition of AMX photodegradation is a result of hole scavenging properties of chlorides and sulfates. Addition of ethanol decreases the reaction rate, which implies that $^{\bullet}OH$ radicals play major role in photodegradation of AMX. Ion chromatography revealed the formation of NH_4^+, NO_3^- and SO_4^{2-} as the result of AMX degradation. The results showed that after 210 min of photocatalytic degradation about 11.2% of nitrogen and about 30.4% of sulfur was transformed. *TOC* elimination was 47%, indicating the formation of products that contain sulfur and/or nitrogen atoms. The catalytic property of nanocrystalline TiO_2 was compared to P25 catalyst and it was found that nanocrystalline TiO_2 has similar catalytic properties as P25.

Acknowledgement

This work has been financially supported by Ministry of Education, Science and Technological Development, Republic of Serbia, under Grant No. 172013.

REFERENCES

[1] B. Halling-Sorensen, S. Nors Nielsen, P.F. Lanzky, F. Ingerslev, H.C. Holten Lutzhoft, S.E. Jorgensen, Chemosphere **36** (1998) 357-393

[2] K. Kummerer, A. Al-Ahmad, V. Mersch-Sundermann, Chemosphere **40** (2000) 710-710

[3] M.C. Moreno-Bondi, M.D. Marazuela, S. Herranz, E. Rodriquez, Anal. Bioanal. Chem. **395** (2009) 921-946

[4] D. Li, M. Yang, J. Hu, Y. Zhang, H. Chang, F. Jin, Water Res. **42** (2008) 307-317

[5] A. Lamm, I. Gozlan, A. Rotstein, D. Avisar, J. Environ. Sci. Health, A **44** (2009) 1512-1517

[6] R. Andreozzi, V. Caprio, C. Ciniglia, M. De Champdore, R.L. Giudice, R. Marrotta, E. Zuccato, Environ. Sci. Technol. **38** (2004) 6832-6838

[7] K. Hirte, B. Seiwert, Gerrit Schüürmann, T. Reemtsma, Water Res. **88** (2016) 880-888

[8] M. Cleuvers, Ecotoxicol. Environ. Safety **59** (2004) 309--315

[9] Y. He, N.B. Sutton, H.H.H. Rijnaarts, A.A.M. Langenhoff, Appl. Cat., B **182** (2016) 132-141

[10] A.O. Ibhadon, P. Fitzpatrick, Catalysts **3** (2013) 189-218

[11] G. Zhang, S. Ji, B. Xi, Desalination **196** (2006) 32-42

[12] E. Elmolla, M. Chaudhuri, J. Hazard. Mater. **170** (2009) 666-672

[13] E.S. Elmolla, M. Chaudhuri, J. Hazard. Mater. **172** (2009) 1476-1481

[14] E.S. Elmolla, M. Chaudhuri, J. Hazard. Mater. **173** (2010) 445-449

[15] D. Klauson, J. Babkina, K. Stepanova, M. Krichevskaya, S. Preis, Catal. Today **151** (2010) 39-45

[16] D. Dimitrakopoulou, I. Rethemiotaki, Z. Frontistis, N.P. Xekoukoulotakis, D. Venieri, D. Mantzavinos, J. Environ. Manage. **98** (2012) 168-174

[17] A. Golubović, I. Veljković, M. Šćepanović, M. Grujić-Brojčin, N. Tomić, D. Mijin, B. Babić, Chem. Ind. Chem. Eng. Q. **22** (2016) 65−73

[18] D. Mijin, M. Savić, S. Perović, A. Smiljanić, O. Glavaški, M. Jovanović, S. Petrović, Desalination **249** (2009) 286--292

[19] D. He, F. Lin, Mater. Lett. **61** (2007) 3385-3387

[20] S.B. Deshpande, H.S. Potdar, Y.B. Khollam, K.R. Patil, R. Pasricha, N.E. Jacob, Mater. Chem. Phys. **97** (2006) 207-212

[21] Y.L. Du, Y. Deng, M.S. Zhang, J. Phys. Chem. Solids **67** (2006) 2405-2408

[22] A.F. Alkain, T.A. Kandiel, F.H. Hussein, R. Dillert, D.W. Bahnemann, Appl. Catal., A **466** (2013) 32-37

[23] G. Colón, M. C. Hidalgo, J. A. Navío, J. Photochem. Photobiol., A **138** (2001) 79-85

[24] M. Koslulski, Chemical Properties of Material Surface, Marcel Dekker, New York, 2001, p. 42

[25] H. Xu, W.J. Cooper, J. Jung, W. Song, Water Res. **45** (2011) 632-638

[26] E.S. Elmolla, M. Chaudhuri, Desalination **252** (2010) 46-52

[27] D.A. Lambropoulou, I.K. Konstantinou, T.A. Albanis, A.R. Fernandez-Alba, Chemosphere **83** (2011) 367-378

[28] I.K. Konstantinou, T.A. Albanis, Appl. Catal., B **42** (2003) 319-335

[29] B. Abramović, S. Kler, D. Šojić, M. Laušević, T. Radović, D. Vione, J. Hazard. Mater. **198** (2011) 123-132

[30] A. Giwa, P.O. Nkeonye, K.A. Bello, K.A. Kolawole, J. Environ. Prot. **3** (2012) 1063-1069

[31] J.P. Hou, J.W. Poole, J. Pharm. Sci. **60** (1971) 503-532

[32] A.D. Deshpande, K.G. Baheti, C.N.R. Chatterjee, Current Sci. **87** (2004) 1684-1695

[33] C. Hu, J.C. Yu, Z. Hao, P.K. Wong, Appl. Catal., B **46** (2003) 35-37

[34] N. Kashif, F. Ouyang, J. Environ. Sci. **21** (2009) 527-533

[35] O.S. Glavaški, S.D. Petrović, V.N. Rajaković-Ognjanović, T.M. Zeremski, A.M. Dugandžić, D.Ž. Mijin, Chem. Ind. Chem. Eng. Q. **22** (2016) 101−110

[36] Y. Wang, K. Lu, C. Feng, J. Rare Earths **31** (2013) 360-365

[37] D.E. Santiago, J. Arana, O. Gonzales-Diaz, M.E. Aleman-Dominiquez, A.C. Acosta-Dacal, C. Fernandez-Rodriquez, J. Perez-Pena, M. Jose, J.M. Dona-Rodriquez, Appl. Catal., B **156-157** (2014) 284-292

[38] V.N. Despotović, B.F. Abramović, D.V. Šojić, S.J. Kler, M.B. Dalmacija, L.J. Bjelica, D.Z. Orčić, Water Air Soil Pollut. **223** (2012) 3009-3020

[39] N. Daneshvar, D. Salari, A.R. Khataee, J. Photochem. Photobiol., A **162** (2004) 317-322

[40] M.R. Sohrabi, M. Davallo, M. Miri, Int. J. Chem. Tech. Res. **1** (2009) 446-451.

K.D. RADOSAVLJEVIĆ[1]
A.V. GOLUBOVIĆ[2]
M.M. RADIŠIĆ[3]
A.R. MLADENOVIĆ[4]
D.Ž. MIJIN[1]
S.D. PETROVIĆ[1]

[1]Tehnološko-metalurški fakultet Univerziteta u Beogradu, Karnegijeva 4, 11120 Beograd, Srbija
[2]Centar za fiziku čvrstog stanja i nove materijale, Institut za fiziku, Univerzitet u Beogradu, Pregrevica 118, 11080 Beograd-Zemun, Srbija
[3]Inovacioni centar Tehnološko-metalurškog fakulteta, Univerzitet u Beogradu, Karnegijeva 4, 11120 Beograd, Srbija
[4]Hemofarm A.D., Kompanija STADA, Vršac, Srbija

NAUČNI RAD

FOTODEGRADACIJA AMOKSICILINA U PRISUSTVU NANOKRISTALNOG TiO_2

Nanokristalni TiO_2 dobijen sol-gel postupkom primenjen je u fotokatalitičkoj degradaciji amoksicilina koristeći Osram Ultra-Vitalux® lampu kao izvor svetlosti. Ispitan je uticaj početne koncentracije katalizatora i soli (NaCl i Na_2SO_4), etanola i pH na reakciju. Pri proučavanju fotodegradacije amoksicilina na različitim pH vrednostima uočena je veća brzina reakcije u kiseloj sredini, u odnosu na neutralnu, što se može objasniti kiselo katalizovanom hidolizom antibiotika. Sa povećanjem pH raste i brzina reakcije kao rezultat intezivnijeg stvaranja hidroksil-radikala i bazne hidrolize antibiotika. Uticaj soli ispitivan je dodatkom natrijum-hlorida i natrijum-sulfata. Uočena inhibicija dodatkom soli posledica je dejstva hloridnih i sulfatnih jona kao hvatača šupljina. Dodatak etanola, takođe, smanjuje brzinu reakcije, što ukazuje na činjenicu da $^{\bullet}OH$ imaju glavnu ulogu u fotodegradaciji amoksicilina. Jonska hromatografija je ukazala na stvaranje NH_4^+, NO_3^- i SO_4^{2-} kao rezultat degradacije amiksicilina. Dobijeni rezultati pokazuju da se oko 11,2% azota i 30,4% sumpora mineralizovalo tokom reakcije. Rezultati dobijeni određivanjem ukupnog organskog ugljenika pokazuju da je mineralizovano 47% amiksicilina i da nastali proizvodi sadrže atome sumpora i/ili azota. Poređenjem sintetisanog TiO_2 i Evonik P25 pokazano je da oba katalizatora imaju slična katalitička svojstva.

Ključne reči: nano-prah, SEM, XRD, optimizacija, HPLC-MS, TOC.

CI&CEQ
Chemical Industry & Chemical Engineering Quarterly

Available on line at
Association of the Chemical Engineers of Serbia *AChE*
www.ache.org.rs/CICEQ

Chem. Ind. Chem. Eng. Q. 23 (2) 197–206 (2017) CI&CEQ

IVANA S. LONČAREVIĆ[1]
ALEKSANDAR Z. FIŠTEŠ[1]
DUŠAN Z. RAKIĆ[1]
BILJANA S. PAJIN[1]
JOVANA S. PETROVIĆ[1]
ALEKSANDRA M. TORBICA[2]
DANICA B. ZARIĆ[3]

[1]Faculty of Technology, University of Novi Sad, Novi Sad, Serbia
[2]Institute of Food Technology, University of Novi Sad, Novi Sad, Serbia
[3]IHIS Tehno Experts d.o.o., Research Development Center, Beograd, Serbia

SCIENTIFIC PAPER

UDC 66.063.8:66.012.3

OPTIMIZATION OF THE BALL MILL PROCESSING PARAMETERS IN THE FAT FILLING PRODUCTION

Article Highlights

- Influence of the ball mill processing parameters on fat filling quality and energy consumption
- Optimization of agitator shaft speed and milling time in fat filling production
- Physical and sensory properties of fat filling are mostly influenced by agitator shaft speed
- Milling energy consumption is mostly influenced by milling time
- Optimization - maximum agitator shaft speed and 30-min milling time

Abstract

The aim of this study was to determine the effect of the main milling variables, i.e., agitator shaft speed (50, 75 and 100%, which is 25, 37.5 and 50 rpm) and milling time (30, 45 and 60 min) on physical and sensory properties of fat filling, as well as on energy consumption during the production in a laboratory ball mill. Within the response surface method, the face centered central composite design is used. A response surface regression analysis for responses was performed and a full quadratic model was fitted to the experimental data. It is shown that agitator shaft speed had the most significant influence on physical properties (particle size distribution, rheological and textural propertes) and sensory characteristics of fat filling, while the milling energy consumption is highly influenced by milling time with contribution 55.4%, followed by agitator shaft speed (40.04%). The model obtained by regression analyses was used to perform the optimization of processing parameters in order to provide the combination of agitator shaft speed and milling time that cost less energy while at the same time do not compromise the quality of the fat filling. Optimization of production of fat filling in a laboratory ball mill would imply the maximum agitator shaft speed and 30-min milling time.

Keywords: fat filling, ball mill milling variables, physical properties, sensory characteristics, optimization.

Fat fillings contain high amount of fat (30-40%) which presents a continuous phase and determines the consistency of the filling. Confectionary products with fat filling can melt faster or slower during the consumption, creating the overall sensory impression [1]. Milling is the next necessary step for obtaining the optimal particle size distribution and thereby physical characteristics and appropriate sensory quality of confectionery suspensions of solids in fat phase [2]. The particle size reduction takes place in a five-roll mill and very often with pre-refining in a three-roll refiner. On the other hand, presently the refining of cocoa spreads, fat fillings and even chocolate mass very often takes place in a ball mill [3]. The mass and the balls are additionally agitated by a shaft with arms, operating at a variable rotation speed. During refining, the mass can also be recycled through the ball mill, thus going through a thick layer of balls, which are kept in continuous movement and forced to bounce against each other [4]. The investigation of

---

Correspondence: I.S. Lončarević, Faculty of Technology, University of Novi Sad, Bulevar cara Lazara 1, 21000 Novi Sad, Serbia.
E-mail: ivana.radujko@tf.uns.ac.rs
Paper received: 17 December, 2015
Paper revised: 20 April, 2016
Paper accepted: 24 May, 2016

https://doi.org/10.2298/CICEQ151217031L

Fišteš *et al.* [5] showed that power requirements and energy consumption of the ball mill depend on processing parameters. Alamprese *et al.* [6] investigated the optimization of working conditions of a ball mill used for chocolate refining process in order to reduce refining time and energy consumption without loss of quality characteristics of the final product. Investigations of Yeganehzad *et al.* [7] and Zarić *et al.* [8] showed that the refining time in a ball mill had a significant effect on rheological properties, particle size, hardness and sensory properties of chocolate.

Having in mind that improving energy efficiency as well as energy saving represents one of major problems in production processes [9], the papers of Scanlon and Lamb [10] and Holdich [11] showed that the ball mill processing parameters have a significant effect on energy consumption and the quality characteristics of the obtained product. However, relatively little research has been published considering the use of ball mill for fat filling production.

This research investigated the interaction effects and optimization of main ball milling variables (agitator shaft speed and milling time) on physical and sensory properties of fat filling, as well as on energy consumption during the fat filling production in a laboratory ball.

EXPERIMENTAL

Materials

Fat filling mass, refined by a 3-roll mill in industrial conditions, consisted of powdered sugar (Crvenka JSC, Serbia), cocoa powder (Centroproizvod JSC, Serbia), soy flour (Sojaprotein JSC, Serbia), milk powder (Imlek JSC, Serbia), and vegetable fat (Dijamant JSC, Serbia). Fat characteristics - fatty acid composition, solid fat content at different temperatures and thermal properties are given in our previous research [12]. Native soybean lecithin (Victoriaoil JSC, Serbia) was used as an emulsifier. The composition of fat filling included: 50% of powdered sugar, 30% of vegetable fat, 7% of cocoa powder, 5.5% of soy flour, 7% of milk powder, 0.5% of lecithin.

Process method

Research included the influence and optimization of processing parameters: agitator shaft speed and milling on physical and sensory characteristics of fat filling produced in a ball mill as well as on milling energy consumption. Selected input factors and responses are listed in Table 1. The extreme levels of the input factors were selected on the basis of previous experiments and the technical limitations of the equipment.

Methods

Fat filling production. At the beginning of production, fat and lecithin were homogenized in a laboratory ball mill (Mašino Produkt, Serbia) at 40 °C for 5 min. Then the fat filling mass was added, and the production of fat filling included defined agitation shaft speed (50, 75, and 100%, or 25, 37.5 and 50 rpm) and milling time (30, 45, and 60 min) for each agitation speed. After the chosen milling time, cream samples were added into sterile plastic cups and capped with plastic lids.

The capacity of laboratory ball mill is 5 kg. It constitutes of a double-jacket cylinder, 0.25 m in diameter and 0.31 m in height and a stirring group. The vertical shaft with horizontal arms, while rotating, puts the steel balls (9.1 mm diameter) in movement. The ball mill is equipped with a temperature control sys-

Table 1. Variables and levels in the experimental design

Input factor	Levels		
	Low (-1)	Medium (0)	High (1)
A: agitator shaft speed, rpm	25	37.5	50
B: milling time, min	30	45	60
Dependent responses			
R1: Particle size parameter *d*(0.1), μm			
R2: Particle size parameter *d*(0.5), μm			
R3: Particle size parameter *d*(0.9), μm			
R4: Hardness, kg			
R5: Work of shearing, kg s			
R6: Thixotropic curve area, Pa/s			
R7: Casson yield stress, Pa			
R8: Casson viscosity, Pa s			
R9: Sensory analysis			
R10: Energy consumption, J/kg			

tem made up of a water jacket equipped with temperature sensors and thermo-regulators controlled by electric board. The maximum temperature is 100 °C, with deviation ±1 °C.

Particle size distribution. The influence of milling variables on particle size distribution in fat filling samples was determined by a Mastersizer 2000 laser diffraction particle size analyzer equipped with a Hydro 2000 µP dispersion unit (Malvern Instruments, England). Fat filling sample was dispersed in sunflower oil at ambient temperature (20±2 °C) and added until adequate obscuration was obtained (10-20%). The results were quantified as volume-based particle size distribution, using Mastersizer 2000 Software. All measurements were performed in triplicate. Obtained particle size distribution parameters included following parameters: $d(0.5)$ - mass median diameter of the volume of distribution, indicating that 50% of the sample has a size smaller than that value, whereas 50% has a larger size; $d(0.1)$ - indicating that that 10% of the sample mass are particles in sizes smaller than that value; and parameter $d(0.9)$ - indicates that 90% are smaller and 10% are larger than that value [13].

Rheological properties. Rheological properties of fat filling samples were determined by a Rheo Stress 600 rotational rheometer (Haake, Germany). The tests were carried out at 40 °C using a concentric cylinder system (sensor Z20 DIN). The shear rate was increased from 0 to 60 s^{-1} within a period time of 180 s, then was kept constant at maximum speed of 60 s^{-1} for 60 s and after that was reduced from 60 to 0 s^{-1}, within 180 s [14].

Textural characteristics. Textural characteristics of fat samples were analyzed using a Texture Analyzer TA.XT Plus (Stable Micro System, UK). The hardness and work of shearing were determined by penetration at ambient temperature of 22±2 °C, according to method Chocolate Spread - SPRD2_SR_PRJ. Each sample was placed into the cone sample holder and pressed down in order to eliminate air pockets. Any excess of sample was scraped off with a knife. The filled cone sample holder was then put in the base holder and 45° cone probe with the diameter of 38 mm was used to penetrate the samples at 3 mm/s.

Sensory analysis. Sensory analysis was made using the scoring procedure described in Popov-Raljić and Laličić-Petronijević [15] with some modifications. A group of 10 experienced panelists, 6 women and 4 men, ages 28 to 45, who had been trained to evaluate the sensory properties of fat filling [16,17], evaluated the following quality parameters using the scores from 1 to 5: appearance (color, brightness, surface), texture (structure, firmness), chewing, smell and taste. The obtained scores of these parameters were multiplied by a weight coefficient (1.0, 0.8, 0.6, 0.6, 1.0) respectively (Table 2).

The category of quality was defined based on the total number of points (<11.2, unacceptable; 11.2--13.1, acceptable; 13.2-15.1, good; 15.2-17.5, very good; 17.6-20, excellent). The fat filling samples were analysed seven days after their stabilization. Cookie samples were plates labeled with three-digit codes from a random number table and served to panelists on white plastic. Evaluation was performed in sensory laboratory of the Faculty of Technology Novi Sad, in partitioned booths, illuminated with fluorescent lights [18].

The milling energy consumption. The milling energy consumption, E [J/kg], was calculated using Eq. (1):

$$E = \frac{Pt}{m} \tag{1}$$

where P [W] is power, m [kg] is the mass of fat filling (5 kg) and t [s] is the time of the milling run determined by the chronometer. Power readings were determined using the Network recorder MC750/UMC750 (Iskra MIS, Slovenia) connected to the ball mill.

Statistical analysis. The main research aims were determination of influences of input factors and their interaction on output factors and optimization of process. According design of experiment (DOE) and response surface method (RSM) within it were used for statistical analysis. Since significant variations at points with extreme values were expected, face centered central composite design with three central points was chosen for analysis.

Influence of 2 input factors: A – agitator shaft speed; B – milling time in a laboratory ball mill on particle size distribution (responses R1-R3), textural characteristics (responses R4 and R5), rheological properties (responses R6-R8), sensory analysis of fat filling (response R9), and energy consumption (R10) was studied.

By specified design, 11 runs were determined and all results were expressed as mean of triplicate measures. Regression analysis was performed, where a full quadratic model was used:

$$R = \beta_0 + \beta_1 A + \beta_2 B + \beta_{12} AB + \beta_{11} A^2 + \beta_{22} B^2 \tag{2}$$

where R is the measured response; β_i and $\beta_{i,j}$, $i,j \in \{0,1,2\}$ are regression coefficients; A, B are the coded levels of input factors, the term AB represents interactions of input factors, while A^2 and B^2 represent

Table 2. Sensory evaluation of the chocolate quality using the scoring procedure

Basic sensory properties	Score	Weight coefficient	Description of the evaluated property
Appearance color, brightness, surface	5	0.6	Smooth, bright surface; irreproachable color
	4		Insignificant deviation of color; smooth, bright surface
	3		Lower quality color; insufficient bright surface; air bubbles (a small number); insignificant packaging demage
	2		Atypical color; matte surface or less separation of oil phase on the surface; a large number of air bubbles; less damage of the packaging
	1		Appearance of gray-white spots on the surface; completely matte surface or separation of oil phase on the surface; packaging demage
Texture Structure, firmnes	5	0.8	Homogeneous, smooth, structure; appropriate firmness; soft, spreadable consistency
	4		Insignificant deviation of firmness and consistency; homogeneous, smooth, structure
	3		Appearance of air bubbles in the mass; firmness and consistency inappropriate; homogeneous, smooth, structure
	2		Grainy structure; inadequate firmnes; low spreadability; insignificant deviation of homogenous structure
	1		Rough grainy structure; inadequate firmnes; low spreadability; unhomogenous structure
Chewig and other textural properties	5	1.0	Appropriate chewiness; melting in the mouth
	4		Slower melting; good chewiness, spreadiness
	3		Average chewiness; spreadiness; weak sandiness
	2		Slow melting; sandiness; stickiness
	1		Slow melting; heavy sandiness; stickiness
Smell	5	0.6	Appropriate; rounded; aromatic; resistant for some period of time
	4		Appropriate; poorer rounded; aromatic
	3		Appropriate; poor rounded; weakly aromatic
	2		Not appropriate; sourish; staled
	1		Foreign odor; sour; staled; mouldy
Taste	5	1.0	Appropriate; rounded; aromatic; resistant for some period of time
	4		Appropriate; less rounded; aromatic
	3		Poorly rounded; poorly aromatic
	2		Sourish; not rounded
	1		Foreign taste; sour; bitter

quadratic terms. The adequacy of the obtained model was confirmed by R^2 coefficient and lack of fit value.

Significance of input factors and their interaction in the observed model were determined by statistical method of analyses of variance (ANOVA), where sum of squares were used to calculate the corresponding contributions. Using 5% level of significance, a factor is considered to affect the response if the p value is less than 0.05.

Constrained optimization procedure maximizes desirability function [21]:

$$D = (d_1 d_2 ... d_n)^{\frac{1}{n}}$$

where d_i, $i \in \{1,2,...,n\}$, are individual desirability functions associated to constrains on responses R_i.

The analyses were carried out using Statistica 12 (Stratosoft, USA) and Design-Expert 10 (trial version).

RESULTS AND DISCUSSION

The influence of main milling variables on physical properties and sensory characteristics of fat filling, and milling energy consumption are shown in Table 3.

The input factors, agitator shaft speed (A) and milling time (B) affected both energy consumption and all quality characteristics of fat filling produced in a laboratory ball mill. Table 4 represents regression coefficients for responses R1-R9, as well as appropriate R^2 coefficients.

Physical and sensory properties of fat filling. Figure 1a shows the curve of particle size distribution

Table 3. The influence of input factors on dependent responses

Run	Input factor		Dependent response									
	A	*B*	*R*1	*R*2	*R*3	*R*4	*R*5	*R*6	*R*7	*R*8	*R*9	*R*10
3	25	30	3.42	20.96	81.92	5.96	5.23	2987	40.25	4.78	11.77	122.98
5	25	45	3.16	14.85	53.07	6.38	5.27	2699	41.09	4.57	12.66	207.30
7	25	60	3.21	14.44	48.31	6.98	5.93	2071	43.28	2.78	14.50	292.40
11	37.5	30	3.26	12.98	44.12	19.13	18.34	4918	41.25	6.58	12.1	182.00
4	37.5	45	2.92	12.74	43.28	18.36	17.59	4057	43.76	7.89	14.84	285.4
6	37.5	45	2.79	12.26	42.48	19.65	19.32	3862	40.24	8.59	14.35	273.6
9	37.5	45	2.99	13.15	44.09	18.06	16.86	4215	45.15	7.26	15.36	294.80
2	37.5	60	2.98	12.44	42.02	19.53	20.57	4548	53.63	8.67	17.37	399.70
8	50	30	3.06	12.75	46.87	23.44	22.81	2192	30.16	10.21	16.53	247.60
1	50	45	2.78	10.55	36.73	24.85	23.39	2950	37.75	12.75	16.28	408.20
10	50	60	2.84	10.82	35.89	24.98	24.52	3230	40.77	14.76	16.86	568.90

Table 4. Regression equation coefficients for responses R1-R10

Coefficient	*R*1		*R*2		*R*3		*R*4		*R*5	
β_0	2.9121	*p*	12.285	*p*	41.313	*p*	18.883	*p*	18.184	*p*
β_1	-0.185	0.0013	-2.688	0.0039	-10.64	0.0104	8.9917	< 0.0001	9.0483	< 0.0001
β_2	-0.118	0.0087	-1.498	0.0369	-7.782	0.0330	0.4933	0.1410	0.7733	0.1027
β_{12}	-0.002	0.9455	1.1475	0.1377	5.6575	0.1435	0.13	0.7224	0.2525	0.6178
β_{11}	0.0397	0.4047	1.0618	0.2502	6.2234	0.1896	-3.557	0.0004	-4.246	0.0009
β_{22}	0.1897	0.0074	1.0718	0.2463	4.3934	0.3330	0.1584	0.7304	0.8795	0.2006
R^2	0.9434		0.8923		0.8653		0.9954		0.9917	
Lack of Fit	0.9432		0.0697		0.1025		0.7439		0.8417	
Coefficient	*R*6		*R*7		*R*8		*R*9		*R*10	
β_0	4232.6	*p*	44.144	*p*	7.9637	*p*	14.722	*p*	285.87	*p*
β_1	102.5	0.5108	-2.657	0.0774	4.265	< 0.0001	1.8233	0.0085	100.34	< 0.0001
β_2	-41.33	0.7868	4.3367	0.0152	0.7733	0.0125	1.355	0.0263	118.07	< 0.0001
β_{12}	488.5	0.0401	1.895	0.2531	1.6375	0.0012	-0.65	0.2763	37.97	0.0006
β_{11}	-1690	0.0006	-6.364	0.0182	0.6208	0.1035	-0.059	0.9332	19.976	0.0249
β_{22}	218.42	0.3722	1.6558	0.4104	-0.414	0.2420	0.2061	0.7703	3.0763	0.6463
R^2	0.9304		0.8633		0.9902		0.8527		0.9967	
Lack of Fit	0.1452		0.4110		0.8495		0.1321		0.5899	

in fat filling after milling on 3 roll mill where parameters *d*(0.1), *d*(0.5) and *d*(0.9) have the following values: 5.18, 45,40 and 110,77 μm, respectively. Milling in laboratory ball mill resulted in decreasing of all particle size parameters and more uniform distribution, getting the appearance of Gaussian curve distribution.

Regarding particle size distribution, increasing the agitator shaft speed generally decreased parameters *d*(0.1), *d*(0.5), and *d*(0.9) in fat filling samples, as also confirmed by negative value of equation coefficient β_1. The example of the influence of agitator shaft speed on particle size distribution is given in Figure 1c. It was also evident that increasing the milling time observed at each particular agitator shaft speed generally decreased all particle size parameters, as confirmed by negative value of β_2 and shown in Figure 1b presenting particle size distribution of fat filling produced under maximum agitator shaft speed and each applied milling time.

Analyzing all samples, the parameter *d*(0.1) (response *R*1) ranged from 2.78 to 3.42 μm, meaning that 10% of the volume distribution of the samples was smaller than the particular d(0.1) value. The 50% of the volume distribution in all samples was smaller than 20.96 μm, which was the highest value for *d*(0.5) achieved in fat filling sample produced with agitator shaft speed of 25 rpm and minimum milling time. The parameter *d*(0.9) indicated that 90% of the volume distribution of all the samples was smaller than 81.92

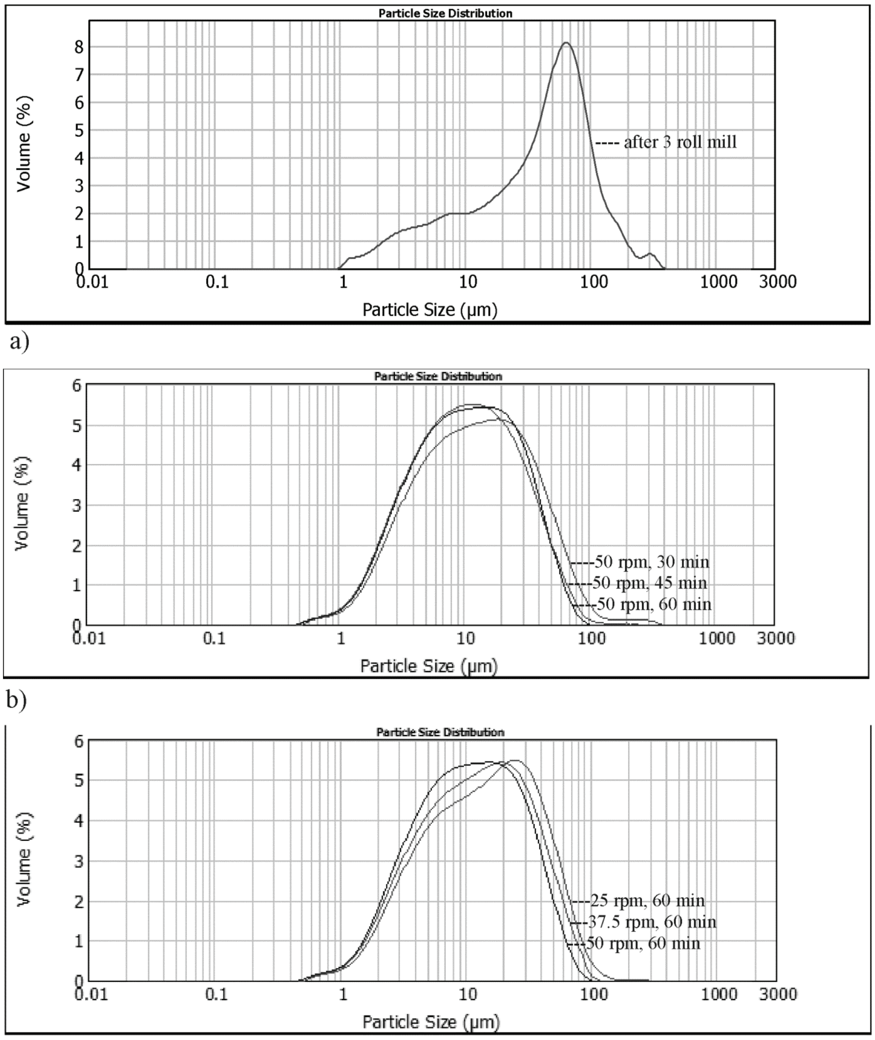

a)

b)

c)

Figure 1. Influence of: a) 3 roll mill pre-refiner; b) milling time observed at maximum agitator shaft speed; c) agitator shaft speed observed at maximum milling time on particle size distribution of fat filling.

µm, which is the value observed in sample with minimal applied agitator shaft speed and milling time.

A fat filling mass, like a cream mass, has a non-uniform particle size distribution and it exhibits thixotropic properties characterized by a plastic flow and yield stress [19]. Decreasing particle size parameters, while increasing the agitator shaft speed and milling time in the laboratory ball mill affected the textural and rheological properties of fat filling in terms of increasing the hardness and Casson viscosity. Figure 2a represents the influence of agitator shaft speed on rheological properties of fat filling produced at maximum milling time, while the influence of milling time on rheological properties observed at maximum agitator shaft speed is shown on Figure 2b.

Afoakwa *et al.* [20] investigated the effects of the particle size distribution and the composition on the rheological properties of dark chocolate, where increase in particle sizes resulted in a decrease in Casson plastic viscosity due to an increased number of particles, and points of contact between them. In this case, the decrease in particle size distribution contributed to higher specific surface area of particles and due to more compact system with higher values of textural parameters and Casson viscosity. The positive values of regression coefficients β_1 and β_2 for responses $R4$ and $R5$ confirm that the increase of main milling variables also increased the values of hardnes and work of shearing of fat filling. It is also obvious that increasing the milling time influenced increasing the values of thixotropic curve area and Casson viscosity while increasing the agitator shaft speed increased Casson yield stress and Casson viscosity.

Affecting textural and rheological properties, particle size distribution also contributed to some

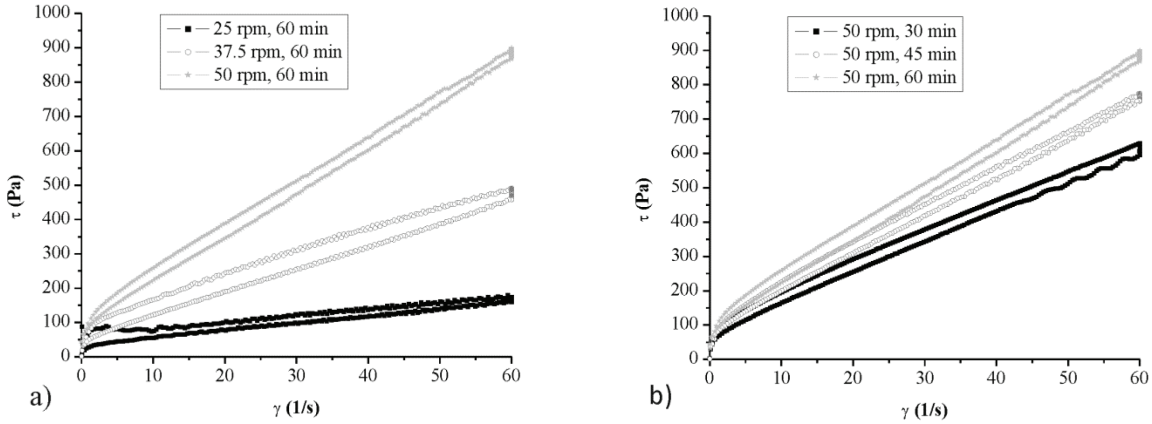

Figure 2. Influence of agitator shaft speed and milling time on rheological properties of fat filling: a) the influence of agitator shaft speed observed at maximum milling time; b) the influence of milling time observed at maximum agitator shaft speed.

sensory properties of fat filling. All fat filling samples were well scored by the panelists 24 h after production (Figure 3).

All fat filling samples had intrinsic color of cocoa 24 h after production, without the presence of white and gray color on the surface. However, the samples produced under maximum agitator shaft speed as well as sample produced uder agitator shaft speed of 37.5 rpm and maximum milling time had a slightly darker color probably due to a higher specific surface area of particles, which contributed to higher sensory scores. On the other hand, lower specific surface area of particles in samples milled under minimum agitator shaft speed and agitator shaft speed of 37.5 rpm and milling time of 30 and 50 min have not contributed to fat phase separation on the fat filling surface, but affected chewiness causing a grainy feeling in the mouth while eating. Also, the consistency of samples produced under minimum agitator shaft speed, especially the sample milled for 30 min, were grainy and inhomogeneous. Furthermore, free fatty phase worsened the smell and taste of those samples. Increasing the milling time on 45 and 60 min improved sensory characteristics of fat filling samples produced under minimal gitator shaft speed where sample milled for 60 min belongs to category of quality – good. Sample milled under agitator shaft speed of 37.5 rpm and maximum milling time had the most aromatic smell and was the least steaky while chewing, compared to all other samples. It is classified in quality category – very good, fallowed by fat filling samples produced under maximum agitator shaft speed that also classified in quality category – very good.

The positive values of coeeficients β_1 and β_2 for response $R9$ indicate improving of sensory characteristics by increasing the main milling parameters. On the other hand, the positive values of those coeffi-

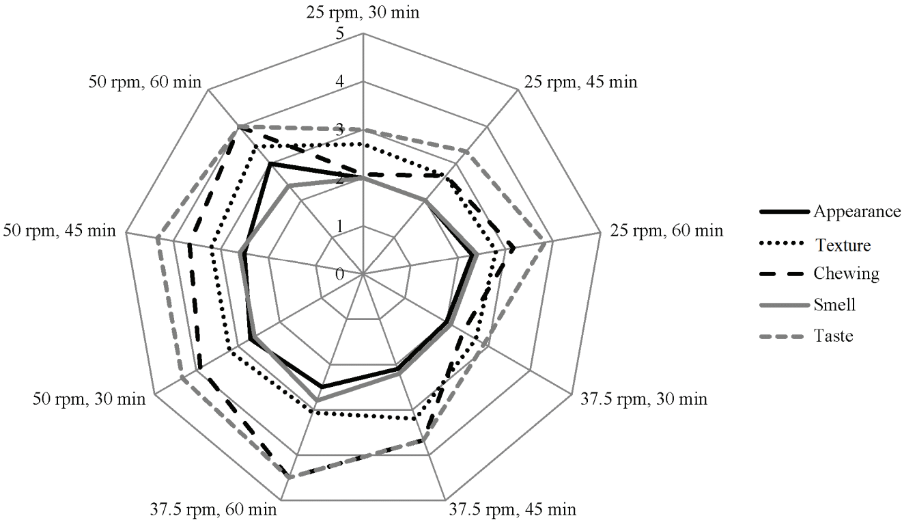

Figure 3. Weight scores of basic sensory properties of fat filling.

cients for response *R*10 certainly indicate higher energy consumption when increasing agitator shaft speed and milling time.

The contribution of input factors on dependent responses is shown on Figure 4.

Increasing the agitator shaft speed had the highest influence on decreasing all particle size parameters with the highest impact on parameter *d*(0.5) with 63.89%. The milling time had less pronounced influence on particle size parameters, compared to agitator shaft speed.

Regarding textural characteristics agitator shaft speed had the contribution of even 93.52% on hardness and 90.52% on work of shearing, while milling time had minimal influence of less than 1%. Thixotropic curve area and Casson viscosity were also the most affected by the agitator shaft speed with the contribution of 86.30% of quadratic term on thixotropic curve area and linear 87.41% on Casson viscosity. On the other hand, both input factors have statistically significant influence on Casson yield stress.

Sensory characteristics of fat filling were most affected by agitator shaft speed (60.87%) followed by milling time (33.62%) where increasing both input factors increased sensory quality.

Energy consumption. Power requirements are highly influenced by the agitator shaft speed. Previous studies of Fišteš *et al.* [5] showed that every increase of agitator shaft speed of the laboratory ball mill led to a statistically significant increase in power requirements. Alamprese *et al.* [6] also stated that the energy consumption of ball mill increased proportionally to the increase in speed and refining time. The results obtained in this study also showed that the both investigated milling parameters have a significant influence on energy consumption.

Although the highest values of milling energy consumption were obtained under maximum agitator shaft speed, the ANOVA under selected design showed that milling time had higher contribution (55.4%) on energy consumption in comparison to agitator shaft speed (40.04%). In terms of reducing

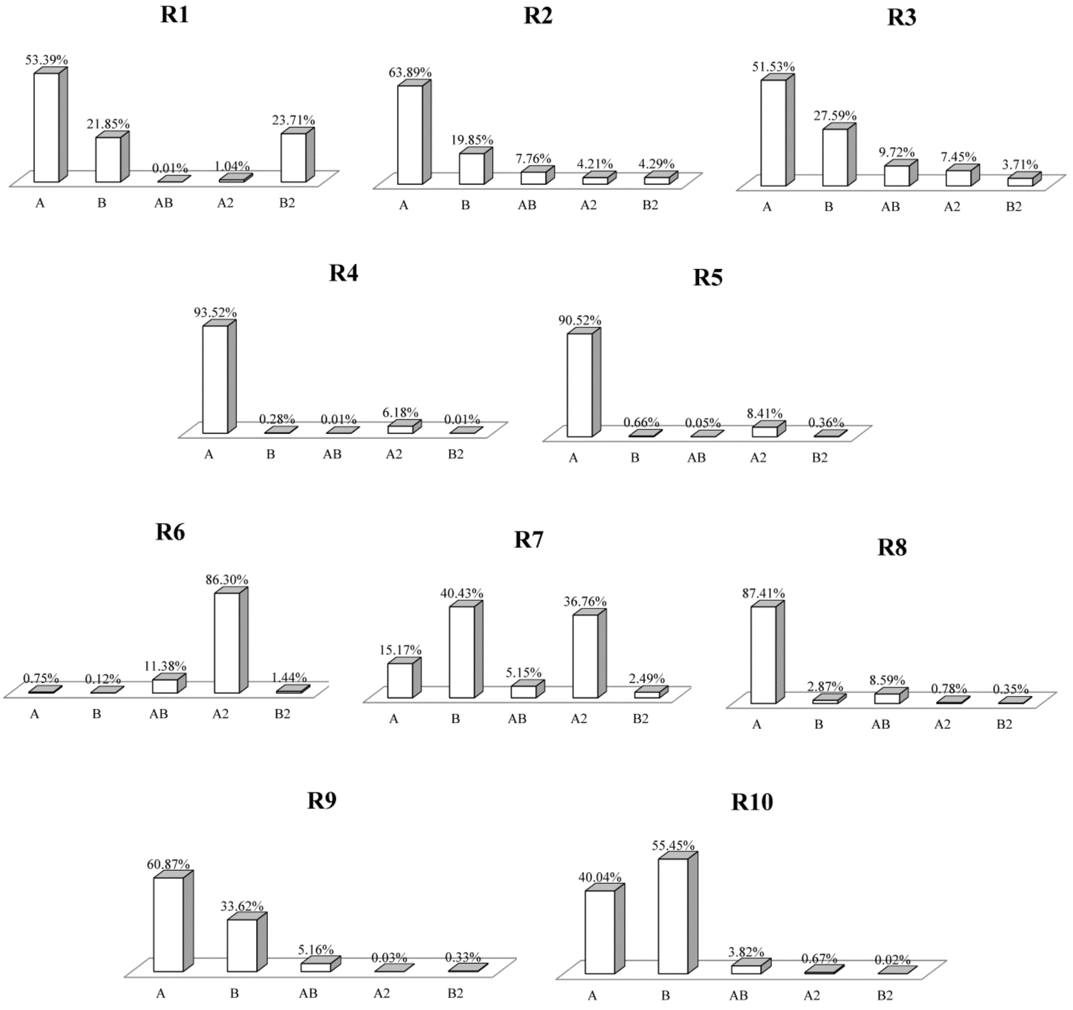

Figure 4. The contribution of input factors on dependent responses.

the energy consumption of the process the milling time should be kept at minimum. Lucisano *et al.* [4] showed that prolonged reefing time could even become a problem because of significant and undesirable reduction in size. Also, with shorter retention time the amount of product that can be processed during a certain period of time is increasing, therefore the capacity of ball mill is also increasing. From the energy efficiency point of view, the agitator shaft speed should be run at lowest possible speed to meet the product quality requirements.

Optimization. Model obtained by regression analyses is used to perform the optimization of processing parameters in order to find the optimal combination of input factors such that $R3$, $R6$, $R7$ and $R10$ have minimal, and $R9$ as it possible higher value. The recommended combination included maximal value of A and minimal value of B, while values of responses are given in Table 5.

Table 5. Optimization of processing parameters on quality characteristics of fat filling and milling energy consumption

Cond.	A	B	$R1$	$R2$	$R3$	$R4$	$R5$	$R6$	$R7$	$R8$	$R9$	$R10$	D
	In range	In range	None	None	Min	None	None	Min	Min	None	Max	Min	
Sol. 1	50	30	3.08	12.08	43.42	23.85	22.84	2416.31	30.55	10.02	15.99	253.22	0.826
Sol. 2	50	27.02	3.18	12.62	45.76	23.80	23.02	2422.86	30.03	9.36	15.94	223.60	0.831

With this input values, using regression coefficients (Table 4), the responses $R3$ (43.42), $R6$ (2416), $R7$ (30.55) and $R10$ (253.2) are obtained within agiator shaft speed of 50 rpm and milling time of 30 min as optimal.

CONCLUSION

The main objective of the study was to determine the effect of agitator shaft speed and milling time on quality of fat filling produced in a laboratory ball mill, as well as to optimize the ball milling parameters in order to reduce energy consumption without compromising the quality of the product.

High values of the determination coefficients ($R2$, 0.86-0.99) indicated that the application of fitted full quadratic model for describing experimental data by means of the theoretical curve was justified. Equation coefficients indicated that the increase of both agitator shaft speed and milling time actually increased the degree of particle size reduction in fat filling, which increased the hardness and Casson viscosity and, at the same time, improved the sensory characteristics of fat filling. On the other hand, the increase of milling variables contributed to higher energy consumption in fat filling production.

The model obtained by regression analyses showed that maximum agiator shaft speed and minimum milling time are found as optimal in fat filling production, where high desirability value of 0.8246 provides significance of the proposed solution.

REFERENCES

[1] B. Pajin, Đ. Karlović, R. Omorjan, V. Sovilj, D. Antić, Eur. J. Lipid Sci. Tech. **109** (2007) 1203-1207

[2] V. Glicerina, F. Balestra, M. Dalla Rosa, S. Romani, J. Food Eng. **145** (2015) 45-50

[3] B. Pajin, D. Zarić, Lj. Dokić, Z. Šereš, D. Šoronja-Simović, R. Omorjan, I. Lončarević, Acta Period. Technol. **42** (2011) 101-110

[4] M. Lucisano, E. Casiraghi, M. Mariotti, Eur. Food Res. Technol. **223** (2006) 797-802

[5] A. Fišteš, D. Rakić, B. Pajin, Lj. Dokić, I. Nikolić, Chem. Ind. **67** (2013) 747-751

[6] C. Alamprese, L. Datei, Q. Semeraro, J. Food Eng. **83** (2007) 629-636

[7] S. Yeganehzad, M. Mazaheri-Tehrani, M. Mohebbi, M.B. Habibi Najafi, Z. Baratian, J. Agr. Sci. Tech. **15** (2013) 125-135

[8] D. Zarić, B. Pajin, I. Lončarević, D. Šoronja-Simović, Z. Šereš, Acta Period. Technol. **43** (2012) 139-148

[9] M. Todorović, D. Živković, M. Mančić, G. Ilić, Chem. Ind. Chem. Eng. Q. **20** (2014) 511-521

[10] M.G. Scanlon, J. Lamb, J. Mater. Sci. **30** (1995) 2577--2583

[11] R.G. Holdich, Fundamentals of Particle Technology; Midland Information Technology and Publishing: Leicestershire, 2002, p.115

[12] I. Lončarević, B. Pajin, R. Omorjan, A. Torbica, D. Zarić, J. Maksimović, J. ŠvarcGajić, J. Texture Stud. **44** (2013) 450-458

[13] Z. Stojanović, S. Marković, Tech.- New Mater. **21** (2012) 11-20

[14] IOCCC 2000. Viscosity of Cocoa and Chocolate Products - Analitycal Method 46. Available from CAOBISCO, rue Defacqz 1, B-1000 Bruxelles, 2000

[15] J. Popov-Raljić, J. Laličić-Petronijević, Sensors **9** (2009) 1996-2016.

[16] ISO 8586-1 (1993)

[17] ISO 8586-2 (2008)

[18] ISO 8589 (2007)

[19] I. Lončarević, B. Pajin, J. Petrović, D. Zarić, M. Sakač, A. Torbica, D.M. Lloyd, R.Omorjan, J. Food Eng. **171** (2016) 67-77

[20] E.O. Afoakwa, P. Alistair, M. Fowler, Eur. Food Res. Technol. **226** (2008) 1259-1268

[21] R.H. Myers, D.C. Montgomery, Response Surface Methodology - Process and Product Optimization Using Designed Experiments, 2nd ed., John Wiley & Sons Inc., Toronto, 2008.

IVANA S. LONČAREVIĆ[1]
ALEKSANDAR Z. FIŠTEŠ[1]
DUŠAN Z. RAKIĆ[1]
BILJANA S. PAJIN[1]
JOVANA S. PETROVIĆ[1]
ALEKSANDRA M. TORBICA[2]
DANICA B. ZARIĆ[3]

[1]Univerzitet u Novom Sadu, Tehnološki fakultet, Bulevar cara Lazara 1, 21000 Novi Sad, Srbija
[2]Naučni institut za prehrambene tehnologije u Novom Sadu FINS, Univerzitet u Novom Sadu, Bulevar cara Lazara 1, 21000 Novi Sad, Srbija
[3]IHIS Tehno Experts d.o.o., Istraživačko-razvojni centar, 11000 Beograd, Srbija

NAUČNI RAD

OPTIMIZACIJA PROCESNIH PARAMETARA KUGLIČNOG MLINA U PROIZVODNJI MASNOG PUNJENJA

Cilj ovog rada bio je da se ispita uticaj procesnih parametara - brzine obrtanja mešača (25, 37,5 i 50 rpm) i vremena mlevenja (30, 40 i 50 min) na potrošnju energije kao i fizičke i senzorske karakteristike masnog punjenja, proizvedenog u laboratorijskom kugličnom mlinu. U okviru metode odzivne površine korišćen je "face centered composite" dizajn. Izvršena je regresiona analiza odzivne površine gde su su eksperimentalno dobijeni podaci fitovani potpunim kvadratnim modelom. Rezultati su pokazali da brzina obrtanja mešača ima najveći uticaj na fizičke karakteristike (raspodelu veličina čestica, reološke i teksturalne karakteristike) kao i na senzorske osobine masnog punjenja. S druge strane, na potrošnju energije prilikom proizvodnje masnog punjenja u kugličnom mlinu najveći uticaj ima vreme mlevenja (55.4%) dok brzina obrtanja mešača ima uticaj od 40.04%. Model dobijen regresionom analizom korišćen je za optimizaciju procesnih parametara kako bi se dobila kombinacija brzine obrtanja mešača i vremena mlevenja koja obezbeđuje minimalnu potrošnju energije bez narušavanja kvaliteta masnog punjenja. U cilju optimizacije proizvodnje masnog punjenja u kugličnom mlinu neophodno je primeniti maksimalnu brzinu obrtanja mešača i minimalno vreme mlevenja.

Ključne reči: masno punjenje, parametri mlevenja, fizičke karakteristike, senzorne karakteristike, optimizacija.

Chemical Industry & Chemical Engineering Quarterly

Available on line at
Association of the Chemical Engineers of Serbia *AChE*
www.ache.org.rs/CICEQ

Chem. Ind. Chem. Eng. Q. 23 (2) 207–216 (2017) CI&CEQ

NILAY GIZLI
MERVE ARABACI

Ege University, Faculty of Engineering, Chemical Engineering Department, Bornova, Izmir, Turkey

SCIENTIFIC PAPER

UDC 66.081:546.562

ENHANCED SORPTION OF Cu(II) IONS FROM AQUEOUS SOLUTION BY IONIC LIQUID IMPREGNATED NANO-SILICA AND NANO-ALUMINA PARTICLES

Article Highlights

- Impregnation of ionic liquid into nano-silica and nano-alumina particles
- Structural and morphological characterization of modified particles
- Enhancement the Cu(II) sorption performance of nanoparticles by modification
- Effect of nanoparticle type, dispersion time, loading ratio on the sorption capacity

Abstract

In this study, the improvement of the Cu (II) ion sorption performance of nano-silica and nano-alumina particles was investigated by the impregnation of 1-ethyl-3-methyl imidazolium bis(trifluorosulfonyl)imide [$Emim^+Tf_2N^-$] ionic liquid (IL). The immobilization process of IL was achieved via the ultrasound-assisted physical impregnation method. The structural and morphological characterization of the adsorbents was investigated by Fourier transform infrared (FT-IR) spectroscopy and scanning electron microscopy (SEM) analysis. The thermal stability of the ionic liquid impregnated nanoparticles was also characterized by thermogravimetric analysis (TGA). The effect of the loading ratio (L_R) and the sonication time (t_D) on the sorption performance of the modified nanoparticles were investigated. The efficient adsorption was obtained by using the particles containing IL at the loading ratio (mL-IL/g-part) of 0.5:1. And the optimum value for the sonication time was chosen as 15 min in ethanol media. The sorption performances of the nanoparticles were enhanced by impregnation up to 92% in the aqueous media. The sorption equilibrium behaviour of the modified nanoparticles was also evaluated. The experimental data indicated that the equilibrium behaviour was in line with the Langmuir sorption isotherms.

Keywords: ionic liquid; nanoparticle; impregnation; copper; sorption.

Copper, one of the most widely used heavy metals, is mainly employed in many industries such as printing, electroplating, metal finishing, and mining. It is a micronutrient for both plants and animals at low concentrations and is recognised as essential to virtually all of them [1]. However, it may become toxic to some forms of aquatic life at elevated concentrations. The copper ions released into the environment accumulate in living organisms. The symptoms of deficiency or excessive exposition to copper can be observed in plants, water organisms, and humans [2,3]. According to environmental regulations worldwide, copper concentrations must be checked in order to identify that they are at an acceptable level before being discharged into the environment. The Environmental Protection Agency (EPA) has established a Maximum Contaminant Level Goal (MCLG) for copper in public drinking water systems at 1.3 mg/L. The EPA has also published a regulation to control lead and copper levels in drinking water [4,5]. Therefore, it is very important to develop techniques for the removal of Cu (II) ions from both municipal and industrial wastewater.

Correspondence: N. Gizli, Ege University, Faculty of Engineering, Chemical Engineering Department, 35100 Bornova, Izmir, Turkey.
E-mail: nilay.gizli@ege.edu.tr
Paper received: 21 January, 2016
Paper revised: 22 May, 2016
Paper accepted: 2 June, 2016

https://doi.org/10.2298/CICEQ160121034G

The removal of copper from potable water and wastewater can mainly be accomplished by using several conventional methods including precipitation, electrochemical and sorption technologies [6-8]. Furthermore, most of these processes are not implemented because of their high cost, the requirement for large amount of toxic solvents, disposal of sludge, low efficiency, and unfavourable selectivity, especially in elevated concentrations [9]. The treatment of wastewaters containing low concentrations of heavy metals is very difficult. Adsorption is one of the commonly recommended methods for heavy metal removal, and extraction, and the pre-concentration of the low concentration levels from the various aqueous environments [10,11].

In general, the efficiency of the adsorption depends on many factors, including the surface area, pore size and distribution of it, as well as the surface chemistry of the adsorbents. The sorbents with a high specific surface area as a result of the micropore character are generally needed for high adsorption efficiency. Nanosorbents have a high porosity (~99%) and high specific surface areas (500-1000 m^2 g^{-1}) as well as low density. Hence, these characteristics make nanosorbents excellent candidates for the adsorption processes [12]. Alumina and silica nanosorbents are the most commonly used adsorbents for preconcentration, the solid phase extraction, and the removal and separation of heavy metal ions at a low level concentration [13]. The hydroxyl groups on the surface of the silica and alumina are the major contributing factors that are responsible for the binding, adsorption, and extraction processes. However, the weak ion exchange properties of these hydroxyl groups are to favour their low interaction behaviour with various species [14]. Therefore, the improvements of the adsorption efficiency of alumina and silica nanosorbents toward heavy metals can be achieved by surface modification *via* the immobilization and incorporation of certain functional groups [15-17]. They combine the unique features and process adv-antages of liquid-liquid extraction and adsorption [18-21].

Room temperature ionic liquids (RTILs) are gaining widespread interest as a green solvent. They are regarded as a potential alternative media in catalytic synthesis, separation, and electrochemical applications as a result of their unique chemical and physical properties. They have an extremely low vapour pressure, good thermal stability, high ionic conductivity, tuneable viscosity, a large electrochemical window, as well as good extractability for various organic compounds and metal ions [22]. The non-flammable and non-volatile nature of ILs provides the advantages for using them as replacement for volatile organic compounds in the solvent extraction processes [23-28]. The application of ionic liquid based on the separation of heavy metal ions from the aqueous phase is a field of intensive research and promising perspective [29-31].

A number of researchers have been devoted to the description of synthesis and the properties of various ILs based on imidazolium cations, focusing on their potential for the extraction of metal ions [9,32-34]. A series of imidazolium based IL were used as an extractant to remove mercury [35] and to leach gold, silver, copper, and base metals from sulphuric ores [31]. Damanska and Rekawek investigated the effect of the alkyl chain length of imidazolium-based ionic liquid on the extraction of Ag^+ and Pb^+ [36]. Rios *et al.* used several imidazolium based ionic liquids as sole extraction agents of metal ions for the selective separation of Zn(II), Cd(II), Cu(II) and Fe (II) from hydrochloride aqueous solutions. They reported the exciting potential of ionic liquids use as green extraction agents in the liquid/liquid extraction of heavy metal ions [37]. Liang *et al.* impregnated the imidazolium based ionic liquids onto silica sorbents in order to take advantage of the chemical functionality of ILs with those of the heterogeneous support material for the pre-concentration of cadmium ions [23]. Mahmoud *et al.* investigated the uptake of lead from the aqueous solution by imidazolium based ionic liquid impregnated nano-silica sorbents [17].

The immobilization of ILs as thin layers on porous materials can be achieved by simple physisorption or by chemical binding to support one of the ions that are composed of IL [38].

In this study, the improvement of Cu (II) ion sorption performance of the nano-silica and nano-alumina particles was investigated by the immobilization of 1-ethyl-3-methyl imidazolium bis(trifluorosulfonyl) imide [$Emim^+Tf_2N^-$] ionic liquid. The incorporation was achieved via the ultrasound assisted physical impregnation method. Ultrasonication, as an unconventional method, is less time-consuming, and ensures the effective mass transfer of IL from the liquid phase onto solid support [39]. The physicochemical and morphological characterization of the adsorbents was investigated by using FT-IR and SEM analysis. The effects of the loading ratio and the sonication time on the sorption performance of the modified nanoparticles were investigated. The sorption equilibrium and kinetic behaviour of the modified nanoparticles were also evaluated.

EXPERIMENTAL

Materials

The nanoparticles Aerosil TT600, Aerosil MOX 80, and Alu-C were obtained from the Evonik Industries. The identifications and typical properties of the nanoparticles used in the experiments are given in Table 1.

The chemicals used during the experiments were of analytical pure grades. The 1-ethyl-3-methylimidazolium bis(trifluormethylsulfonyl)imide [$Emim^+$ Tf_2N^-] used as an IL was obtained from Sigma Aldrich. The stock solution (1000 mg L^{-1}) of Cu(II) was prepared by dissolving appropriate amounts of $CuSO_4·5H_2O$, in deionized water. The working solutions of different concentrations were prepared by diluting the stock solutions with deionized water. The $CuSO_4·5H_2O$ was supplied from Merck, Germany.

The copper ion concentrations of the solution were obtained by using a flame-atomic absorption spectrophotometer (AAS), Pelkin Elmer, Varian 10+ model.

Impregnation

The impregnation of the ionic liquid onto the particles was obtained by following the physical impregnation method [18]. A known amount of nanoparticles were dispersed into 25 mL of ethanol by the addition of the accurate amount of ionic liquid and sonicated at a 35 Hz frequency for 5, 10, and 15 min. All the obtained samples were dried in a vacuum at 50 °C for 24 h in order to remove the ethanol. The ratio of the IL (mL) per nanoadsorbent amount (g) was selected as 0.5:1, 1:1 and 2:1 (mL IL/g nanoparticles).

Characterization

The structural characterizations of the modified adsorbents were achieved by using a Fourier transform infrared spectrometer. A FT-IR spectrometer (Pelkin Elmer Spectra 100) with high resolution in the wave number range of 650-4000 cm^{-1} was used to identify the functional groups both before and after the modification of the nanoparticles with IL.

The morphological characterization was performed by using a scanning electron microscopy (Quanta 400 F field emission) equipped with an energy dispersive X-ray (EDX) spectrometer. The microscope was operated at an accelerating voltage of 20.00 kV. The particles were coated with a gold layer in order to make them conductive.

Batch adsorption studies

The adsorption studies were carried by contacting 0.01 g. of adsorbent with the 10 mL of aqueous solution containing 10^{-2} M Cu(II) ions, during 24 h at 30 °C. The initial pH of the Cu(II) solution was adjusted to the value of 6.

The uptake of Cu(II) by the adsorbent was calculated from the following equation:

$$q_e = (c_0 - c_e)\frac{V}{W} \tag{1}$$

where q_e is the Cu (II) uptake (mg/g), c_0 and c_e are the initial and equilibrium Cu(II) concentrations in the aqueous phase (mg/L), V is the volume of solution (mg/L), and W is the amount of adsorbent (g).

The sorption percentage of the nanoparticles was calculated as follows:

$$\text{Sorption}(\%) = 100\frac{c_0 - c_e}{c_0} \tag{2}$$

The effect of the loading ratio on the adsorption of Cu(II) was investigated by using the adsorbents containing a various amount of ionic liquid. The ratio of the IL (mL) per nanoadsorbent amount (g) was selected as 0.5:1, 1:1 and 2:1 (mL IL/g nanoparticles).

To determine the equilibrium behaviour of the IL impregnated nanoparticles, the adsorption experiments were performed with the initial Cu(II) concentrations that ranged from 1-50 mg/L.

RESULTS AND DISCUSSION

Surface modification and characterization

Scanning electron microscopy (SEM) *via* surface imaging can be directly implemented in order to prove the existence of ionic liquid on the solid structure. The morphological changes of the nanoparticles impregnated with the ionic liquid at various ratios are shown in Figure 1. It is evident from Figure 1 that the immobilization of the IL on the surface of the silica and alumina nanoparticles had led to a pronounced

Table 1. Properties of the nanoparticles

ID	Nanoparticle	Size, nm	Surface area, m^2/g	pH Value	Content
S1	Aerosil TT600	40	200	3.5-4.5	SiO_2 (100%)
S2	Aerosil MOX80	30	80	3.5-4.5	SiO_2 (99%)/Al_2O_3 (1%)
S3	Alu-C	20	100	3.5-4.5	Al_2O_3 (100%)

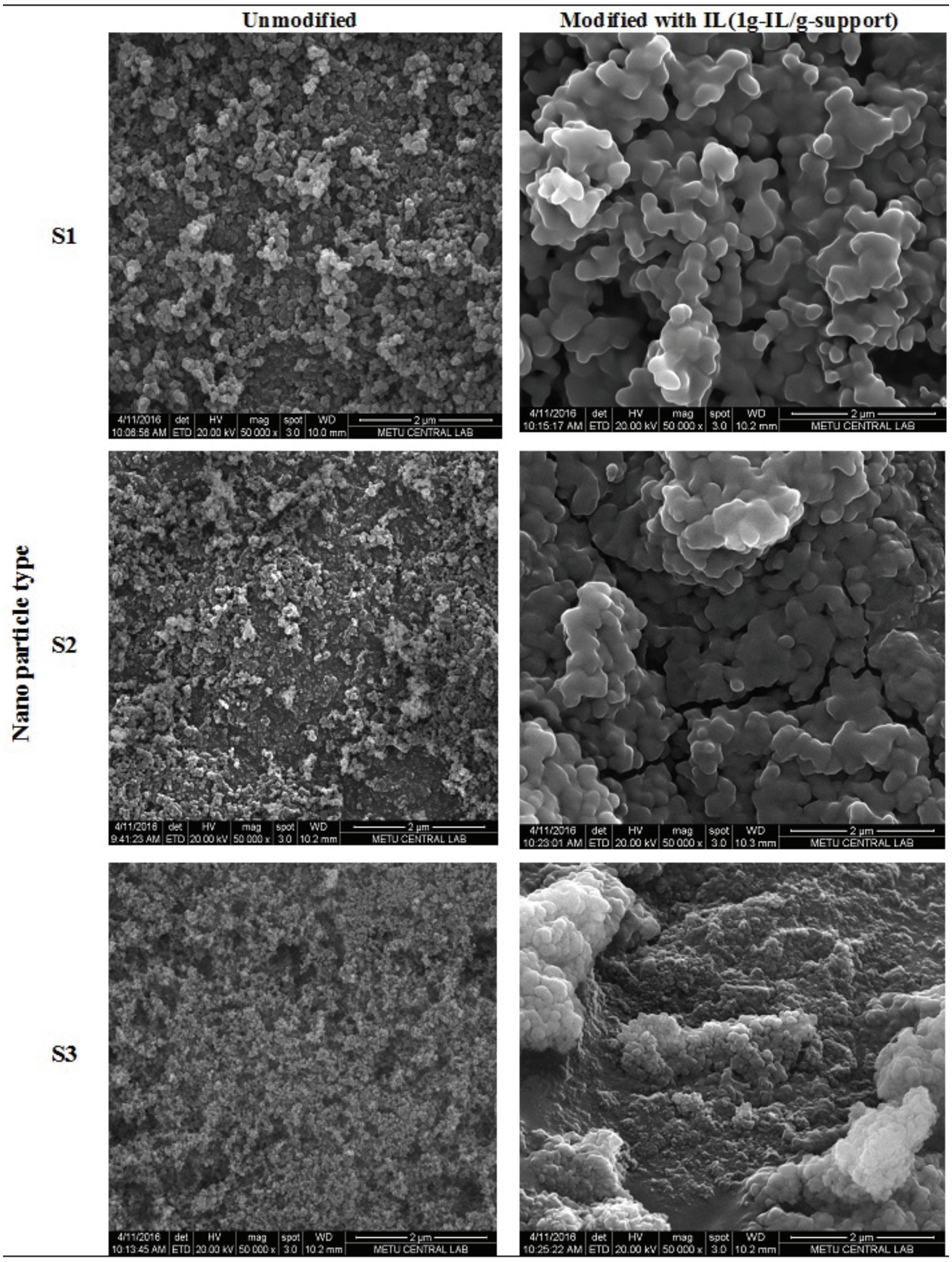

Figure 1. SEM images of the unmodified and modified particles magnified to 50000×.

and characterized change on the surface morphology. It was clearly observed that the IL covered the surface of the nanoparticles, which led to a decrease in the surface area by modification.

EDX analyses are used to study the overall chemical composition and the distribution of the chemical elements of interest in the unmodified and modified nanoparticle. The elementary compositions of prepared adsorbents are tabulated in Table 2.

The impregnation of nanoparticle supports is evidenced by the presence of the characteristic elements of EMIMTf2N type ionic liquid. These are mainly N and F and C.

The surface modification of the nano-sorbents can also be investigated by using Fourier transform infrared (FTIR) spectroscopic analysis [14]. The FTIR spectra of S1, S2 and S3 nanoparticles are shown in Figure 2a-c, respectively.

The characteristic peaks of the imidazolium ionic liquid around the position of 3159 and 1520 cm^{-1} in Figure 2, were attributed to the C-H and C=C vibrations of the imidazole ring in Figure 2. In addition, the infrared region of the ionic liquid spectrum between 1400 and 1000 cm^{-1} was mainly dominated and characterized by several peak assignments that are related to the anion moiety [15]. In all spectra of the

Table 2. The elementary composition of unmodified and modified nanoparticles

Element	Particle type					
	S1		S2		S3	
	Unmodified	Modified	Unmodified	Modified	Unmodified	Modified
C	-	26.26	-	33.32	-	25.62
N	-	8.92	-	-	-	7.44
O	42.23	26.45	58.14	24.86	44.87	25.93
F	-	17.95	-	17.77	-	14.75
Al	-	0.18	0.2	0.23	55.13	18.00
Si	32.95	12.42	33.05	13.16	-	-
Others[a]	24.82	7.83	8.81	10.66	-	8.25

[a] Other elements, such as Au, Pb, comes from sample preparation step during SEM analysis

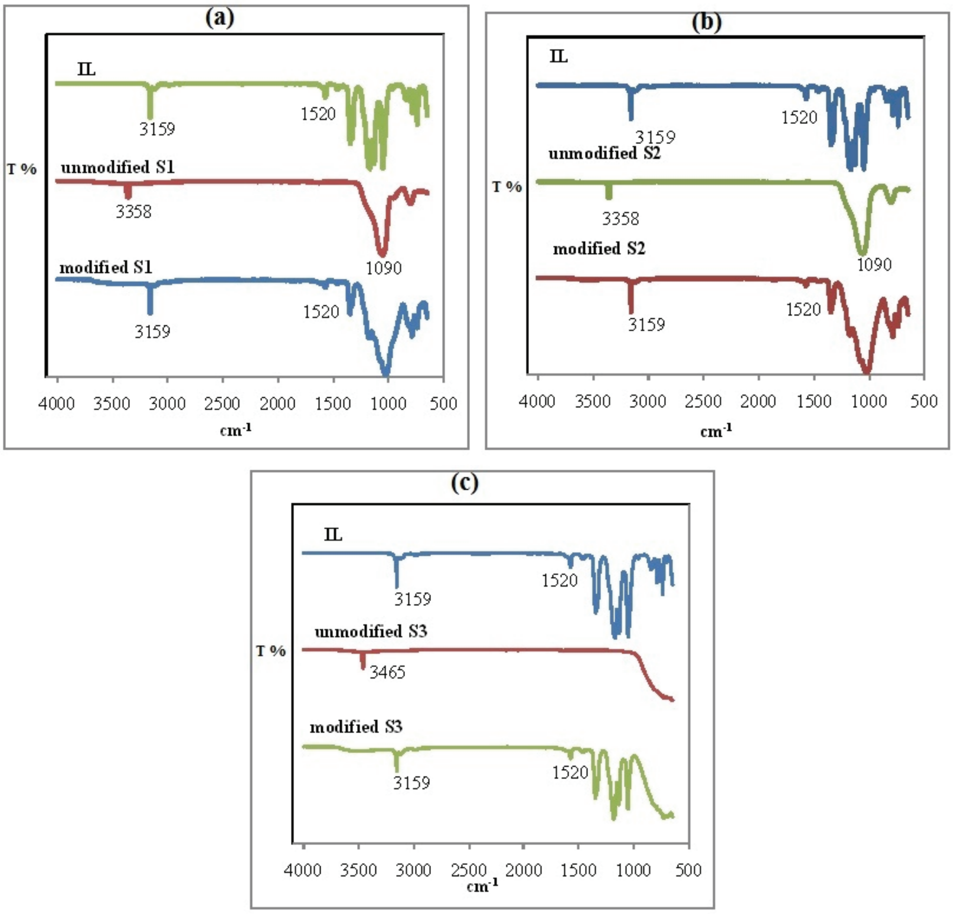

Figure 2. FTIR spectra of: a) S1, b) S2 and c) S3.

silica nanoparticles (Figure 2a and b), the bands around 1090 cm^{-1}, which assigned the stretching vibrations of the Si-O-Si groups of the silica backbone, were observed. In Figure 2c, the vibrations of Al-O-Al can be attributed at 914 cm^{-1} (asymmetric stretching). It can also be seen in all the spectra of modified nanoparticles, that two new adsorption peaks at the position of 3159 and 1520 cm^{-1} appeared after nanoparticles were treated with IL. These adsorption peaks, which can be attributed to the C-H and C=C vibrations of the imidazole ring, indicate that the ionic liquid was impregnated onto the nanoparticles. The peaks at the position of 3358 and 3465 cm^{-1} of the unmodified silica and alumina particles, respectively, which are attributed the O-H vibration of particle surfaces, disappear or decrease by modification with the IL. This indicates that the Tf_2N in the imidazolium cation is in interaction with the hydroxyl group of silica and alumina surface. The possible chemical structure of modified nano silica particles with [Emim$^+$Tf$_2$N$^-$] (supplementary material, available from the author upon request) is assigned as proposed by Mahmoud and Al-Bishri [16].

Figure 3 shows the thermal behavior of [Emim$^+$Tf$_2$N$^-$] and the prepared adsorbents at the impregnation ratio of 1:1.

Figure 3 shows that [Emim$^+$Tf$_2$N$^-$] started to decompose at 350 °C and decomposed almost completely at 500 °C. The weight loss of the prepared adsorbents at the impregnation ratio of 1:1 were below 3% at the temperature range of 20-350 °C. However, the nanoparticle supports started to decompose at moderately low temperatures (around 30 °C) and the mass losses of all types of nanoparticles were around 15% at the temperature range of 20-600 °C. It can be concluded that the immobilization of [Emim$^+$Tf$_2$N$^-$] may lead to improvement in the thermal stability of silica and alumina nanoparticles at the temperature range of 20-350 °C.

Adsorption performance

The change in the sorption performance of the nanoparticles by modification with the IL is shown in Table 3.

Table 3. Cu(II) adsorption performance (sorption percentage, %) of nanoparticles

Particle type	State	
	Unmodified	Modified
S1	24	40
S2	34	53
S3	61	92

The Cu(II) sorption performances of the unmodified nanoparticles S1 (200 m^2/g), S2 (80 m^2/g) and S3 (100 m^2/g) were found to be 24, 34 and 61% respectively. Although a greater removal performance for S1 may be expected by considering their specific surface areas, S2 and S3 exhibited a higher sorption percentage because of their alumina content. The corresponding values of the particles loaded with IL (the volume/mass ratio of 0.5:1 and 10 min. dispersion time) were found to be 40, 53 and 92%, respectively. It is clear that the sorption capacities of the nanoparticles are enhanced with the impregnation of IL. As shown by Hua *et al.*, when a modifier is immobilized at the surface of the nanoparticles, the removal, and the removal mechanism is changed accordingly [13]. Metal ions are not only removed by adsorption on the surface of the nanoparticles but also by a surface attraction and/or chemical-bonding interaction on the immobilized IL.

Effect of loading ratio of IL

The effects of the ionic liquid loading ratio (L_R) on the sorption percentage (%) at different dispersion times (t_D) are shown in Figure 4. It is evident that impregnation of the nanoparticles at a ratio of 0.5:1 show a higher sorption performance up to 40, 52 and 92% for S1 S2 and S3, respectively. A further increase in the impregnation ratio (1:1 and 2:1) tends to decrease the sorption performances of all types of nanoparticles. This decline in the sorption percentages can be attributed to the decrease in the value of the surface area by filling the pores of the particles with IL.

Effect of dispersion time

The dispersion of the nanoparticles in the IL solution is one of the key factors in order to obtain an effective impregnation as well as high sorption capacity values. Therefore, several dispersion time intervals (5, 10 and 15 min) in an ultrasonic bath were used to evaluate such time effect on the Cu(II) ion sorption by the IL impregnated nanoparticles. The

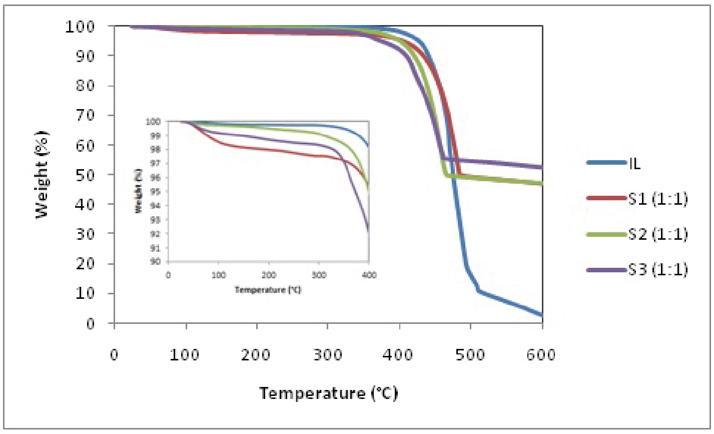

Figure 3. TGA curves of [Emim$^+$Tf$_2$N$^-$] ionic liquid and prepared adsorbents (loading ratio 1:1 mL IL/g particle).

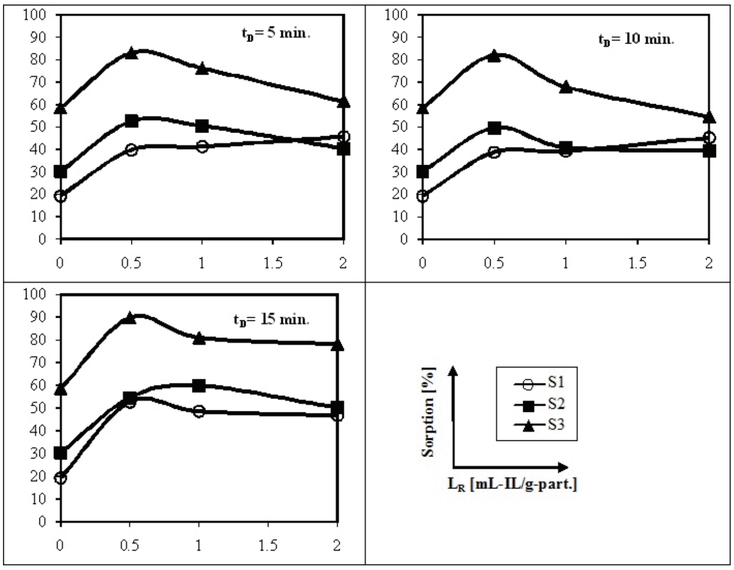

Figure 4. Cu(II) sorption performance of nanoparticles having the different ionic liquid loading ratio.

results of this study are shown in Figure 5. It is evident that the prolonged dispersion of the nanoparticle in the ethanol-ionic liquid mixture during preparation increases the sorption capacity of all types of nanoparticles.

Equilibrium behaviour

The equilibrium behaviour of the silica and alumina nanoparticles modified with IL are shown in Figure 6. It is clear that the initial concentration of the Cu(II) ion in the solution had remarkable effects on the equilibrium sorption performances of the modified particles due to the higher availability of the metal ions for sorption. In addition, the modified alumina particles (S3) have a higher sorption equilibrium capacity than the others because of having a high surface area along with the alumina content.

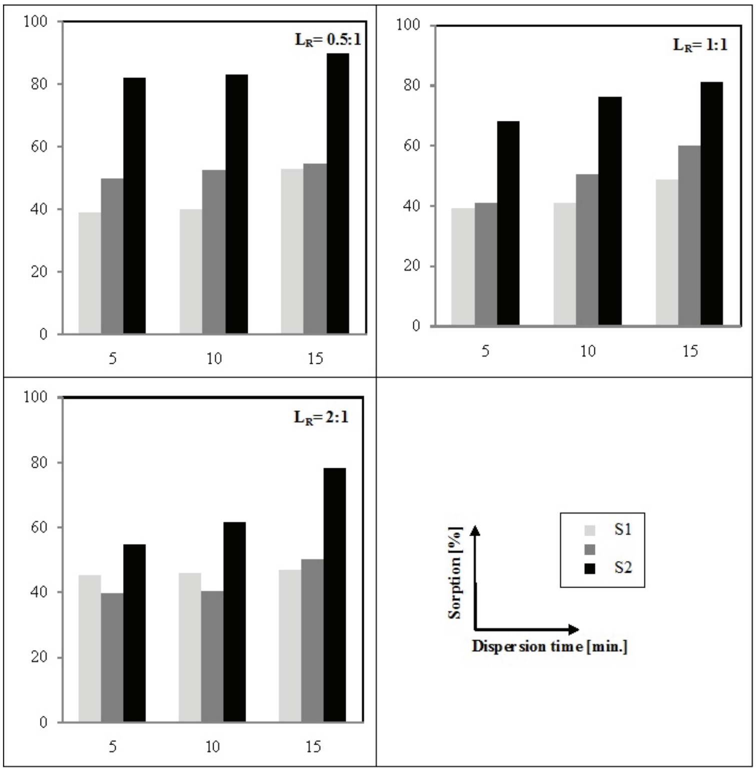

Figure 5. Effect of dispersion time on the sorption performances.

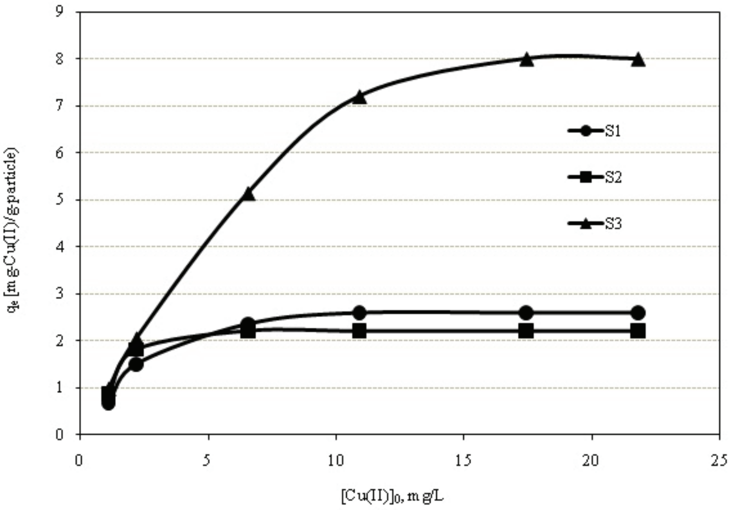

Figure 6. Equilibrium behaviour of the nanoparticles impregnated with IL at a ratio of 0.5:1.

The equilibrium adsorption isotherms are some of the most important data for determining the sorption performances of the modified particles through the potential affinity between the metal ion and the adsorbent, the bond energy and the sorption capacity. The most commonly employed models, namely the Langmuir and Freundlich adsorption models, were used in this study in order to describe the relationship between the amount of Cu(II) ion adsorbed per unit weight of the modified nanoparticles q$_e$ and the liquid-phase equilibrium concentration (c_e) of the Cu(II) ions. The linear forms of the Langmuir and Freundlich isotherms are represented by Eqs. (3) and (4), respectively:

$$\frac{c_e}{q_e} = \frac{1}{q_{max} b} + \frac{c_e}{q_{max}} \tag{3}$$

where c_e is the equilibrium concentration (mg/L), q_{max} is the monolayer adsorption capacity (mg/g) and b is the constant related to the free adsorption energy (Langmuir constant, L/mg):

$$\log q_e = \log k_F + \frac{1}{n} \log c_e \tag{4}$$

where k_F is a constant indicative of the adsorption capacity of the adsorbent (mg/g) and the constant $1/n$ indicates the intensity of the adsorption.

The calculated parameters of the adsorption isotherms along with regression coefficients are listed in Table 4. The Langmuir isotherm model had the highest values of the regression coefficients when compared to the Freundlich isotherm models, which showed the homogeneous nature of the adsorbent. The maximum adsorption capacity and Langmuir constant were calculated from the slope and intercept of the linear plots c_e/q_e *versus* c_e (supplementary material, available from the author upon request) which give a straight line of slope $1/q_e$ which correspond to complete the monolayer coverage (mg/g) and the intercept is $1/q_{max}b$. Maximum adsorption capacity, q_{max}, were found as 2.61, 2.25 and 8.25 mg/g for S1, S2 and S3, respectively. Based on these values, it can be accomplished that S3 has very good potential among other prepared sorbents, for the removal of Cu(II) from an aqueous solution. Affinity between sorbent and sorbate can be represented by the constant b which is related to the free adsorption energy can be used to calculate separation factor (R_L) describing the essential characteristics of the isotherm. R_L is calculated using the formula:

$$R_L = \frac{1}{1 + bc_0} \tag{5}$$

where R_L is a dimensionless constant called separation factor, b is the Langmuir equilibrium constant and c_i is the initial concentration of the metal ion (mg L^{-1}). If $0 < R_L < 1$, the nature of the sorption is considered favourable. The separation factor value for S3

Table 4. Equilibrium isotherm parameters and regression coefficients

Model	Coefficient	Nanoparticle		
		S1	S2	S3
Langmuir	q_{max} / mg g^{-1}	2.61	2.25	8.25
	b / L mg^{-1}	3.10	7.51	0.91
	r^2	0.99	0.99	0.99
Freundlich	k_F / mg g^{-1}	1.56	1.66	3.01
	n	0.29	0.18	0.50
	r^2	0.78	0.63	0.93

decreased from 0.001 to 0.021, as the initial concentrations of Cu(II) ions increased from 1 to 50 mg L^{-1}. Moreover, the calculated R_L at different concentrations of Cu(II), fall within the range $0 < R_L < 1$, revealing that the sorption of Cu(II) by S3 sorbent is favourable at all the metal concentrations investigated.

CONCLUSIONS

In this study, modification nano-silica and nano-alumina particles were obtained by the immobilization of 1-ethyl-3-methyl imidazolium bis(trifluorosulfonyl)-imide type ionic liquid in order to improve the Cu(II) ion sorption performance. Based upon the experimental results, Cu(II) sorption percentages achieved with modified nanoparticles were higher than that of modified nanoparticles due to synergistic effect of electrostatic interaction with IL and Cu(II) ions. The Cu(II) sorption performances of nanoparticles Aerosil TT600, Aerosil MOX80, and Alu-C were increased by modification, from 23.80, 34.13 and 61.13% to the values of 40, 52 and 92%, respectively.

The sorption performance of modified nanoparticles was directly affected by the amount of IL confined (mL IL/g nanoparticle). The impregnation of the nanoparticles at a ratio of 0.5:1 showed higher sorption percentages up to 90%. Further increase in the impregnation ratio (1:1 and 2:1) results in a decrease in sorption capacity. Adsorption isotherm data of Cu(II) ions on ionic liquid impregnated nano-silica and nano-alumina particles were well fit with Langmuir adsorption isotherm model. The maximum monolayer capacity was found to be 8.25 for IL impregnated silica nanoparticle. The R_L value, showed favorable sorption of Cu(II).

All the experimental data indicated that the IL impregnated nano-silica and nano-alumina particles are promising agents in the removal of Cu(II) ions from aqueous media. Although 92% removal was obtained, the complete removal can be technically feasible through the multi-stage contact.

Acknowledgement

The authors are grateful to the Scientific and Technological Research Council of Turkey (TUBITAK) for financial support under Contract No. 213M537.

REFERENCES

[1] J.S. Valentine, E.B.Gralla, Science **278** (1997) 817-818

[2] D. Özçelik, H. Uzun, Biol. Trace Elem. Res. **127** (2009). 45-52

[3] S.S. Metwaly, M.A. Hassan, R.F. Aglan, J. Environ. Chem. Eng. **1** (2013) 252-259

[4] M.R. Awual, G.E. Eldesoky, T. Yaita, M. Naushad, H. Shiwaku, Z.A. Abthman, S. Suziki, Chem. Eng. J. **279** (2015) 639-647

[5] N-B. Chang, C. Houmann, K-S. Lin, M. Wanielista, Chemosphere **144** (2016) 1280-1289

[6] H. Benaissa, M.A. Elouchdi, Chem. Eng. Process. **46** (2007) 614-622

[7] F. Fu, Q. Wang, J. Environ. Manage. **92** (2011) 407-418

[8] M. Bilal, J.A. Shah, T. Ashfaq, S.S. Gardazi, A.A. Tahir, A. Pervez, H. Haroon, Q.J. Mahmood J. Hazard. Mater. **263** (2013) 322-333

[9] A. Stojanovic, B. Keppler, Sep. Sci. Technol. **47** (2012) 183-203

[10] M.E. Mahmoud, O.F. Hafez, A. Alrefaay, M.M. Osman, Desalination **253** (2010) 9-15

[11] Y. Tian, P. Yin, R. Qu, C. Wang, H. Zheng, Z. Yu, Chem. Eng. J. **162** (2010) 573-579

[12] M. E. Mahmoud, Desalination **266** (2011) 119-127

[13] M. Hua, S. Zhang, B. Pan, W. Zhang, L. Lv, Q. Zhang, J. Hazard. Mater. **211-212** (2012) 317-331

[14] M.E. Mahmoud, O.F. Hafez, M.M. Osman, M.M. Yakout, A. Alrefaa., J. Hazard. Mater. **176** (2010) 906-912

[15] A. Afkhami, M. Saber-Tehrani, H. Bagheri, J. Hazard. Mater. **181** (2010) 836-844

[16] M.E. Mahmoud, H.M. Al-Bishri, Chem. Eng. J. **166** (2011) 157-167

[17] H.M. Al-Bishri, T.M. Abdel-Fattah, M.E. Mahmoud, J. Ind. Eng. Chem. **18** (2012) 1252-1257

[18] N. Kabay, J.L. Cortina, A. Trochimczuk, M. Streat, React. Funct. Polym. **70** (2010) 484-496

[19] J. Lemus, J. Palomar, M.A. Gilarranz, J.J. Rodriguez, Adsorption **17** (2011) 561-571

[20] M. Blahusiak, S. Schlosser, J. Annus, React. Funct. Polym. **87** (2015) 29-36

[21] L. Lupa, A. Negrea, M. Ciopec, P. Negrea, R. Voda, Sep. Purif. Technol. **155** (2015) 75-82

[22] L. Fischer, T. Falta, G. Koellensperger, A. Stojanovic, D. Kogelnig, M. Galanski, R. Krachler, B. K. Keppler, S. Hann, Water Res. **45** (2011) 4601-4614

[23] P. Liang, L. Peng, Talanta **81** (2010) 673-677

[24] G-T. Wei, Z. Yang, C-J Chen, Anal. Chim. Acta **488** (2003) 183-192

[25] M.L. Dietz, Sep. Sci. Technol. **41** (2006) 2047-2063

[26] T.P.T. Phama, C-W Cho, Y-S Yuna, Water Res. **44** (2010) 352-372

[27] C. Shi, D. Duan, Y. Jia, Y. Jing, J. Mol. Liq. **200** (2014) 191-195

[28] Y. Yuan, S. Liang, H. Yan, Z. Ma, Y. Liu, J. Chromatogr., A. **1408** (2015) 49-55

[29] D. Han, K. H. Row, Molecules **15** (2010) 2405-2426

[30] L.B. Escudero, R.A. Olsina, R.G. Wuilloud, Talanta **116** (2013) 133-140

[31] J.A. Whitehead, J. Zhang, N. Pereira, A. McCluskey, G. A. Lawrance, Hydrometallurgy **88** (2007) 109-120

[32] H. Zhao, S. Xia, P. Ma, J. Chem. Technol. Biotechnol. **80** (2005) 1089-1096

[33] Y. Zhang, D. Kogelnig, C. Morgenbesser, A. Stojanovic, F. Jirsa, I. Lichtscheidl-Schultz, R. Krachler, Y. Li, B.K. Keppler, J. Hazard. Mater. **196** (2011) 201- 209

[34] E.M. Martinis, P. Berton, R.P. Monasterio, R.G. Wuilloud, Trends Anal. Chem. **29** (2010) 1184-1201

[35] M.V. Mancini, N. Spreti, P. Di Profio, R. Germani, Sep. Purif. Technol. **116** (2013) 294-299

[36] U. Domanska, A. Rekawek, J. Solution Chem. **38** (2009) 739-751

[37] A.P. Rios, F.J. Hernandez-Fernandez, F.J. Alguacil, L.J. Lozano, A. Ginesta, I. Garcia-Diaz S. Sanchez-Segado, F.A. Lopez, C. Godinez, Sep. Purif. Technol. **97** (2012) 150-157

[38] P. Virtanen, H. Karhu, K. Korda, J. Mikkola, Chem. Eng. Sci. **62** (2007) 3660 – 3671

[39] S. Kalidhasan, A.S.K. Kumar, V. Rajesh, N. Rajesh, J. Hazard. Mater. **213-214** (2012) 249-257.

NILAY GIZLI
MERVE ARABACI

Ege University, Faculty of Engineering, Chemical Engineering Department, Bornova, Izmir, Turkey

NAUČNI RAD

POBOLJŠANA SORPCIJA Cu(II) IZ VODENIH RASTVORA NANOČESTICAMA SILIKE I ALUMINE IMPREGNISANIM JONSKOM TEČNOŠĆU

U ovom radu izvršeno je poboljšanje sorpcije Cu(II) jona impregnisanjem čestica nano-silike i alumine jonskom tečnošću (IL) 1-etil-3-metilimidazolijum bis(trifluorosulfonil)imid [Emim$^+$Tf2N]. Jonska tečnost je naneta fizičkom metodom impregnacije uz primenu ulztrazvuka. Strukturna i morfološka karakterizacija adsorbensa ie izvršena infracrvenom spektroskopijom sa Furijeovom transformacijom (FT-IR) i skening elektronskom mikroskopijom (SEM). Termička stabilnost nano-čestica impregnisanih jonskom tečnošću su analizirane termogravimetrijskom analizom (TGA). Istraživani su efekti odnosa jonske tečnosti i nanočestica (L_R) i vremena sonifikacije (t_D) na sorpcione karakteristike modifikovanih nanočestica. Efikasna adsorpcija je postignuta korišćenjem čestica sa jonskom tečnošću pri odnosu 0,5 mL IL/g čestica. Optimalno vreme sonifikacije je 15 min u etanolnom medijumu. Sorpcione karakteristike nanočestica su poboljšane impregnacijom u vodenoj sredini do 92%. Takođe, ocenjena je priroda sorpcione ravnoteže modifikovanih nanočestica. Eksperimentalni podaci ukazuju da je ravnoteža u skladu sa Langmuir sorpcionom izotermom.

Ključne reči: jonska tečnost; nanočestice; impregnacija; bakar; sorpcija.

CI&CEQ
Chemical Industry & Chemical Engineering Quarterly

Available on line at
Association of the Chemical Engineers of Serbia *AChE*
www.ache.org.rs/CICEQ

Chem. Ind. Chem. Eng. Q. 23 (2) 217–227 (2017)   CI&CEQ

WAHEED UR REHMAN
WAHEED ZEB
AMIR MUHAMMAD
WAJID ALI
MOHAMMAD YOUNAS

Department of Chemical Engineering, University of Engineering & Technology, Peshawar, Pakistan

SCIENTIFIC PAPER

UDC 66.048.1:663.815:663.8

OSMOTIC DISTILLATION AND QUALITY EVALUATION OF SUCROSE, APPLE AND ORANGE JUICES IN HOLLOW FIBER MEMBRANE CONTACTOR

Article Highlights

- Evaluation of OD process for fruit juice concentration in hollow fibre membrane contactor
- Higher water flux was achieved in feed-in-shell flow configuration
- High final concentration was achieved at ambient temperature and pressure
- Quality evaluation of fruit juices before and after OD process was performed
- Quality characteristics of fruit juice concentrates were improved after OD process

Abstract

Sucrose solution, apple and orange juices were concentrated through osmotic distillation (OD) process using a mini-module Liqui-Cel^{TM} *hollow fibre membrane contactor. Mass transport characteristics of water molecules from feed to stripping solution were studied. Process parameters such as feed temperature, feed flow rate and concentration of stripping solution* ($CaCl_2$) *were varied. Sucrose solution was concentrated from 135 to 510 g TSS kg*$^{-1}$ *in 340 min using feed-in-lumen flow configuration at a start-up water flux of 0.250 L m*$^{-2}$ *h*$^{-1}$ *and a temperature of 30 °C. Similarly, it was concentrated up to 510 g TSS kg*$^{-1}$ *in 200 min using feed-in-shell flow configuration at a start-up water flux of 0.505 L m*$^{-2}$ *hr*$^{-1}$ *and a temperature of 30 °C. In a total recycle time of 340 min, clarified apple and orange juices were concentrated up to 500 g TSS kg*$^{-1}$ *using feed-in-lumen flow configuration at a start-up water flux of 0.204 and 0.294 L m*$^{-2}$ *hr*$^{-1}$*, respectively. It was found that quality parameters of fruit juices were well improved after the osmotic distillation process. The process therefore has good potential for application in the fruit processing industry for concentration of fruit juices.*

Keywords: osmotic distillation, hollow fiber membrane contactor, sucrose solution, apple juice, orange juice.

In Pakistan, agriculture contributes more than 24% to gross domestic production (GDP). Annual production of fresh fruits is about 7.36 million tons. While exports are growing at an average rate of 15% annually, there are huge losses of 30-40% due to lack of processing facilities [1]. Being distorted in shape, many fruits are rejected during the export process. However, these rejected fruits possess pleasant aromas and high sugar content and can be utilized in the fruit juice concentration industry [2]. The production of higher quality fruit juices can contribute towards the increased export earnings and sustainable economic growth. One of the challenging problems for food scientists and process engineers is the development of innovative, energy efficient, environment friendly and higher aroma recovery processes for the concentration of fruit juices [3]. Membrane separation processes are one of the solutions that can safely address this challenge. There are wide applications of membrane technology in the production of quality food products, the main benefits being easy operation, better quality product, low operational cost and possibility of

---

Correspondence: W. Ur Rehman, Department of Chemical Engineering, University of Engineering & Technology, Peshawar, P.O. Box 814, Pakistan.
E-mail: contactwaheed@hotmail.com;
m.younas@uetpeshawar.edu.pk

Paper received: 20 July, 2015
Paper revised: 4 May, 2016
Paper accepted: 14 June, 2016

https://doi.org/10.2298/CICEQ150720035R

treating different products with the same processing facility [4-5].

Production of fruit juice concentrates reduces handling losses, storage volumes and transportation costs along with stability against microbial and chemical degradation [7]. Color degradation and loss in thermo-sensitive compounds due to thermal treatment are some of the major issues in the conventional juice concentration processes [8]. Compared with traditional juice concentration techniques, several membrane-based processes, such as reverse osmosis, direct contact osmosis, membrane distillation and osmotic distillation have been used for the concentration of fruit juices [9-14]. Osmotic distillation (OD) offers several advantages, like better product quality, low energy consumption, higher final concentration and operation at ambient temperatures [9,15-17]. Disadvantages of OD include membrane pore wetting, low permeate flux and flux decay that are still the barriers for its development [18-20].

OD works on the principle of water activity gradient across the micro-porous hydrophobic membrane. On one side of the membrane is a diluted feed solution, while on the other side is a concentrated salt solution. The process works under atmospheric pressure and at ambient temperature [8,21]. The mass transfer occurs by three mechanisms: evaporation of vapours from feed side due to higher vapour pressure, transfer of vapour inside the micro-pores of hydrophobic membrane and condensation of vapour at lower vapour pressure side, *i.e.*, salt solution [22]. The concentration of fruit juices and sucrose solution through OD has been studied by various researchers for evaluation of evaporative flux and preservation of juice quality [16,23-26]. Courel *et al.* [25] investigated the effects of operating conditions on evaporative flux for concentrating sucrose solution through OD in flat sheet membrane. The most important parameter in OD is the selection of proper stripper solution. A variety of organic solvents (such as glycerol and polyglycerol) and inorganic salts (NaCl, $CaCl_2$, $MgCl_2$ and $MgSO_4$) have been used in different studies [27]. Although organic solvents offer the advantages of lack of scaling and corrosion effects as well as equivalent water flux rates, yet their higher costs make them uneconomical. On the other hand, NaCl, $MgCl_2$ and $MgSO_4$ have a limited driving force because of low solubility. Among all these strippers, $CaCl_2$ is found to be the most effective stripper.

Although flat sheet membranes have been used in studies on fruit juices concentration through OD, hollow fibre membrane contactors are the preferred choice for industrial scale OD processes. The reasons are high active surface area, low manufacturing cost, easy scale up and separation of components at low pressures [28]. It has been found to be a cost-effective technology and is therefore used to supplant or replace other technologies that may or may not be membrane based [29]. Module design is critical to optimizing process performance [30]. Concentration of fruit juices through OD in hollow fibre membrane contactors is currently an attractive research area that requires further exploration for optimization, intensification and commercialization of the process [7,11,15,31]. The added advantage of OD in hollow fibre membrane contactors is the preservation of total phenolic compounds after the concentration of fruit juices [32,33]. On the other hand, some of the problems being faced in hollow fiber membrane contactors are lower flux, concentration polarization effects and pore wetting [34]. Concentration polarization and fouling reduces membrane efficiency. Though routine cleaning of membrane with chemicals reduces the part of adsorption resistance, irreversible fouling of membrane cannot be completely eliminated [35]. Sanaz *et al.* thoroughly reviewed the impact of membrane wetting on mass transfer resistance and absorption efficiency, the effect of influencing parameters (operational conditions, type and concentration) and membrane (hydrophobicity, pore size and porosity) properties on wetting phenomenon, as well as different methods to prevent membrane wetting, along with their advantages and drawbacks [36].

In the present study, an attempt is made to inves-tigate flux decay, quality analysis of fruit juices and optimisation of process parameters through OD in a laboratory scale hollow fiber membrane contactor module using lumen and shell side counter current flow configurations. Sucrose solution and clarified apple and orange juices were used as feed to evaluate process performance. Quality tests like total soluble solids, pH, total acidity, ascorbic acid, density and total phenol were conducted to find the effect of osmotic distillation on product quality.

EXPERIMENTAL

Materials (process fluids)

Sucrose solution was prepared by dissolution of sugar in deionised water. Clarified juice was obtained by removing pulp from juice through a multichannel tubular ceramic membrane module (Nanjing H&C Water Treatment Equipment Co., Ltd, Model HCCM-200-40-19-06) having a membrane surface area of 0.08494 m^2 and mean pore diameter of 2 μm. In the current study, calcium chloride ($CaCl_2$) solution was used as a stripper because of low cost, easy availability in the local market and higher solubility of $CaCl_2$ in water causing higher driving force across the membrane [37,38]. Concentration of sucrose solution was measured with a microprocessor-controlled hand held digital refractometer, (0-800 g TSS kg^{-1}), PAL-1, Atago, Japan. Effects of operating variables on water flux across the membrane were determined using feed in-lumen and feed in-shell flow configurations at stripper concentrations of 6, 5 and 3.5 M, feed temperatures of 23, 30 and 35 °C and feed velocities of 0.0052, 0.0044 and 0.0037 m s^{-1}.

Membrane contactor specifications

Experimental study for the concentration of fruit juices through OD was performed in a Liqui-Cel^{TM} mini-module (model X-50) hollow fibre membrane contactor. The product data sheet according to manufacturer is given in Table 1.

Table 1. Hollow fiber membrane contactor specifications

Liqui-Cel^{TM} contactor module	X-50
Total fibers	7400
Porosity	40%
Mean diameter of pore	4×10^{-8} m
Fiber internal diameter	2.4×10^{-4} m
Fiber external diameter	3×10^{-4} m
Modular length	121.8×10^{-3} m
Shell diameter	42.5×10^{-3} m
Membrane material	Polypropylene
Interfacial surface area	0.54 m^2

Membrane setup

The experimental setup as shown in Figure 1 consisted of hollow fibre membrane contactor, two laboratory scale peristaltic pumps and flow meters. Maximum flow rate of the pump was limited to 120 mL min^{-1}. Flow rates of feed and stripper streams were measured with flow meters and were varied by adjusting the rotating knob. The operating pressure was kept constant in both streams during the experiment. The membrane contactor was connected through flexible food grade plastic pipes to two small storage tanks, one for fruit juice and the other one for stripper, with a capacity of 0.5 and 2 L, respectively. Temperature was measured with a digital temperature sensor and controlled in a regulated temperature bath. Feed and stripper solutions were constantly stirred with magnetic stirrers during the experiment.

Plan of experiment

At the start of each experiment, the module was first washed with deionised water. Initially, sucrose solution and thereafter, fruit juices were used as feed solutions in experimental setup for OD process. Each experiment was repeated three times and the mean value was taken. The accuracy of values was noted to be among 4-10%. The stripper was introduced on the shell side, while the sucrose solution as a feed was passed through the lumen side of the contactor in a counter flow fashion. The flow configuration was then reversed, *i.e.*, the sucrose solution was fed on the shell side and the stripper on the lumen side of the membrane contactor. Both streams were recirculated to their respective storage tanks, thus operating in total recycled mode. The permeated volume of water across the membrane was measured by determining the change in volume of feed solution in fixed time duration. The water flux was then calculated according to the basic definition of flux:

$$J=\frac{1}{A}\frac{\Delta V}{\Delta t} \tag{1}$$

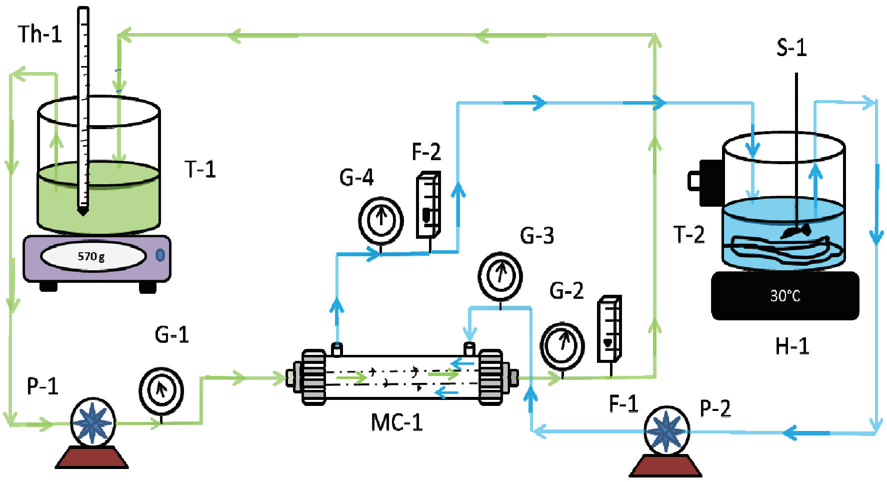

Figure 1. Experimental setup for osmotic distillation.

J = flux (L m^{-2} h^{-1}), ΔV = change in volume of feed in storage tank (L), Δt = Time duration in which change in volume is noted (min) and A= surface area of the membrane (m^2).

Membrane cleaning is essential for increasing the life of contactor and achieving stable flux in OD processes. The hollow fiber membrane contactor module was thoroughly cleaned after each experimental run. The membrane setup was washed with deionised water for about 30 min without recycle. After that, 2% NaOH solution was circulated at a flow rate of 88 mL min^{-1} for 40 min, followed by 2% citric acid solution for 20 min to avoid any bacterial and fungal activity within the membrane. Finally, the contactor was washed with deionised water followed by absolute alcohol. The module was dried by purging air through lumen and shell sides of the contactor at room temperature and at a flow rate of 0.84 m^3 h^{-1} (14.33 L min^{-1}) for about 30 min. The membrane module was re-usable after drying.

Quality tests for fruit juices

Fruit juices were analysed for quality parameters before and after OD process. Total soluble solids were calculated with a hand held refractometer. pH was determined using a digital pH meter. Acidity, vitamin C and moisture contents were evaluated using standard Association of Official Analytical Chemists [39] methods. Total phenolics were mentioned as mg L^{-1} of gallic acid and calculated using the Folin--Ciocalteu (FC) reagent method [40]. Thermal properties such as thermal conductivity were measured with needle probes. Thermal conductivity was determined by inserting a needle probe into the sample and measuring its response. A thermocouple and a heater were attached to the probe. This method is suitable for measurement of thermal conductivity in materials that are in liquid or semi-liquid form. Specific heat capacity and latent heat of fusion were determined with an electrical calorimeter, which constituted the combination of container, stirrer, lid, thermometer, immersion heater and shield assembly. The feed solution was heated by an electrical immersion heater and the input energy (H) and the rise in temperature were determined. If the mass of the feed solution is m and its specific heat capacity is c, then:

$$Q = mC_p(\theta_1 - \theta_o) + q \tag{2}$$

where Q is heat flux, θ_0 and θ_1 are the initial and final temperatures of the solution and q is the heat loss. Using the cooling correction, the value of q may be found.

Thermal diffusivity was calculated from conductivity, density and specific heat capacity relationship using Eq. (2):

$$\alpha = \frac{k}{\rho c_p} \tag{3}$$

ρ: density of liquid (kg m^{-3}), k: thermal conductivity (W m^{-1} K^{-1}), c_p: specific heat capacity (J k^{-1} K^{-1}) and α: thermal diffusivity (m² s^{-1}).

RESULTS AND DISCUSSION

Effect of temperature on feed concentration and water flux

Feed-in-lumen flow configuration

Sucrose solution concentration was investigated experimentally for three sets of feed temperatures (23, 30 and 35 °C). Stripper concentration was taken as 5 M throughout. Feed and stripper velocities were fixed at 0.0044 and 0.0015 m s^{-1} respectively, during all three sets of experiments. Sucrose concentration in the feed tank is plotted as a function of time in total recycled mode in Figure 2. It was found that rising temperature of the sucrose solution caused an increase in sucrose concentration. The driving force for the process is given by a difference in water activity between the stripping solution and the feed solution. Increase in temperature reduced the viscosity of stripping and feed solutions, thereby improving the evaporation flux. Thus, at a specific time of operation, the concentration is higher for higher temperatures. It is shown that an increase in feed temperature from 23 to 35 °C caused an increase in the feed concentration by 180 g TSS kg^{-1} in 340 min. However, temperature should be adjusted in such a way that the quality of solution remains unaffected after concentration.

Water flux as a function of processing time in total recycled mode is also shown in Figure 2. Experimental investigation showed that feed with higher temperature has higher flux as compared to that at low temperature. The increase in flux due to temperature has already explained by Hongvaleerat *et al.* [16]. Increasing temperature from 23 to 35 °C raised the average flux by 25%.The irregular trend in water flux decline is due to the pulsating flow rate caused by peristaltic pumps at low flow rates, which consequently caused the concentration polarization to be dominant in the boundary layers.

Relatively high values of flux were observed in the beginning of the experiment. This is due to the fact that the feed was very dilute and all the membrane surface area was available for OD. The obtained results were in agreement with the results

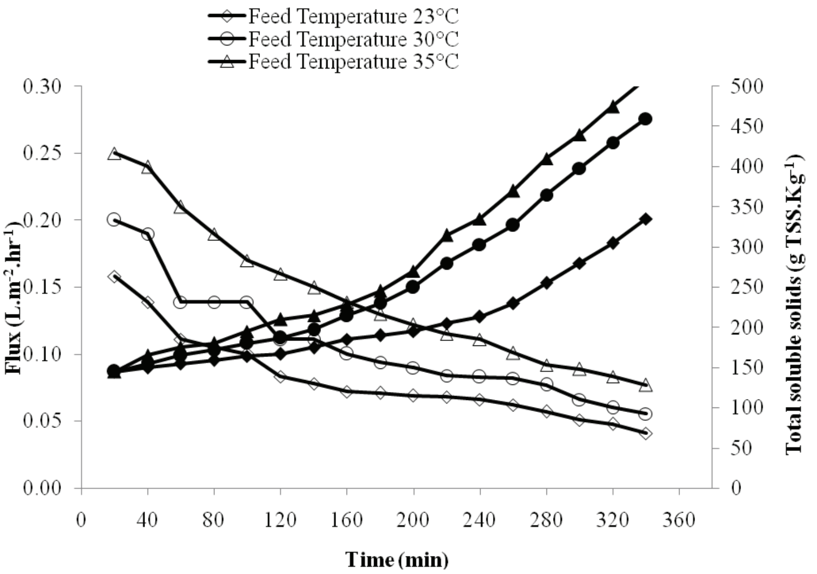

Figure 2. Effect of temperature on feed concentration for feed-in-fiber flow configuration (feed flow rate: 0.0044 m s^{-1}, initial feed concentration: 135 g TSS kg^{-1}, brine conc.: 5 M. Counter current flow. Empty markers show flux while filled markers show TSS).

obtained for sucrose solution at laboratory scale studied by Courel *at al.* [25]. The observations showed decreasing flux trend with the operating time because of increased concentration polarization effects. If the driving force is low, the concentration polarization effect is less pronounced [41]. The decrease in water flux is also due to dilution of the stripper solution. The vapour pressure of stripper solution is decreased, which consequently leads to a decrease of driving force for water transport from the feed across the membrane [42]. This can be overcome by using higher volumes of stripper solution to prevent excessive dilution during the operation. The stripper solution may be regenerated by evaporating the water. Flux decline can be reduced by proper adjustment of process parameters. This gradual intermittent flux decline is observed as the feed sucrose concentration is increased in a recycled based continuous operation of OD. The water flux was noted to be 0.158 and 0.250 L m^{-2} h^{-1} at the feed temperature of 23 and 35 °C, respectively, at the start of the experiment. However, flux decline was observed with the passage of juice processing time and it was noted to be 0.051 and 0.089 L m^{-2} h^{-1}, respectively, after 300 min of continuous recycled based processing. Gradual decline of water flux at high feed concentration is attributed to the strong influence of the concentration level on water flux during slight decrease in stripper concentration [42, 43].

Feed-in-shell flow configuration

Experiments were conducted with feed-in-shell flow configuration to observe sucrose concentration in feed tank and water flux across the membrane. The temperature was fixed at 23, 30 and 35 °C for the individual set of experiments in total recycled mode. Figure 3 shows that the feed concentration increases with the passage of time and with the increase in feed temperature. As discussed earlier, the driving force for the process is water activity gradient between the stripping solution and the feed solution. Increase in temperature reduced the viscosity of stripping and feed solutions, thereby improving the evaporation flux. Hence, at a specific time of operation, the concentration is higher for higher temperatures. Sucrose concentration increased up to 400, 470 and 530 g TSS kg^{-1} in 200 min at feed temperatures of 23, 30 and 35 °C, respectively. Figure 3 also shows that in the feed-in-shell flow configuration, the sucrose solution was concentrated to a certain value, e.g. 400 g TSS kg^{-1} in 180 min, as compared to feed-in-lumen flow configuration, which took 280 min to reach this value.

Temperature also has a substantial effect on permeate water flux, as illustrated in Figure 3. Incremental change in the feed bulk temperature from 23 to 35 °C resulted in higher water permeate fluxes and was observed to be ~2 times higher. The highest flux was 0.505 L m^{-2} h^{-1} at 35 °C. The results plotted in Figures 2 and 3 show higher average flux for feed-in-shell flow configuration as compared to that for feed-in-lumen flow configuration. This is due to the fact that on the shell side of the membrane contactor there are lower concentration polarization effects as compared to the lumen side of the membrane contactor [43]. Likewise, the lumen side of the membrane contactor offers lower surface area as compared to the shell

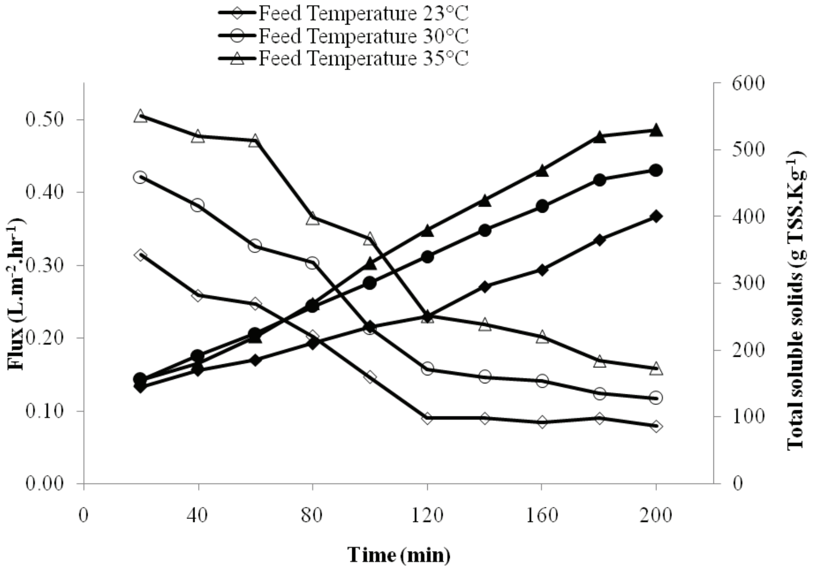

Figure 3. Effect of temperature on feed concentration for feed-in-shell flow configuration (feed flow rate: 0.0044 m s^{-1}, initial feed concentration: 135 g TSS kg^{-1}, brine conc.: 5 M, counter current flow. Empty markers show flux while filled markers show TSS).

side of the membrane contactor. Moreover, less fluctuation and deviation in sucrose concentration and water flux is observed for feed-in-shell flow configuration.

Effect of feed velocity

OD experiments were also carried out to investigate the effect of feed velocity on sucrose solution concentration and water flux across the membrane at three different feed velocities of 0.0052, 0.0044 and 0.0037 m s^{-1}. During these experiments, other process parameters were held constant. Initial sucrose and stripper solution concentrations were taken as 135 g TSS kg^{-1} and 5 M in their respective storage tanks. The temperature was kept constant at 30±2 °C during the experiments.

Figure 4 shows the plot of sucrose solution concentration in feed tank as a function of time at different feed velocities. It is shown that sucrose concentration increases with the passage of time. Furthermore, higher sucrose concentration was observed for feed velocity of 0.0052 m s^{-1}, followed by 0.0044 and 0.0037 m s^{-1}. Investigations from literature have shown that increasing the flow velocity reduces the concentration polarization effects, thereby increasing the water flux across the membrane [44].

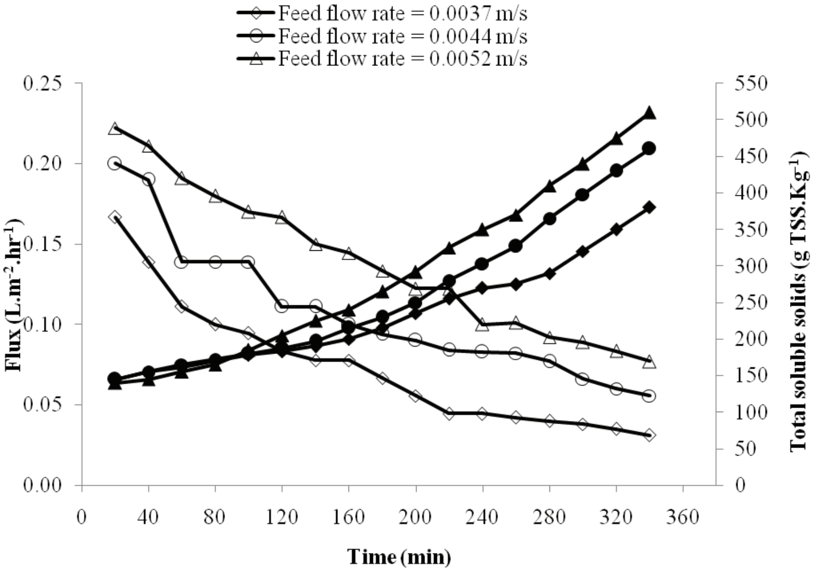

Figure 4. Effect of feed velocity on feed concentration for feed-in-fiber flow configuration (brine conc.: 5 M, temperature: 30 °C, initial feed concentration: 135 g TSS kg^{-1}. Empty markers show flux while filled markers show TSS).

Likewise, water flux across the membrane is also shown in Figure 4. It can be observed that feed flow velocity of 0.0052 m s^{-1} exhibits a higher average flux of 0.222 L m^{-2} h^{-1} as compared to that at 0.0044 and 0.0037 m s^{-1} which was 0.194 and 0.167 L m^{-2} h^{-1}, respectively. The flux decreases gradually and reaches 0.077, 0.056 and 0.031 L m^{-2} h^{-1} against the feed flow velocities of 0.0052, 0.0044 and 0.0037 m s^{-1}, respectively, in 340 min.

Effect of stripper concentration

Concentration gradient has been proven to be the driving force across the membrane in OD processes. In order to study the effect of concentration gradient, sucrose feed solution of 135 g TSS kg^{-1} was processed with three different concentrations of stripper solution, *i.e.*, 6, 5 and 3.5 M. All other parameters were kept constant. The results are shown in Figure 5. It has been shown that the increase in concentration of sucrose solution was much low for stripper concentration of 3.5 M due to low driving force across the membrane. In case of 6 M stripper solution, the sucrose solution concentration reached the highest value of 530 g TSS kg^{-1} in 340 min of processing time as compared to 460 g TSS kg^{-1} for 5 M stripper solution. On the other hand, sucrose solution was concentrated to only 370 g TSS kg^{-1} at 3.5 M stripper solution in 340 min of processing time. Similar effects have also been observed by Babu *et al.* [45].

Several researchers have observed that increasing the stripper concentration causes an increase in vapour pressure gradient across the membrane [46-51]. Hence, high concentration of sucrose solution was achieved in less time when the stripper solution was more concentrated thereby reducing the operation time. Although stripper concentration of 6 M resulted in a higher final sucrose concentration, due to higher tendency of $CaCl_2$ crystallization at this concentration and trade-off issue between the concentration and the cost of the stripper for economical operation, 5 M concentration of stripper was chosen for further experiments.

The relationship between water fluxes across the membrane as a function of operating time is also represented from experimental data in Figure 5. The observed average initial fluxes for 3.5, 5 and 6 M stripper solutions were 0.156, 0.200 and 0.228 L m^{-2} h^{-1} respectively, after lapse of 20 min, showing an increasing trend with the increase in stripper concentration. This is due to the increase in the driving force across membrane with increase of stripper concentration. The decrease in water flux across the membrane is due to the fact that concentration polarization occurs with the passage of operational time and with increase in feed concentration.

Concentration of fruit juices

Clarified apple juice concentration

Clarified apple juice obtained from local market was processed in membrane contactor against 5 M $CaCl_2$ solution. Feed-in-shell and feed-in-lumen flow configurations were used to concentrate juice at 30 °C. It can be observed from Figure 6 that clarified apple juice was concentrated from an initial value of 132 g TSS kg^{-1} to a final value of 470 g TSS kg^{-1} in total recycled mode in 320 min for feed-in-lumen flow

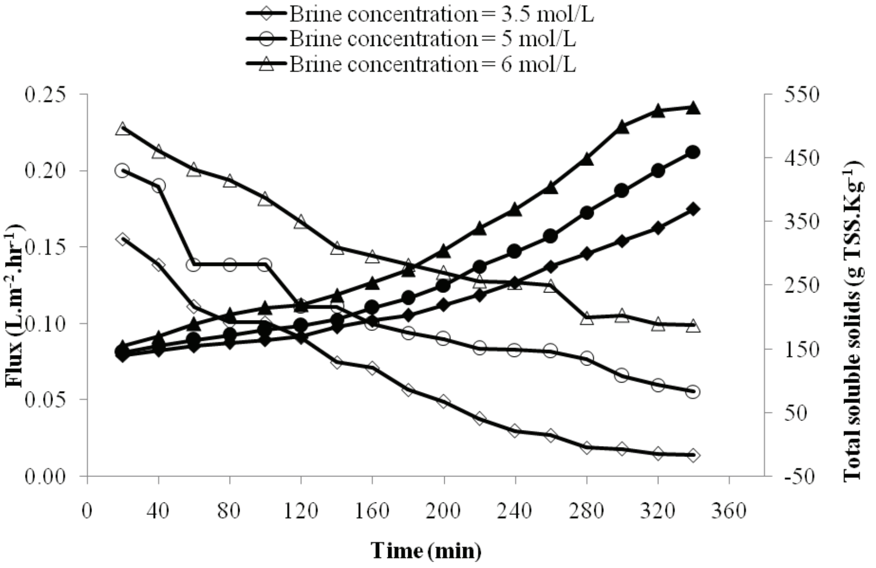

Figure 5. Effect of brine concentration on feed concentration for feed-in-fiber flow configuration (feed flow rate: 0.0044 m s^{-1}, feed temperature: 30 °C, initial feed concentration: 135 g TSS kg^{-1}. Empty markers show flux while filled markers show TSS).

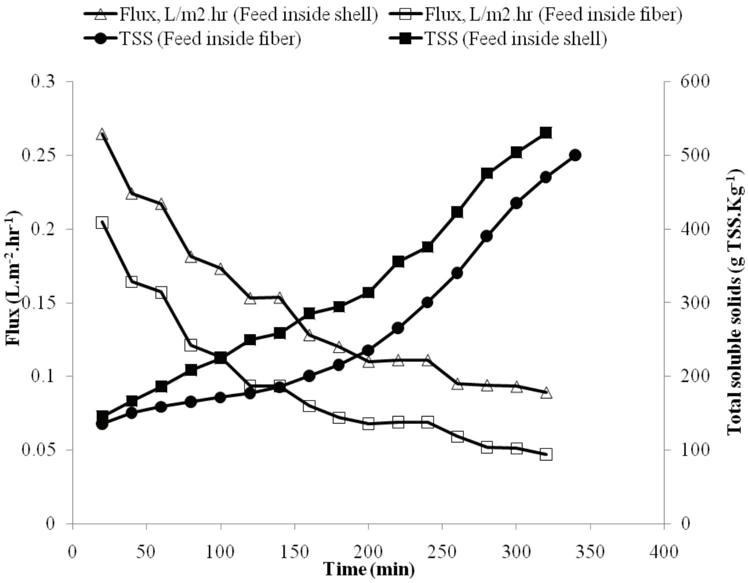

Figure 6. Effect of flow configuration on feed concentration and water flux for apple juice (feed flow rate: 0.0044 m.s^{-1}, brine conc.: 5 M, initial feed concentration: 132 g TSS kg^{-1}).

configuration. Similarly in 320 min, juice was concentrated to a value of 530 g TSS kg^{-1} in total recycled mode for feed-in-shell flow configuration. The concentration profile is similar to that for sucrose solution. It can also be observed that water flux dropped from 0.204 to 0.047 L m^{-2} h^{-1} for feed-in-lumen flow configuration and from 0.264 to 0.089 L m^{-2} h^{-1} for feed-in-shell flow configuration. However, there was a faster flux decline at the start of the experiment. After that, the flux showed a gradual sluggish decrease with the processing time. Aguiar *et al.* [9] conducted experiments to concentrate clarified apple juice up to 512 g TSS kg^{-1} through OD in flat sheet membrane. They observed water flux ranging from 0.01 to 1.55 L m^{-2} h^{-1}.

The qualitative tests as reported in Table 2 have shown that OD results in an increase in some of the characteristics (total soluble solids, pH, total acidity, ascorbic acid, density and total phenol) of apple juice after concentration in hollow fibre membrane contactor which can be attributed to the decrease in water content of final juice concentrate. On the other hand, thermal properties like thermal conductivity, specific heat capacity, latent heat and thermal diffusivity of the apple juice were found to decrease with increasing concentration of juice. Possible reason for this fall may be the lower water content in concentrated juice. The final achieved concentration was 510 g TSS kg^{-1}.

Clarified orange juice concentration

The clarified orange juice was also processed through OD. Orange juice was concentrated up to 500 g TSS kg^{-1} with an average flux of 0.081 L m^{-2} h^{-1} at a

Table 2. Physicochemical and thermal properties of fruit juices before and after osmotic distillation (values are mean±SD, n = 3)

Parameter	Orange juice		Apple juice	
	Clarified	Concentrate	Clarified	Concentrate
Total soluble solids, g TSS kg^{-1}	118±3.06	500±13.05	132±7.51	510±10.54
pH	3.74±0.08	3.86±0.11	4.08±0.08	4.16±0.14
Total acidity, mg citric acid/100 mL	16.96±0.47	70.2±1.70	5.376±0.37	19.8±0.65
Ascorbic acid, mg/100 mL	118±6.24	420±6.66	15±0.60	53.1±0.72
Density, g L^{-1}	1,045.7±45.00	1,235.5±21.67	1,060.59±31.13	1,256±41.00
C_t total phenol, mg/100 mL	64.39±1.46	250.3±5.46	52.68±2.60	187.5±3.61
Moisture content, %	88.1±1.99	49.2±2.95	85.61±1.64	48.8±1.28
Thermal conductivity, k, J s cm^{-1}	0.582±0.02	0.391±0.01	0.570±0.06	0.389±0.01
Specific heat capacity, c_p, kJ kg^{-1} C^{-1}	3.878±0.12	2.905±0.13	3.815±0.11	1.895±0.16
Latent heat, J kg^{-1}	29,513.5±301.56	16,482.0±260.58	28,679.35±297.81	16,348.0±271.92
Thermal diffusivity, $\alpha\times10^4$, m^2 s^{-1}	1.436	1.088	1.409	1.633

temperature of 30 °C, operating time of 360 min in total recycled mode, stripping solution concentration of 5 M and feed flow velocity of 0.0044 m s^{-1} as shown in Figure 7. In this case, the water flux ranged from 0.294 to 0.081 L m^{-2} h^{-1}. Comparing the water flux achieved for clarified orange juice with that for sucrose solution, it is found from Figures 2, 3, 6 and 7 that water flux is greater for clarified orange juice as compared to that for sucrose solution, under similar operating conditions. For example, flux achieved for clarified orange juice is 0.294 and 0.127 L m^{-2} h^{-1} after a lapse of 40 and 200 min, respectively. It is larger than that achieved for apple juice that is 0.200 and 0.090 L m^{-2} h^{-1} at the same operating conditions. High values of flux obtained for clarified orange juice are attributed to low total soluble solids as compared to apple juice. It can also be observed that orange juice concentrated more quickly as compared to apple juice. For example, orange juice concentrated to 470 g TSS kg^{-1} in 300 min as compared to apple juice concentrated to 435 g TSS kg^{-1} in same time.

Clarified orange and apple juices and their concentrates were also tested for the main physicochemical characteristics. These included the total soluble solids, pH, total acidity, ascorbic acid, total phenol, moisture content, thermal conductivity, specific heat, latent heat and thermal diffusivity. The quality results of juice samples before and after OD are listed in Table 2. Results are quoted as mean ± standard deviation (*SD*) of three independently determined values. As mentioned earlier, the qualitative tests as reported in Table 2 show an increase in some of the characteristics (total soluble solids, pH, total acidity, ascorbic acid, density and total phenol) of apple juice after concentration in hollow fibre membrane contactor which can be attributed to the decrease in water content of final juice concentrate. On the other hand, thermal properties like thermal conductivity, specific heat capacity, latent heat and thermal diffusivity of the orange juice were found to decrease with increasing concentration of juice. Lower water content in concentrated juice may also be the possible cause for this fall. Total acidity and ascorbic acid appeared to be lower in apple juice concentrate as compared to orange juice concentrate. Total acidity for apple and orange juice concentrates was 19.8 and 70.2 mg/100 mL of citric acid, respectively in 300 minutes of total recycled mode. Similarly, ascorbic acid for apple and orange juice concentrates was 53.1 and 420 mg/100 mL of ascorbic acid, respectively in 300 min of total recycled mode. Quality perseverance of fruit juice can also attributed to high molecular weights and low diffusivity through the membrane. pH of both orange and apple juice concentrates was 4±1.5, which is more suitable for conservation during storage [42].

CONCLUSIONS

The present study aimed to evaluate the performance of osmotic distillation (OD) process for the concentration of sucrose solution and apple and orange juices. OD was able to concentrate sucrose solution and clarified apple and orange juices up to 510 g TSS kg^{-1} at feed temperature of 30 °C, stripper

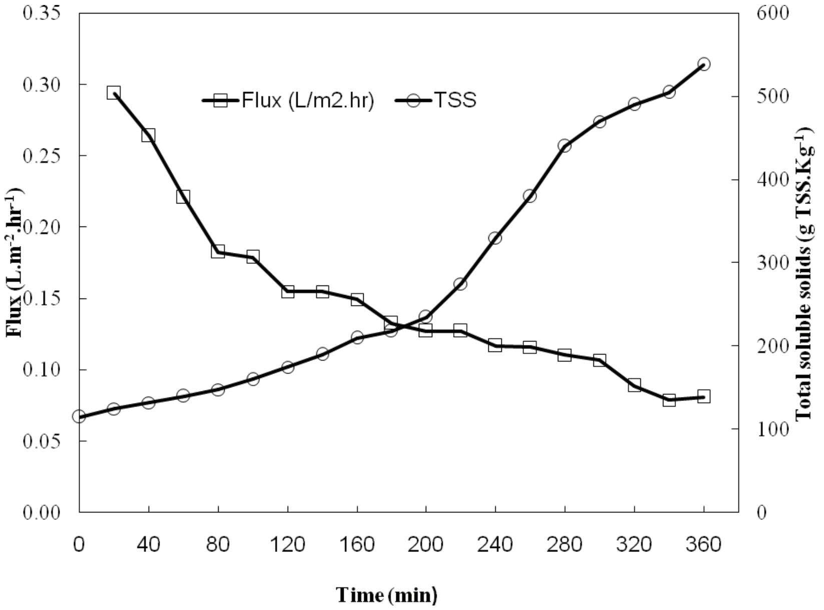

Figure 7. Variation of flux and °Brix with respect to time for orange juice (feed flow rate: 0.0044 m s^{-1}, brine conc.: 5 M, initial feed concentration: 118 g TSS kg^{-1}, configuration: feed-in-fiber).

concentration of 5 M and feed flow velocity of 0.0044 m s^{-1}. Feed-in-shell flow configuration showed relatively low flux decline and faster increase in feed concentration as compared to feed-in-lumen flow configuration, as there was low pore blockage in case of shell side feed flow. The results have shown that increase in temperature, stripper concentration, and flow rates tend to enhance the OD performance. Optimization of process parameters and increasing the membrane exposed area will improve OD flux, thereby reducing the operation time. The quality tests confirmed that OD can improve quality characteristics of fruit juice concentrates.

Nomenclature

OD	Osmotic distillation
TSS	Total soluble solids
Molarity (M)	mol solute/liter of solution

Acknowledgments

The authors acknowledge the financial sponsorship of Directorate of Science & Technology (DoST), Peshawar KPK under the Developmental Scheme titled “DF&TC”. The authors also acknowledge the technical support of Food Engineering Division, Nuclear Institute for Food and Agriculture (NIFA) Peshawar, the department Genie des Procedes Membranaire in Institut Euopeen des Membrane at French National Centre of Scientific Research (CNRS), Montpellier, France.

REFERENCES

[1] Pakistan bureau of statistics, Government of Pakistan, http://www.pbs.gov.pk/content/agriculture-statistics

[2] F. Vaillant, M. Cisse, M. Chaverri, A. M. Perez, M. Dornier, F. Dhuique, C. Mayer, Innovative Food Sci. Emerg. Technol. **6** (2005) 213-220

[3] E. Drioli, E. Fontananova, Chem. Eng. Res. Des. **82** (2004) 1557-1562

[4] E. Drioli, L. Giorno, Comprehensive Membrane Science and Engineering. Elsevier, Oxford, 2010, pp. 11-16

[5] S. Nene, G. Patil, K. Raghavarao, in Handbook of Membrane Separations: Chemical, Pharmaceutical, Food, and Biotechnological Applications, A.K. Pabby, S.S.H. Rizvi, A.M. Sastre, Eds., CRC Press, London, 2008, pp. 513--552

[6] F. Lipnizki, in Membrane Technology, K.V. Peinemann, S. Pereira, L. Giorno, Eds., Vol. 3: Membranes for Food Applications. Wiley-VCH, New York, 2010, pp. 1-20

[7] G. Daufin, J. P. Escudier, H. Carrere, S. Berot, L. Fillaudeau, M. Decloux, Food Bioprod. Process. **79** (2001) 89--102

[8] B. Jiao, A. Cassano, E. Drioli, J. Food Eng. **63** (2004) 303-324

[9] I.B. Aguiar, N.G.M. Miranda, F.S. Gomes, M.C.S. Santos, D.G.C. Freitas, R.V. Tonon, L.M.C. Cabral, Innovative Food Sci. Emerg. Technol. **16** (2012) 137-142

[10] A.P. Echavarría, V. Falguera, C. Torras, C. Berdun, J. Pagan, A. Ibarz, Food Sci. Technol-LEB **46** (2012) 189--195

[11] D.F. Jesus, M.F. Leite, L.F.M. Silva, R.D. Modesta, V.M. Matta, L.M.C. Cabral, J. Food Eng. **81** (2007) 287-291

[12] A. Kozak, S. Banvolgyi, I. Vincze, I. Kiss, E. Bekassy-Molnar, G. Vatai, Chem. Eng. Process. **47** (2008) 1171--1177

[13] A. Cassano, C. Conidi, R. Timpone, M.D. Avella, E. Drioli, J. Food Eng. **80** (2007) 914-921

[14] A. Versari, R. Ferrarini, G.B. Tornielli, G.P. Parpinello, C. Gostoli, E. Celotti, J. Food Sci. **69** (2004) E422-E427

[15] L.F. Sotoft, K.V. Christensen, R. Andresen, B. Norddahl, Chem. Eng. Process. **54** (2012) 12-21

[16] C. Hongvaleerat, L.M.C. Cabral, M. Dornier, M. Reynes, S. Ningsanond, J. Food Eng. **88** (2008) 548-552

[17] B. Koroknai, Z. Csanadi, L. Gubicza, K. Belafi-Bako, Desalination **228** (2008) 295-301

[18] K.W. Lawson, D.R. Lloyd, J. Membr. Sci. **124** (1997) 1-25

[19] K. Schneider, T.J.V. Gassel, Chemie Ingenieur Technik **56** (1984) 514-521

[20] M.S. El-Bourawi, Z. Ding, R. Ma, M. Khayet, J. Membr. Sci. **285** (2006) 4-29

[21] S. Banvolgyi, S. Horvath, E. Stefanovits-Benyai, E. Bekassy-Molnar, G. Vatai, Desalination **241** (2009) 281-287

[22] B.R. Babu, N.K. Rastogi, K.S.M.S. Raghavarao, J. Membr. Sci. **322** (2008) 146-153

[23] A. Cassano, M. Marchio, E. Drioli, Desalination **212** (2007) 15-27.

[24] C. Conidi, A. Cassano, E. Drioli, J. Membr. Sci. **375** (2011) 182-190

[25] M. Courel, M. Dornier, J.M. Herry, G. M. Rios, M. Reynes, J. Membr. Sci. (2000) 170-281

[26] V.D. Alves, I.M. Coelhoso, J. Food Eng. **74** (2006) 125--133

[27] J. Warczok, M. Gierszewska, W. Kujawski, C. Guell, Sep. Purif. Technol. **57** (2007) 425-429

[28] A. Gabelman, S. Hwang, J. Membr. Sci. **159** (1999) 61--106

[29] A.K. Pabby, A.M. Sastre, J. Membr. Sci. **430** (2013) 263--303

[30] N.C. Mat, Y. Lou, G.G. Lipscomb, Curr. Opin. Chem. Eng. **4** (2014) 18-24

[31] W. Kunz, A. Benabiles, R. Ben-Aım, J. Membr. Sci. **121** (1996) 25-36

[32] C. Zambra, J. Romero, L. Pino, A. Saavedra, J. Sanchez, J. Food Eng.**144** (2015) 58-65

[33] F. Destani, A. Cassano, A. Fazio, J. Vincken, B. Gabriele, J. Food Eng. **117** (2013) 263-271

[34] R. Bagger-Jorgensen, A.S. Meyer, M. Pinelo, C. Varming, G. Jonsson, Innovative Food Sci. Emerg. Technol. **12** (2011) 388-397

[35] W. Ali, W. Rehman, M. Younas, M. I. Ahmad, S. Gul, Pol. J. Chem. Technol. **17** (2015) 42-48

[36] S.M. Sedghi, D. Rodrigue, J. Brisson, M.C. Iliuta, J. Membr. Sci. **452** (2014) 332-353

[37] J. Ananthaswamy, G. Atkinson, Chem. Eng. Data **30** (1985) 120-126

[38] K. Belafi-Bako, B. Koroknai, J. Membr. Sci. **269** (2006) 187-193

[39] K. Arlington, in Official Methods of Analysis of the Association of Analytical Chemists, Helrich, USA: Association of Analytical Chemists AOAC, 1990, pp. 910-928

[40] S. George, P. Brat, P. Alter, M. J. Amiot, J. Agr. Food Chem. **53** (2005) 1370-1373

[41] F. Vaillant, E. Jeanton, M. Dornier, G.M. O'Brien, M. Reynes, M. Decloux, J. Food **Eng. 47** (2001) 195-202

[42] A. Cassano, C. Conidi, E. Drioli, J. Food Eng. **107** (2011) 366-373

[43] R.J. Thanedgunbaworn, M.H. Nguyen, J. Membr. Sci. **290** (2007) 105-113

[44] K.S. Deshmukh, M.M. Tajane, Int. J. Chem. Biological Eng. **3** (2010) 3-5

[45] B.R. Babu, N.K. Rastogi, K.S.M.S. Raghavarao, J. Membr. Sci. **272** (2006) 58-69

[46] K.S. Bahçeci, H.G. Akıllıoğlu, V. Gökmen, Innovative Food Sci. Emerg. Technol. **31** (2015) 131-138

[47] J. Kujawa, E.G. Burrieza, H.A. Arafat, M. Kurzawa, A. Wolan, W. Kujawski, Food Bioprocess Tech. **8** (2015) 2146-2158

[48] C. Zambra, J. Romero, L. Pino, A. Saavedra, J. Sanchez, J. Food Eng. **144** (2015) 58-65

[49] W. Kujawski, A. Sobolewska, K. Jarzynka, C. Güell, M. Ferrando, J. Warczok, J. Food Eng. **116** (2013) 801-808

[50] P. Onsekizoglu, J. Membr. Sci. **442** (2013) 264-271

[51] F. Destani, A. Cassano, A. Fazio, J.P. Vincken, B. Gabriele, J. Food Eng. **117** (2013) 263-271.

WAHEED UR REHMAN
WAHEED ZEB
AMIR MUHAMMAD
WAJID ALI
MOHAMMAD YOUNAS

Department of Chemical Engineering, University of Engineering & Technology, Peshawar, Pakistan

NAUČNI RAD

OSMOTSKA DESTILACIJA I EVALUACIJA KVALITETA ŠEĆERNOG RASTVORA I SOKOVA JABUKE I POMORANDŽE U KONTAKTORU SA MEMBRANOM U OBLIKU ŠUPLJIH VLAKANA

Rastvor saharoze i sokovi jabuke i pomorandže su koncentrisani procesom osmotske destilacije (OD) pomoću mini-modula kontaktora sa membranom u obliku šupljih vlakana Likui-CelTM. Proučavane su parakteristike prenosa mase vode iz napojnog u stripping rastvor. Varirani su parametri procesa kao što su: temperatura i protok napojnog rastvora i koncentracije striping rastvora ($CaCl_2$). Rastvor saharoze je koncentrisan od 135 do 510 gTSS/kg za 340 min korišćenjem konfiguracije toka napojnog rastvora kroz vlakna membrane pri početnom fluksu vode 0,250 L/(m^2 h) i temperaturi od 30 °C. Slično, ovaj rastvore je koncentrisan do 510 gTSS/kg za 200 min pomoću konfiguraciju toka napojnog rastvora kroz omotač pri početnom fluksu vode 0,505 L/(m^2 h) i temperaturi od 30 °C. Pri ukupnom vremenu reciklisanja od 340 min, bistri sokovi jabuke i pomorandže su koncentrisani do 500 gTSS/kg koristeći konfiguraciju toka napojnog rastvora kroz vlakna pri početnom fluksu vode 0,204 i 0,294 L/(m^2 h), redom. Utvrđeno je da su parametri kvaliteta voćnih sokova poboljšani nakon procesa osmotske destilacije. Zbog toga, proces ima dobar potencijal za primenu u prerađivačkoj industriji za koncentraciju voćnih sokova.

Ključne reči: osmotska destilacija, kontaktor sa membranom u obliku šupljih vlakana, sastvor saharoze, sok jabuke, sok pomorandže.

CI&CEQ
Chemical Industry & Chemical Engineering Quarterly

Available on line at
Association of the Chemical Engineers of Serbia *AChE*
www.ache.org.rs/CICEQ

Chem. Ind. Chem. Eng. Q. 23 (2) 229–236 (2017) CI&CEQ

MILENKO KOŠUTIĆ[1]
JELENA FILIPOVIĆ[1]
ZVONKO NJEŽIĆ[1]
VLADIMIR S. FILIPOVIĆ[2]
VLADIMIR M. FILIPOVIĆ[3]
BOJANA BLAGOJEVIĆ[4]

[1]Institute for Food Technology in Novi Sad, Serbia
[2]Faculty of Technology, University of Novi Sad, Novi Sad, Serbia
[3]Institute of Medicinal Plant Research "Dr Josif Pančić", Belgrade, Serbia
[4]Faculty of Sciences, University of Novi Sad, Novi Sad, Serbia

SCIENTIFIC PAPER

UDC 664.696:66

FLAKES PRODUCT SUPPLEMENTED WITH SUNFLOWER AND DRY RESIDUES OF WILD OREGANO

Article Highlights

- Sunflower and wild oregano was used to create flakes product with improved chemical properties
- Value added corn flakes has changed physical characteristics
- The sensory properties of flakes product with additional components were changed

Abstract

This paper investigates the effects of simultaneous addition of sunflower (3, 6 or 9 g/100 g of sample) and dry residue of wild oregano (0.5 or 1 of sample), on the physical texture and chemical properties of corn flakes to obtain new products with altered nutritional properties. The chemometric analysis pointed at the versatile beneficial contributions of sunflower in corn flakes enriched with dry residue of wild oregano enabling the optimization of corn flakes formula. The presented data point that addition of milled sunflower in investigated corn flakes products improved nutritive properties while addition of dry residue of wild oregano improved physical characteristics of corn flakes products. Regarding quality (sample CF11, score value of 0.59) maximum scores have been obtained with the addition of 6 g/100 g of sunflower and 1 g/100 g of dry residue of wild oregano per 100 g of sample for corn flakes formulation. Production of corn flakes with addition of wild oregano residues contributed to the food waste valorisation in the food industry.

Keywords: wild oregano, sunflower, corn flakes, physical-texture properties, chemical properties.

Cereals constitute the staple food of the human race. In accordance with the modern nutritionist opinions, cereal products, such as ready to eat breakfast cereals, flakes are the most common food in the daily diet, flakes and snacks. Heat treating of cereals is used for improving their hygiene, nutritional, physicochemical and other properties thus increaseing the nutrient value of some nutrients, improving sensory properties and providing the microbiological safety of the products [1-3]. Extrusion technology makes it possible to apply different sources of ingredients for the enrichment of cereal-based flakes or snack products. Extrusion is a relatively new technological process during which raw material is subjected to high temperature and high pressure during which raw material is also mechanically treated by shear forces (friction). Ingredients and formulation play an important role in developing the texture of the extruded product and ultimately the acceptability of the extruded product to the consumer [3-6]. Nowadays, consumers prefer to eat healthier foods in order to prevent diseases, but fast and easy to prepare. For this reason industry and researchers are involved in optimizing extruded technology to improve the physical and chemical properties, quality, taste, microbiology and functionality of food products such as flakes [2,3,7,8]. The industry, as a whole, faced the need to develop a positive message to consumers on flakes food with improved nutritional value. Among the ingredients that could be included in corn flakes formulation are milled sunflower and wild oregano, which may significantly

---

Correspondence: M. Košutić, Institute for Food Technology in Novi Sad Bulevar cara Lazara 1, Novi Sad, Serbia.
E-mail: milenko.kosutic@fins.uns.ac.rs
Paper received: 22 January, 2016
Paper revised: 13 April, 2016
Paper accepted: 18 May, 2016

https://doi.org/10.2298/CICEQ160413036K

improve its chemical and nutritive properties [3,7]. Sunflower seeds contain around 20% protein, high levels of potassium (710 mg/100 g) and magnesium (390 mg/100 g), respectively and are especially rich in polyunsaturated fatty acids (approximately 31.0%) in comparison to other oilseeds: soy (3.5%), peanut (13.1%), cottonseed (18.1%), flaxseed (22.4%), sesame seed (25.5%) and safflower seed (28.2%) respectively [9]. Wild oregano is a natural source of antioxidants and may be used as an ingredient in food products [10]. The residue after distillation of oil from wild oregano, which is one of the strongest natural antioxidants, certainly belongs to the group of food waste that can be used for developing of functional cereal-based products.

In this study, the effect of varying the proportion of sunflower (3, 6 and 9 g/100 g of sample) and wild oregano dry residue (0.5 and 1 g/100 g of sample) on the physical, texture and chemical properties of corn flakes was studied with the aim to obtain new products with good techological quality along with improved nutritional properties. The waste from distillation of wild oregano, as well as sunflower proteins, add new value to human nutrition.

MATERIAL AND METHODS

Materials

Corn flour used in this study was obtained from the mill Žitoprodukt d.o.o., Bačka Palanka, Serbia, produced in 2014 with following characteristics: moisture content of 13.3%, sugar, protein, cellulose, starch and lipid content (% dry matter basis) of: 0.87, 5.59, 0.98, 79.43 and 1.57, respectively [11]. Sunflower variety "Cepko" was produced in 2014 by "Vitastil" Erdevik, Serbia with following characteristics of samples, protein, starch, lipid and cellulose, content of 26.67, 6.73, 54.05 and 8.21 (% dry matter basis), respectively [11]. Sunflower was dehulled and milled in a Hammer mill 2300 rev/min with 2.5 mm sieve. Wild oregano (*Origanum minutiflorum* O. Schwarz & P.H. Davis) harvest 2013 was produced by Inan tarim ECODAB – Antalia, Turkey.

Dry residue of wild oregano

Dry residue of wild oregano was prepared as follows: distillation of wild oregano (*Origanum minutiflorum*) was carried out in the pilot plant distiller based on water vapor principle in the Institute of Medicinal Plant Research "Dr Josif Pančić" in Pančevo, Serbia. For distillation mini distiller was used. The distillation duration time was 2.5 h. Residue from distillation was dried with naturally air flow on to place protected from sun, milled at a facility Repro Trade d.o.o., Temerin, Serbia, on the hammer mill (2300 rpm, sieve hole diameter 1.5 mm) and prepared for further research.

Methods

Extrusion of flakes

The flakes were obtained by extrusion in a twin-screw extruder (Yuninan Daily Extrusion, Republic of China) in industrial conditions on Repro Trade d.o.o. Extrusion parameters were as a follows: length of monolit screws 140 cm, screw speed of 180 rpm, temperature profile: 114/125/131 °C. A triple die 6 mm diameter aperture was used and a knife rotating at 1300 rpm cut the emerging product into pelets about 5 mm in length. The moisture of raw material mixture prior extrusion was adjusted to 22%. Corn flour, was replaced by milled sunflower in the quantity 3, 6 or 9 g/100 g of sample, and dry residue of wild oregano added in the quantity of 0, 0.5 or 1 g/100 g of sample based on corn flour and milled sunflower. Table 1 describes corn formulation enriched with different quantities of milled sunflower and dry residue of wild oregano. Obtained extrudates were dried in drying unit at temperature of 84 °C, cooled for 30 min at controlled temperature 25±1 °C and stored at 4 °C in sealed plastic bags until required for analyses.

Texture analysis

Texture properties of flakes were measured by Texture Analyzer TA.HD plus (Stable Micro System, UK) equipped with a 50-kg load cell. Hardness and work of compression of flakes product were measured using a 45 mm cylinder probe (P/45R) by compressing 10 individual flakes at one turn. The maximum force and work of compression correlate to the hardness of the sample. The following settings were used: pre-test speed: 2 mm s^{-1}; test-speed: 2 mm s^{-1}; post-test speed: 10 mm s^{-1}; distance: 2.5 mm; trigger force: 10 g. The tests were performed on 5 replicates per batch.

Flakes color

Flakes color attributes were measured instrumentally using a Chroma meter (CR-400, Konica, Minolta, Tokyo, Japan) tri-stimulus colourimeter. The results were expressed in terms of L^* - brightness (from 0 (black) to 100 (white)), a^* - greenness/redness (from $-a^*$ (green) to $+a^*$ (red)), b^* - blueness/yellowness (from $-b^*$ (blue) to $+b^*$ (yellow)), W - whiteness, C - differences in coloration, h - differences in tone, DW - dominant wavelength as per CIELab system. The measurements were observed under constant lighting conditions, at 28 °C, using a white control (L^* = 98.76, a^* = -0.04, b^* = 2.01) [8].

Table 1. Flakes formulation with different quantities of milled sunflower and dry wild residue oregano

Sample	Quantity of corn g/100 g flour	Quantity of sunflower g/100 g flour	Quantity of dry wild oregano residue g/100 g sample	Quantity of salt g/100 g sample
CF0	100	0	0	0
CF1	100	0	0	2
CF2	97	3	0	2
CF3	94	6	0	2
CF4	91	9	0	2
CF5	100	0	0.5	2
CF6	97	3	0.5	2
CF7	94	6	0.5	2
CF8	91	9	0.5	2
CF9	100	0	1	2
CF10	97	3	1	2
CF11	94	6	1	2
CF12	91	9	1	2

Physical characteristics

Bulk density (*BD*) was measured by a bulk density tester (Tonindustrie, West und Goslar, Germany). It was determined by loose pouring the flakes samples into a 1000 ml measuring-cylinder. The inner diameter of the steel cylinder was 53 mm. The flakes samples were subsequently transferred to a funnel with a valve mounted in the bottom. The measuring cylinder was placed underneath at the center and the valve opened. Filling of the cylinder continued until a pile of flakes had developed on the top. Then excess flakes were gently removed by pulling a scrape one time over the edge of the cylinder. The sample was weighed on an electronic scale, and the bulk density was recorded (g ml^{-3}). The results are presented as means of six measurements.

Expansion ratio (*ER*) was determined according to Kaludjerski and Filipović [12], where expansion ratio was calculated as:

ER = volume flakes (ml)/crude flakes prior flaking volume (ml)

Basic chemical analyses

Basic chemical analyses (protein, starch, lipid, sugar and moisture) of flakes were determined according to the official methods of AOAC [11]. Measurements of all analysed responses are done in triplicates.

Statistical analyses

Descriptive statistical analyses for all obtained results were expressed as the mean ± standard deviation (*SD*). Post-hoc Tukey's HSD test was evaluated for comparison of physical and textural attributes with color attributes and chemical composition for different formulations of corn flakes.

Principal component analysis (PCA), used as the pattern recognition technique, was applied within assay descriptors to characterize and differentiate various analyzed samples. The PCA analyses of the obtained results were performed using StatSoft Statistica® 10.0 (StatSoft Inc., 2010, USA) software.

Score analysis

Score analysis uses min-max normalization of corn flakes quality parameter responses and transfer them from their unit system in new dimensionless system which allows further mathematical calculation of different types of responses [13]. The maximum value of normalized score presents the optimum value of all analyzed responses [14] and indicates the optimum quantity of added sunflower flour and wild oregano residue in corn flakes formulation.

RESULTS AND DISCUSSION

Physical and texture characteristics of flakes product

The bulk density of flakes product is important in relation to their packaging requirement and the ability to float or sink when poured into water or milk [1]. Effect of sunflower and dry residue of wild oregano addition on bulk density is shown in Table 2. The bulk density of flakes varies from 150 to 323 g dm^{-3}. With addition of sunflower (3, 6 and 9 g/100 g sample) bulk density of extruded product statistically significantly increased and addition of dry residue of wild oregano (0.5 and 1 g/100 g sample) statistically significantly decreased bulk density of extruded product. With addition of sunflower (3, 6 and 9 g/100 g sample)

Table 2. Characterisation of corn flakes with sunflower flour and wild oregano; the results are presented as mean ± SD; different letter within the same column indicates significant differences ($p < 0.05$), according to Tukey's test. Number of repetitions: $n = 3$. Experimental cases (samples) are detail explained in Table 1

Sample	Physical and texture attributes				Color attributes							Chemical composition			
	BD g ml^{-1}	*ER* ml g^{-1}	*H* kg	*WOC* kg s^{-1}	*L**	*a**	*b**	*W*	*C*	*h*	*DW*	*P*	*Lip*	*St*	*S*
CF0	176.30 ±1.86^{a}	7.86 ±1.77^{ab}	26.46 ±4.59^{a}	10.62 ±2.19^{ab}	85.018 ±0.88^{a}	-0.99 ±0.26^{a}	36.36 ±1.69^{ab}	60.66 ±1.87^{abcd}	36.38 ±1.69^{ade}	91.57 ±0.46^{a}	575.69 ±0.14^{a}	5.40 ±0.09^{a}	2.15 ±0.02^{a}	78.76 ±0.05^{a}	0.56 ±0.01^{a}
CF1	215.00 ±3.60^{b}	6.46 ±1.89^{ab}	14.35 ±2.68^{ab}	8.27 ±1.17^{abc}	85.50 ±0.85^{a}	-1.06 ±0.11^{a}	34.06 ±2.19^{ac}	62.97 ±2.34^{bcd}	34.08 ±2.18^{ab}	91.80 ±0.30^{a}	575.62 ±0.09^{abc}	5.48 ±0.20^{a}	2.0 ±0.02^{b}	78.72 ±0.03^{a}	0.69 ±0.02^{b}
CF2	227.51 ±2.14^{c}	6.21 ±0.00^{ab}	15.63 ±5.8^{ab}	8.86 ±1.18^{abc}	82.23 ±0.12^{b}	-1.17 ±0.11^{ab}	38.54 ±0.95^{b}	58.86 ±1.60^{bc}	38.55 ±0.95^{d}	91.74 ±0.14^{a}	575.62 ±0.05^{abc}	5.92 ±0.03^{b}	3.85 ±0.03^{c}	78.52 ±0.09^{b}	0.69 ±0.03^{b}
CF3	242.34 ±6.06^{d}	6.00 ±0.00^{ab}	17.22 ±7.99^{ab}	10.10 ±2.30^{abc}	81.80 ±0.43^{b}	-1.26 ±0.13^{ab}	36.88 ±1.58^{ab}	58.61 ±2.27^{abd}	36.90 ±1.58^{ad}	91.98 ±0.28^{a}	575.55 ±0.09^{abc}	6.31 ±0.09^{c}	5.30 ±0.06^{d}	78.07 ±0.08^{c}	0.58 ±0.01^{a}
CF4	323.41 ±3.00^{e}	4.20 ±0.00^{a}	20.64 ±7.85^{ab}	11.40 ±3.27^{b}	79.26 ±0.87^{c}	-1.52 ±0.14^{b}	35.78 ±2.14^{ab}	57.55 ±0.484^{a}	35.82 ±2.13^{acde}	92.45 ±0.37^{a}	575.39 ±0.11^{bc}	6.42 ±0.23^{c}	6.72 ±0.02^{e}	77.82 ±0.09^{d}	0.62 ±0.01^{a}
CF5	161.60 ±1.60^{f}	8.60 ±0.00^{b}	15.51 ±1.51^{ab}	7.79 ±1.91^{abc}	83.15 ±0.45^{ab}	-1.12 ±0.21^{ab}	30.95 ±0.80^{cd}	64.74 ±0.83d^{e}	30.97 ±0.80^{b}	92.08 ±0.39^{a}	575.54 ±0.12^{abc}	5.27 ±0.02^{a}	2.06 ±0.03^{ab}	78.36 ±0.05^{e}	0.68 ±0.01^{b}
CF6	194.67 ±0.46^{g}	7.01 ±1.31^{ab}	16.42 ±5.36^{ab}	8.42 ±1.97^{abc}	82.20 ±0.47^{b}	-1.12 ±0.12^{ab}	33.05 ±1.29^{ac}	62.44 ±1.33^{bcd}	33.07 ±1.28^{abf}	91.95 ±0.27^{a}	575.57 ±0.08^{abc}	5.35 ±0.09^{a}	3.72 ±0.02^{f}	78.30 ±0.06^{e}	0.74 ±0.03^{b}
CF7	222.41 ±0.29^{ch}	5.82 ±1.89^{ab}	18.53 ±4.14^{ab}	9.17 ±2.57^{abc}	79.05 ±0.75^{c}	-1.37 ±0.20^{ab}	33.52 ±0.57^{ac}	60.45 ±0.76^{abc}	33.55 ±0.57^{ab}	92.34 ±0.70^{a}	575.44 ±0.12^{abc}	5.72 ±0.22^{ab}	5.8 ±0.06^{g}	77.80 ±0.06^{d}	0.86 ±0.00^{c}
CF8	302.41 ±1.27^{i}	4.43 ±0.00^{a}	23.76 ±2.70^{a}	12.17 ±1.01^{b}	78.13 ±0.28^{c}	-1.44 ±0.05^{ab}	32.40 ±0.15^{ac}	60.88 ±0.18^{abcd}	32.43 ±0.15^{be}	92.55 ±0.10^{a}	575.37 ±0.03^{c}	6.19 ±0.05^{bc}	6.81 ±0.01^{e}	77.65 ±0.06^{f}	0.85 ±0.01^{c}
CF9	150.20 ±1.21^{j}	9.36 ±1.77^{b}	8.88 ±3.95^{b}	4.94 ±0.40^{c}	82.51 ±0.64^{b}	-1.05 ±0.16^{a}	27.26 ±1.00^{d}	67.59 ±1.10^{e}	27.28 ±1.00^{f}	92.20 ±0.34^{a}	575.52 ±0.10^{abc}	5.71 ±0.05^{ab}	2.10 ±0.03^{a}	78.38 ±0.05^{e}	0.87 ±0.01^{c}
CF10	197.51 ±0.52^{gk}	7.10 ±1.29^{ab}	9.62 ±1.79^{b}	5.35 ±1.69^{ac}	80.74 ±0.35^{bc}	-1.00 ±0.04^{a}	29.68 ±1.28^{cd}	64.60 ±1.23^{de}	29.70 ±1.28^{bf}	91.93 ±0.10^{a}	575.59 ±0.03^{abc}	5.93 ±0.02^{b}	3.90 ±0.01^{c}	78.28 ±0.03^{e}	0.84 ±0.00^{c}
CF11	213.17 ±0.17^{bl}	6.36 ±1.23^{ab}	14.15 ±2.17^{ab}	7.00 ±1.09^{abc}	77.85 ±0.59^{c}	-1.00 ±0.16^{a}	32.44 ±0.69^{ac}	60.70 ±0.31^{abcd}	32.46 ±0.40^{ab}	91.76 ±0.27^{a}	575.63 ±0.08^{abc}	6.24 ±0.02^{bc}	5.25 ±0.01^{d}	77.78 ±0.02^{d}	0.83 ±0.02^{c}
CF12	253.71 ±2.60^{d}	5.86 ±1.47^{ab}	28.34±3 .74^{d}	17.68 ±1.00^{d}	74.25 ±0.88^{d}	-0.96 ±0.13^{a}	32.04 ±1.60^{c}	59.44 ±1.42^{abc}	32.06 ±1.60^{bc}	91.72 ±0.28^{a}	575.64 ±0.08^{abc}	7.21 ±0.01^{d}	6.78 ±0.04^{e}	77.76 ±0.05^{d}	0.84 ±0.03^{c}

expansion ratio of extruded product statistically significantly decreased, the addition of wild oregano residue (0.5 and 1 g/100 g sample) statistically significantly increased expansion ratio of flakes product, probably due to the interaction of wild oregano with starch. Besides that, the cellulose component can rupture cell walls and prevent air bubbles from expanding to their maximum potential [16]. The results of bulk density are inversely proportional to the results for the expansion ratio (Table 2), *i.e.*, flakes products with added sunflower had higher bulk density statistically significantly lower expansion ratio proportionally to sunflower share [16,17] also confirmed that sunflower share in the corn flour for flakes product decreased expansion of products.

One of the most important quality parameters of flakes is the time during which, when soaked in milk, their texture is still acceptable for consumers. The textural characteristics hardness and work of compression of flakes product with sunflower and wild oregano residue addition are presented in Table 2. The highest value for hardness (28.34 g) was observed for sample CF12, while the lowest hardness value was noticed for sample CF9 (8.88 g). Statistically significant differences in hardness were not observed between following samples CF0, CF1, CF2, CF3, CF4, CF5, CF6, CF7, CF8, CF11 and CF12, while other samples (CF9 and CF10) were statistically different. Addition of sunflower results in increasing hardness. These results are in accordance with data reported by Jozinović *et al.* [17], who concluded that texture properties are highly influenced by expansion ratio, *i.e.*, extrudates with higher expansion ratio had lower hardness and work of compression. Sunflower also influenced mechanical and microstructural properties of flakes product obtained from high amylose corn starch and sunflower protein concentrate and hardness increased as also observed by Zhu *et al.*

[18]. Share of wild oregano contributes to increased hardness (CF5, CF6, CF7, C8 and CF12) where presence of fibers in oregano caused the increase of product hardness probably due to their cell wall thickness as stated by Yanniotis *et al.* [19], Lazou and Krokida [20] and Nascimento *et al.* [21]. Addition of sunflower (3, 6 or 9 g/100 g sample) contributes to a higher value of work of compression as compared to the flakes without sunflower. Addition of wild oregano (0.5 or 1 g/100 g sample) caused continual of the work of compression decreased (CF1, CF2, CF3, CF5, CF6, CF7, C9, CF10 and CF11) contrary to samples CF4, CF8 and CF12 with maximum share of sunflower probably due to corn proteins and starch complexing with sunflower lipids.

The color characteristics of corn flakes are important sensory characteristics of a product. These attributes are significant in creating sensory expectations of consumers, which could affect their perception and acceptance of the product [8]. Different values in various color coordinates were observed for different flakes formulations (Table 2). Statistically significant differences between all flakes samples were found for L^* coordinate (brightness) due to sunflower and dry residue of wild oregano content which contributed to the decrease of the brightness value L^*. The highest L^* (85.50) was observed for sample CF1, while the lowest L^* value (74.25) was noticed for sample CF12, with the greatest shares of sunflower and wild oregano. Content of sunflower and wild oregano contributed to decrease of brightness L^*, which led to the formation of darker flakes product. Similar results were observed by Jozinović *et al.* [17]. The share of green colour (a^*) coordinate was found to have no statistically significant difference among all samples. Statistically significant differences in yellow color (b^*) were observed in samples with increasing share of sunflower thus positively contributing to favorable yellow color of flakes product. The addition of wild oregano influenced statistically significant ($p < < 0.05$) decrease of yellow (b^*). Additon of sunflower influenced statistically significant decrease of colour attribute of whiteness (W), while addition of wild oregano in flakes samples caused statistically insignificant increase of whiteness (W). The highest the differences in coloration C (38.55) were measured in sample CF2 and the lowest C (27.28) for sample CF9. Share of sunflower contributed to statistically insignificant increased coloration (C) but share of wild oregano addition contributed to statistically significant decreased coloration (C) leading to a more intensive coloration of flakes product. The difference in tone (h) was statistically insignificantly different for most of the samples indicating that there were no influences of addition of sunflower flour and dry residue of wild oregano on difference in tone. The maximum value of h was observed in sample CF8 (92.55) and the lowest value of h (91.57) was found in sample CF0. Values of dominant wavelength ranged between 575.37 (sample CF8) and 575.69 (sample CF0), thus indicated that sunflower and wild oregano addition were not statistically significantly affecting the dominant wavelength. Influence of various raw materials on the color of extruded products was attributed to the diverse reactions that basically include the Maillard reaction [3].

Flakes products are complex multi-component systems consisting of biomacromolecules such as proteins, carbohydrates and lipids. Carbohydrates (78.07-80.19%) dominated in corn flakes (Table 2). There were great possibilities for the improvement of functional characteristics of flakes products [8,22]. The addition of sunflower flour to flakes product improved proteins and nutritive properties (Table 2).

Investigated corn flakes were characterized by low crude protein content in the sample without sunflower (CF0, CF1, CF5 and CF9). The minimum (5.27±0.02% d.m.) was observed in CF5. The addition of sunflower statistically significantly contributed to the increase of protein in corn flakes because a part of the corn flour was replaced with constituent richer in proteins. Statistically significant differences in lipid content were observed for almost all flakes samples, Table 2. As expected, the maximum of lipid content (6.78± 0.04% d.m.) was obtained for CF12 (maximum sunflower and maximum of wild oregano addition), while the minimum of 2.15±0.02% was observed in CF0. Lipid content in corn flakes depended only on the content of sunflower, since wild oregano was a non-lipid constituent. Starch content reached maximum value (78.76% d.m.) in CF0 and, as expected, the minimum of starch 77.65% d.m. was observed in CF8, where addition of sunflower flour statistically significantly decreased starch content in samples of flakes product. Statistically significant differences in sugar content were not observed between following group of samples: group I (CF0, CF3 and CF4), group II (CF1, CF2, CF5 and CF6), group III (CF7, CFCF8, CF9, CF10, CF11 and CF12) while other samples were statistically different.

Score calculation

Score analysis quantifies different responses of corn flakes quality parameters in dimensionless values that represent score values which were comparable between samples of corn flakes with different formulations. In that way, score values allow the possibility of comparing total quality of the analyzed samples, and optimization of its formulation.

Figure 1 shows score values of corn flake samples with different quantity of added sunflower flour and wild oregano residue, where it can be seen that increase of quantity of dry wild oregano residue increased total quality of the corn flake samples while addition of medium quantities of sunflower flour resulted in optimum total quality parameters. Corn flakes sample CF11 achieved the maximum score value of 0.59, indicating on optimal combination of added quantities of sunflower flour and dry wild oregano residue.

PCA

The PCA allows a considerable reduction in the number of variables and the detection of structure in the relationship between measuring parameters and different samples of corn flakes formulations that give complementary information [23]. The full auto scaled data matrix consisting of corn flakes samples with 0, 3, 6 and 9 g/100g of added sunflower flour and 0, 0.5 and 1 g/100g of added wild oregano residue was submitted to PCA. For visualizing the data trends and for the discriminating efficiency of the used descriptors a scatter plot of samples using the first two principal components (PCAs) from PCA of the data matrix was obtained (Figure 2).

As can be seen, there was a neat separation of the 12 samples of corn flakes formulation, according to physical and texture attributes, color attributes and chemical composition Samples were grouped according to quantity of added sunflower flour (samples are connected with tin line) and quantity od added wild oregano residue (samples were encircled with tin line border).

Samples located on the bottom part of the graphic had added dry wild oregano residue in their formulations, while samples located on the right half of the graphic had added increased quantity of sunflower flour (6 and 9%). Samples that were located in lower right quadrant of the graphic (CF11, CF7, CF12 and CF8) were characterized by increased protein and lipid contents and increased antioxidant activity. Corn flakes samples located in upper right corner, which do not have added dry wild oregano residue while having added increased quantity of sunflower flour in formulations (CF3 and CF4) had increased texture parameters of hardness, work of compression and bulk density. Samples located in upper left quadrant of the graphic (CF0, CF1 and CF2, which had no added dry wild oregano residue and 0 or 3% of added quantity of sunflower flour in their formulations) were characterized with increased starch content, dominant wavelength and brightness. Corn flakes samples with added quantity of dry wild oregano residue (0.5 and g/100 g) and 0 and 3 of added quantity of sunflower flour (CF5, CF6, CF9 and CF10), which were located in lower left quadrant of the graphic were characterized by increased expansion ratio, whiteness and share of green color.

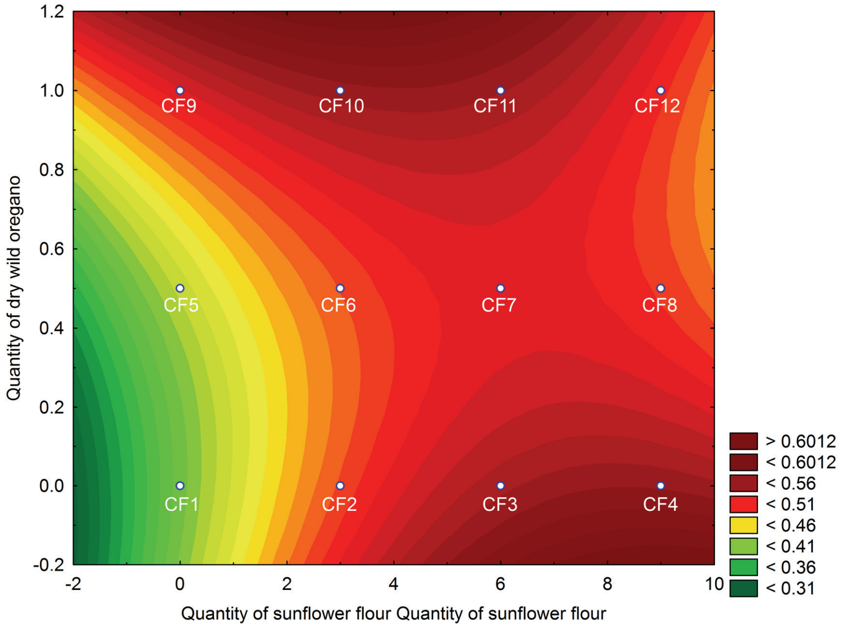

Figure 1. Score values contour plots of corn flakes samples with different quantities of added dry wild oregano residue and sunflower flour.

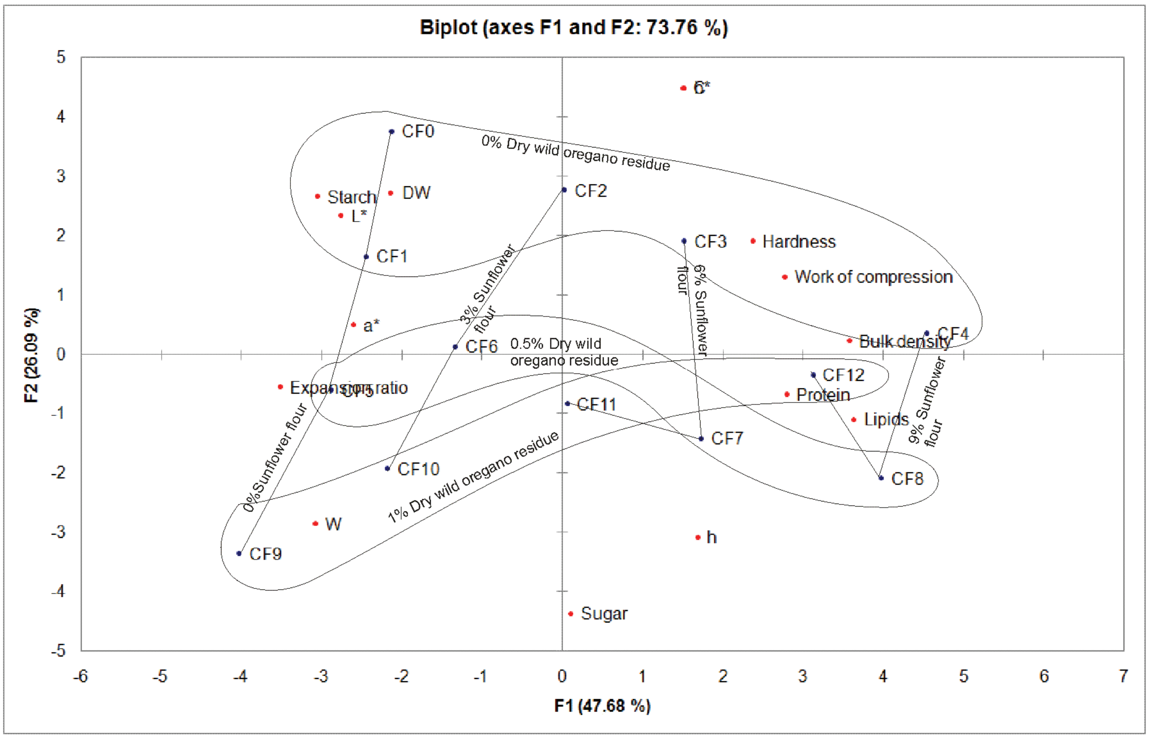

Figure 2. Biplot diagram of corn flakes samples regarding dry wild oregano residue and sunflower flour content.

Quality results showed that the first two principal components account for 73.76% of the total variance and could be considered sufficient for data representation. Concerning physical and texture attributes, color attributes and chemical composition, bulk density (with 12.25% contribution based on correlation), expansion ratio (11.79%) and lipid content (12.61%) mostly contributed to the first factor calculation, while share of yellow (19.29%) and difference in coloration (19.26%) contributed more to the second factor coordinate calculation.

CONCLUSIONS

Based on data resulting from the investigations it can be concluded:

1. Addition of sunflower adversely influenced corn flakes physical characteristics and addition of dry residue wild oregano positively influenced physical characteristics.
2. Sunflower and dry residue of wild oregano have affected corn flakes texture by increasing hardness and work of compression.
3. Addition of sunflower and dry residue wild oregano significantly changed the color of flakes product.
4. Addition of sunflower insignificantly increased the content of protein and lipids.
5. Application of PCA, as the multivariate method of analysis, has provided better visualization in differentiation of the samples. Properties of physical, texture and chemical attributes are the dominant variable in the first principle component, while the color attributes were the most dominant variable in the second principle component, thus stressing the role of share of sunflower and dry residue of oregano.
6. Score analysis was used to calculate total quality of tested samples and to point at optimal formulation of corn flakes as a functional food. Corn flakes sample CF11 achieved maximum score value of 0.59 indicating on optimal combination of added quantities of sunflower flour and dry residue of wild oregano.

Acknowledgements

These results are part of the project supported by the Ministry of Education, Science and Technological Development of the Republic of Serbia, III 46005 and TR 31027.

REFERENCES

[1] B. Sumithra, S. Bhattacharya, J. Food. Eng. **88** (2008) 419-428

[2] S. Kannadhason, K. Muthukumarappan, KA. Rosentrater, J. Aquac. Feed Sci. Nutr. **1** (2009) 6-21

[3] S. Filipović, Š. Kormanjoš, M. Sakač, J. Filipović, Đ. Psodorov, Đ. Okanović, in Prceedings of 2nd Workshop Feed

to food FP7 REGPOT-3, Novi Sad, Serbia, 2010, pp. 97--116

[4] N.Md. Nor, A. Carr, A. Hardacer, C. Bernnan, JFS **2** (2013) 160-169

[5] R.P. Singh, D.R. Heldman, Extrusion Processes for Foods. Introduction to Food Engineering, Academic press, Cambridge, 2014, pp. 743-766

[6] A.R. Shaviklo, M. Azaribeh, Y. Moradi, P. Zangeneh, LWT **63** (2015) 307-314

[7] U. Gawlik-Dziki, M. S´Wieca, D. Dziki J. Agr. Food Chem. **60** (2012) 4603-4612

[8] J. Filipović, L. Pezo, V. Filipović, J. Brkljača, J. Krulj, LWT **63** (2015) 43-51

[9] B. Škrbić, B. Filipčev, Food. Chem. **108** (2008) 119-129

[10] F. Shahidi, A. Chandrasekara, Handbook of Antioxidants for Food Preservation, Woodhead publishing, Cambridge, 2015, pp. 413-432

[11] AOAC, Official methods of analysis (17th ed.), Method No. 930.25, Association of Official Analytical Chemists, Arlington, VA, 1990

[12] G. Kaluđerski, N. Filipović, Methods for the investigation of cereals, flour and final product quality, Faculty of Technology, Novi Sad, 1998, pp. 291-303

[13] T. Jayalakshmi, A. Santhakumaran, IJCTE **3** (2011) 89-93

[14] V. Filipovic, B. Loncar, M. Nicetin, V. Kneževic, I. Filipovic, L. Pezo, J. Food Process Eng. **37** (2014) 533-542

[15] H.W. Chiu, J.C. Peng, S.J. Tsai, J.R. Tsay, W.B. Lui, Food Bioprocess Technol. **6** (2013) 1494-1504

[16] A.A. Anton, R. Gary Fulcher, S.D. Arntfield, Food. Chem. **113** (2009) 989-996

[17] A. Jozinović, D. Šubarić, D. Ačkar, J. Babić, B. Miličevic, J. Food Eng. **172** (2016) 31-37

[18] L.J. Zhu, R. Shukri, N.J. De Mesa-Stonestreet, S. Alavi, H. Dogan, Y.C. Shi, J. Food Eng. **100** (2010) 232-238

[19] S. Yanniotis, A. Petraki, E. Soumpasi, J. Food Eng. **80** (2007) 594-599

[20] A. Lazou, M. Krokida, J. Food Eng. **100** (2010) 392-408

[21] E.M. Nascimento, D.G.C. Do, C.W.P. Carvalho, C.Y. Takeiti, D.D.G.C. Freitas, J.L.R. Ascheri, Food Res. Int. **45** (2012) 434-443

[22] C. Bruneel, B. Pareyt, K. Brijs, J.A. Delcour, Food Chem. **120** (2010) 371-378

[23] L. Fongaro, K. Kvaal, Food Res. Int. **51** (2013) 693-705.

FIZIČKO-HEMIJSKE KARAKTERISTIKE KORN FLEJKSA OBOGAĆENOG KONZUMNIM SUNCOKRETOM I DIVLJIM ORIGANOM

MILENKO KOŠUTIĆ[1]
JELENA FILIPOVIĆ[1]
ZVONKO NJEŽIĆ[1]
VLADIMIR FILIPOVIĆ[2]
VLADIMIR FILIPOVIĆ[3]
BOJANA BLAGOJEVIĆ[4]

[1]Naučni institut za prehrambene tehnologije u Novom Sadu, Univerzitet u Novom Sadu, Bulevar cara Lazara 1, 21000 Novi Sad, Srbija
[2]Tehnološki fakultet, Univerzitet u Novom Sadu, Bulevar cara Lazara 1, 21000 Novi Sad, Srbija
[3] Institut za proučavanje lekovitog bilja Dr Josif Pančić, Tadeuša Košćuška 1, 11000 Beograd, Srbija
[4]Prirodno matematički fakultet, Univerzitet u Novom Sadu, Trg Dositeja Obradovića 3, 21000 Novi Sad, Srbija

NAUČNI RAD

U ovom radu je ispitan uticaj dodatka konzumnog suncokreta (3, 6 ili 9 g/100 g po uzorku) i suvog ostatka divljeg origana (0.5 ili 1 g/100 g po uzorku), u skladu sa primenjenim eksperimentalnim planom 3x4, na fizičke, teksturalne i hemijske osobine korn fleksa za dobijanje novog proizvoda poboljšanih nutritivnih karakteristika. Metod odzivne površine je odabran za procenu uticaja konzumnog suncokreta i divljeg origana na kvalitet korn fleksa. Hemometrijska analiza je ukazala na doprinos konzumnog suncokreta i suvog ostatka divljeg origana na optimizaciju sirovinskog sastava fleks proizvoda. Prikazani podaci pokazuju da dodavanje mlevenog suncokreta imalo uticaj na poboljšanje nutritivnih svojstava dok je dodatak suvog ostatka divljeg origana uticao na poboljšanje fizičkih karakteristika korn fleksa. Uzorak KF 11 ima maksimalnu vrednost ocene 0.59 što ukazuje na optimalnu kombinaciju dodatih količina suncokretovog brašna (6 g / 100g uzorka) i suvog ostatka divljeg origana (1g / 100g uzorka). Proizvodnja korn fleksa sa dodatkom suvog ostatka divljeg origana doprinosi valorizaciji sporednih proizvoda u prehrambenoj industriji.

Ključne reči: divlji origano, suncokret, korn flejks, fizičko-teksturalne karakteristike, hemijski sastav.

CI&CEQ
Chemical Industry & Chemical Engineering Quarterly

Available on line at
Association of the Chemical Engineers of Serbia *AChE*
www.ache.org.rs/CICEQ

Chem. Ind. Chem. Eng. Q. 23 (2) 237–244 (2017) CI&CEQ

THE REDUCTION OF OIL POLLUTANTS OF PETROLEUM PRODUCTS STORAGE-TANKS SLUDGE USING LOW-COST ADSORBENTS

ZAHRA BEAGOM MOKHTARI-HOSSEINI[1]
RAZIEH HOSSEINABADI[2]
ASHRAFALSADAT HATAMIAN ZARMI[3]

[1]Chemical Engineering Department, Faculty of Petroleum and Petrochemical Engineering, Hakim Sabzevari University, Sabzevar, Iran
[2]Faculty of Engineering, Islamic Azad University Shahrood Branch, Shahrood, Iran
[3]Faculty of New Sciences and Technology, University of Tehran, North Karegar Ave., Tehran, Iran

SCIENTIFIC PAPER

UDC 502/504:665:6656:661.183

Article Highlights

- The oil pollutants of sludge were reduced using low-cost adsorbents
- Sawdust was introduced as low cost, flammable and available adsorbent
- Process parameters were screened by Plackett-Burman design
- Process parameters were optimized by response surface method
- Freundlich isotherm provided best fit of the equilibrium data

Abstract

Disposal of storage tank sludge in oil depots is a major environmental concern due to the high concentration of hydrocarbons involved. This paper investigates the reduction of the sludge oil pollutants with initial oil and grease concentration of about 50 mass% using low cost adsorbents. Among the examined adsorbents, sawdust indicated the maximum removal of oil and grease. The screening and optimizing of process parameters were evaluated employing Plackett-Burman design and response surface method. For the optimized conditions, more than 60 mass% of oil and grease from the sludge was removed. Moreover, it was found that sawdust adsorption of the oil and grease approximately followed the Freundlich isotherm. The results indicated that oil pollutants of sludge could be reduced using sawdust as a low-cost, available and flammable adsorbent so that thus saturated adsorbents could be used as fuel in certain industries.

Keywords: low-cost adsorbent, oil and grease, response surface methodology, sludge of storage tank.

Studies conducted on the environmental and health effects of petroleum hydrocarbons show that most of these substances are toxic and resistant to biodegradation. Hydrocarbons can enter the food chain and cause mutations in the organism cells [1]. Accordingly, it is necessary to take into account the issue of environmental pollution caused by oil hydrocarbons and to offer proper solutions.

Sludge is formed in the storage tanks of crude oil and petroleum products owing to the fact that the heavier petroleum hydrocarbons settle along with solid particles and water. The sludge deposited at the bottom of the storage tank reduces the product quality and the tank capacity as well as corrodes the pipes and the tank. Therefore, it has to be removed during tank cleaning operations and sent for further treatment or disposal. The sludge hydrocarbons have to be removed prior to its disposal [2].

Various methods such as evaporation, dispersion on surface, oxidation, demulsification, adsorption and electrochemical method have been employed to eliminate or separate the oil hydrocarbon from the wastewater and waste oil [3-10]. Nowadays, membrane processes such as microfiltration, ultrafiltration, nanofiltration and reverse osmosis have also been recommended to remove oil hydrocarbon from water [11-18].

A variety of methods have been developed for the treatment of oily sludge, including those designed for recovering and reclaiming valuable fuel from the

---

Correspondence: Z.B. Mokhtari-Hosseini, Chemical Engineering Department, Faculty of Petroleum and Petrochemical Engineering, Hakim Sabzevari University, P.O. Box 9617976-487, Sabzevar, Iran.
E-mail: z.mokhtari@hsu.ac.ir, zb_mokhtari@yahoo.com

Paper received: 22 September, 2015
Paper revised: 25 April, 2016
Paper accepted: 21 July, 2016

https://doi.org/10.2298/CICEQ150922037M

existing oily sludge; among which solvent extraction, centrifugation treatment, surfactant enhanced oil recovery (EOR), freeze/thaw treatment, sludge pyrolysis, microwave irradiation, electrokinetic method, ultrasonic irradiation and froth flotation are frequently mentioned. A number of technologies are also available for the disposal of oily sludge, including incineration, stabilization/solidification, oxidation, and biodegradation [2,19-22].

The adsorption of oil pollutants is one of the methods used for the treatment of oil wastewaters. Several investigations have focused on the adsorption of oil pollutants from gaseous, liquid and solid wastes employing natural adsorbents due to the suitable adsorption properties [1,6-9,23-27]. Natural adsorbents used are often mineral adsorbents such as zeolite and bentonite, activated carbon, organic materials like chitosan, cotton fiber and agricultural wastes such as rice and wheat wastes, tea, coffee and coconut hysteresis, peanut wastes, shell and stems of various agricultural products, etc. [1,9,24-27].

Optimization of process parameters increases the process efficiency and reduces the cost of the process itself [28,29]. Many variables such as the adsorbent dose and size, the contact time, physical conditions such as temperature, pressure and agitation could affect the adsorption process. To reduce the number of experiments in spite of the large number of variables, the statistical design of the experiments were used in many studies. Applying statistical methods such as Plackett-Burman design (PBD) and response surface methodology (RSM) has gained a lot of impetus in optimizing the process and understanding the interactions among various physicochemical parameters [30-32].

Employing natural adsorbents in the removal of oil and organic contaminants from aqueous and gaseous environments has demonstrated remarkable results [1,6-9,23-27]. In this study, we examined the adsorption of hydrocarbons from the sludge of petroleum product tanks using natural adsorbents such as wheat straw, pine fruit, walnut shell, almond shell and sawdust. After selecting the best natural adsorbent, the effective process variables were identified through Plackett-Burman statistical experimental design. Based on thus obtained data, important factors were optimized using response surface method by Box-Behnken design.

MATERIALS AND METHODS

Materials and apparatus

Sludge samples were obtained from the outdoor pool where the discharged storage tank sludge of the National Iranian Oil Products Distribution Company located in Shahroud was stored. Wheat straw, pine fruit, walnut shell, almond shell and sawdust were used as natural adsorbents. All the chemicals used in this research were of analytical grade.

The magnetic stirrer used for adsorption processes was a MSH-20D Wise Stir model supplied by Daihan Scientific Company. The total petroleum hydrocarbon (TPH) of the sludge was determined using Gas Chromatography and Flame Ionization Detection (HP - Agilent 6890 FID uECD). The pH measurements were carried out using a Metrohm 780 pH meter. A&D HR-200 laboratory balance was used for weighing of materials.

Adsorbent selection

Five natural adsorbents (wheat straw, pine fruit, walnut shell, almond shell and sawdust) were separately crushed and sieved. The adsorption efficiency of each adsorbent was then investigated for 40 g L^{-1} of adsorbent dose (2 g adsorbent in 50 ml sludge), 2.00-2.36 mm adsorbent size, at 35 °C temperature, 400 rpm agitation and 30 min contact time.

Statistical experimental design

Screening variables. The review of published reports [1,6-9,23-27] indicated that pH, contact time, amount and size of the adsorbent, initial adsorbate concentration, temperature, agitation and the presence of other adsorbates, could have effect on the adsorption process. In a sludge sample, initial adsorbate concentration and the presence of other adsorbates are constant. Plackett-Burman statistical method was employed in screening six other factors: pH, contact time, the amount and size of adsorbent, temperature and agitation. Table 1 shows the selected levels of variables, determined *via* preliminary experiments and the limitations of the operation conditions. The experiments were conducted according to the matrix of PBD (Table 2).

Optimization of effective variables: Box-Behnken design was used in optimizing the process parameters that were found to be important for oil and grease adsorption based on the screening results of Plackett-Burman design, while other factors were kept at a constant level of 35 °C temperature, 500 rpm agitation and pH 6.03. The ranges of variables for BBD are presented in Table 1. Table 3 presents BBD for three variables with coded values. The results of the experimental designs were analyzed and interpreted using Minitab 16 statistical software.

Table 1. Selected levels of variables for PBD and BBD related to the oil and grease removal from sludge via sawdust

Variable		PBD		BBD		
		Coded value				
		+1	-1	-1	0	+1
θ	Temperature, °C	50	32	-	-	-
pH	pH	9	5	-	-	-
s	Agitation, rpm	500	150	-	-	-
t	Contact time, min	60	10	10	30	50
m	Adsorbent dosage, g/L	60	10	20	40	60
d	Particle size, mm	2.36-4.75	0.425-0.850	0.30-0.60	1.18-1.70	2.36-4.75

Table 2. Plackett-Burman design matrix and the corresponding results for oil and grease removal from sludge via sawdust

Trail	*θ*	Coded factors						Removal efficiency, mass%
		pH	*s*	*t*	Virtual factor	*m*	*d*	
1	+1	+1	+1	-1	+1	-1	-1	28.25±0.45
2	-1	+1	+1	+1	-1	+1	-1	52.67±0.62
3	-1	-1	+1	+1	+1	-1	+1	25.13±0.53
4	+1	-1	-1	+1	+1	+1	-1	53.83±0.53
5	-1	+1	-1	-1	+1	+1	+1	35.12±1.07
6	+1	-1	+1	-1	-1	+1	+1	40.64±0.00
7	+1	+1	-1	+1	-1	-1	+1	21.21±0.00
8	-1	-1	-1	-1	-1	-1	-1	19.78±1.60

Table 3. Box-Behnken design matrix and the corresponding results for oil and grease removal via sawdust

Trail	Coded value			Removal efficiency mass%
	m	*t*	*d*	
1	-1	-1	0	36.90±0.00
2	+1	-1	0	47.24±0.53
3	-1	+1	0	39.22±1.07
4	+1	+1	0	50.98±0.00
5	-1	0	-1	26.92±0.53
6	+1	0	-1	55.70±0.45
7	-1	0	+1	36.01±0.00
8	+1	0	+1	42.78±0.53
9	0	-1	-1	43.40±0.98
10	0	+1	-1	61.14±0.53
11	0	-1	+1	35.47±0.53
12	0	+1	+1	33.33±0.53
13	0	0	0	51.52±0.53
14	0	0	0	50.89±0.98
15	0	0	0	50.80±0.00

Adsorption isotherm

To find a model that represents the adsorption isotherms of oil and grease by sawdust, a determined volume of sludge (c_0 = constant) was kept in contact with different doses of sawdust (10-60 g/L) at 35 °C and 500 rpm until equilibrium concentration. The equilibrium adsorption capacity (q_e) was then determined. Subsequently, the agreement of the obtained data with the three proposed isotherm models, Linear, Langmuir and Freundlich was studied.

Analysis

The total petroleum hydrocarbon (TPH) of the sludge was determined using Gas Chromatography and Flame Ionization Detection (HP - Agilent 6890 FID uECD) according to EPA8015B standard methods. Oil and grease were also measured according to EPA9071B standard methods.

In adsorbent selection and optimization stages, grease and oil of the sludge were measured by gravimetric method using *n*-hexane as a solvent; which involved adding the solvent to the sample, stirring on the magnetic stirrer, inertia and phase separation, distilling of the certain volume of solvent phase, weighing residual materials, and calculating the amount of oil and grease in the whole sample. The amount of the solvent used was determined by employing preliminary experiments for extracting the total oil and grease in the sludge before adsorption.

RESULTS AND DISCUSSION

Composition of the preliminary sludge sample

The amount of TPH and oil and grease in the sludge sample was determined according to

EPA8015B and EPA9071B, respectively. The results showed that the amount of TPH and oil and grease in the sludge was 13.5 and 59.38 mass%, respectively.

The initial oil and grease concentration (56.1 mass%) was also determined using gravimetric methods explained above in the analysis section which corresponded to the amount obtained using EPA9071B. Therefore, the gravimetric method was used for the subsequent experiments.

Adsorbent selection

The removal efficiency of five natural adsorbents, namely sawdust, walnut shell, almond shell, pine fruit and wheat straw was studied under the same conditions. Figure 1 shows the removal efficiency of oil and grease from the sludge by the adsorbents that possess the ability of adsorbtion. Sawdust was selected for further study as its removal efficiency was far greater than the other adsorbents.

Variable screening

Plackett-Burman design is the best design for a rapid screening of numerous variables from a multivariant system. In this design, the interactions could be completely ignored so that the main effects could be calculated through fewer experiments. Six variables (pH, contact time, temperature, agitation, dose and size of the adsorbent) were evaluated using the eight-run PBD. Table 2 displays PBD and the obtained corresponding results, whereas Figure 2 depicts the main effects of the investigated variables and illustrates the fact that adsorbent dosage is the most significant factor with a positive effect on the removal efficiency of oil and grease using sawdust. This means that at higher adsorbent dose removal efficiency was higher. Adsorbent size and contact time are also significant factors with respectively negative and positive effects. Increasing the adsorbent

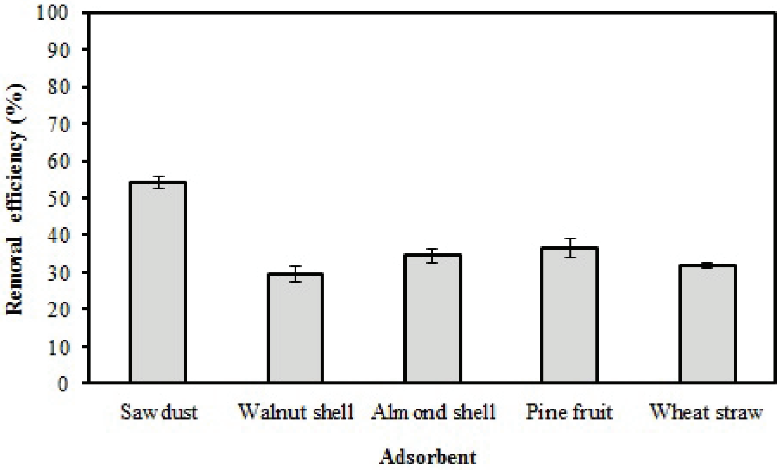

Figure 1. Removal efficiency of oil & grease using different natural adsorbents under the same condition. The bars represent the standard deviation of mean.

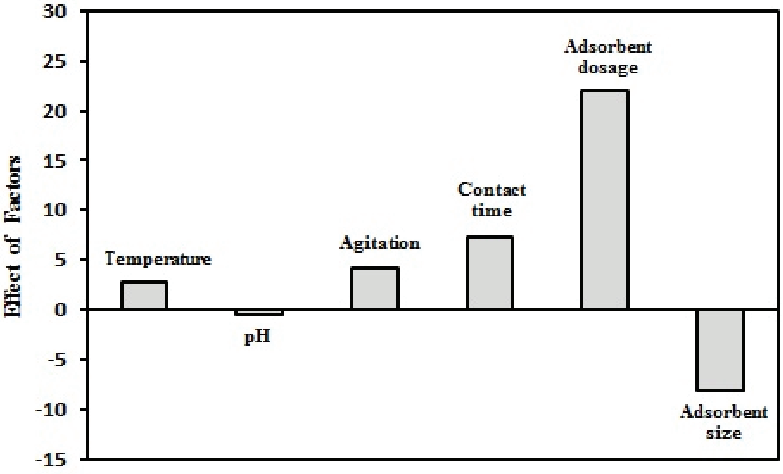

Figure 2. The main effects of studied variables using PBD.

surface and reducing the particle size leads to increase in the adsorption and removal efficiency. Increasing the contact time raises contact probability and increases the adsorption efficiency. However, contact time is effective as long as the adsorbent is not saturated. Therefore, adsorbent dose, particle size and contact time were selected for further optimization studies.

Optimization

RSM was employed in investigating the optimum conditions of oil and grease removal and in building models. Based on the screening results obtained *via* Plackett-Burman design, particles size (d), contact time (t) and adsorbent dose (m) were selected as the independent input variables while the removal efficiency (%) of oil and grease was considered as the dependent output variable. Box-Behnken design was employed to analyze the interactive effect of those parameters and to arrive with an optimal condition. The experimental design protocol (developed by Minitab 16 Software) and the corresponding results are presented in Table 3. The experimental results of the BBD were fitted with a second order polynomial equation. The values of regression coefficients were calculated and the fitted equation for predicting the removal efficiency (Y) was as follows:

$$\begin{aligned} Y &= 51.070+7.208m+2.707t-4.947d- \\ &-5.236m^2-2.250t^2-5.481d^2-0.357mt- \\ &-5.504md-4.969td \end{aligned} \tag{1}$$

The coefficients of the regression model (Eq. (1)) that appear as one constant, three linear, three quadratic and three interaction terms are listed in Table 4.

The significance of each coefficient was determined by p-values. The p-values imply that the first order main effects of all factors and the second order main effects of particle size and adsorbent dosage are significant in terms of removal efficiency. For the interaction terms, contact time - particle size and adsorbent dosage - particle size was found to be the most significant with $p < 0.05$.

The suitability of fitting with the proposed quadratic models was confirmed by the determination coefficient (R^2). In this case, the value of the determination coefficient ($R^2 = 0.8679$) indicated that 86.79% of the variability in the response could be explained by the model as far as removal efficiency was concerned.

The 2D contour plots are the graphical representations of the regression equation and are plotted in order to understand the response variation that results as variation of the two independent variables while the other independent variable is kept constant. Moreover, the 2D contour plots indicate the interaction among independent variables and locate the optimum level of each variable for maximum response. Figure 3 indicates contour plots for removal efficiency.

As shown in Figure 3, the variation in each factor changes the removal efficiency. Figure 3a shows that the increase in the contact time and the decrease in particle size increase the removal efficiency. Additionally, for larger particle size, removal efficiency is relatively independent from contact time, whereas for smaller particle sizes, the response depends on the contact time suggesting that there is an interaction between contact time and particle size. Figure 3b demonstrates the variation of removal efficiency with the variation of particle size and adsorbent dosage where the maximum response is obtained at maximum adsorbent dosage and minimum particle size. It also illustrates the direct and reverse relationship of relative adsorbent dosage and relative particle size with removal efficiency. Furthermore, for larger particle sizes and higher adsorbent dosages, removal efficiency is independent of the adsorbent dosage and for smaller particle sizes and lower adsorbent dosages; removal efficiency is independent of the

Table 4. Analysis of BBD results for oil & grease removal by sawdust

Parameter	Regression coefficient	*t*-value	*p*-value
Constant	51.070	30.626	0.000
Adsorbent dosage (m)	7.208	7.059	0.000
Contact time (t)	2.707	2.651	0.015
Particle size (d)	-4.947	-4.844	0.000
m^2	-5.236	-3.484	0.002
t^2	-2.250	-1.497	0.150
d^2	-5.481	-3.647	0.002
mt	0.357	0.247	0.808
md	-5.504	-3.811	0.001
dt	-4.969	-3.441	0.003

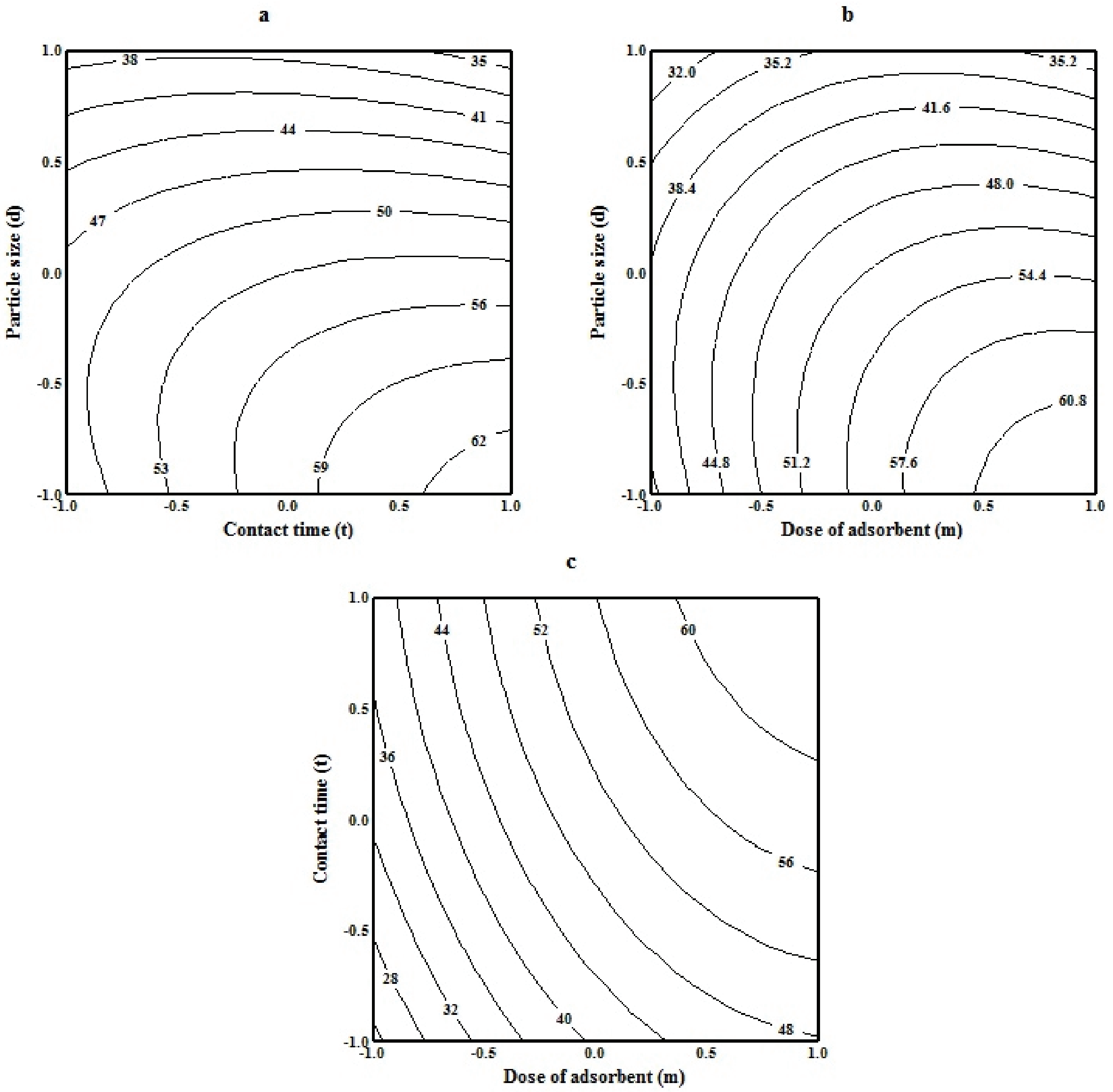

Figure 3. Contour plots of removal efficiency: a) vs. particle size and contact time, b) vs. particle size and adsorbent dosage and c) vs. adsorbent dosage and contact time at optimal levels of other components (d, t and m are coded variables).

particle size representing the interaction between particle size and adsorbent dosage Figure 3c represents the rise in the removal efficiency with the increase in contact time and adsorbent dosage.

The optimum condition for maximum response was obtained using Minitab 16 software. For the studied range of variables, the optimum condition for removal efficiency was *d* = -1, *t* = 1 and *m* = 1 means 0.3-0.6 mm particle size, 50 min of contact time and 60 g/L adsorbent dose. Under those conditions, the removal efficiency predicted by the software was 63.79 mass% and for the experimental study it was actually 61.6±0.1 mass%. This indicates the consistency of the results and confirms the validity of the model.

Adsorption isotherm

To find a model that would indicate the adsorption isotherms of oil and grease by sawdust, experimental data were fitted with three isotherm models including Linear, Langmuir and Freundlich. The model parameters were determined through the linear regression of the experimental data. Higher values of R^2 for Freundlich isotherm revealed that this model best fits the experimental data in comparison with other models.

CONCLUSION

Reducing the oil pollutants in storage tank sludge is necessary prior to its disposal as it would definitely entail the environmental problems. In the present research, low-cost adsorbents such as wheat straw, pine fruit, walnut shell, almond shell and sawdust were used to reduce hydrocarbons in the sludge and among them sawdust was introduced as the best adsorbent. Process parameters were screened and optimized using statistical experimental designs (Plackett-Burman and Box-Behnken design). Screening showed that contact time and adsorbent dose and size were effective variables and finally the optimum amounts of these variables were found to be 0.3-0.6 mm, 50 min and 60 g/L. Under such conditions, more than 60 mass% of the hydrocarbon was adsorbed by sawdust. This study demonstrated that sawdust could be used as a low-cost, widely available and flammable adsorbent for the reduction of oil pollutants from the storage tank sludge.

Acknowledgment

We gratefully acknowledge Iran Ministry of Science, Research and Technology and The University of Hakim Sabzevari for their financial support.

REFERENCES

[1] E.A. Eman, Am. J. Environ. Prot. **2** (2013) 161-169

[2] G. Hu, J. Li, G. Zeng, J. Hazard. Mater. **261** (2013) 470-–490

[3] U. Daiminger, W. Nitsch, P. Plucinski, S. Hoffman, J. Membr. Sci. **106** (1995) 195-205.

[4] M.R.G. Santos, M.O.F. Goulart, J. Tonholo, C.L.P.S. Zanta, Chemosphere **64** (2006) 393-399

[5] M. Santander, R.T. Rodrigues, J. Rubio, Colloids Surfaces, A **375** (2011) 237-244

[6] M. Sueyoshi, R.S. Al-Maamari, B. Jibril, M. Tasaki, K. Okamura, H. Kuwagaki, H. Yahiro, K. Sagata, Y. Han, J. Anal. Appl. Pyrolysis **97** (2012) 80-87

[7] D. Wang, E. McLaughlin, R. Pfeffer, Y.S. Lin, Sep. Purif. Technol. **99** (2012) 28-35

[8] L. Vlaev , P. Petkov, A. Dimitrov, S. Genieva, J. Taiwan Inst. Chem. Eng. **42** (2011) 957-964

[9] S.M. Sidik, A.A. Jalil, S. Triwahyono, S.H. Adam, M.A.H. Satar, B.H. Hameed, Chem. Eng. J. **203** (2012) 9-18

[10] M. Nikkhah, T. Tohidian, M.R. Rahimpour, A. Jahanmiri, Chem. Eng. Res. Des. **94** (2015) 164-172

[11] Y.S. Li, L. Yana, C.B. Xiang, L.J. Hong, Desalination **196** (2006) 76-83

[12] H.J. Li, Y.M. Cao, J.J. Qiong, X.M. Jie, T.H. Wang, J.H. Liu, Q. Yuan, J. Membr. Sci. **279** (2006) 328-335

[13] B. Chakrabarty, A.K. Ghoshal, M.K. Purkait, Chem. Eng. J. **165** (2010) 447-456

[14] H. Ohya, J.J. Kim, A. Chinen, M. Aihara, S.I. Semenova, Y. Negishi, O. Mori, M. Yasuda, J. Membr. Sci. **145** (1998) 1-14

[15] E. Gorouhi, M. Sadrzadeh, T. Mohammadi, Desalination **200** (2006) 319-321

[16] S. Rezaei Hosein Abadi, M.R. Sebzari, M. Hemati, F. Rekabdar, T. Mohammadi, Desalination **265** (2011) 222-–228

[17] D.H.H. Phuoc, T.S. Chung, J. Membr. Sci. **452** (2014) 117-126

[18] S. Zhang, P. Wang, X. Fu, T.S. Chung, Water Res. **52** (2014) 112-121

[19] M.B. Mendonça, M.C. Cammarota, D.D.C. Freire, M. Ehrlich, J. Hazard. Mater. **110** (2004) 113-118

[20] A. Al-Futaisi, A. Jamrah, B. Yaghi, R. Taha, J. Hazard. Mater. **141** (2007) 557-564

[21] J. Zhang, J. Li, R.W. Thring, X. Hu, X. Song, J. Hazard. Mater. **203-204** (2012) 195-203

[22] M. Elektorowicz, S. Habibi, R. Chifrina, J. Colloid Interface Sci. **295** (2006) 535-541

[23] R. Crisafully, M.A.L. Milhome, R.M. Cavalcante, E.R. Silveira, D.D. Keukeleire, R.F. Nascimento, Bioresour. Technol. **99** (2008) 4515-4519

[24] A.L. Ahmad, S. Sumathi, B.H. Hammeed, Chem. Eng. J. **8** (2005) 179-185

[25] A. Imran, J. Environ. Manage. **113** (2012) 170-183

[26] A. Bhatnagar, Chem. Eng. J. **157** (2010) 277-296

[27] K. Kannan, K. Senthilkumar, P. Akilamudhan, V. Sangeetha, B. Manikandan, Int. J. Biosci., Biochem. Bioinf. **2** (2012) 398-402

[28] D.C. Montgomery, Douglas, C., Design and Analysis of Experiments, sixth ed., John Wiley and Sons, New York, 2001

[29] Z.B. Mokhtari-Hosseini, E. Vasheghani-Farahani, A. Heidarzadeh-Vazifekhoran, S.A. Shojaosadati, R. Karimzadeh, K. Khosravi Darani, Bioresour. Technol. **100** (2009) 2436-2443

[30] C. Hana, H. Pua, H. Li, L. Denga, S. Huanga, S. Heb, Y. Luo, J. Hazard. Mater. **254-255** (2013) 301-309

[31] Y. Liua, J. Wanga, Y. Zhenga, A. Wanga, Chem. Eng. J. **184** (2012) 248-255

[32] D. Podstawczyk, A. Witek-Krowiak, K. Chojnacka, Z. Sadowski, Bioresour. Technol. **160** (2014) 161-165.

ZAHRA BEAGOM MOKHTARI-HOSSEINI[1]
RAZIEH HOSSEINABADI[2]
ASHRAFALSADAT HATAMIAN ZARMI[3]

[1]Chemical Engineering Department, Faculty of Petroleum and Petrochemical Engineering, Hakim Sabzevari University, Sabzevar, Iran
[2]Faculty of Engineering, Islamic Azad University Shahrood Branch, Shahrood, Iran
[3]Faculty of New Sciences and Technology, University of Tehran, North Karegar Ave., Tehran, Iran

NAUČNI RAD

SMANJENJE ZAGAĐIVAČA IZ MULJA REZERVOARA ZA SKLADIŠTENJE NAFTNIH DERIVATA KORIŠĆENJEM JEFTINIH ADSORBENASA

Odlaganje mulja iz rezervora za naftu u depoima nafte je od velike važnosti za zaštitu životne sredine zbog visokih koncentracija ugljovodonika. U ovom radu analizirana je redukcija polutanata nafte iz mulju sa početnom koncentracijom ulja i masti od oko 50 % koristeći jeftine adsorbense. Od svih analiziranih adsorbenasa, piljevina pokazuje maksimalno uklanjanje ulja i masti. Optimizacija procesnih parametara urađena je primenom Plackett-Burman dizajna i metode odzivne površine. Pod optimalnim uslovima uklanja se više od 60 % ulja i masti iz mulja. Nađeno je da adsorpcija ulja i masti na piljevini sledi Frojndlihovu izotermu. Ovi rezultati pokazuju da polutanti iz mulja mogu biti redukovani jeftinom piljevinom koja posle zasićenja može biti korišćena kao gorivo u industriji.

Ključne reči: jeftini adsorbens, ulje i masti, metoda odzivne površine, mulj iz rezervoara.

Chemical Industry & Chemical Engineering Quarterly

Available on line at
Association of the Chemical Engineers of Serbia *AChE*
www.ache.org.rs/CICEQ

Chem. Ind. Chem. Eng. Q. 23 (2) 245–249 (2017) CI&CEQ

LI CHEN
GUOYAN LUAN

Institute of Petrochemical Technology, Jilin Institute of Chemical Technology, Jilin, China

SCIENTIFIC PAPER

UDC 544.23:546.711:543.42:66

MORPHOLOGY CONTROL OF MnO_2 NANOPARTICLES: EFFECT OF P123 POLYMER IN ETHANOL-WATER SYSTEM

Article Highlights

- A series of MnO_2 nanoparticles were synthesized in the ethanol-water system
- The morphology changed from rod-like into sheet-like shape
- P123 polymer played a crucial role in controlling the morphology

Abstract

A series of MnO_2 nanoparticles were synthesized by two-step reaction in the ethanol-water system with urea as reducing agent. During the novel routine, P123 polymer plays a crucial role in controlling the morphology. Then, characterization and systematic investigations of the samples by transmission electron microscopy and scanning electron microscopy confirmed that the morphology of MnO_2 nanoparticles changed as the raw materials ratio changed. Finally, X-ray diffraction and X-ray photoelectron spectroscopy were employed to confirm the crystal structure and the exact components. These results indicated the particles showed a rod-like shape without P123 and changed into sheet-like shape after the addition of P123. Therefore, this idea could be developed for the controllable synthesis of other metal oxide-based nanomaterials.

Keywords: MnO_2, P123, morphology, nanoparticles.

MnO_2 nanoparticles, with good physical and chemical properties, have become attractive candidates for heterogeneous catalysis and energy storage systems, especially due to environmental awareness in the recent years [1-4]. This low-cost and environment-friendly material had attracted more and more attentions and many researchers engaged in synthesis of MnO_2 nanoparticles with various approaches [5-7]. However, in practical applications, the crystallinity and morphology of MnO_2 nanoparticles have direct effects on the performances.

Up to now, several morphologies of MnO_2 nanoparticles were reported, including hollow spheres, urchins, thin films, nanopillars and other one-dimensional (1D) or three-dimensional (3D) nanostructured MnO_2 [8-13]. These types of nanoparticles had specific surface area and good structural stability, leading to remarkable improvement compared with the traditional MnO_2 powder. Unfortunately, the synthesis methods are not well-controlled and there is a lack of studies on the relationship between the morphology and the raw materials.

It is known that P123, one type of poly(ethylene oxide)-poly(propylene oxide)-poly(ethylene oxide) block copolymers, exhibits particular behavior in aqueous solution and has been introduced to synthesize loads of nanomaterials [14-17]. In fact, it is also a highly effective agent for controlling the nucleation and growth of crystals. In previous reports, it was employed as a template for the synthesis of MnO_2 nanoparticles [18-19]. However, the performances were still unsatisfying. In this study, a series of MnO_2 nanoparticles were synthesized with P123 polymer introduced into the novel ethanol-water system. The exact function of P123 polymer was also investigated.

Correspondence: L. Chen, Institute of Petrochemical Technology, Jilin Institute of Chemical Technology, Jilin, 132022, PR China.
E-mail: chenli16@126.com

Paper received: 16 March, 2016
Paper revised: 27 July, 2016
Paper accepted: 4 August, 2016

https://doi.org/10.2298/CICEQ160316038C

EXPERIMENTAL

Materials and reagents

Potassium permanganate and urea ($CO(NH_2)_2$) were purchased from Guangfu Fine Chemical Plant (Tianjin, China). Ethanol was purchased from Xilong Chemical Co., Ltd. Pluronic P123 (EO:PO:EO = = 20:70:20, average *Mn* = 5800) was purchased from Sinopharm Chemical Reagent Co., Ltd. All chemicals are of analytical grade and used without any further purifications. Water used in the experiment was distilled for three times before.

Preparation of MnO_2 nanoparticles

A certain amount of P123 was dissolved in 100 mL ethanol-water system (ethanol:water = 1:5) with continuous stirring on magnetic stirring devices. Then, $KMnO_4$ and $CO(NH_2)_2$ powder were added into the transparent colloidal dispersion sequentially and stirred for another 30 min. After aging for 24 h, the mixture was transferred into 80 mL Teflon-lined autoclave and maintained at 90 °C for 24 h. After cooling to room temperature, the as-obtained solid was filtered, and washed with water and ethanol for three times, respectively. Finally, the collected solid was dried in a vacuum oven at 60 °C for 12 h. The as-prepared samples were placed in a crucible and heated in a furnace at 500 °C for 2 h under the air atmosphere to obtain the product. In order to make a comparison, a series of the product were synthesized under different conditions, which were denoted as M-*X* (Table 1), where *X* represents the experiment number.

Transmission electron microscopy (TEM)

TEM was conducted on JEM-2000EX (JEOL, 200 kV). All samples for TEM tests were prepared by dropping a suspension of each sample onto the carbon holey grid (JEOL, 400 meshes). The suspension was prepared with the solid dispersed in ethanol using an ultrasonic bath for 15 min.

Scanning electron microscopy (SEM)

SEM images were obtained on JSM-5600 (JEOL, 25 kV) and each sample was gilded to enhance the conductivity before characterization.

X-Ray diffraction (XRD)

The samples were tested on the Rigaku D/max--2500 X-ray powder diffractometer using CuKα radiation (λ = 0.1542 nm) with scattering angles (2θ) of 5--80°, operating at 40 kV and a cathode current of 30 mA.

X-Ray photoelectron spectroscopy (XPS)

XPS was conducted on the Thermo Escalab 250 with a monochromatic AlKα source at room temperature with the sample (M-1) cleaned before. All the binding energies were referenced to the C1s peak at 284.8 eV.

RESULTS AND DISCUSSIONS

A series of MnO_2 nanoparticles, labeled as M-1 to M-6, were synthesized under various reaction conditions. The whole designed routine mainly included two stages, hydrothermal reaction and high-temperature thermal treatment. The growth of nanoparticles was conducted in the ethanol-water system in the presence of P123 polymer and urea. The product was obtained after P123 polymer was removed completely by calcination.

TEM studies were employed to reveal the morphology of the samples in details. As is shown in Figure 1a, the M-1 sample showed a rod-like structure with the length of 300 to 500 nm. However, as the addition of P123 polymer, the morphology witnessed significant changes. The remained samples presented the special sheet-like structure. By comparison from M-2 to M-4 (Figure 1b-d), excessive amount of P123 polymer would lead to serious agglomeration and the sheet-like structure was not obvious. Even some samples demonstrated other structural shapes. For example, in terms of M-4, some short rod-like structure could be found. Therefore, the P123 polymer played an important role on the morphology of MnO_2 nanoparticles. Actually, at the room temperature, after the addition of $KMnO_4$, P123 molecules were absorbed on the surface of MnO_4^- to form micelles in the presence of ethanol. As for P123 polymer, when the reaction temperature was above the critical micellar temperature (CMT), the PPO blocks would

Table 1. The various reaction conditions for synthesis of MnO_2 nanoparticles

Sample	$CO(NH_2)_2$, g	P123, g	$KMnO_4$, g	H_2O, mL	C_3H_6O, mL
M-1	2.5	0	1.0	25	5
M-2	2.5	1.5	1.0	25	5
M-3	2.5	0.5	1.0	25	5
M-4	2.5	2.5	1.0	25	5
M-5	1.5	1.5	1.0	25	5
M-6	0.5	1.5	1.0	25	5

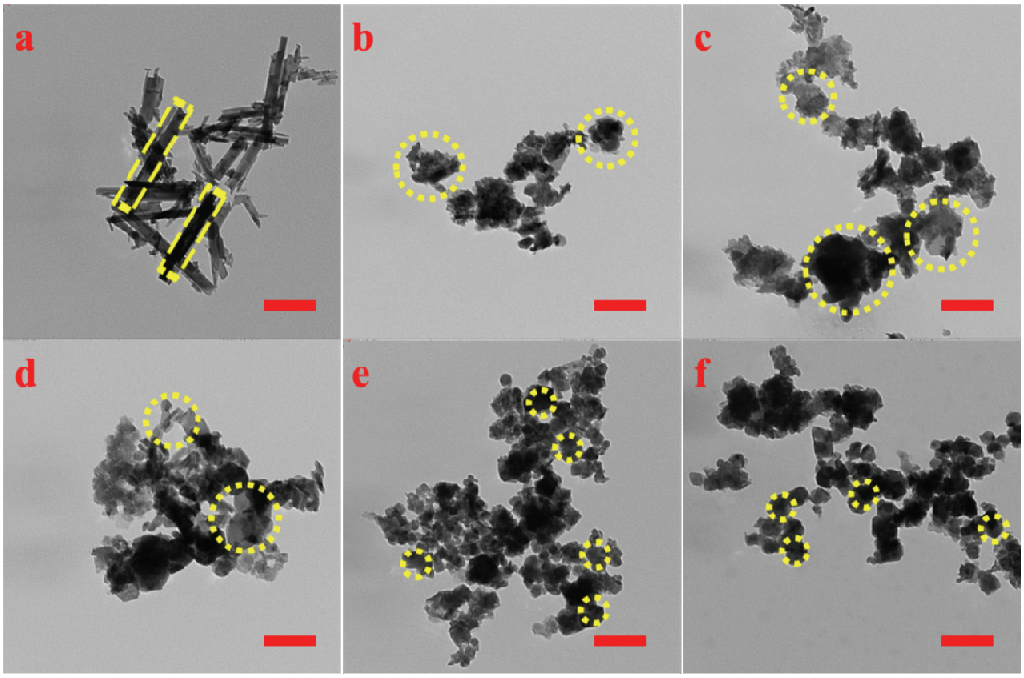

Figure 1. TEM images of the as-synthesized samples; a-d corresponds to the sample M-1 to M-6, respectively. The bar: 200 nm.

become insoluble while the PEO blocks would be still soluble. Hence, the previous growth kinetic would be modified, leading to a sheet-like structure from a rod-like one.

Interestingly, in the following experiments, if the amount of $CO(NH_2)_2$ decreased, the sheet-like structure became clear with an exact pentagon, as is shown in M-5 (Figure 1e) and M-6 (Figure 1f). Combined with the previous literature, the K^+ might also have effect on the structure of the product and the main idea was that high-concentration K^+ stacked between the MnO_2 sheets, making the structure stable [20]. Meanwhile, the nanoparticles could be distributed around the P123 polymer under the action of hydrogen bonds between ethanol and water to form a uniform state.

SEM was used to confirm the state of aggregation of the MnO_2 nanoparticles. The shape showed in M-1 (Figure 2a) had obvious differences with other ones. On average, M-2 (Figure 2b) and M-3 (Figure 2c) found no uniform shapes and many blocks were relatively big. On contrary, the small blocks with uni-

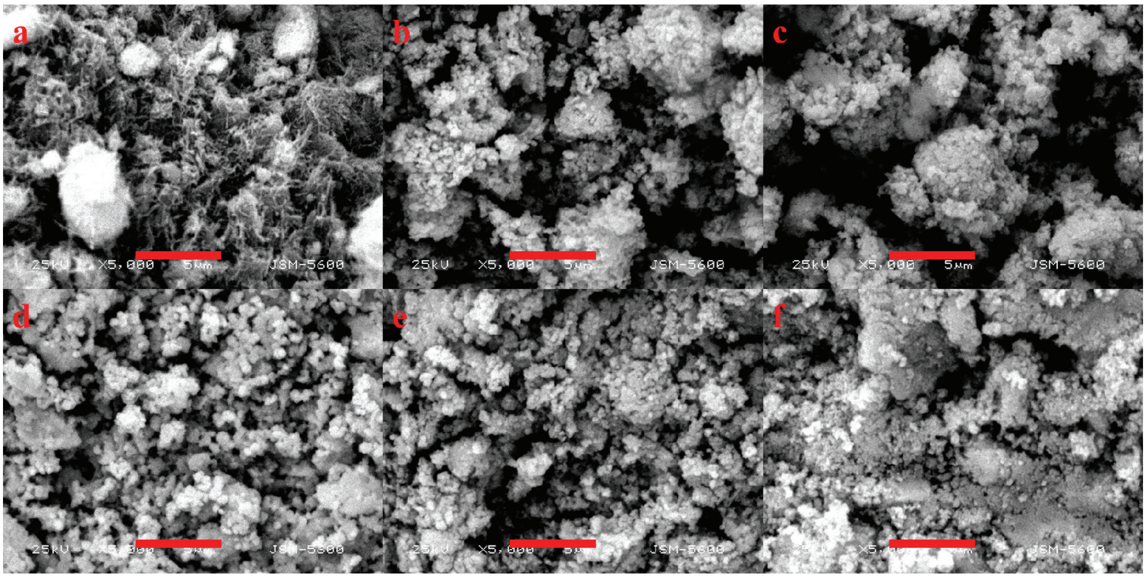

Figure 2. SEM images of the as-synthesized samples; a-d corresponds to the sample M-1 to M-6, respectively. The bar: 5 μm.

form shape appeared in M-4 (Figure 2d), M-5 (Figure 2e) and M-6 (Figure 2f). Therefore, the last three samples demonstrated more compact state and smaller particle sizes.

The crystal structure was confirmed by XRD analyses (Figure 3). M-1 showed the typical peaks corresponding to α-MnO_2, which held a tetragonal structure with I 4/m and lattice parameters of $a = b = 9.785$ Å, $c = 2.863$ Å (JCPDS card No. 44-0141). But after the addition of P123 polymer, the crystal structure of M-2 to M-6 changed into $K_{0.5}Mn_2O_4\cdot1.5H_2O$, a monoclinic structure with C/2m and lattice parameters of $a = 5.15$ Å, $b = 2.844$ Å, $c = 7.159$ Å (JCPDS card No. 42-1317). That is to say, the growth kinetic was changed and the P123 could restrict the movement of K^+, which also participated in the growth of sheet-like structure. Furthermore, the intensity of all diffraction peaks indicated that they were highly crystallized.

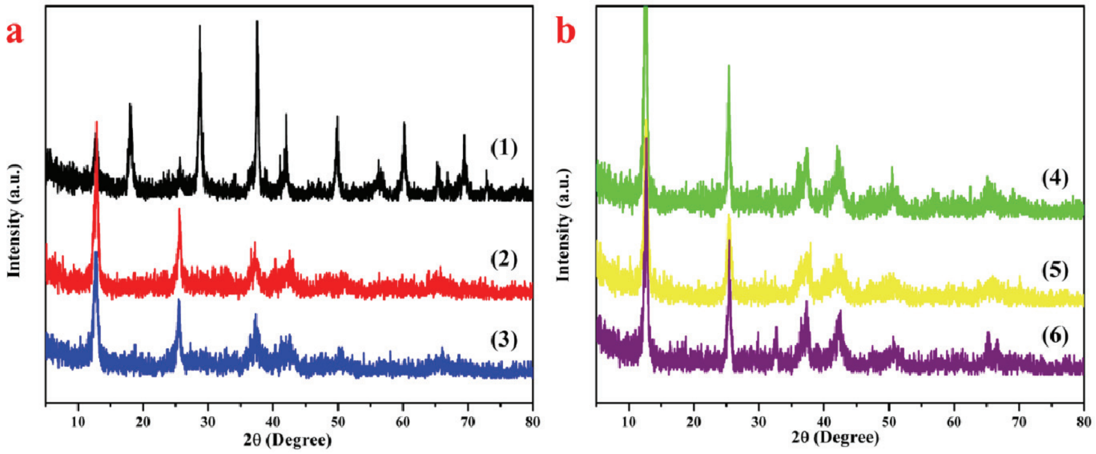

Figure 3. XRD patterns of the as-synthesized samples; 1-6 corresponds to the sample M-1 to M-6, respectively.

XPS, a powerful tool to identify the elements' states in bulk material, has been used to further elucidate the chemical composition of the as-synthesized MnO_2 nanoparticles. The peaks associated with Mn could be observed in the spectrum (Figure 4). The Mn $2p_{3/2}$ and Mn $2p_{1/2}$ peaks were centered at 642.3 and 654.0 eV, respectively. This indicated the presence of MnO_2 (Mn^{4+}) with a spin energy separation of 11.7 eV, which was in good accordance with the previous data on MnO_2 [21].

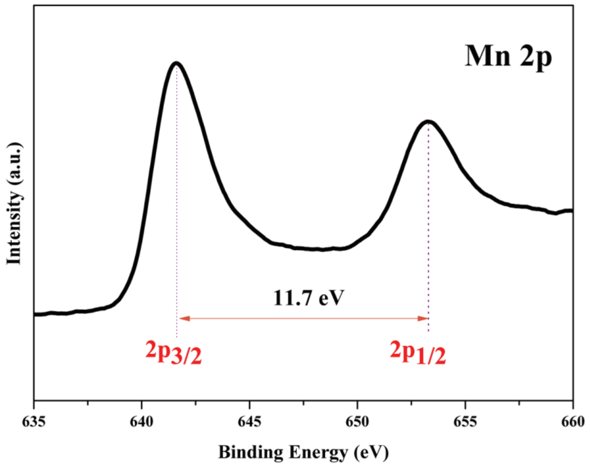

Figure 4. Mn 2p spectrum of the as-synthesized samples.

CONCLUSIONS

A series of MnO_2 nanoparticles were synthesized in the ethanol-water system and these results proved that P123 polymer played a crucial role on the morphology of the particles. Without the P123 polymer, the particles showed a rod-like shape and dense stacking state. However, the morphology changed into sheet-like shape and the density had a close relationship with the amount of P123 polymer. This is beneficial to control morphology of MnO_2 nanoparticles and this idea could be developed for the synthesis of other metal oxide-based nanomaterials.

Acknowledgements

This work was supported by Department of Education of Jilin Province (Grant No: 2015434).

REFERENCES

[1] J.G. Wang, F. Kang, B. Wei, Prog. Mater. Sci. **74** (2015) 51-124

[2] Y.M. Dong, H.X. Yang, K. He, A.Q. Song, A.M. Zhang, Appl. Catal., B: Environ. **85** (2009) 155-161

[3] N. Sui, Y. Duan, X. Jiao, D. Chen, J. Phys. Chem., C **113** (2009) 8560-8565

[4] C.L. Yu, G. Li, L.F. Wei, Q.Z. Fan, Q. Shu, J.C. Yu, Catal. Today **224** (2014) 154-162

[5] M. Huang, F. Li, F. Dong, Y.X. Zhang, L.L. Zhang, J. Mater. Chem., A **3** (2015) 21380-21423

[6] F.Y. Cheng, Y. Su, J. Liang, Z. Tao, J. Chen, Chem. Mater. **22** (2010) 898-905

[7] W.F. Wei, X.W. Cui, W.X. Chen, D.G. Ivey, Chem. Soc. Rev. **40** (2011) 1697- 1721

[8] J.G. Wang, Y. Yang, Z.H. Huang, F. Kang, Mater. Chem. Phys. **140** (2013) 643-650

[9] S. Park, I. Nam, G.-P. Kim, J.W. Han, J. Yi, ACS Appl. Mater. Interf. **5** (2013) 9908-9912

[10] X. Xie, C. Zhang, M.-B. Wu, Y. Tao, W. Lv, Q.-H. Yang, Chem. Commun. **49** (2013) 11092-11094

[11] M.-S. Wu, Appl. Phys. Lett. **87** (2005) 153102

[12] Z. Yu, B. Duong, D. Abbitt, J. Thomas, Adv. Mater. **25** (2013) 3302-3306

[13] M. Xu, L. Kong, W. Zhou, H. Li, J. Phys. Chem., C **111** (2007) 19141-19147

[14] F. Ye, H. Guo, H. Zhang, X. He, Acta Biomater. **6** (2010) 2212-2218

[15] S. Bayati, L. Galantini, K.D. Knudsen, K. Schillén, Langmuir **31** (2015) 13519- 13527

[16] X. Jia, X. Zhu, Y. Cheng, Z. Chen, G. Ning, Y. Lu, F. Wei, Small **11** (2015) 3135-3142

[17] L. Sierra, S. Valange, J. Barrault, J-L. Guth, Micropor. Mesopor. Mat. **113** (2008) 352-361

[18] R. Jiang, T. Huang, J. Liu, J. Zhuang, A. Yu, Electrochim Acta **54** (2009) 3047-3052

[19] P.K. Nayak, N. Munichandraiah J Solid State Electrochem. **16** (2012) 2739-2749

[20] R. Chen, P. Zavalij, M.S. Whittingham, Chem. Mater. **8** (1996) 1275-1280

[21] S.J. Lee, A. Gavriilidis, Q.A. Pankhurst, A. Kyek, F.E. Wagner, P.C.L. Wong, K.L. Yeung, J. Catal. **200** (2001) 298-308.

LI CHEN
GUOYAN LUAN

Institute of Petrochemical Technology,
Jilin Institute of Chemical Technology,
Jilin, China

NAUČNI RAD

KONTROLA MORFOLOGIJE MnO$_2$ NANOČESTICA: UTICAJ POLIMERA P123 U ETANOLNO-VODENOM SISTEMU

Serija MnO$_2$ nanočestica je sintetisana dvostepenom reakcijom u etanolno-vodenom sistemu sa ureom kao redukujućem agensom. Za vreme novog postupka, polimer P123 igra krucijalnu ulogu u kontroli morfologije. Karakterizacija i sistematično istraživanje uzoraka pomoću transmisione elektronske mikroskopije i skening elektronske mikroskopije pokazuje da se morfologija MnO$_2$ nanočestica menja sa promenom odnosa sirovina. X-difrakcionom i X-fotoelektričnom spektroskopijom su potvrđene kristalna struktura i komponente. Rezultati pokazuju da u odsustvu P1213 čestice izgledaju poput štapića, a da se menjaju u pločasti oblik nakon dodatka P123. Zbog toga bi ovakav pristup mogao biti dalje razvijen radi kontrole sinteze ostalih nanomaterijala baziranih na metalnim oksidima.

Ključne reči: MnO$_2$, P123, morfologija, nanočestice.

CI&CEQ
Chemical Industry & Chemical Engineering Quarterly

Available on line at
Association of the Chemical Engineers of Serbia *AChE*
www.ache.org.rs/CICEQ

Chem. Ind. Chem. Eng. Q. 23 (2) 251–258 (2017) CI&CEQ

MOHSEN BEIGI[1]
MEHDI TORKI-HARCHEGANI[2]
MAHMOOD MAHMOODI-ESHKAFTAKI[3]

[1]Department of Mechanical Engineering, Tiran Branch, Islamic Azad University, Tiran, Iran
[2]Young Researchers and Elite club, Shahrekord Branch, Islamic Azad University, Shahrekord, Iran
[3]Department of Farm Machinery Mechanics, Jahrom Universtiy, Jahrom, Iran

SCIENTIFIC PAPER

UDC 544.4:633.18:66.047:519.87

PREDICTION OF PADDY DRYING KINETICS: A COMPARATIVE STUDY BETWEEN MATHEMATICAL AND ARTIFICIAL NEURAL NETWORK MODELING

Article Highlights

- Drying curves of paddy were modeled using mathematical and ANN modeling techniques
- Among the applied models, the Midilli model was determined as the best one describing drying curves
- ANN with 4-10-14-1 topology, tansig transfer function and LM algorithm provided the best results
- ANN modelling had better performance in prediction of drying curves

Abstract

The present study aimed at investigation of deep bed drying of rough rice kernels at various thin layers at different drying air temperatures and flow rates. A comparative study was performed between mathematical thin layer models and artificial neural networks to estimate the drying curves of rough rice. The suitability of nine mathematical models in simulating the drying kinetics was examined and the Midilli model was determined as the best approach for describing drying curves. Different feed forward-back propagation artificial neural networks were examined to predict the moisture content variations of the grains. The ANN with 4-18-18-1 topology, transfer function of hyperbolic tangent sigmoid and a Levenberg-Marquardt back propagation training algorithm provided the best results with the maximum correlation coefficient and the minimum mean square error values. Furthermore, it was revealed that ANN modeling had better performance in prediction of drying curves with lower root mean square error values.

Keywords: mathematical modeling, artificial neural networks, feed forward-back propagation, Paddy.

Rice, as a cereal grain, is the most important grain providing more than one-fifth of the calories consumed worldwide by humans. Depending on some factors such as harvesting method, variety, number of cuttings and growth location, harvested rough rice may have an average moisture content ranging from 18 to 26 mass% ($g_{water}/g_{wet\ matter}$) [1]. Generally, these high levels of moisture content are not suitable for safe processing, usage and/or storage and it is recommended they should be kept at 13 mass% for storage and in the range of 10-13 mass% for milling [2]. Therefore, immediate and proper drying of the freshly harvested grains is essential for high quality grains.

Open sun drying is the traditional method still used for dehydrating agricultural products due to some advantages, *e.g.*, simplicity and low costs. However, it poses some serious problems, *e.g.*, long drying time, dust and microbial contamination as well as fluctuation in the quality of the dried materials. To overcome these problems, industrial drying equipment has been employed. Over recent decades, to dehydrate different agricultural and food products, various artificial methods such as convective hot air drying, microwave drying, vacuum drying, infrared drying, etc., have gained popularity as alternative

---

Correspondence: M. Beigi, Department of Mechanical Engineering, Tiran Branch, Islamic Azad University, Tiran, Iran.
E-mail: mohsenbeigi59@gmail.com
Paper received: 24 May, 2016
Paper revised: 30 July, 2016
Paper accepted: 9 August, 2016

https://doi.org/10.2298/CICEQ160524039B

drying techniques. Recently, some new methods such as continuous fluidized bed microwave drying [3], super-heated steam fluidized bed drying [4] and spouted bed drying [5] are reported as energy and quality efficient drying methods for paddy. However, their usage in industrial setting is still limited and fixed deep bed hot air dryers are the most common method used for paddy drying [6].

Mathematical modelling is widely used to predict drying behaviour of materials being dried, design new dryers, and control of the process. Theoretical, semi-theoretical and empirical models are the key proposed mathematical models used to describe the drying behaviour of agricultural materials. Theoretical models are built based on the understanding of the fundamental phenomena and mechanisms involved during drying process, whereas the two other models are built by fitting model parameters to experimental data. Although theoretical simulations could give an explanation for phenomena occurring during the process, they are more difficult to execute and require a substantial amount of computing time. The empirical models are derived from a direct correlation between moisture content and drying time and neglect fundamentals of drying process. The semi-theoretical models offer a compromise between theory and ease of application and generally are derived from direct solution of Fick's second law by assuming some simplifications [7]. To date, several researchers have investigated regression modelling of various agricultural and food products drying curves, *e.g.*, sweet cherry [8], rapeseed [9], pomegranate arils [10], onion [11], mushroom [12], potato [13], tomato [14] and red seaweed [15].

Artificial neural network (ANN) is a mathematical model for human perception and inspired by biological neural systems. Generally, artificial neural network is a famous tool to simulate complex and non--linear problems. It has brilliant capability to accommodate several input variables to estimate several output variables, even without prior information of the process relations [16]. These networks are important tool being increasingly applied for process control and for a variety of other areas including dynamic modelling, prediction and fault analysis of processes [17]. Lately, several researchers have used the ANNs modelling methods to simulate drying process [17-21].

Although many researchers have simulated the drying process using mathematical models and ANNs, no study considered different thin layers of drying bed, as a critical parameter, in the deep-bed grain dryers. The main objectives of the presented study were to determine the suitable mathematical model and ANN topology for prediction of variations in the grains moisture ratio of different thin layers in the deep bed column of rough rice during hot air drying, and compare the performance of the applied modelling techniques in prediction of drying curves.

EXPERIMENTAL

The common rough rice variety in Isfahan province (central Iran), namely Sazandegi, was selected for the study. Fresh rough rice samples were sealed in polyethylene bags to avoid moisture variation due to evaporation, and stored at 4-6 °C until the experiments were conducted. Prior to each drying experiment, the samples were placed in the laboratory for 4 h to warm up at room temperature. The initial moisture content of the samples was determined using ASAE standard (2001) [22], and applying Eq. (1):

$$M_0 = 100\frac{W_0 - W_\mathrm{d}}{W_\mathrm{d}} \tag{1}$$

where W_d and W_0 are the mass (g) of dried and fresh samples, respectively.

The average value for paddy moisture content was obtained approx. 29.9 mass%. Drying conditions were selected for different combinations of drying air temperature (40, 50, 60 and 70 °C), and drying air velocity at two levels of 0.4 and 0.9 m s^{-1}. Drying time of 100 min was selected for each experiment.

A novel drying column (made of a Plexiglas cylinder with 20 cm in height, 14 cm internal diameter and 5 mm thickness) was fabricated in order to separate the drying bed into four easily removable individual thin layers (each of 5 cm height). The layers of drying column; marked by numbers 1 to 4 from bottom to the top, were filled with wet rough rice and weighed on a digital laboratory balance (Sartorius 18100P with accuracy of 0.01 g, Sartorius Co., Germany). Then, the layers were attached together according to their numbers, as if they were a drying column with a height of 20 cm. The drying chamber was removed in 5 min intervals, the layers were separately weighed, and the instantaneous moisture content for each layer was computed using Eq. (2) [23]:

$$M = \frac{W(M_0 + 100)}{W_0} - 100 \tag{2}$$

where M and M_0 are the moisture content at any given time and the initial moisture content, respectively. Also, W and W_0 are the weight of the samples at any given time (g) and the initial weight of the fresh samples (g), respectively.

Using Eq. (3), the moisture content data were converted to dimensionless moisture ratio (MR) [24]:

$$MR = \frac{M - M_e}{M_0 - M_e} \tag{3}$$

where M_e is the equilibrium moisture content obtained by drying the paddy at the applied air temperatures and velocities until constant weight.

Mathematical modeling

To describe the drying curves of the samples, nine most widely used mathematical models (listed in Table 1) were selected. Curve fitting tool of MATLAB 7.10 (MathWorks, Inc., Natick, MA) and nonlinear regression technique were applied to fit the models to the experimental moisture ratio data. The fit goodness of the mathematical models was evaluated and compared in terms of two famous statistical factors including root mean square error (*RMSE*) and chi-square (χ^2). These parameters are defined as stated in literature [24]:

$$RMSE = \left[\frac{1}{N}\sum_{i=1}^{N}\left(MR_{\mathrm{pre},i} - MR_{\exp,i}\right)^2\right]^{\frac{1}{2}} \tag{4}$$

$$\chi^2 = \frac{\sum_{i=1}^{N}\left(MR_{\exp,i} - MR_{\mathrm{pre},i}\right)^2}{N - Z} \tag{5}$$

where $MR_{\exp,i}$ is the i-th experimental moisture ratio, $MR_{\mathrm{pre},i}$ is the i-th predicted moisture ratio, N is the observation number and Z is the number of constants.

Amongst models, the model having minimum *RMSE* and χ^2 was selected as the best one to describe the drying curves.

Artificial neural networks (ANNs) modelling procedure

In this study, multilayer feed-forward back propagation neural networks (MFBPNNs) were used. Although multilayer feed-forward neural networks (MFNNs) are popular structures among artificial neural networks widely used to predict and control food processing operations and solve complex problems by modelling complex input-output relations, these networks often end up being over trained and adopt trials-and-errors to seek for possible values of parameters for convergence of the global optimum [25]. The back-propagation learning algorithm (BPLA) is a widely used method for MFNN learning in many applications with the great advantage of simple implementation [26]. Using the gradient-descent search method to adjust the connection weights, in the learning process, it increases the ANNs accuracy. The back-propagation ANNs have been successfully used by some researchers in diverse applications, *e.g.*, pattern recognition, location selection and performance evaluations [27-29].

To predict the variations in paddy moisture ratio changes versus drying time, the input layer consisted of four datasets of inlet air temperature, inlet air velocity, drying bed depth and drying time. To select for the best network architecture, several network configurations and various model parameters, including the number of hidden layers, the number of neurons in the hidden layers, different transfer functions, and the training algorithms, might be evaluated [30]. In this study, three and four layer network configurations of ANNs and the hyperbolic tangent sigmoid (Tansig) and log sigmoid (logsig) transfer functions were used. The tansig and logsig functions are defined in Eqs. (6) and (7), respectively [20]:

$$Y_j = \tanh(X_j) = \frac{\exp(X_j) - \exp(-X_j)}{\exp(X_j) + \exp(-X_j)} \tag{6}$$

$$Y_j = \frac{1}{1 + \exp(-X_j)} \tag{7}$$

where X_j is defined as:

$$X_j = \sum_{i=1}^{m} W_{ij} Y_i + b_i \tag{8}$$

Table 1. Mathematical models applied to the drying curves

Model number	Model name	Model expression
1	Newton	$MR = \exp(-kt)$
2	Page	$MR = \exp(-kt^n)$
3	Modified Page	$MR = a\exp(-(kt)^n)$
4	Henderson and Pabis	$MR = a\exp(-kt)$
5	Logarithmic	$MR = a\exp(-kt) + b$
6	Two term exponential	$MR = a\exp(-kt) + (1-a)\exp(-kat)$
7	Wang and Singh	$MR = 1 + at + bt^2$
8	Diffusion Approach	$MR = a\exp(-kt) + (1-a)\exp(-kbt)$
9	Midilli	$MR = a\exp(-kt^n) + bt$

In these equations, m is the number of neurons in the output layer, W_{ij} is the weight of connections between layers i and j, Y_i is the output of the neurons in layer i, and b_j is the bias of the neurons in layer j.

In addition, several back-propagation training algorithms, *e.g.*, scaled conjugate gradient (SCG), Polak-Ribiere conjugate gradient (PCG), BFG quasi-Newton (BFG), and Levenberg-Marquardt (LM) were applied to train the network [31].

The number of neurons in the input and output layers depend on the input and output variables, respectively. Therefore, for each combination, 4 and 1 neurons were applied to the input and the output layers, respectively. Furthermore, the number of neurons in the hidden layer(s) was determined by calibration through several runs.

In order to improve the generalization of ANN models, in this study, early stopping method was used. The obtained experimental data were divided into three subsets. The first subset was used for computation of the gradient and updating weights and biases of the network (the training subset), the second one was used for prevention over fitting (the validation subset), and the last part was allocated to compare the predicted results (the test subset) [18,20]. A total of 70% of the data sets obtained from the experiments were applied for the training, 15% for validations, and the remaining 15% to test the model [18,20,31].

The performance of the developed ANNs models was determined based on the least mean square error (MSE) [20]:

$$MSE = \frac{\sum_{j=0}^{P}\sum_{i=0}^{P}(d_{ij}-y_{ij})^2}{PN} \tag{9}$$

where P is the number of output neurons, N is the number of exemplars in the dataset, y_{ij} is the network output for exemplar i at processing element j, and d_{ij} is the desired output for exemplar i at processing element j.

RESULTS AND DISCUSSION

Mathematical modelling of drying curves

Statistical analysis results obtained through fitting experimental moisture ratio data with the mathematical models are shown in Table 2. As the results show, the Midilli model with sum values of $RMSE$ = = 0.112233 and χ^2 = 0.000559, was found to be the best model for describing drying kinetics of the paddy. In contrast, among the applied models, the Newton model was found to be the worst fit with sum values of $RMSE$ = 1.69229 and χ^2 = 0.096669. In a similar manner, Midilli model has been introduced as the best mathematical model to describe drying curves of some other agricultural crops such as lemon slices [24], potato pulp waste [32], apple slices [33] and white mulberry [34].

Table 2. Sum of RMSE and χ^2 values of the models

Model	Sum of χ^2	Sum of RMSE
Newton	0.096669	1.69229
Page	0.002720	0.24478
Modified Page	0.002679	0.24643
Henderson and Pabis	0.041328	1.09044
Logarithmic	0.006547	0.36337
Two-term exponential	0.000881	0.13766
Wang and Singh	0.038598	0.98070
Midilli	0.000559	0.11233
Diffusion approach	0.000793	0.13364

In order to evaluate the Midilli model, the predicted moisture ratio at any particular drying condition by using the model was compared with experimental data and the results for some randomly selected drying curves are shown in Figure 1. The results indicate the suitability of the Midilli model in describing the drying kinetics of the paddy. For the other drying conditions, similar results were also obtained.

ANNs prediction of rough rice drying curves

Table 3 presents the results of ANNs modelling of the paddy moisture ratio variations during drying process. The effects of hidden layer number and neuron number in each hidden layer on precision of the moisture ratio variation predictions are presented in Table 3. As shown, among the applied networks, the network with a topology of 4-18-18-1, transfer function of tansig and a LM training algorithm had better estimation with the minimum mean square error. The obtained results are comparable with previously reported in the literature by different researchers. Jafari *et al.* (2015) [11] examined different topologies of ANNs to predict the drying curves of onion slices and introduced the feed forward-back propagation network with Levenberg-Marquardt training algorithm, hyperbolic tangent sigmoid transfer function and 2-5-1 topology as the best neural network system. Zare *et al.* (2015) conducted a study to investigate combined hot air/infrared drying process and reported that feed forward-back propagation neural network with topology of 4-8-14-1, training algorithm of Levenberg-Marquardt and a transfer function of hyperbolic tangent sigmoid had the best prediction of drying curves [18]. Momenzadeh *et al.*

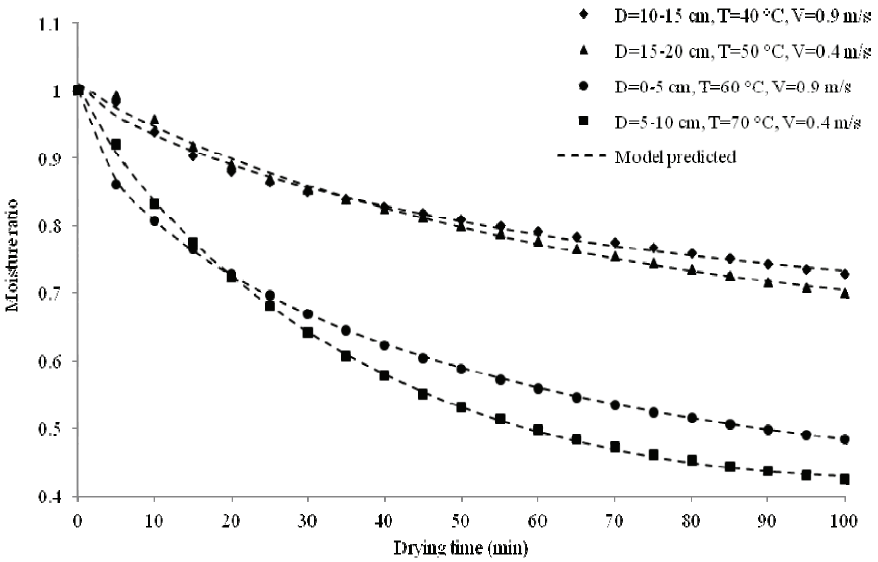

Figure 1. Comparison between moisture ratio data predicted by the Midilli model and the experimental ones for the rough rice during hot air drying.

Table 3. The results of artificial neural networks modeling in prediction of moisture ratio of the rough rice

Network topology	Transfer function	Training algorithm	Number of training cycles	*MSE*
4-6-1	Logsig	SCG	93	0.712
4-6-1	Logsig	CGP	132	0.7591
4-6-1	Logsig	BFG	33	0.728
4-6-1	Logsig	LM	31	0.807
4-6-1	Tansig	SCG	48	0.535
4-6-1	Tansig	CGP	168	0.236
4-6-1	Tansig	BFG	103	0.0422
4-6-1	Tansig	LM	400	0.0323
4-6-10-1	Logsig	SCG	106	0.791
4-6-10-1	Logsig	CGP	48	0.757
4-6-10-1	Logsig	BFG	87	0.837
4-6-10-1	Logsig	LM	42	0.746
4-6-10-1	Tansig	SCG	246	0.107
4-6-10-1	Tansig	CGP	108	0.141
4-6-10-1	Tansig	BFG	107	0.017
4-6-10-1	Tansig	LM	163	0.0051
4-18-18-1	Logsig	SCG	101	0.773
4-18-18-1	Logsig	CGP	100	0.681
4-18-18-1	Logsig	BFG	69	0.757
4-18-18-1	Logsig	LM	17	0.829
4-18-18-1	Tansig	SCG	196	0.051
4-18-18-1	Tansig	CGP	350	0.0198
4-18-18-1	Tansig	BFG	88	0.0096
4-18-18-1	Tansig	LM	37	0.00055
4-30-30-1	Logsig	SCG	113	0.734
4-30-30-1	Logsig	CGP	41	0.827
4-30-30-1	Logsig	BFG	78	0.803
4-30-30-1	Logsig	LM	37	0.723
4-30-30-1	Tansig	SCG	321	0.0216
4-30-30-1	Tansig	CGP	292	0.0354
4-30-30-1	Tansig	BFG	67	0.0182
4-30-30-1	Tansig	LM	34	0.0007

(2012) applied artificial neural network to predict drying time of green pea in a microwave-assisted fluidized bed dryer and found that a network with logsig transfer function and back propagation algorithm made the most accurate predictions [35]. Yousefi *et al.* (2012) [36] estimated the moisture content of papaya fruit during drying in a cabinet dryer by using artificial neural networks and reported the multi-layer perceptron network with 3-9-1 topology, LM training algorithm and the logsig transfer function as the best network to predict the drying curves.

To assess the performance of the preferred artificial network in modelling rough rice drying curves, the predicted moisture content values were plotted (Figure 2). As presented, the ANN could be successfully used to predict paddy moisture ratio variations during the drying process. Moreover, the variation in the experimental and predicted moisture ratio of the grains is illustrated by randomly selected drying condition, Figure 3. These figures show very good agreement between experimental data and those obtained from ANN. Similar results were calculated for other drying conditions indicating a suitable prediction.

Comparison between mathematical and ANNs modeling techniques

Based on the obtained results, the applied mathematical models and ANNs could predict variation of moisture ratio values of the rough rice kernels during drying process with high accuracy. However, the Midilli model and the best ANN were compared by using *RMSE* indicator. For the drying layers at different drying conditions, *RMSE* values were calculated by using Eq. (4) and the results are listed in Table 4. As shown, for all the conditions, the ANN performed better in prediction of moisture ratio variation in comparison with the Midilli model. The obtained results indicate the capability of ANNs in predicting the drying curves, especially when we consider the simple arithmetic operations and low computing time of the artificial neural networks. Similar results have been reported in the literature about advantageous application of ANNs and a high accuracy obtained for final selected topologies in predicting drying curves of different products such as Elaeagnus angustifolias [37], mushroom [38], papaya fruit [36] and onion [11].

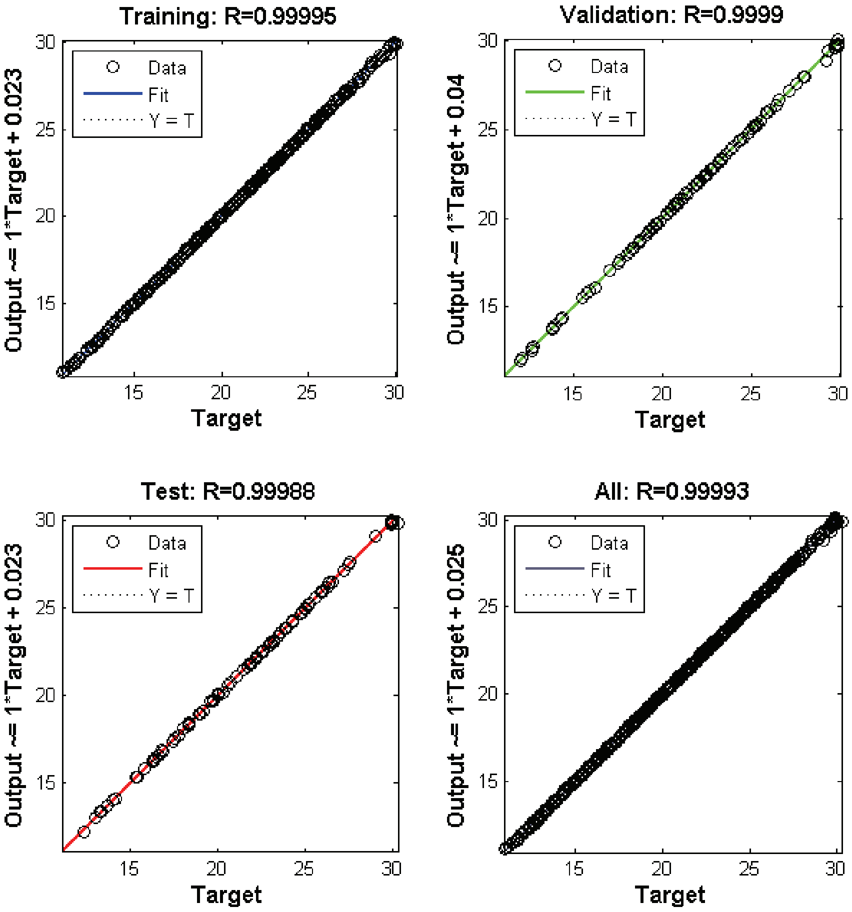

Figure 2. Comparison between experimental and predicted values of moisture ratio of the rough rice during training, validation and testing of the best ANN model, provided in MATLAB.

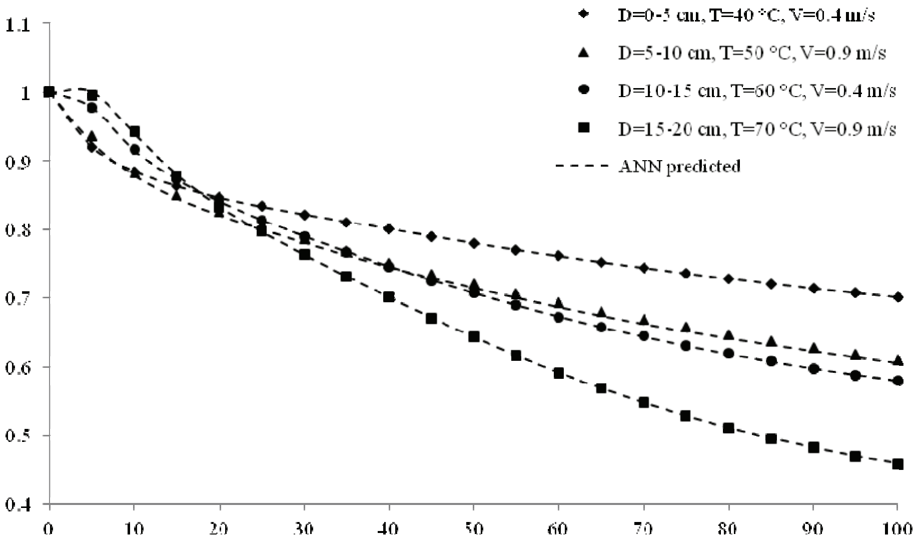

Figure 3. Comparison between moisture ratio data predicted by the best ANNs and the experimental ones for the rough rice during hot air drying.

Table 4. RMSE values for the Midilli model and the best ANN at different drying conditions

Temperature °C	Velocity m s^{-1}	Layer 1 (0-5 cm)		Layer 2 (5-10 cm)		Layer 3 (10-15 cm)		Layer 1 (15-20 cm)	
		Midilli model	Best ANN	Midilli model	Best ANN	Midilli model	Best ANN	Midilli model	Best ANN
40	0.4	0.002432	0.000471	0.004238	0.000561	0.005444	0.000483	0.005616	0.000619
	0.9	0.002841	0.000539	0.008346	0.00127	0.003964	0.000397	0.009431	0.002164
50	0.4	0.003237	0.000374	0.002974	0.000548	0.003983	0.000607	0.005924	0.001151
	0.9	0.003125	0.000518	0.006109	0.001125	0.004167	0.000591	0.006281	0.002781
60	0.4	0.004106	0.000603	0.004813	0.001089	0.003146	0.000485	0.003562	0.000672
	0.9	0.002941	0.001092	0.001466	0.001132	0.003328	0.000836	0.004916	0.00159
70	0.4	0.004686	0.000507	0.003642	0.000736	0.004645	0.000629	0.005394	0.000696
	0.9	0.007139	0.001104	0.004518	0.000821	0.005108	0.000752	0.004170	0.000864

CONCLUSIONS

Deep bed column (20 cm) of rough rice kernels was dried using a hot air dryer at different air conditions including four temperature levels (40, 50, 60 and 70 °C) and two flow rate levels (0.4 and 0.9 m s^{-1}). The drying bed was divided into 4 thin layers (each 5 cm in height) and the kinetics of the thin layers of the grains was investigated. Among the nine famous mathematical models used for prediction of the drying curves, the Midilli model was found to be the best for describing drying curves according to the minimum *RMSE* and chi-square values. The different artificial neural networks were examined to predict the variation in moisture ratio of the rough rice during the drying process. The ANN with 4-18-18-1 topology, transfer function of hyperbolic tangent sigmoid and a Levenberg-Marquardt back propagation training algorithm was found to be the best model for prediction of variations in the rough rice moisture content during hot air drying. The comparison between the Midilli model and the best ANN showed that ANN modeling could be effectively used for prediction of grain drying curves.

REFERENCES

[1] M. Torki-Harchegani, M. Sadeghi, A. Moheb, Z. Naghavi, Heat Mass Transfer **50** (2014) 1717-1725

[2] N.S. Babamiri, E.A. Asli-Ardeh, Int. J. Agric. Crop Sci. **6** (2013) 529-533

[3] C. Sangdao, S. Songsermpong, M. Krairiksh, Drying Technol. **29** (2011) 35-46

[4] S. Soponronnarit, S. Prachayawarakorn, W. Rordprapat, A. Nathakaranakule, W. Tia, Drying Technol. **24** (2006) 1457-1467

[5] D. Evin, H. Gul, V. Tanyildizi, Drying Technol. **26** (2008) 1577-1583

[6] M.S.H. Sarker, M. Nordin Ibrahim, N.A. Aziz, P.M. Salleh, Energy Convers. Manage. **77** (2014) 389-395

[7] M. Torki-Harchegani, D. Ghanbarian, A. Ghasemi Pirbalouti, M. Sadeghi, Renew. Sustain. Energy Rev. **57** (2016) 407-418

[8] I. Doymaz, O. Ismail, Food Bioprod. Process. **89** (2011) 31-38

[9] L.A. Duc, J.W. Han, D.H. Keum, J. Stored Prod. Res. **47** (2011) 32-38

[10] S. Minaei, A. Motevali, E. Ahmadi, M. H. Azizi, J. Agric. Sci. Technol. **14** (2012) 311-325

[11] S.M. Jafari, M. Ganje, D. Dehnad, V. Ghanbari, J. Food Process. Preserv. (2015), doi: 10.1111/jfpp.12610

[12] Y. Tulek, J. Agric. Sci. Technol. **13** (2011) 655-664

[13] R. Amiri Chayjan, J. Agric. Sci. Technol. **14** (2012) 1229--1241

[14] R. Sadin, G.R. Chegini, H. Sadin, Heat Mass Transfer **50** (2014) 501-507

[15] A. Fudholi, K. Sopian, M.Y. Othamn, M.H. Ruslan, Energy Build. **68** (2014) 121-129

[16] S. Haykin, Neural networks, a comprehensive foundation, Macmillan College, New York, 1994

[17] N. Behroozi Khazaei, T. Tavakoli, H. Ghassemian, M.H. Khoshtaghaza, A. Banakar, Comput. Electron. Agric. **98** (2013) 205-213

[18] D. Zare, H. Naderi, M. Ranjbaran, Drying Technol. **19** (2015) 1-13

[19] K. di Scala, G. Meschino, A. Vega-Gálvez, R. Lemus--Mondaca, S. Roura, R. Mascheroni, Food Sci. Technol. **33** (2013) 411-416

[20] M. Tohidi, M. Sadeghi, S.R. Mousavi, S.A. Mireei, Turk. J. Agric. For. **36** (2012) 738-748

[21] I. Farkas, P. Reményi, A. Biró, Comput. Electron. Agric. **29** (2000) 99-113

[22] ASAE Standard (2001), ASAE S352.2 FEB03

[23] D. Ghanbarian, M. Baraani Dastgerdi, M. Torki-Harchegani, Heat Mass Transfer (2015), doi: 10.1007/s00231--015-1629-9

[24] M. Torki-Harchegani, M. Ghasemi-Varnamkhasti, D. Ghanbarian, M. Sadeghi, M. Tohidi, Heat Mass Transfer **52** (2016) 281-289

[25] Z.G. Che, T.A. Chinag, Z.H. Che, Int. J. Innovative Comput. Inf. **7** (2011) 5839-5850

[26] B. Choi, J.H. Lee, D.H. Kim, Neurocomputing **71** (2008) 3640-3643

[27] M. Bongards, Water Sci. Technol. **43** (2001) 189-196

[28] Y.M. Wu, Y.Q. Wang, L. Li, Chin. J. Mech. Eng. **17** (2006) 2140-2144

[29] Z.H. Che, Comput. Ind. Eng. **58** (2010) 625-637

[30] L. Momenzadeh, A. Zomorodian, D. Mowla, Food Bioprod. Process. **89** (2011) 15-21

[31] P. Tripathy, S. Kumar, Int. J. Therm. Sci. **48** (2008) 1452--1459

[32] W.T. Carvalho, T.F. Oliveira, F.A. Silva, M. Caliari, M.S. Soares Júnior, Food Sci. Technol. **34** (2013) 116-122

[33] M. Beigi, Heat Mass Transfer (2015), doi: 10.1007/s00231-015-1646-8

[34] D. Evin, J. Mech. Sci. Technol. **25** (2011) 2711-2718

[35] L. Momenzadeh, A. Zomorodian, D. Mowla, J. Agric. Sci. Technol. **14** (2012) 513-522

[36] A. Yousefi, V. Asadi, S.M. Nassiri, M. Niakousari, S. Khodabakhsh Aghdam, Philipp. Agric. Sci. **95** (2012) 246-251

[37] A. Abbaszadeh, A. Motevali, M.H. Khoshtaghaza, M. Kazemi, Int. Food Res. J. **18** (2011) 1321-1328

[38] A. Ghaderi, S. Abbasi, A. Motevali, S. Minaei, Chem. Ind. Chem. Eng. Q. **18** (2012) 283-293.

MOHSEN BEIGI[1]
MEHDI TORKI-HARCHEGANI[2]
MAHMOOD MAHMOODI-ESHKAFTAKI[3]

[1]Department of Mechanical Engineering, Tiran Branch, Islamic Azad University, Tiran, Iran
[2]Young Researchers and Elite club, Shahrekord Branch, Islamic Azad University, Shahrekord, Iran
[3]Department of Farm Machinery Mechanics, Jahrom Universtiy, Jahrom, Iran

NAUČNI RAD

PREDVIĐANJE KINETIKE SUŠENJA PIRINČA: KOMPARATIVNO PROUČAVANJE MATEMATIČKOG MODELOVANJA I VEŠTAČKE NEURONSKE MREŽE

Ovaj rad je imao za cilj istraživanje sušenje grubih pirinčanih zrna u sloju različite debljine pri različitim temperaturama i protocima vazduha. Izvršeno je poređenje matematičkog modela sušenja u tankom sloju i veštačke neuronske mreže. Devet matematičkih modela je korišćeno za simulaciju kinetike sušenja, a kao najbolji pokazao se model Midillija. Istražene su i mogućnosti predviđanja promene vlaćnosti zrna različitim veštačkim neuronskim mrežama (VNM). VNM sa topologijom 4-18-18-1, prenosnom hiperboličko tangento sigmoidnom funkcijom i Levenberg-Marquardt algoritmom sa pozitivnim i negativnim povratnim prostiranjem za treniranje je dala najbolje rezultate sa maksimalnim koeficijentom korelacije i minimalnom srednjom kvadratnom greškom. Osim toga, otkriveno je da je VNM imala bolje performanse u predviđanju krive sušenje sa manjom srednja srednjom kvadratnom greškom.

Ključne reči: matematičko modelovanje, veštačke neuronske mreže, pozitivno-negativno povratno prostiranje, Paddy.

CI&CEQ
Chemical Industry & Chemical Engineering Quarterly

Available on line at
Association of the Chemical Engineers of Serbia *AChE*
www.ache.org.rs/CICEQ

Chem. Ind. Chem. Eng. Q. 23 (2) 259–267 (2017) CI&CEQ

SEYED MOHAMMAD SADEGH HOSSEINI DAVARANI[1]
HASSAN HASHEMIPOUR[1]
ALIREZA TALEBIZADEH[2]

[1]Department of Chemical Engineering, Faculty of Engineering, Shahid Bahonar University of Kerman, Kerman, Iran
[2]Department of Chemical Engineering, Faculty of Engineering, Vali-e-Asr University of Rafsanjan, Rafsanjan, Iran

SCIENTIFIC PAPER

UDC 66.094.3:547.211:544

OLEYLAMINE-MODIFIED IMPREGNATION METHOD FOR THE PREPARATION OF A HIGHLY EFFICIENT Ni/SiO$_2$ NANOCATALYST ACTIVE IN THE PARTIAL OXIDATION OF METHANE TO SYNTHESIS GAS

Article Highlights

- A silica-supported nickel nanocatalyst was prepared by oleylamine-modified impregnation method
- Oleylamine was added to the precursor solution to improve Ni dispersion and Ni-silica interaction
- The modified catalyst showed high catalytic activity for the partial oxidation of methane

Abstract

In this research, a novel modified wet impregnation method has been successfully developed to synthesize 5% Ni/SiO$_2$ nanocatalyst with high catalytic activity and stability for the partial oxidation of methane. Oleylamine was used as a capping agent in the impregnation solution to improve Ni dispersion and interaction with silica surfaces. The product was analyzed and characterized by X-ray diffraction (XRD), Fourier transform infrared (FT-IR) spectroscopy, N$_2$ physisorption measurement and transmission electron microscopy (TEM) and temperature-programmed H$_2$ reduction (H2-TPR). Partial oxidation of methane over the modified catalyst was performed in a continues-flow fixed-bed reactor under atmospheric pressure at 700 °C. The modified catalyst showed 91% CH$_4$ conversion, 86% H$_2$ yield and 95% CO selectivity, and these results almost remained constant within 5 h reaction on stream. The excellent catalytic performance of the catalyst was reasonably attributed to the small and uniform distribution of Ni nanoparticles on the support, and structural characterization confirmed this conclusion.

Keywords: 5% Ni/SiO$_2$, oleylamine, partial oxidation of methane, wet impregnation.

Steam reforming and catalytic partial oxidation of methane (CPOM) are the important processes in the hydrogen production [1]. CPOM is a slightly exothermic process and occurs more rapidly than the steam reforming, thereby permitting the use of a small reactor volume and consequently some economic advantages in hydrogen production [2-4]. In addition, CPOM process generates a favorable H$_2$/CO ratio, suitable for methanol or Fisher-Tropsch synthesis [5-8]. Noble metals (Rh, Pt, Ru and Ir) are highly active and selective catalysts for CPOM. However, for industrial applications, nickel catalysts have been mainly used because nickel is much cheaper and more available than noble metals [9-15].

Activity and stability of the catalyst also depend on the nature of its support. Among different binary oxides, alumina is an important catalyst support in the CPOM reaction. The main advantage of this oxide is related to its acid/base characteristics facilitating interaction between the metal species and alumina surface [16]. Furthermore, silica has better textural property than alumina and it is a suitable porous sup-

---

Correspondence: S.M.S. Hosseini Davarani, Department of Chemical Engineering, Faculty of Engineering, Shahid Bahonar University of Kerman, Kerman, Iran.
E-mail: chehosseini@gmail.com
Paper received: 11 December, 2015
Paper revised: 26 February, 2016
Paper accepted: 12 August, 2016

https://doi.org/10.2298/CICEQ151211040H

port for catalyst preparation [17]. Unlike alumina support, silica interacts with metals weakly and preparation of highly dispersed metal active sites on the silica surface is more difficult. It would be more interesting to prepare a silica-supported catalyst with high surface area and with improved metal-silica interaction. In practice, high dispersion of active sites on the silica could be achieved by applying innovative synthesis methodology, such as emulsion or sol-gel [13,18].

The wet impregnation method is one of the conventional processes for preparing the solid catalyst and it works best if ion/solid interaction is involved [19]. The first step of the wet impregnation, deposition of metal ions on the surface support is very important, and this step affects quality of the final catalyst. Various techniques have been investigated in order to modify the wet impregnation for preparation of the high dispersion catalysts, such as the addition of ammonia, ethylene diamine or ethylene glycol into the impregnation solution [20-25]. Usage of organic additives, such as polyols, sugars or polyacids and α- or γ-cyclodextrin is efficient route to optimize metal dispersion over an alumina or silica support [26,27].

An effective approach to decrease the metal particle size is the addition of organic compounds that could coordinate with metal cation. Oleyamine is a long chain alkyl amine, which could act as a solvent, surfactant, reducing or capping agent for the synthesis of nanoparticles [28]. Although oleylamine (OAm) is insoluble in water, it exhibits high affinity to metals through its -NH_2 functional groups. According to the recent research study, OAm-capped Ag nanoparticles were successfully synthesized in aqueous solution. Although oleylamine was hydrophobic, it had functionalized Ag particles in an aqueous media [29].

According to the literature, to date, no researcher has used oleylamine as a modifying agent for catalyst preparation. In the present work, using oleylamine in the impregnation solution, a modified 5% Ni/SiO_2 catalyst was produced. The catalytic performance of the modified catalyst was studied for partial oxidation of methane and compared with conventional catalyst. The prepared catalysts were characterized by XRD, FTIR, TPR, N_2-physisorption and TEM analyses to elucidate their catalytic performance.

EXPERIMENTAL

Catalyst preparation

A 5% Ni/SiO_2 catalyst was prepared as follows: Ni $(NO_3)_2{\cdot}6H_2O$ was dissolved completely in 10 ml of distilled water and then 2 ml of oleylamine (OAm) was added to the solution under magnetic stirring. Then, 1 g of the porous silica gel (granulometry: 63–200 μm) pretreated under vacuum at 160 °C for 6 h, was introduced into the reaction vessel and the resulting suspension was evaporated slowly at 40 °C, under mild stirring for 24 h to obtain a wet gel. Thus obtained product was dried under vacuum and finally calcined for 4 h at 500 °C in order to be considered as a modified catalyst. An unmodified 5% Ni/SiO_2 catalyst was also prepared using the same procedure, but without oleylamine addition. All the chemicals used were analytical reagent grade and obtained from Merck and Aldrich Companies. For the sake of convenience, the modified and unmodified catalysts were denoted as M-Ni/SiO_2 and UM-Ni/SiO_2, respectively.

Catalyst characterization

X-ray diffraction (XRD) was used to investigate the crystalline phases of the Ni species in the catalysts. The XRD patterns were collected by a D_8-Advance Bruker diffractometer with CuKα radiation (λ = = 1.5406 Å) in a step scanning mode over 2θ angle between 10 and 80° at a scan speed of 1.5°/min.

The functional groups of the catalysts were investigated by Fourier-transform infrared spectroscopy (FTIR) using a Matson 1000 spectrometer. The spectrometer was used in the transmission mode with a resolution of 5 cm^{-1} in the range of 400-4000 cm^{-1}.

The specific surface area and pore size distribution of the calcined catalysts were measured by analysis of nitrogen isotherms collected at 77 K using a BEL Sorp adsorption-desorption apparatus. Prior to the measurements, the samples (0.1 g each) were degassed at 573 K for 2 h under vacuum.

The reduction behavior of the catalysts was characterized by using temperature-programmed H_2 reduction (H_2-TPR). The TPR test was carried out according to the following procedure: 50 mg of each sample was loaded into U-shaped quartz reactor and heated up to 1000 °C in a flow of 7% H_2/Ar gas mixture (20 ml/min) at the heating rate of 10 °C/ min. The H_2 consumption was monitored with a thermal conductivity detector (TCD). It should be noted that XRD, FTIR and TPR analyses were carried out on the calcined catalysts.

The Ni dispersion on the catalyst samples was examined by transmission electron microscopy (TEM) using a Philips CM20 instrument. Prior to TEM analysis, the catalysts were reduced in a flow of 5 vol.% H_2 at 800 °C for 1 h and then ultrasonically dispersed in ethanol. The obtained suspension was deposited on a carbon-coated copper grid.

Catalyst testing

The partial oxidation of methane was carried out in a quartz fixed-bed reactor with a 7.0 mm inner diameter and 43 cm in length, at atmospheric pressure. The reaction temperature was controlled by an electrical tube furnace and a digital temperature controller (TC NX4 Han young). The gas flow rates were adjusted by mass flow controllers (Alicat). For the reaction study, 100 mg of the reduced catalyst was loaded into the center of the reactor. Subsequently, the bed temperature was increased to 700 °C at a heating rate of 10 °C/ min. Argon was passed through the reactor during heating. Gas feed, consisting of CH_4, O_2 and Ar (high purity, 99.999%) with mole ratio of 2/1/4, entered into the reactor with a flow rate of 50 ml/min. The water vapor in the product stream was condensed and separated by cool trapping. The reaction products were analyzed by an online gas chromatograph (GC-2550 TG) equipped with a TCD using Ar as the carrier gas. The mass balance of carbon and hydrogen is typically within a ±5% error range. The conversion of CH_4 (x_{CH_4}), the selectivity of CO (S_{CO}) and the yield of H_2 (Y_{H_2}) were calculated using the following equations:

$$x_{CH_4} = 100\frac{F_{CH_4}(\text{in}) - F_{CH_4}(\text{out})}{F_{CH_4}(\text{in})} \tag{1}$$

$$S_{CO} = 100\frac{F_{CO}(\text{out})}{F_{CO}(\text{out}) + F_{CO_2}(\text{out})} \tag{2}$$

$$Y_{H_2} = 100\frac{F_{H_2}(\text{out})}{2F_{CH_4}(\text{in})} \tag{3}$$

RESULTS AND DISCUSSION

Characterization

The XRD patterns of M-Ni/SiO_2 and UM-Ni/SiO_2 are presented in Figure 1. A broad peak around 22°, related to the amorphous structure of the SiO_2, appeared in both catalysts spectra [30]. The characteristic peaks at 37, 43, 63 and 72° related to the NiO phase are clearly observed in UM-Ni/SiO_2 and these peaks are entirely matched to (111), (200), (220) and (311) crystal planes, respectively.

As evident in Figure 1, the NiO characteristic peaks are broad for M-Ni/SiO_2, indicating that the NiO species are small enough in size to be highly dispersed on the support surfaces. The NiO crystallite size in M-Ni/SiO_2 and UM-Ni/SiO_2 samples, estimated according to the XRD patterns, were 5.4 and 10.8 nm, respectively (Table 1).

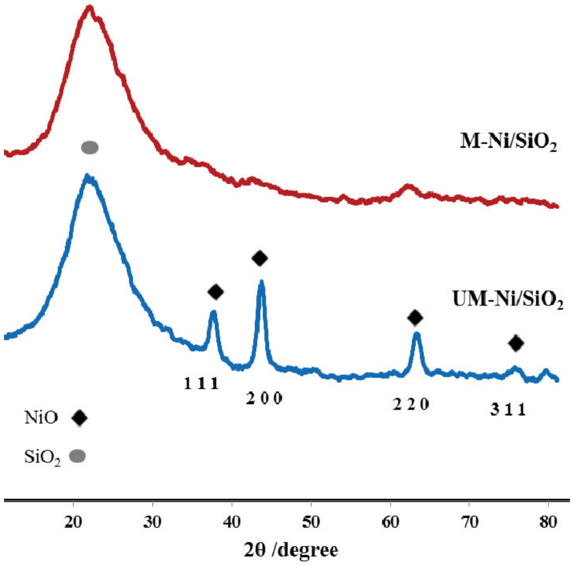

Figure 1. XRD patterns of the calcined catalyst samples.

Table 1. Results of BET surface area, pore volume, pore diameter and nickel crystallite size of the catalyst samples

Sample	Surface area m^2/g	Pore volume cm^3/g	Average pore diameter, nm	D_{XRD} nm
Silica gel	500	0.8	6	-
M-Ni/SiO_2	304	0.63	9.7	~5.4
UM-Ni/SiO_2	270	0.6	11	~10.8

The FTIR spectra of silica gel, M-Ni/SiO_2 and UM-Ni/SiO_2 are shown in Figure 2. According to the FTIR spectrum of silica gel, the specified types of silica structural bands are visible. A broad band at around 3447 cm^{-1} is related to -OH groups (hydrogen bond), which can be attributed to Si-OH vibrations. The bands observed at 1100 and 807 cm^{-1} indicate Si-O-Si and Si-O vibrations, respectively. The free water adsorbed on the silica surface is characterized by a band at 1618 cm^{-1} [31].

Some researchers determined that in the case of Ni/SiO_2 catalyst, the characteristic vibrations of silica are affected by the NiO species, so that the effect is more evident in the samples containing higher nickel loading. The band intensities slightly increase with the increase of Ni content [30]. Compared to UM-Ni/SiO_2 FTIR spectrum, the Si-O bands and O-H band in M-Ni/SiO_2 are seen with higher intensity (Figure 2). Since Ni loading in both catalysts is equal, these results indicate that the distributed species of NiO in M-Ni/SiO_2 are smaller size than in UM-Ni/SiO_2.

Figure 3A shows N_2-physisorption isotherms of the calcined catalyst samples. Isotherms hysteresis loops in both catalysts seem to be of type H1, as defined by IUPAC [32]. Type H1 is often related to porous materials which consist of agglomerates of approximately uniform spheres.

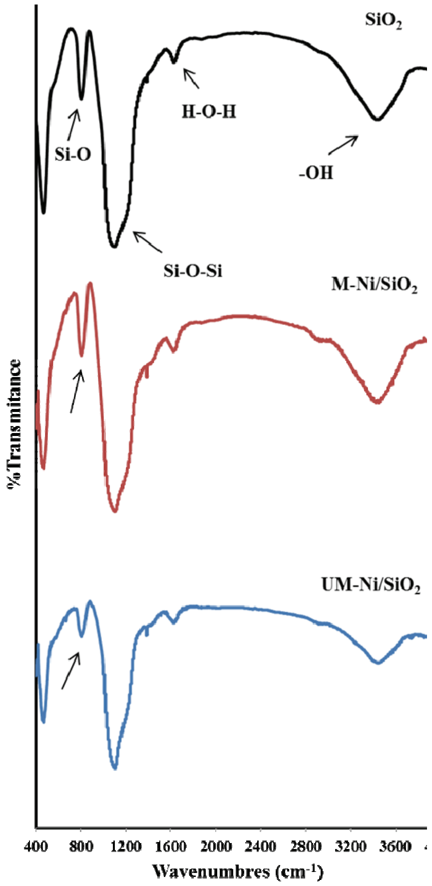

Figure 2. FTIR spectra of the silica gel and calcined catalyst samples.

Table 1 shows the specific surface area and pore volume of the silica gel and the two calcined catalysts. In comparison to silica gel as pure support, the BET surface area of both catalysts is decreased. This decrement could be the result of pore blockage after the metal oxide impregnation or pore collapsing due to the further heating and phase reconstitution.

Although, the pore volume of the catalyst samples is approximately the same, but the specific surface area of the modified catalyst (303 m^2/g) is higher than the unmodified catalyst (270 m^2/g). This result indicates that the M-Ni/SiO$_2$ catalyst has smaller pores than the UM-Ni/SiO$_2$ catalyst, as confirmed by the pore size distribution of the catalysts (Figure 3B). Therefore, it seems that the M-Ni/SiO$_2$ catalyst with higher specific surface area and smaller pore size could show greater activity and selectivity in the partial oxidation of methane.

TPR analysis is used mainly in catalysis research to evaluate the interaction of active metal site with the oxide support [33]. Figure 4 shows TPR profiles of the catalyst samples. According to the TPR profile of UM-Ni/SiO$_2$, the reduction peak around 380 °C is related to free NiO particles and the peak around 430 °C could be assigned to NiO species that interacted weakly with silica [34]. Based on the TPR results of UM-Ni/SiO$_2$, it is anticipated that during CPOM reaction, the NiO species could be sintered and that catalyst could become quickly deactivated. The TPR profile of M-Ni/SiO$_2$ showed that the most of the reduction reactions occurred at around 650 °C, as con-

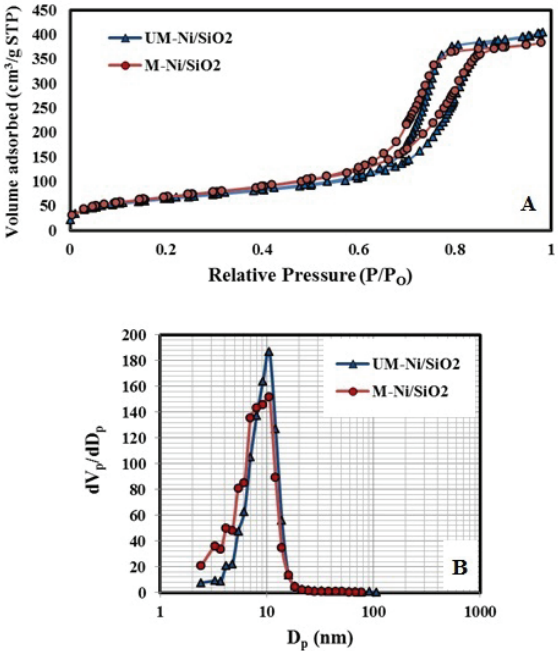

Figure 3. N_2 adsorption-desorption isotherms (A) and pore size distribution (B) of the calcined catalyst samples.

cluded by the majority of NiO species strong interaction with the silica support.

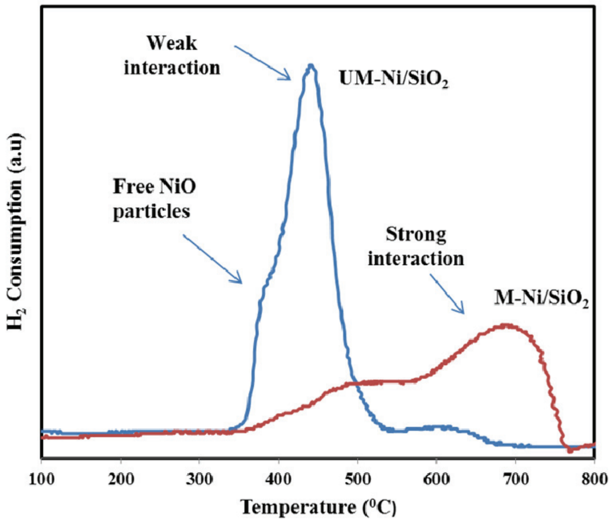

Figure 4. H_2-TPR profiles of the calcined catalyst samples.

Table 2 shows the TPR hydrogen consumption and the amount of reduced NiO in catalyst samples. Although, M-Ni/SiO$_2$ catalyst showed difficult reducibility, the majority of the NiO species were reduced after high temperature reduction.

Table 2. TPR hydrogen consumption and reduced NiO of the catalyst samples

Sample	TPR hydrogen consumption[a], mol/10^{-5}	Nominal Ni load, mol/10^{-5}	Reduced NiO, %
UM-Ni/SiO$_2$	3.87	4.26	90.8
M-Ni/SiO$_2$	3.61	4.26	84.8

[a]Based on calculating the TPR peak area of both catalysts. Before calculating the area of the TPR peak, the baseline of the TPR graph was corrected

XRD and FTIR analyses reasonably indicated that the NiO species in M-Ni/SiO$_2$ were very small, as clearly proved by TEM images (Figure 5).

Figure 5A represents a TEM image of the modified catalyst (M-Ni/SiO$_2$). As clearly observed, small Ni species are homogeneously dispersed in the catalyst, so that the average size is about 5 nm. This result relates to the enhanced interaction between Ni and silica (see TPR results). Based on Figure 5B, the catalyst prepared by conventional method (UM-Ni/ /SiO$_2$) resulted in larger Ni species and lower dispersion than the modified catalyst.

Catalytic performances

CH_4 conversion, H_2 yield and CO selectivity of the catalysts are presented in Figure 6.

It is obvious that both catalysts showed higher performance at the beginning of reaction, although

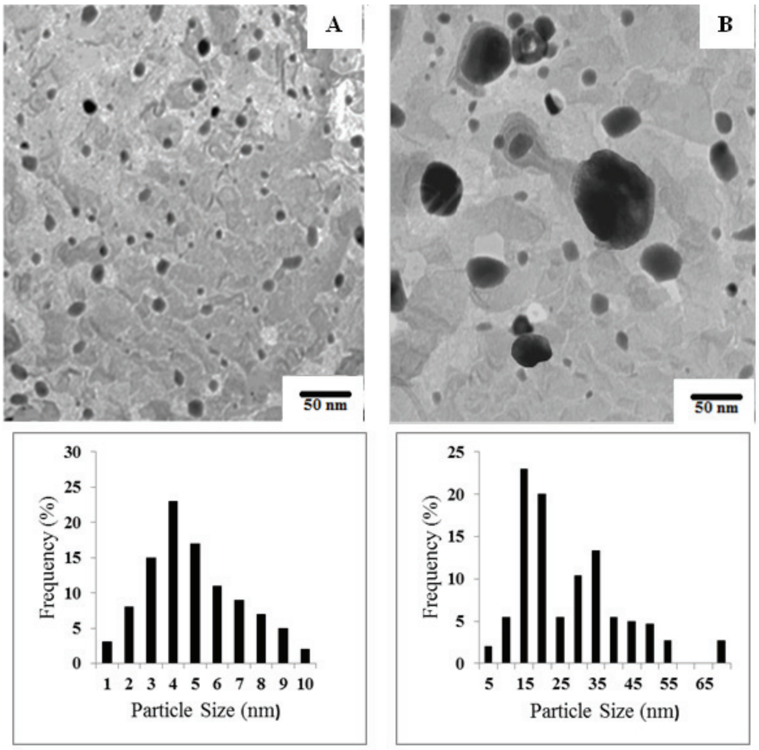

Figure 5. TEM images of reduced catalysts: A) M-Ni/SiO$_2$ and B) UM-Ni/SiO$_2$; the Ni particle size distribution was obtained by measuring at least 100 particles; the average Ni particle size (nm) was calculated by the following normal statistical formula: ($d = \Sigma n_i d_i / \Sigma n_i$).

the unmodified catalyst (UM-5% Ni/SiO$_2$) presented lower overall performance and deactivated rapidly (conversion: 77 to 33%, H$_2$ yield: 71 to 40% and CO selectivity: 92 to 69%). Also, these results indicate that H$_2$ yield and CO selectivity decreased as methane conversion decreased (based on experimental observations, the rate of water formation in trap is increased). The modified catalyst (M-5% Ni/SiO$_2$) showed 91% CH$_4$ conversion, 86% H$_2$ yield and 95% CO selectivity, and these results almost remained constant within 5 h reaction on stream.

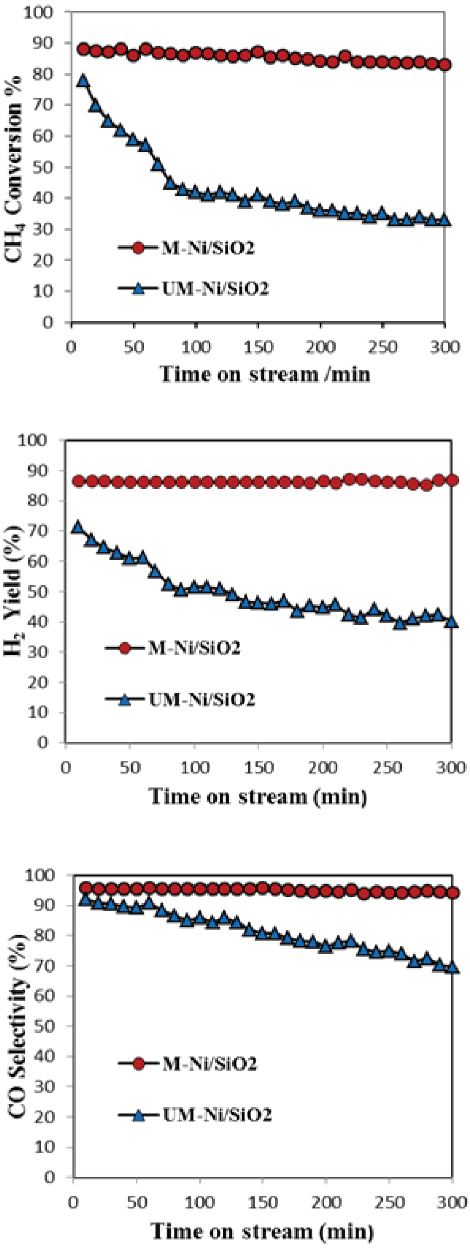

Figure 6. Catalytic performances of the reduced catalyst samples during 5 h partial oxidation of methane in a quartz reactor under condition of: t = 700 °C, feed flow rate, 50 ml/min, CH_4:O_2 mole ratio: Ar = 2:1:4.

According to the literature, the weakly interacting Ni species in Ni/SiO$_2$ catalyst has been reported as the “free state” of the Ni active phase because of its mobility, which leads to migration and aggregation of the particles at high temperatures [35,36]. Based on TPR results (Figure 4), there are weak interactions between Ni species and silica surfaces in UM- Ni/SiO$_2$ catalyst. Therefore, it seems that Ni sintering is a major reason for the deactivation of UM-Ni/SiO$_2$ catalyst. However, in M-Ni/SiO$_2$, nickel species are highly dispersed on the catalyst and the enhanced interaction between Ni species and silica surface might be responsible for its high activity and good resistance to agglomeration of the nickel particles. In addition, since the carbon balance (>95%) had not changed noticeably during the reaction, it seems that the deactivation of UM-Ni/SiO$_2$ catalyst was not related to coking.

Effect of oleylamine. The results section was devoted to the characterization and catalytic activity of the catalyst samples and it was concluded that oleylamine-modified impregnation method had significant effects on the structure of the synthesized catalyst due to improvement of metal-support interaction and nickel particle size reduction. In this section, the authors would like to highlight the possible interaction between Ni ions and silica surfaces in the first step of the impregnation process, in the absence and presence of oleylamine, which would help understand how oleylamine improves the structure of the catalyst.

The impregnation procedure could be described by the concept of interfacial coordination chemistry [37]. The main step in this process is the adsorption of transition-metal complexes on the oxide surfaces. The adsorption could be explained in terms of electrostatic interaction of the cationic complex with a negatively charged surface and inner-sphere complex formation where specific surface groups substitute some of the original ligands of the complex [38]. According to Kiselev-Zhuravlev model (2000), amorphous silica possesses about 4.9 OH per nm^2, approximately half of them present in the vicinity as proposed by the model [39]. Surface silanol groups act as an amphoteric material and depending on the solution pH and exist as SiOH, SiO$^-$ or SiOH^{2+} species. At pH values higher than the isoelectric point of silica gel (pH ≈2.2), negative charge is present on the silica surface [37]. However, negative charge carried by a silica surface at pH <8 is low [38]. When nickel (II) nitrate is dissolved in water, an aqueous Ni complex ([Ni(H$_2$O)$_6$]$^{2+}$) is formed (under ambient conditions) [40]. When the Ni solution (pH 4.8) is impregnated onto silica gel, some of the Ni aquo complexes are adsorbed by negative charge on the silica surface and could be grafted onto the silica, through the substitution of water ligands by SiO^- surface groups (Scheme 1A). On the other hand, Ni aquo complexes are linked together via water molecules, which may cause condensation of the complexes by olation or oxolation bridge between the two complexes [21]. These processes result in polynuclear species which leads to large distributed Ni species during drying and calcination treatment. These large species could be sintered and completely separated from silica under high temperature conditions. The TPR results of UM-Ni/SiO_2 (Fig 4) confirmed this conclusion, especially when the free NiO particles were observed in the catalyst.

Scheme 1B shows the suggested interaction of nickel with silica in the presence of oleylamine. It seems that reaction of oleylamine (OAm) with Ni(II) ion at 4:1 molar ratio, results in the formation of $[Ni(OAm)_4(H_2O)_2]^{2+}$ complex. Although oleylamine (OAm) is insoluble in water, it exhibits high affinity for metal ions through its $-NH_2$ functional groups. When the modified solution (pH=8.2) is impregnated on silica gel, the amount of negatively charged SiO^- groups are increased. Therefore, number of the grafted Ni species is increased. In addition, the grafted complexes are protected by hydrophobic head of OAm molecules and the condensation reactions could not occur. As a result, during removal of the OAm ligands by calcination, the grafted complexes transform into small Ni species that strongly interact with the support. According to the FTIR results (Fig 2) carbon vibration band was not observed in the FTIR spectrum of the M-Ni/SiO_2 catalyst, indicating that no carbonaceous residues remain on the fresh catalyst surface. This result proves that all of the organic matter was removed after calcination treatment.

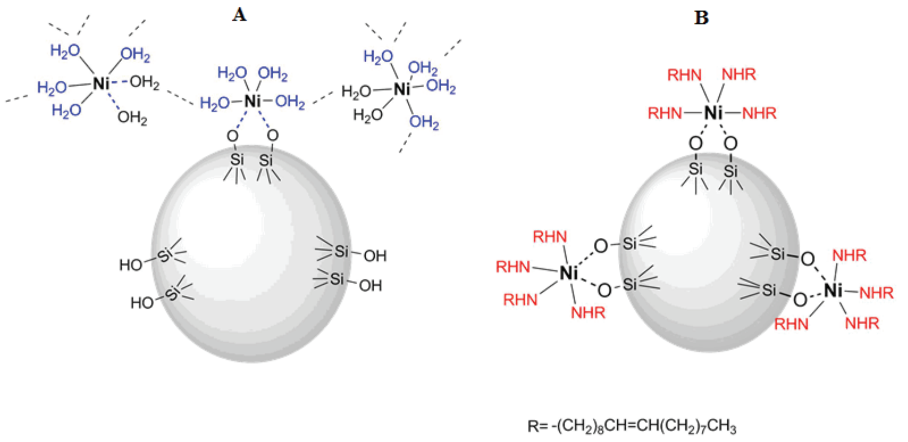

Scheme 1. The Ni interaction with silica: A) in the absence of oleylamine and B) in the presence of oleylamine.

CONCLUSION

In this work, a modified 5% Ni/SiO_2 catalyst (M-Ni/SiO_2) was prepared by impregnation method using $Ni(NO_3)_2 \cdot 6H_2O$ as a nickel precursor, oleylamine as a capping agent and silica gel as a support. XRD, FTIR, TEM, N_2 physisorption and TPR analyses of the M-Ni/SiO_2 catalyst indicated that Ni species were small enough and interacted strongly with silica surfaces. The catalyst performance was evaluated for partial oxidation of methane and results showed excellent activity and stability compared to the unmodified catalyst (UM-Ni/SiO_2).

The preparation of impregnated catalysts is a complex process. The chemistry that occurs in the impregnation solution is of great importance and could be used to vindicate obtained results. In aqueous solution, Ni ions could form polynuclear species and could not interact with the silica surface strongly, which resulted in Ni species agglomeration during calcination treatment. To the contrary, $[Ni(OAm)_4(H_2O)_2]^{2+}$ complex was formed between Ni ion and oleylamine, which is effective for Ni species being isolated on the support surfaces. The strong interaction of the small Ni species with silica improves the catalytic performance of M-Ni/SiO_2 for the partial oxidation of methane.

REFERENCES

[1] N.Z. Muradov, T.N. Veziroglu, Int. J. Hydrogen Energy **30** (2005) 225-237

[2] A.P.E. York, T. Xiao, M.L.H. Green, Top. Catal. **22** (2003) 345-358

[3] H. Özdemir, M.A. Öksüzömer, M.A. Gurkaynak, Int. J. Hydrogen Energy **35** (2010) 12147-12160

[4] R. Liu, M. Yang, C. Huang, W. Weng, H. Wan, Chin. J. Catal. **34** (2013) 146-151

[5] D.B. Bukur, M. Sivaraj, Appl. Catal., A **231** (2002) 201-214

[6] H. Yun Hang, E. Ruckenstein, Adv. Catal. **48** (2004) 297-345

[7] B.C. Enger, R. Lodeng, A. Holmen, Appl. Catal., A **346** (2008) 1-27

[8] Y. Changlin, H. Jiubiao, Z. Wanqin, F. Qizhe, J. Energy Chem. **23** (2014) 235-243

[9] J.B. Claridge, M.L.H. Green, S.C. Tsang, A.P.E. York, A.T. Ashcroft, P.D. Battle, Catal. Lett. **22** (1993) 299-305

[10] K. Nakagawa, N. Ikenaga, T. Suzuki, Catal. Today **64** (2001) 31-41

[11] J. Barbero, M.A. Pen, J.M. Campos-Martin, J.L.G. Fierro, P.L. Arias, Catal. Lett. **87** (2003) 211-218

[12] K. Pil, K.Younghun, K. Heesoo, S. In Kyu, Y. Jongheop, Appl. Catal., A **272** (2004) 157-166

[13] S. Takenaka, H. Umebayashi, E. Tanabe, H. Matsune, M. Kishida, J. Catal. **245** (2007) 392-400

[14] M.D. Salazar-Villalpando, D.A. Berry, T.H. Gardner, Int. J. Hydrogen Energy **33** (2008) 2695-2703

[15] H. Sufang, W. Hongmiao, Y. Wanjin, M. Liuye, L. Hui, Z. Xiaoming, Int. J. Hydrogen Energy **34** (2009) 839-843

[16] M. Trueba, S.P. Trasatti, Eur. J. Inorg. Chem. (2005) 3393-3403

[17] H. Jiubiao, Y. Changlin, B. Yadong, W. Longfu, C. Jianchai, C. Xirong, Chin. J. Catal. **34** (2014) 8-20

[18] N. Nakamura, R. Takahashi, S. Sato, T. Sodesawa , S. Yoshida, Phys. Chem. Chem. Phys. **2** (2000) 4983-4990

[19] J.P. Brunelle, B. Delmon, P. Grange, P.A. Jacobs, G. Poncelet, Preparation of Catalysts II, Elsevier, Amsterdam, 1979, pp. 211

[20] F. Négrier, E. Marceau, M. Che, C.R.D. de Caro, C. R. Chimie **6** (2003) 231-240

[21] K.Q. Sun, E. Marceau, M. Che, Phys. Chem. Chem. Phys. **8** (2006) 1731-1738

[22] G.L. Bezemer, P.B. Radstake, K. Koot, A.J. van Dillen, K.P. Geus, K.P. de Jong, J. Catal. **237** (2006) 291-302

[23] E. Marceau, A. Löfberg, J.M. Giraudon, F. Négrier, M. Che, L. Leclercq, Appl. Catal., A **362** (2009) 34-39

[24] P. Robinson, V. Arun, K. Abdulrashid, C. Aniz, K.M. Yusuff, Chem. Eng. Commun. **199** (2012) 321-334

[25] S. Ahmed, C. Govindappa, J. Indurkar, Synth. React. Inorg. Met.-Org. Chem. **44** (2014) 429-433

[26] F. Bentaleb, C. Michel, A.C. Dubreuil, Catal. Today **235** (2014) 250-255

[27] L. Huimin, L. Yuming, W. Hao, L. Jiaxiong, H. Dehua, Chin. J. Catal. **36** (2015) 283-289

[28] S. Mourdikoudis, L.M. Liz-Marzán, Chem. Mater. **25** (2013) 1465-1476

[29] M. Karimipour, E. Shabani, M. Mollaei, M. Molaei, J. Nanopart. Res. **17** (2015) 2-8

[30] C. Wenjia, Y. Lin, Z. Li, R. Yuanhang, Y. Bin, C. Xueying, H. Heyong, Materials **7** (2014) 2340-2355

[31] E.C. Lovell, J. Scott, R. Amal, Molecules **20** (2015) 4594-4609

[32] K.S.W. Sing, D.G.Everett, W.A.W. Haul, L. Moscow, R.A. Pierroti, Pure Appl. Chem. J. Catal. **57** (1985) 603-619

[33] K. Mette, S. Kühl, A. Tarasov, H. Düdder, K. Kähler, M. Muhler, R. Schlögl, M. Behrens, Catal. Today **242** (2015) 101-110

[34] B. Mile, D. Stirling, M.A. Zammitt, A. Lovell, M. Webb, J. Catal. **114** (1988) 217-219

[35] M.C.J. Bradford, M. A Vannice, Appl. Catal., A **142** (1996) 73-96

[36] Z. Xu, Y. Li, J. Zhang, L. Chang, R. Zhou, Z. Duan, Appl. Catal., A **210** (2001) 45-53

[37] E. van Steen, G.S. Sewell, R.A. Makhothe, C. Micklethwaite, H. Manstein, M. de Lange, C.T. O'Connor, J. Catal. **162** (1996) 220-229

[38] J.F. Lambert, M. Hoogland, M. Che, J. Phys. Chem., B **101** (1997) 10347-10355

[39] L.T. Zhuravlev, Colloids Surfaces, A: Physicochem. Eng. Aspects **173** (2000) 1-38

[40] G. Lawrance, Introduction to coordination chemistry, John Wiley & Sons Ltd., London, 2009, pp. 17.

SEYED MOHAMMAD SADEGH HOSSEINI DAVARANI[1]
HASSAN HASHEMIPOUR[1]
ALIREZA TALEBIZADEH[2]

[1]Department of Chemical Engineering, Faculty of Engineering, Shahid Bahonar University of Kerman, Kerman, Iran
[2]Department of Chemical Engineering, Faculty of Engineering, Vali-e-Asr University of Rafsanjan, Rafsanjan, Iran

NAUČNI RAD

METODA IMPREGNACIJE MODIFIKOVANA OLEILAMINOM ZA PRIPREMU VISOKO EFIKASNOG Ni/SiO$_2$ NANOKATALIZATORA AKTIVNOG U PARCIJALNOJ OKSIDACIJI METANA DO SINTETSKOG GASA

U ovom istraživanju nova modifikovana metoda vlažne impregnacije je razvijen au cilju sinteze 5% Ni/SiO$_2$ nanokatalizatora sa visokom kataliutičkom aktivnošću i stabilnošću radi parcijalne oksidacije metana. Oleilamin je iskorišćen kao agens za kaptiranje u rastvoru za impregnaciju radi poboljšanja disperzije i interakcije nikla sa površinom silicijum-dioksida. Proizvod je analiziran i okarakterisan pomoću difrakcije X-zraka (XRD), FTIR spektroskopije, N$_2$ fizisorpcije i transmisione elektronske mikroskopije. Parcijalna oksidacija metana u prisustvu modifikovanog katalizatora je izvedena u kontinualnom reaktoru sa nepokretnim slojem pod atmosferskim protiskom na 700 °C. Modifikovanim katalizatorom ostvaruje se konverzija metana od 91%, prinos vodonika 86% i selektivnost ugljen- monoksida 95%. Dobijene vrednosti ostaju konstantne i narednih 5 h. Odlična katalitička performansa katalizatora se pripisuje malim i uniformno distribuiranim nanočestesticama nikla, čija strukturna karatkterizacija potvrđuje dati zaključak.

Ključne reči: 5% Ni/SiO$_2$, oleilamin, parcijalna oksodacija metana, vlažna impregnacija.

CI&CEQ
Chemical Industry & Chemical Engineering Quarterly

Available on line at
Association of the Chemical Engineers of Serbia *AChE*
www.ache.org.rs/CICEQ

Chem. Ind. Chem. Eng. Q. 23 (2) 269–277 (2017) CI&CEQ

SEPARATION OF OIL DROPS FROM WATER USING STAINLESS STEEL FIBER BED

ARPAD KIRALJ[1]
TATJANA VULIĆ[1]
DUNJA SOKOLOVIĆ[2]
RADMILA ŠEĆEROV SOKOLOVIĆ[1]
PERO DUGIĆ[3]

[1]University of Novi Sad, Faculty of Technology, Novi Sad, Serbia
[2]University of Novi Sad, Faculty of Technical Science, Novi Sad, Serbia
[3]University of Banja Luka, Faculty of Technology, Banja Luka, Bosnia and Herzegovina

SCIENTIFIC PAPER

UDC 544.7:66.06:628.3

Article Highlights

- Separation of mineral oil droplets with stainless steel fibers bed different geometry was investigated
- The separation efficiency for all operating conditions were higher than 90%
- Low bed permeability is most favourable for the separation of mineral oil droplet from water
- Separation of oil using stainless steel fibers is extremely sensitive to changes in oil properties

Abstract

This study is focused on the separation of oil droplets from water by applying a stainless steel fiber bed. The separation efficiency was followed by monitoring the oil concentration of three mineral oils that have a wide range of viscosity from 10 to 170 mP s, as well as neutralization number from 0.10 to 1.70 mg KOH/l. The bed properties were varied by altering the bulk density of the filter material, which resulted in a change of bed permeability from 0.7×10^{-9} *to* 5.389×10^{-9} m^2 *and bed porosity from 91 to 98%. All experiments were conducted in a wide range of superficial velocity from 10 to 50 m/h. It can be concluded that high separation efficiency was achieved using stainless steel fibers, reaching values over 90%. Low bed permeability is most favorable for work at the selected conditions for the separation. The operation of stainless steel fiber bed is very sensitive to changes in the properties of oils. For lower viscosity of oily contaminants, the required efficiency of separation is achieved at lower superficial velocity through the fibrous bed. This phenomenon can be considered as a serious drawback since the bed coalescers often have to separate oils of different quality over time.*

Keywords: liquid-liquid separation, oily water, bed coalescence, fiber material, stainless steel.

Both oil-in-water and water-in-oil emulsions are widespread in industry and in nature. When it is necessary to carry out the separation of the dispersed phase, the emulsion stability, phase concentration and droplet size predominantly influence the separation technique. In the case of emulsions that have droplets smaller than 100 μm, one of the most economically acceptable separation techniques is coalescence filtration [1-4].

Coalescence filtration has a fiber bed through which the emulsion flows. If proper conditions are achieved, the saturated oil phase is formed in the pores, so-called capillary-conducted phase, that allows new incoming droplets to be coalesced in its volume, while large globules break off from this volume and exit the bed. Visually, the explained phenomenon involves small droplets entering the bed and larger droplets exiting the bed enabling separation by settling [1,5-9].

Many parameters influence the filtration and bed coalescence: bed thickness [10-15], nature of filter material [16-21], superficial flow velocity [2,3,13-15], orientation of the fluid flow [2,3,22], the properties of

---

Correspondence: D. Sokolović, Univeristy of Novi Sad, Faculty of Technical Science, Trg Dositeja Obradovića 6, 21000 Novi Sad, Serbia.
E-mail: dunjaso@uns.ac.rs
Paper received: 10 June, 2016
Paper revised: 29 July, 2016
Paper accepted: 12 August, 2016

https://doi.org/10.2298/CICEQ160610041K

both fluids [2,3,10,11,23] and the bed geometry [3,9,14,15,24].

The materials' nature is defined by their chemical structure and roughness. According to the chemical structure, materials can have high surface energy, such as glass, metals, ceramics, or low surface energy as polymers [16-26]. This applies only to materials with smooth surfaces. If the surface roughness is increased then the surface energy of the polymer can also increase and become high. In literature, this double impact of surface energy is not emphasized enough in the liquid-liquid separation using bed coalescers.

Some opinions have been published noting that polymer materials are used for the separation of oil from water due to their oleophilic surface, and high surface energy materials are commonly used for the separation of water droplets from oil [14,15,18,19]. This approach shows the importance of surface wettability of fibers with dispersed phase. Accordingly, it should be noted that there are no reliable techniques for determining the wetting angle of curved surfaces, such as granules and fibers. It was found that the wetting angle depends on the surface geometry and not only on the roughness but also on the dimensions [27-32].

A significant number of authors studied the influence of oil properties on the separation of oil droplets from water [2,3,10,11,23]. It is important to underline whether pure chemicals or oils with complex structures are used. The authors agree that bed coalescence is most efficient for the separation of oil droplets with higher viscosity. Šećerov Sokolović *et al.* pointed out that the polarity of mineral oil is an essential feature that significantly influences the separation efficiency [3,24].

In addition, Šećerov-Sokolović *et al.* think that the fiber bed geometry is very important and significantly contributes to the reduction or increase of separation efficiency in the filtration process but it is not enough investigated [1-3,8,23]. The properties that uniquely determine the bed geometry of fibers are not defined in the literature. Šećerov-Sokolović *et al.* revealed that the dependence of porosity on permeability, as well as constant fiber diameter determines the fiber bed geometry and underlined that it is necessary to maintain the same bed geometry during investigation of some other influences. It has been observed in some published research that the change of filter material and fiber diameter was not systematically investigated, which disabled the possibility to give conclusions about simultaneous impact of these two effects [33-37]. Davies, Austin and Jefreys [34,35] examined the influence of fibers nature on the separation of both, isooctane from the water, and water from isooctane. In the case where the water was dispersed phase the highest separation efficiency was achieved using glass fibers, slightly lower efficiency was obtained with stainless steel fibers, even lower with nylon and the lowest with teflon fibers. The authors found that the separation efficiency is inversely proportional to the value of surface energy of materials. However, when the water was the continuous phase and isooctane the dispersed phase, the dependence of the separation efficiency in relation to the surface energy did not change. It should be noted that the selected polymers, nylon and teflon, are not good representatives for polymer fibers, since these fibers are inelastic and sharp, and due to the liquid flow and the hydrodynamic forces influence they behave more like steel and glass fibers. This statement is confirmed by the fact that in today's practice and research these polymers are no longer used. In addition, during these experiments, the porosity of the bed and the diameters of fibers were not constant. The authors argue that these properties are important in determining the overall efficiency of the system, but due to the little differences in the studied beds these properties were not crucial for the separation efficiency. The authors also concluded that the wettability of fibers with the dispersed phase that should be separated has no influence, but insist that roughness has a much greater impact on the separation efficiency.

Fahim and Akbar [14,15] used a fiber bed of combined glass and stainless steel fibers for the separation of jet fuel from water. They investigated the influence of the superficial velocity, bed thickness and inlet concentration of jet fuel on the pressure drop and separation efficiency. Glass fibers with 15 μm diameter and stainless steel fibers with 180 μm diameter were used. During the experiments, the oil content was monitored, as well as the droplet size distribution of the dispersed phase at the bed exit. The authors defined the separation efficiency through changes in the droplet diameters. As a result of visual inspection of the coalescence process inside the fiber bed, the authors observed that, when entering the bed, the droplets of the dispersed phase first attach to the surfaces of glass fibers. Thereafter, when the droplet diameters of dispersed phase are enlarged they transfer to the stainless steel fibers. In this way the capillary-conducted phase is formed. The authors considered that the surface of glass fibers has different wettability towards jet fuel compare to the wettability of steel fibers due to the earlier formation of the oil membrane. The fact that was ignored by the authors was that the geometry of the glass fiber bed is completely different, due to the significantly smaller fiber diameter, by which the flow conditions, specific surface area of fibers bed and the size and shape of the pore space are significantly different when compared to the stainless steel fiber bed with much larger fiber diameter. Several authors varied fiber diameter in their studies and concluded that thinner fibers are more efficient for the droplet separation than thicker fibers [6,7,10,11,25,26].

Rebelein and Blass [36] examined the influence of the dispersed phase properties, the droplet diameter, the characteristics of fiber material, bed length and the superficial velocity on the separation of both, oil in water emulsions, and water in oil emulsions. The tested materials were glass and stainless steel fiber as well as polytetrafluoroethylene (PTFE). The diameters of fibers were: glass 12 μm, stainless steel 5 and 12 μm, and PTFE 40 μm. The authors concluded that the stainless steel fiber bed achieved the highest separation efficiency for the oil in water system. Simultaneous variation of both fiber nature and fiber diameter, made by these authors (also noticed in other published research) disables the possibility to obtain relevant conclusions. The PTFE fibers were about three to eight times thicker than steel fibers, which is not emphasized as an important factor in explanation of the results.

Magiera and Blass [37] examined the influence of the oil properties, droplet diameter, fiber diameter, fiber nature and bed length on the separation for both, oil in water and water in oil emulsions. Following fiber beds were investigated: glass fibers of 2.5 and 12 μm diameters, stainless steel fibers of 2.8 and 12 μm diameters, and teflon fibers of 60 μm diameter. The authors concluded that the high energy fibers were more efficient in the separation of dispersed droplets than the low energy fibers. Since in this study it was not specified which system was investigated oil-in--water or water-in-oil, it can be concluded that the findings relate to both systems. The same problem regarding the simultaneous variation of both fiber nature and fiber diameter, with the low energy fibers significantly thicker than the high energy fibers, leading to different bed geometry, was made in this study.

Painmanakul and colleagues [38] examined the influence of bed length, superficial velocity and the material nature on the separation efficiency of palm oil from the water. The authors have investigated commercial fibers of stainless steel and polymers. Material properties were determined based on the wetting angle measurements and critical surface tension of materials. The separation efficiency was monitored by determining the chemical oxygen demand (*COD*) in oily water before and after the flow through the fiber bed. The authors did not provide any information about the fiber properties, especially not the fiber diameters. Only photographs of the tested materials were presented. The efficiency of both fiber types as coalescence filter bed was tested. As a result, the polymer fibers exhibited extremely low separation efficiency of 44.4%. The stainless steel, which, according to the photographs, looks more like chips than fibers, showed separation efficiency of 40.2%. It can be assumed that the main reason for such low separation efficiency for both materials is badly selected bed geometry. In addition, the authors monitored the efficiency using *COD*. The values obtained in this way include also the dissolved organic part opening the question of the published research relevance.

Li and colleagues [39] investigated efficiency of commercial stainless steel fiber felt diameter of fiber 5 μm and modified fiber felt using different procedures for separation of oil droplets from water. Target of modifications were to change wettability or roughness and pore size of filter media. The dispersed oil phase was: *n*-hexadecane, *n*-octane, soybean and engine oil. Inlet concentration of the oil was 1000 mg/l. Mean droplet size was from 2 to 4 μm. Flow mode was vertical down. Fluid flow was 50 ml/min. They concluded that modified felts separate oil from water with high separation efficiency. The effects of pore size and surface wettability were investigated on model water with *n*-hexadecane. When the surface is amphiphobic, the separation is more sensitive to the change of pore size.

The aim of this study was to investigate the possibility of stainless steel fibers application maintaining constant diameter of this high surface energy, not wettable with the mineral oil droplets of different properties that have to be separated from the emulsion. In addition, the goal of this research was to determine the impact of the steel fiber bed geometry change, altered by the variation of the bed bulk density, which was achieved by compression of the fiber material.

EXPERIMENTAL

Experimental setup of the bed coalescer and operating procedure

The experiments were performed on a pilot plant bed coalescer capacity of 100 l/h with horizontal fluid flow orientation, the design of which has been described in detail in a previous paper [13,22]. Naphtenic crude oil (A), its vacuum distillation fractions (A4), and petroleum semiproduct with a high paraffinic content without additives (P1) were used as the dispersed phase for bed coalescence experiments. All three dispersed phases were mineral oils of different properties containing natural emulsifiers such as asphaltenes. Oil droplets were dispersed in tap water by adding oil to the supply tank. The oil-in-water model emulsions with constant oil concentration (500 mg/L) were prepared in a two tanks (80 l each), by continuous agitating with a stainless steel impeller (650 rpm). In order to ensure the inlet mean droplet diameter of about 10 μm, each oily sample was continuously stirred 45 min prior to the experiment and onwards until the end of experiment. The mean inlet droplet size of the number distribution was dependent of the properties of the dispersed oil phase and it was determined by an Elzone 280 PC particle counter and Olympus BH.2 RFCA microscope:

- 9-10 μm (min. 0.8 μm, max. 31 μm) for oil A/water,
- 10-12 μm (min. 0.9 μm, max. 33 μm) for oil A4/water and
- 9-10 μm (min. 0.9 μm, max. 28 μm) for oil P1/water.

The steady-state regime of bed coalescence was achieved from the very beginning of the experiment by pre-oiling the fibers. The filter media were stainless steel fibers. The following parameters were kept constant in a coalescence experiment: bed length (5 cm), bed permeability, and working temperature (20 °C). Each oily water sample was tested for four bed permeabilities. The oil-in-water emulsion was pumped through a membrane dosage pump at superficial velocities ranging from 10 to 50 m/h. The selected velocity was kept constant for 1 h. Composite samples of oil-in-water emulsion were collected at the sampling point downstream of the bed and settling zone after 45 min of experiment start up at 5 min intervals.

Properties of dispersed oils

Three different kinds of dispersed oils were used with a wide range of physical and chemical properties. Their properties have been published previously [24]. Density was determined according to ISO 3675. Kinematic viscosity was measured using glass capillary viscometers according to the standard ISO 3104. Neutralization number was determined by potentiometric titration (ISO 6619). Mean molecular weight was estimated according to standard method ASTM d 2502-67 from kinematic viscosity measurements. Interfacial tension and surface tension measurements were done according the du Noüy ring method and stalagmometric method, respectively. Emulsivity was established using a centrifuge technique [40].

In this study mineral oils that are multicomponent mixtures of hydrocarbons with different structures were used. The selected oils significantly differ in all properties. Viscosity was in the range from 10 to 170 mP s, neutralization number from 0.10 to 1.70 mgKOH/l and emulsivity from 54 to 100%.

Properties of the bed

The stainless steel fibers were needle-punched and non-woven with random orientation. The surface morphology and size of the fibers were characterized by scanning electron microscopy (Figure 1).

Circular cross-section profile smooth fibers with average length of 30 mm and average diameter of 40 μm was used in the experiments. Due to compressibility of fibers, it was possible to vary the bed permeability over a wide range from 0.7×10^{-9} to 5.389×10^{-9} m^2 corresponding to bed porosity from 91 to 98%. The bed permeability was calculated from the measured pressure drop across the bed for tap water, because the data was complied with Darcy's law.

Effluent oil concentration

Samples of oily water were stabilized and adjusted to pH 2 by adding HCl. Oil from the sample

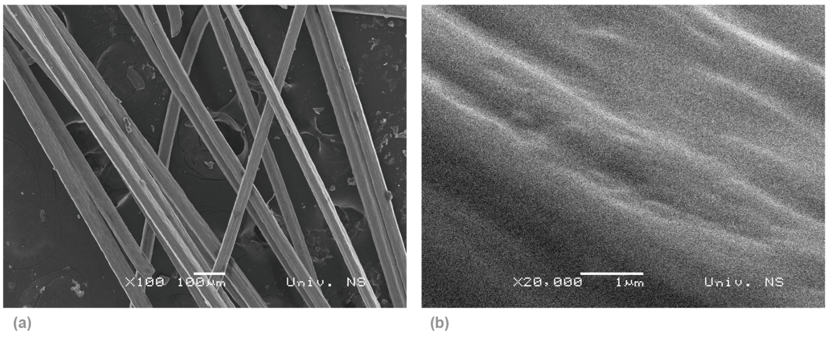

Figure 1. Surface morphology of used filer media. a) 100×; b) 20.000×.

was extracted with CCl_4. The effluent oil concentration was determined by FTIR spectrometry using a ThermoNicolet 5700 spectrometer.

RESULTS AND DISCUSSION

Dependence of the effluent oil concentration on the superficial velocity, properties of oil and bed geometry

Due to the simultaneous analyses of the influence of three independent variables: the superficial velocity, the oil properties and bed geometry, it is more convenient to use 3D diagrams and contour diagrams that was already discussed in the published study of Šećerov Sokolović et al. [3,24].

The dependence of effluent oil concentration, superficial velocity and the bed permeability for oil A4 is given in Figure 2, in the form of a 3D diagram in Figure 2a, and contour diagram in Figure 2b.

The equivalent diagrams for oils A and P1 are given in Figures 3 and 4, respectively.

The 3D diagram noticeably reveals that the dependency of the effluent concentration, superficial velocity and bed permeability is drastically different in all the three oils investigated. Observing the oil A4, it was detected that there is an area bounded with velocity and permeability, where extremely low effluent oil concentrations are achieved. This area is located in a velocity range below 30 m/h and applies to all permeability values. For oil A such an area almost non-existent. At low permeability for almost all range of superficial velocity effluent concentration is relatively low, while all other areas are unfavorable for work. The higher the permeability is higher effluent oil concentration is achieved. Oil P1 has almost no area with low effluent concentration.

In order to observe the boundary of the recommended concentration values, it is necessary to analyze the contour diagrams. The lines within these diagrams are lines of equal concentration of oil in effluent and can be called iso-concentration. In these dia-

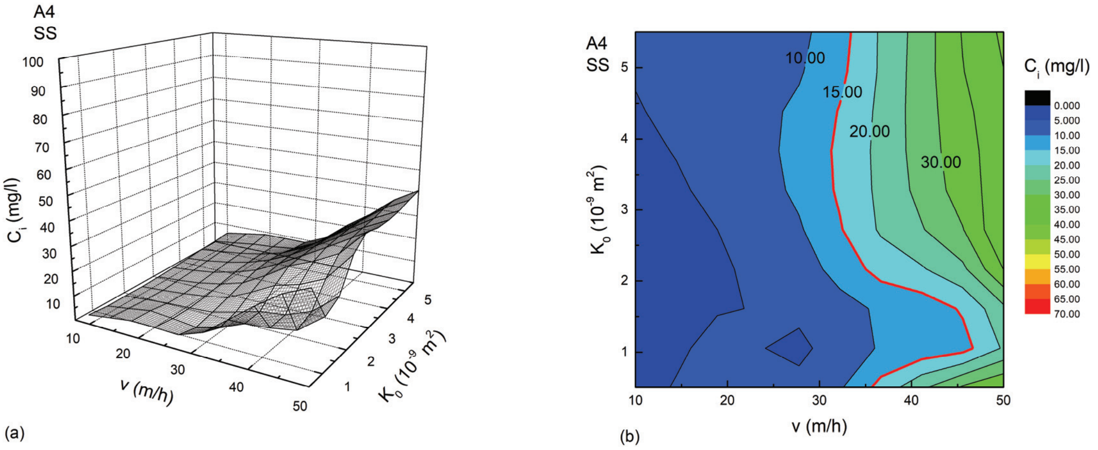

(a) (b)

Figure 2. a) Three-dimensional diagram and b) contour diagram representing the interdependence of effluent oil concentration, superficial velocity and bed permeability for oil A4.

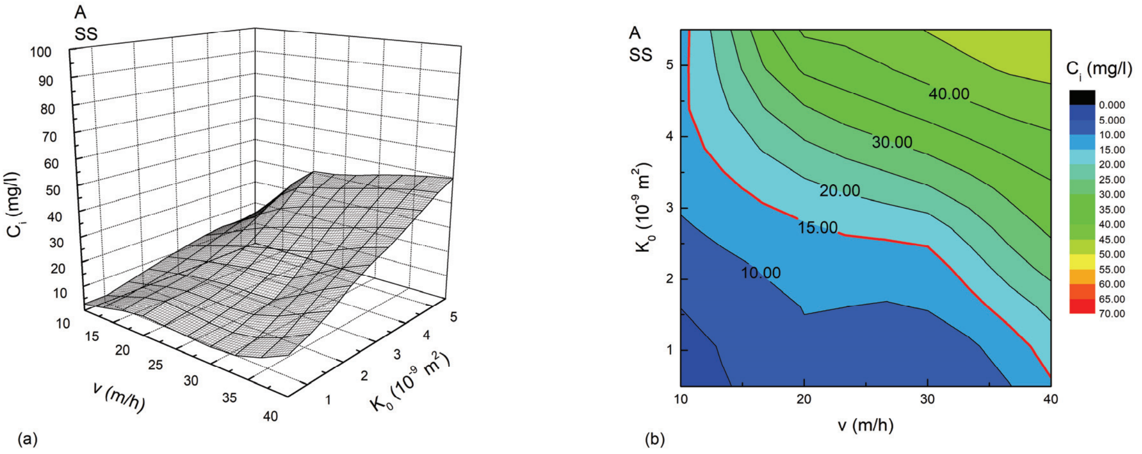

(a) (b)

Figure 3. a) Three-dimensional diagram and b) contour diagram representing the interdependence of effluent oil concentration, superficial velocity and bed permeability for oil A.

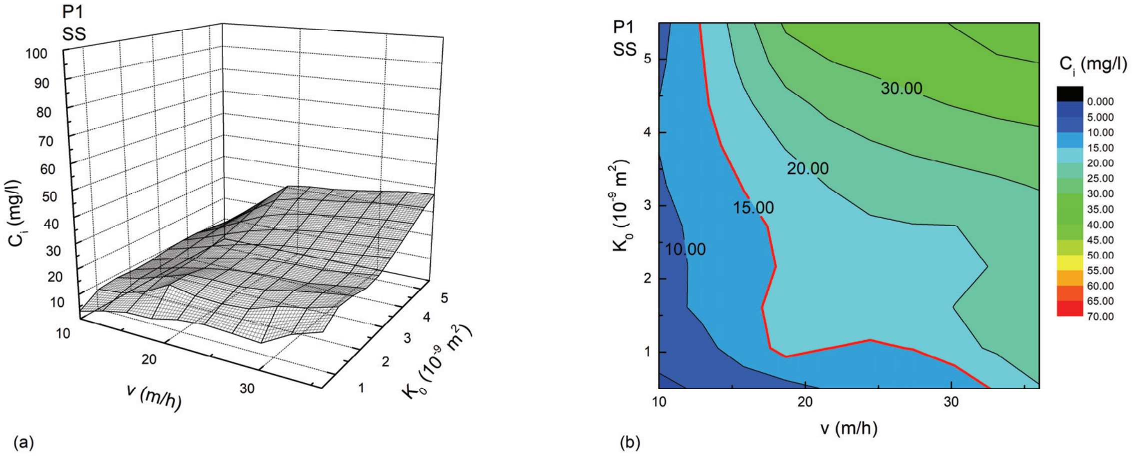

Figure 4. a) Three-dimensional diagram and b) contour diagram representing the interdependence of effluent oil concentration, superficial velocity and bed permeability for oil P1.

grams are thickened lines correspond to the recommended concentration of 15 mg/l.

In the contour diagram for oil A4, Figure 2b, the precise area suitable for work is shown, as well as the numerical values of selected independent variables. For the whole range of bed permeability and superficial velocity, being even slightly higher than 30 m/h, the effluent oil concentration is below the recommended. For the area of low bed permeability (below 2.000×10^{-9} m^2) it is possible to achieve the working velocity even at higher values of 45 m/h. The working velocity is the superficial velocity that obtains the required quality of effluent.

However, for the oil A, Figure 3b, the area of high bed permeability is completely unsuitable for the work. By reducing the bed permeability, the area of working velocity increases up to 40 m/h.

Based on the contour diagram for oil P1, Figure 4b, it is clear that the working area for this oil is incomparably smaller than for the previously discussed oils. For the full range of permeability, the effluent quality can be achieved at superficial velocity of slightly less than 20 m/h, while for this oil, low permeability is most favorable and provides maximum working velocity, which is slightly greater than 30 m/h.

Based on the presented results, two facts could be point out: first, low bed permeability for the selected working conditions and selected properties of stainless steel fibers is most favorable for work; and second, the separation of oil droplets using stainless steel fibers is extremely sensitive to changes in oil properties, which is bad for practice. In petroleum and petrochemical industry, the bed coalescer is often a central part of wastewater treatment plant, and must operate with different types of oily contaminants. If the selected filter material is sensitive to the change of oil properties, it would mean that the coalescer cannot successfully respond to such a task.

Dependence of the separation efficiency on the superficial velocity, properties of oil and bed geometry

If the analysis of oil droplet separation using stainless steel fiber bed is executed only based on separation efficiency, limitations are not visible and one could make completely different conclusions. This will be illustrated by the following analysis. In resulting figures contour diagram is given of the dependence of separation efficiency, superficial velocity and bed permeability of oil A4, Figure 5.

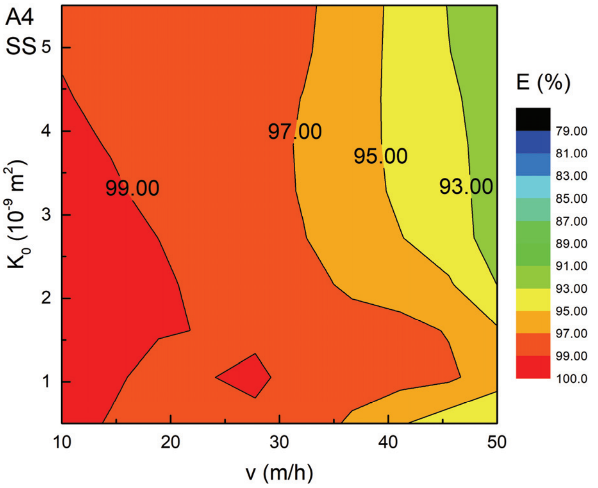

Figure 5. Contour diagram representing the interdependence of separation efficiency, superficial velocity and bed permeability for oil A4.

Based on these results we can conclude that the selected stainless steel fiber bed can successfully separate droplets of all investigated oils, and that high efficiency over 90% was achieved. Compared with other authors, who achieved separation efficiency from 40 to 50% using stainless steel fibers, it can be noted that the selection of appropriate fiber properties and bed properties in the presented research initiated incomparable greater separation efficiency of oil droplets. Regarding the influence of bed permeability, it is evident that with low permeability higher separation efficiency is achieved for a wide range of superficial velocity. The range of efficiency in these circumstances is from 99 to 97%. The size of the area where the separation efficiency is 99% varies for different oils, and it is the highest for oils A4, but very low for the other two investigated oils.

From the results of separation efficiency, any limitations cannot be established regarding working conditions and effluent quality, since the value of efficiency is very high, over 90%.

Influence of oil properties on separation using stainless steel fibers bed

It has already been pointed out that the size of working area, limited between superficial velocity and bed permeability with satisfactory effluent concentration of 15 mg/l, is influenced by the oil properties, which was perceived as a disadvantage. Figure 6 shows the 3D plot of the dependence of the effluent oil concentration, the oil viscosity and bed permeability at constant superficial velocity of 30 m/h. It is clear that the current superficial velocity is suitable for work in a wide range of oil viscosity and bed permeability, and that the areas that are unfavorable are with low oil viscosity and high value of bed permeability. Figure 7 presents the dependence of separation efficiency, oil viscosity and bed permeability, where it is also noteworthy that the lowest values of efficiency is achieved in this area, as well as low oil viscosity and high bed permeability.

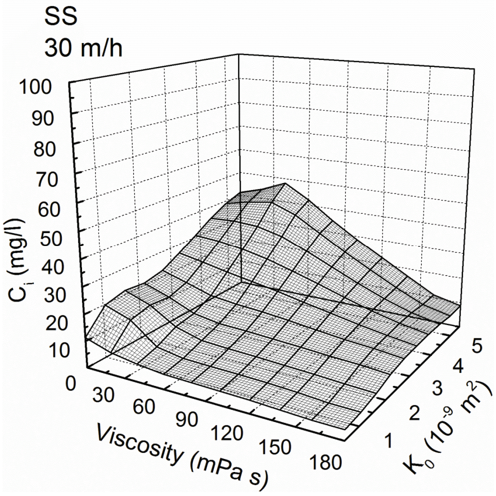

Figure 6. Three-dimensional diagram representing the interdependence of effluent oil concentration, oil viscosity and bed permeability for superficial velocity of 30 m/h.

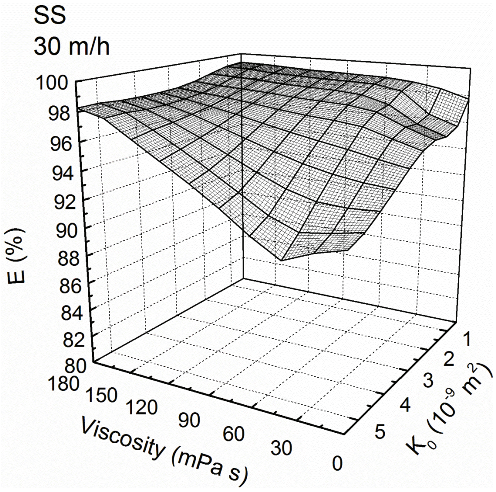

Figure 7. Three-dimensional diagram representing the interdependence of separation efficiency, oil viscosity and bed permeability for superficial velocity of 30 m/h.

When using stainless steel fiber beds, it could be pointed out that the low permeability has a positive effect on the coalescence of droplets and subsequent separation efficiency. At low bed permeability, the bed is the most compressed provoking smallest pores, and then the superficial velocity is the highest. During the visual monitoring of the experiment it was observed that a significant amount of oil does not form a capillary-conducted phase behind the bed, as presented in Figure 8.

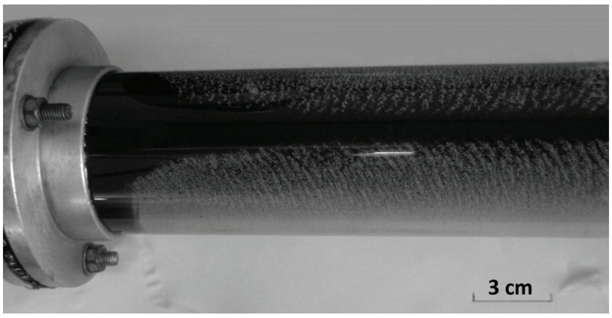

Figure 8. Mineral oil after separation of emulsion using stainless steel fiber bed.

Therefore, it can be argued that in the pores of stainless steel fiber beds predominantly the coalescence mechanism between the droplets is present that are under these conditions, the closest to each other. Previous studies of most authors found that increasing the viscosity of the dispersed oil increases separation efficiency [3,10,11,24]. This was also confirmed with a stainless steel fiber bed in the horizontal flow mode. It is thought that viscous oil formed in the pores is difficult to push out of the bed by hydrodynamic forces, and their presence in the pores facilitates the coalescence in their volume.

CONCLUSION

Based on successful selection of bed geometry for stainless steel fibers, high separation efficiency of tested mineral oils of different properties was reached. The efficiency for all operating conditions were higher than 90%. If analysis of the results is directed towards the reached effluent oil concentration, then it can be concluded that the stainless steel fiber bed can achieve an effluent concentration of 15 mg/l for all investigated oils, but at different values of superficial velocity. Superficial velocity of 30 m/h at low bed permeability provides the recommended quality effluent. Low permeability of stainless steel fiber bed and selected working conditions are the most favorable for the high-efficiency separation of mineral oil droplet from water. Separation of oil droplets using stainless steel fibers is extremely sensitive to changes of oil properties. This can lead to operation problems in industrial application, where the composition of influent is not well defined. It can be assumed that at low bed permeability the coalescence between droplets is the predominant mechanism.

Acknowledgment

The work was supported by the Ministry of Education, Science and Technological Development of the Republic of Serbia, Grant number 172022.

REFERENCES

[1] R. Šećerov Sokolović, S. Sokolović, S. Šević, J. Hazard. Mater. **162** (2009) 410-415

[2] R.M. Šećerov Sokolović, S.M. Sokolović, Coalescence in Porous Bed, Faculty of Technology, Novi Sad, 2000, pp. 13-63 (in Serbian)

[3] D. Govedarica, D. Sokolović, Emulsion separation with fiber bed, Faculty of Technical Sciences, Novi Sad, 2014, pp. 91-110

[4] D.D. Govedarica, R.M. Šećerov Sokolović, A.I. Kiralj, O.M. Govedarica, D. Sokolović, M.S. Hadnadjev-Kostic, Hem. Ind. **69** (2015) 339-345

[5] L.A. Spielman, S.L. Goren, Ind. Eng. Chem. **62** (1970) 11-24

[6] L.A. Spielman, S.L. Goren, Ind. Eng. Chem. Fundam. **11** (1972) 66-72

[7] L.A. Spielman, S.L. Goren, Ind. Eng. Chem. Fundam. **11** (1972) 73-83

[8] R.M. Šecerov Sokolović, D.S. Sokolović, D.D. Govedarica, Hem. Ind. **70** (2016) 367-381

[9] M. Stewart, K. Arnold, Emulsions and Oil Treating Equipment: Selection, Sizing and Troubleshooting, Elsevier, New York, 2009, pp. 158-168

[10] R.N. Hazlett, Ind. Eng. Chem. Fundam. **8** (1969) 625-632

[11] R.N. Hazlett, H.W. Carhart, Filtr. Sep. **9** (1972) 456–462

[12] R.M. Šećerov Sokolović, T. Vulić, S. Sokolović, Sep. Purif. Technol. **56** (2007) 79-84

[13] R.M. Šećerov Sokolović, S.M. Sokolović, B.D. Đoković, Ind. Eng. Chem. Res. **36** (1997) 4949-4953

[14] M.A. Fahim, A.M. Akbar, J. Environ. Sci. Health **19** (1984) 299-319

[15] M.A. Fahim, F.M. Othman, J. Dispersion Sci. Technol. **8** (1987) 507-523

[16] Z. Chu, Y. Feng, S. Seeger, Angew. Chem. Int. Ed. **54** (2015) 2328-2338

[17] S. Basu, J. Colloid Interface Sci. **159** (1993) 68-76

[18] H. Sharifi, J.M. Shaw, Chem. Eng. Sci. **51** (1996) 4817--4826

[19] S. Bansal, V. Von Arnim, T. Stegmaier, H. Planck, J. Hazard. Mater. **190** (2011) 45-50

[20] S.U. Patel, P.S. Kulkarni, S.U. Patel, G.G. Chase, Sep. Purif. Technol. **87** (2012), 54-61

[21] P.S. Kulkarni, S.U. Patel, G.G. Chase, Sep. Purif. Technol. **85** (2012) 157-164

[22] R. Šećerov Sokolović, T. Vulić, S. Sokolović, Ind. Eng. Chem. Res. **45** (2006) 3891-3895

[23] R.M. Šećerov Sokolović, T.J. Vulić, S.M. Sokolović, R.P. Marinković Nedučin, Ind. Eng. Chem. Res. **42** (2003) 3098-3102

[24] R.M. Šećerov Sokolović, D.D. Govedarica, D.S. Sokolović, Ind. Eng. Chem. Res. **53** (2014) 2484-2490

[25] S. Agarwal, V. Von Arnim, T. Stegmaier, H. Planck, A. Agarwal, Ind. Eng. Chem. Res. **52** (2013) 13164-13170

[26] S. Agarwal, V. Von Arnim, T. Stegmaier, H. Planck, A. Agarwal, Sep. Purif. Technol. **107** (2013) 19-25

[27] B. Yang, Q. Chang, C. He, Y. Zhang, Chem. Eng. Process. **46** (2007) 975-981

[28] D. Zang, F. Liu, M. Zhang, X. Niu, Z. Gao, C. Wang, Chem. Eng. J. **262** (2015) 210-216

[29] G. Viswanadam, G.G. Chase, J. Colloid Interface Sci. **367** (2012) 472-477

[30] H. Lu, Q. Yang, X. Xu, H.-L. Wang, Chem. Eng. Technol. 39 (2016) 255-262.

[31] [31] D. Hu, X. Li, L. Li, C. Yang, Sep. Purif. Technol. **149** (2015) 65-73

[32] D. Quéré, Annu. Rev. Mater. Res. **38** (2008) 71-99

[33] X. Yao, Y. Song, L. Jiang, Adv. Mater. **23** (2011) 719-734

[34] G.A. Davies, G.V. Jeffreys, Ind. Eng. Chem. Fundamen. **9** (1970) 519-520

[35] D.G. Austin, G.V. Jeffreys, J. Chem. Technol. Biotechnol. **31** (1981) 475-488

[36] F. Rebelein, E. Blass, Filtr. Sep. **27** (1990) 360-363

[37] R. Magiera, E. Blass, Filtr. Sep. **34** (1997) 369–376

[38] P. Painmanakul, K. Kongkangwarn, N. Chawaloesphonsiya, World. Acad. Sci. Eng. Technol. **58** (2009) 317-322

[39] Li, X., Hu, D., Cao, L., Yang, C., RSC Adv. **5** (2015) 71345-71354

[40] D. Govedarica, R. Šećerov-Soković D. Soković, S. Soković, Ind. Eng. Chem. Res. **51** (2012) 16085-16091.

ARPAD KIRALJ[1]
TATJANA VULIĆ[1]
DUNJA SOKOLOVIĆ[2]
RADMILA
ŠEĆEROV SOKOLOVIĆ[1]
PERO DUGIĆ[3]

[1]Univerzitet u Novom Sadu, Tehnološki fakultet, Novi Sad, Srbija
[2]Univerzitet u Novom Sadu, Fakultet tehničkih nauka, Srbija
[3]Univerzitet u Banjoj Luci, Tehnološki fakultet, Bosna i Hercegovina

NAUČNI RAD

SEPARACIJA KAPI ULJA IZ VODE PRIMENOM VLAKNASOTG SLOJA OD NERĐAJUĆEG ČELIKA

U ovom radu ispitivana je separacija kapi ulja iz vode primenom vlaknastog sloja od nerđajućeg čelika. Efikasnost separacije je praćenja preko koncentracije uljne faze nakon sloja. Ispitivana je efikasnost separacije tri mineralna ulja koja imaju širok opseg viskoznosti od 10 do 170 mP s, kao i neutralizacionog broja do 0.10 do 1.70 mg KOH/l. Karakteristike sloja su varirane promenom nasipne gustine filtarskog materijala što rezultira promenom permeabilnosti sloja u opsegu od 0.7×10^{-9} *do* 5.389×10^{-9} m^2 *i promenom poroznosti sloja od 91 do 98%. Svi eksperimenti su realizovani u širokom opsegu radne brzine od 10 do 50 m/h. Na osnovu realizovanih eksperimenata uočava se da se postižu visoke vrednosti efikasnosti, preko 90%, primenom vlaknastog sloja od nerđajućeg čelika. Niska permeabilnost sloja je pogodnija za rad kod ovog filtarskog materijala. Međutim, vlaknasti sloj od nerđajućeg čelika veoma je osetljiv na promenu prirode ulja koje se separiše, što može predstavljati ozbiljan nedostatak u primeni ovog materijala za kolescentu filtraciju, sa obzirom na činjenicu da je priroda ulja u realnim otpadnim vodama izrazito promenljijiva.*

Ključne reči: tečno-tečna separacija, zauljene vode, koalescencija u sloju, vlaknasti materijali, nerđajući čelik.

CI&CEQ
Chemical Industry & Chemical Engineering Quarterly

Available on line at
Association of the Chemical Engineers of Serbia *AChE*
www.ache.org.rs/CICEQ
Chem. Ind. Chem. Eng. Q. 23 (2) 279–289 (2017) CI&CEQ

DAMJAN KONOVŠEK[1]
ZDRAVKO PRAUNSEIS[1]
JURIJ AVSEC[1]
GORAZD BERČIČ[2]
ANDREJ POHAR[2]
SIMON ZAVŠEK[3]
MILAN MEDVED[1]

[1]Faculty of Energy Technology, University of Maribor, Slovenia
[2]National Institute of Chemistry, Ljubljana, Slovenia
[3]Velenje Coal Mine, Velenje, Slovenia

SCIENTIFIC PAPER

UDC 553.94(497.4Velenje): 662.76.075.5

UNDERGROUND COAL GASIFICATION – THE VELENJE COAL MINE ENERGY AND ECONOMIC CALCULATIONS

Article Highlights

- Energy and economic calculations for underground coal gasification were performed
- The location for the pilot experiment in Velenje Coal Mine was reviewed
- A new procedure for the estimation of the energy efficiency was proposed
- The energy analyses for different examples of coal exploitation were compared
- The viability of the underground coal gasification project in Velenje was determined

Abstract

Underground coal gasification (UCG) is a viable possibility for the exploitation of vast coal deposits that are unreachable by conventional mining and can meet the energy, economic and environmental demands of the 21st century. Due to the complexity of the process, and the site-specific coal and seam properties, it is important to acknowledge all the available data and past experiences, in order to conduct a successful UCG operation. Slovenia has huge unmined reserves of coal, and therefore offers the possibility of an alternative use of this domestic primary energy source. According to the available underground coal gasification technology, the energy and economic assessment for the exploitation of coal to generate electricity and heat was made. A new procedure for the estimation of the energy efficiency of the coal gasification process, which is also used to compare the energy analyses for different examples of coal exploitation, was proposed, as well as the technological schemes and plant operating mode in Velenje, and the use of produced synthetic coal gas (syngas). The proposed location for the pilot demonstration experiment in Velenje Coal Mine was reviewed and the viability of the underground coal gasification project in Velenje was determined.

Keywords: underground coal gasification, syngas, clean coal technology, energy analysis, economic analysis.

Coal will remain the leading energy resource in the following decades [1,2], which is why the development of technologies, which will enable and maintain the coal's competitiveness against other energy resources, is expected. In recent years, there has been increased interest in clean coal technologies, one of which is the process of underground coal gasification (UCG), which combines the technologies of excavation and transformation of coal into useful energy [3]. UCG is the unconventional utilisation of coal, with the use of injection and production boreholes, which are employed for the conversion of coal to gas [3]. Gases from coal can be directly produced *in situ* by providing the gasification agent (air, oxygen) into the ignited coal seam, and collected on the surface [3,4]. This allows for the extraction of deep and un-minable coal and lignite resources [1,5,6]. The produced syngas can serve as a fuel for energy production or can be further processed in the chemical industry (hydrogen, ammonia, methanol, liquid fuels, *etc.*) [6-9].

The UCG process is one of the most innovative technologies being developed around the world [1,4], and offers the possibility to use the energy from coal

---

Correspondence: A. Pohar, National Institute of Chemistry, Ljubljana, Slovenia.
E-mail: andrej.pohar@ki.si
Paper received: 4 June, 2016
Paper revised: 26 July, 2016
Paper accepted: 17 August, 2016

https://doi.org/10.2298/CICEQ160504042K

in an economically viable and environmentally friendly manner, since it causes far less gas emissions and solid particle production after the combustion of coal, as is the case with conventional coal-fired power plants [10,11].

However, the UCG technology is still not commercially feasible in spite of many statements, methodologies, suggestions, monitoring techniques, *etc*. Commerciallization could be reached in the next 5 to 10 years as many field tests are currently running worldwide (South Africa, Australia, India, USA, China, *etc*.) [5,11-12]. Some of the well-documented UCG operations are those at Angren (Uzbekistan), Queensland (Australia), Alberta (Canada), Walanchabi City (China), Majuba (South Aferica) [6]. UCG development is hindered by the infancy of the technology and the limited operational experience on a commercial large scale [13]. Apart from this, UCG has experienced a lot of uncertainty in its development life due to coal shortage/abundance and the fluctuations in the price of other resources such as natural gas and oil [10]. While it can be said that it is possible to gasify all coal types, some specific conditions require a specific UCG method. UCG tests throughout the world have been made at different operating conditions in different coal types, at different depths and in different thicknesses of coal seams. Very few tests were done on lignite and none in thick seams where the underground gasifier control would be difficult [7,14]. Tests show how the variations in geological setting, hydrogeological conditions, coal composition, and UCG process realisation affect process control, dirt transport, economy of the process, environment and people's health [7,14]. Many tests were realised in shallow deposits (less than 100 m deep) [7,11], which is not the target depth for commercial UCG development. The pressures that can develop and the possibility of gas migration (escape) limit these processes in shallow deposits [14].

In Slovenia, UCG studies started at the beginning of the 1980s with laboratory investigations of smaller samples, and continued with test gasification of larger blocks of lignite. Research has been done on Velenje lignite and Zasavje brown coal. A study on the sustainable development of Velenje mining had been performed [15] and in 2002 a feasibility study of UCG was done in the Velenje coalmine. One of the thickest layers of lignite in the world, which is found in the Šaleška Valley, contributed to the development of innovative excavation methods and other technologies like UCG [8]. Because the research was interrupted, some important parts of UCG are still missing: assessment of the use of the process products, along with the economic and final evaluation.

All phases of research performed so far have been performed with the intention to gather evidence about the possibility of performing the UCG process in the coal seam of the Velenje basin. This research represents a demonstration and an important foundation for the implementation of an *in situ* pilot test of UCG in Velenje.

EXPERIMENTAL

The geometry of the test and the operating parameters for the Velenje UCG have been estimated and adjusted on the basis of the modular gasification scheme of the company Carbon Energy Pty Ltd. (CEPL), which was made in the framework of a test in Bloodwood Creek in Australia [16]. The latter offers the most comprehensive data available. Carbon Energy is one of the leading companies in the world in the field of advanced coal technologies such as UCG. Different experiences from previous tests performed around the globe were also taken into account in our procedure.

The energy-economic estimate of the implementation of the pilot testing and modular operation of the plant for the exploitation of syngas is our copyright work, as there are no data available in contemporary literature on the actual implementation of the UCG process for commercial purposes. A new procedure for the estimation of the energy efficiency of the selected UCG method, which is also used to compare the energy analyses for different examples of coal exploitation, is presented, as well as the procedure of economic analysis of the implementation of the pilot UCG test at the Velenje Coal Mine. This part contains the new calculation method for the aforementioned analysis. The following calculations were performed for the estimation of the energy efficiency of the selected UCG method:

- The calculation of the energy efficiency obtained from coal using traditional conventional coal mining. This served as the basis for how much energy might be obtained from an anticipated quantity of coal. The calculation was made on the assumption that coal is excavated and used in a thermal power plant.
- The calculation of the energy efficiency with the use of the UCG method with the assumption of ideal gasification efficiency.
- The calculation of the energy efficiency with the use of the UCG method with the assumption of realistic 80% gasification efficiency. 80% efficiency

means that 80% of the original heating value of the coal feedstock is recovered at the surface in the form of the energy of the produced syngas. The loss of the heating value is simply the consequence of the irreversible heat loss to the surrounding, which becomes larger once more overburned is exposed [17].

- The calculation of the energy efficiency of the UCG method in comparison with a traditional method with a coefficient of energy efficiency of UCG with realistic efficiency and energy efficiency of traditional mining method.

The value of coal per tonne can be calculated from the calorific value (h_{lignite}; GJ/t) and selling value (SV; €/GJ):

$$V = h_{\mathrm{lignite}} \times SV \tag{1}$$

The energy value of 1 module (W_{module}; GJ):

$$W_{\mathrm{module}} = h_{\mathrm{lignite}} \times m_{\mathrm{module}} \tag{2}$$

where m_{module} is the mass of 1 module. The calorific power of 1 module ($P_{\mathrm{coalmodule}}$) can be calculated:

$$P_{\mathrm{coalmodule}} = \frac{W_{\mathrm{module}}}{t} \eta_{\mathrm{gasification}} \tag{3}$$

where t is the time of operation and $\eta_{\mathrm{gasification}}$ is the gasification efficiency.

RESULTS AND DISCUSSION

The research performed so far indicates that, given the properties of the Velenje coal field, the most appropriate UCG technology method combines the ELW method (Extended Linked Wells) and the modified CRIP (Controlled Retraction Injection Point) method for ignition and underground gasification, as shown in Figure 1. This UCG technology is founded on the data of the Australian company Carbon Energy Pty Ltd. (CEPL) [16]. The geometry of the test and operational parameters of UCG in Velenje have been estimated on the basis of the modular gasification scheme of the company CEPL, which was made in the framework of the test in Bloodwood Creek in Australia. The CEPL technology includes two parallel wells drilled from the surface to the block of coal, which come closer together near the vertical ignition well. Then the CRIP method of gasification and controlled retraction of ignition point and reaction cavity is used. Here, the well in the coal seam is linked to the vertical wells, while the gasifier in the injection well retracts towards the entrance.

UCG energy analysis

The energy value of a coal module is calculated for conventional mining, *e.g.*, if the lignite is excavated and used in a thermal power plant. The field of coal of one UCG module in the size of 600 m×180 m×8 m comprises m_{module} = 1,149,120 t ≈ 1.1 Mt of coal. The calorific value of coal or the average energy value of lignite of h_{lignite} = 10 GJ/t and the specific weight or the volumetric mass of coal of ρ_{lignite} = 1.33 t/m^3 were used. The calorific value of lignite is low (10 GJ/t) due to the high moisture content. In contrast, the calorific value for coal is around 25.5 GJ/t, *e.g.*, Polish hard coal [18], or 28.5 GJ/t Mannville sub-bituminous coal [19]. The economic or operational cycle of one module of coal is t_{UCG} = $t_{\mathrm{UCGmodule}}$ = 2.3 years = 28 months = 20,160 h. The expected energy value of one burnt module of coal is W_{module} = 11,491,200 GJ.

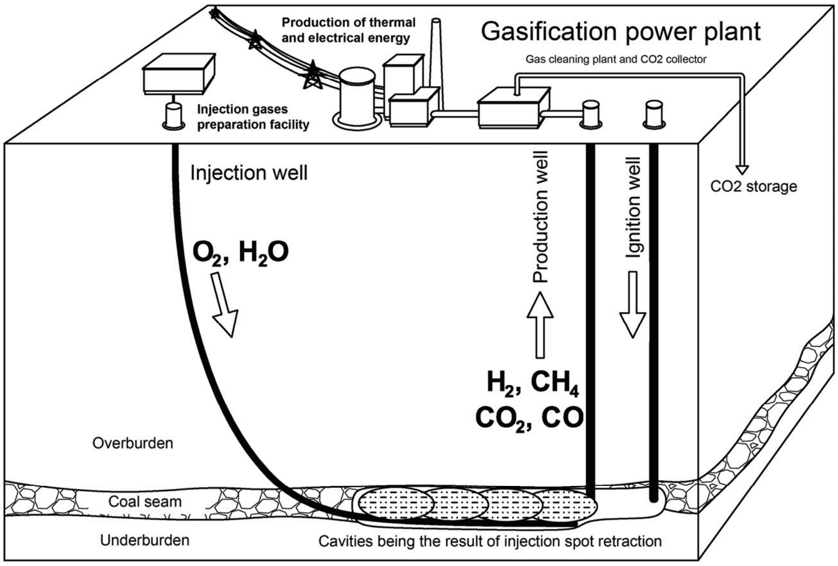

Figure 1. In situ principle of coal gasification according to the CRIP method.

The available calorific power of one module of coal with traditional mining is $P_{\text{coalmodule}}$ = 158.33 MW.

The expected available thermal energy (operational energy) of dry gas of one module at thermodynamic equilibrium (T_{UCG} = 880 K, p_{UCG} = 10 bar) with injected oxygen is calculated to be W_{gas} = = 10,714,012 GJ. Thus, the expected thermal power of gas at the surface or the available thermal operational power of the UCG plant, respectively is P_{module} = 147.62 MW. By comparing the available energy of the obtained gas and energy of coal, which is the subject of gasification, we can estimate the efficiency of gasification, which, given these conditions, accounts for $\eta_{\text{UCGprocess}}$ = 93.2%. According to these calculations, 93.2% of all available energy in a certain coal seam can be obtained through gas. This confirms our assumptions that the energy value of the gasification products is slightly lower with the UCG method than with traditional mining.

Table 1 comprises a summary of the energy analysis for different examples of coal exploitation.

Below is a detailed presentation of underground coal gasification with the gasification efficiency of 80%. Further on, the energy and economic analysis are presented.

An optimal feed rate of reagents and the obtained syngas depend on the type of coal, thickness of a coal seam and conditions under which the gasification process takes place. This paper contains indicative average values expected for the operational cycle of one module. The flow of gas injected into the module has to be adjusted during the procedure in order to maintain a stable ratio between the oxygen flow and the surface of the combustion cavity formed during the procedure. This maintains the ratio between the extracted and released heat, which in turn ensures constant operating conditions and therefore a constant composition of syngas. The calculations are made on the assumption of equilibrium temperature, which ensures a satisfactory compatibility with experimental measurements. The fact that the coal used during laboratory test was not identical to the coal in the seam (humidity, operating pressure), must be taken into account. It can also be assume that the oxygen to vapour ratio has a lower impact on the economics of UCG itself, as geological properties of coal (such as thickness and gradient of the seam) have a stronger effect.

In Figure 2, the results of the calculations are presented, which were made on the assumption of coal gasification efficiency of $\eta_{\text{gasification}}$ = 80% and at a pressure of 10 bar [19]. This means that with the efficiency of 80%, the same amount of energy from the coal will be transferred to the energy of the syngas formed during the gasification procedure. It has to be taken into account that even if the gasification efficiency changes, the calorific values of the syngas remain unchanged, as in the case when different

Table 1. Energy analysis of coal exploitation

Size per one module of coal	Conventional mining	UCG at ideal efficiency	UCG at 80% efficiency of gasification
Energy value	W_{module} = 11,491,200 GJ	W_{gas} = 10,714,012 GJ	$W_{\text{gas80\%}}$ = 9,269,846 GJ
Thermal power of a power plant	$P_{\text{coal module}}$ = 158.33 MW	P_{module} = 147.62 MW	$P_{\text{gas80\%}}$ = 127.73 MW

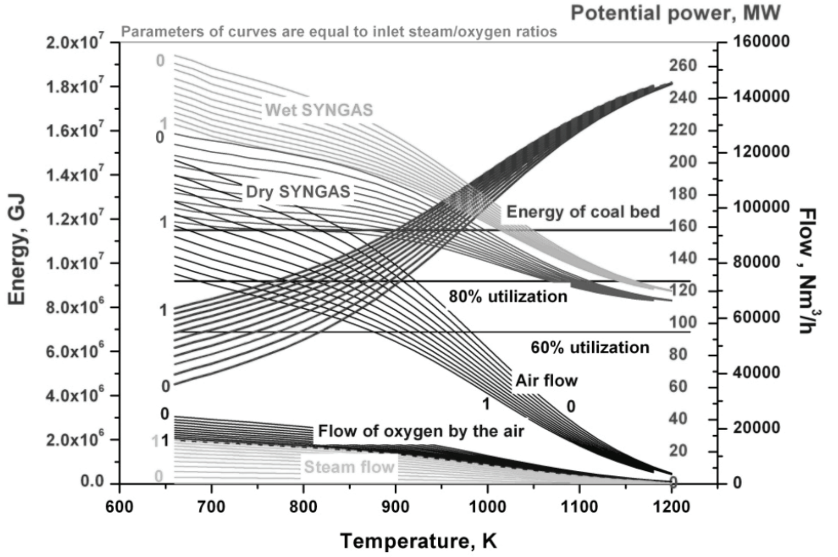

Figure 2. Material flows for the operation of the test module in the stream of both oxygen and steam [19].

flows of reagents and products are used. The water content can also be noticed on the diagrams, which means that both dry and wet coal syngas can be compared. The starting point is an equimolar mixture of steam and oxygen, which means that the molar ratio of both elements is 1:1. The chart also features individual curves of which each indicates a 10% decrease of water intake until the stage of gasification with pure oxygen (no steam is present at this stage) is reached.

According to the results of Velenje lignite laboratory gasification, the most appropriate steam/oxygen ratio is 1:1 [14]. It is generally believed that the best conditions for lignite UCG are obtained, if the Velenje lignite is gasified with the mixture of H_2O and O_2 in a 1:1 ratio, which means that this is the best gasification agent or the best gasification ratio.

The flows of individual gas streams with 80% coal gasification are represented in Figure 2 for both borderline cases: in oxygen or air stream with added steam or without it. With the gasification efficiency of $\eta_{\text{gasification}}$ = 80%, the optimal conditions of gasification are established at the temperature of $T_{\text{UCG80\%}}$ = 782 K and pressure of $p_{\text{UCG}} = p_{\text{UCG80\%}}$ = 10 bar. The anticipated available thermal power of the UCG process with the gasification efficiency of 80% is estimated at $P_{\text{UCG80\%}}$ = 126 MW.

The aforementioned method was also used in the report "Sizing and economics of power plant based on reserves, products and energy utilization of UCG process", which was prepared by PV (Velenje Coal Mine) as an enclosure to a study of IREET (Energy, Ecology and Technology Research Institute, Ljubljana). In it, costs are specified for the installation, maintenance and operation of a virtual energetic plant that would operate on lignite and use the process scheme proposed by Carbon Energy. A default size of the gasification field was assumed to be 600 m×180 m×8 m and the rate of the progression of the combustion front was set to 3 cm/h.

Figure 2 shows operational parameters for a test gasification of a hypothetical field of lignite with the assumed operational period of 2.3 years in the stream of both oxygen and steam. A constant speed of advancement or progression of combustion and/or gasification front is also taken into account. In reality, only the conditions indicated in the lower left part of the chart are possible, where the "energy" lines lie below the "energy of coal". Optimal gasification is observed with the following parameters: efficiency of 80%, 1:1 steam/oxygen ratio, temperature of $T_{\text{UCG80\%}}$ = 782 K, pressure of $p_{\text{UCG80\%}}$ = 10 bar and at the thermal power energy line of $P_{\text{UCG80\%}}$ = 126 MW.

The gasification efficiency of $\eta_{\text{gasification}}$ = 80% is assumed for further calculations, which means that the same amount of energy from coal obtained with a conventional method will be transferred to the energy of syngas formed during the gasification process.

The estimated values of previous chemical tests, the obtained available thermal energy and the required material flows at the default rate of gasification and different efficiencies for one module in the stream of oxygen and steam are represented in Table 2.

Table 2. Material flows for the operation of the test module in the stream of both oxygen and steam [13]; energy of one module of coal: 11,491,200 GJ

Parameter	Value		
Gasification efficiency, %	80	80	60
H_2O:O_2 ratio	1:1	0:1	0:1
Quantity of dry gas obtained, m^3/h	38,744	44,991	39,851
Quantity of oxygen needed, m^3/h	13,538	15,875	19,784
Quantity of steam needed, m^3/h	13,538	-	-
Quantity of water needed, kg/h	10,878	-	-
Available heat, MW	126	126	95

At the gasification efficiency of $\eta_{\text{gasification}}$ = 80% the volume of dry syngas at $q_{\text{gas80\%}}$ = 38,744 m^3/h or of wet syngas at $q_{\text{gasH2080\%}}$ = 65,595 m^3/h was taken into account, enabling the available thermal power of $P_{\text{UCG80\%}}$ = 126 MW. With a 1:1 oxygen/steam ratio, q_{O2} = 13,538 m^3/h of oxygen and the same amount of steam q_{steam} = 13,538 m^3/h or water q_{H_2O} = 10,878 kg/h is needed, which is shown in Figure 3. The flows of gases were defined or calculated for a default speed of advancement of a combustion front, a default composition of lignite and an assumed chemical equilibrium under certain conditions. The entire required quantity of air, oxygen, water and steam for one module are of indicative nature only and are used to estimate how much energy will be possible to obtain by gasification of one coal module.

According to data from Table 2, at the gasification efficiency of 80% the quantity of dry syngas obtained from one module equals to $K_{\text{gasUCG80\%}}$ = = 7,810,790,400 m^3.

A calorific value of $q_{\text{gas80\%}}$ = 11,868 kJ/m^3 of dry syngas is taken into account at a temperature of $T_{\text{UCG80\%}}$ = 782 K, as temperature has an almost insignificant effect on the calorific value of the obtained gas in the temperature range between 700 and 900 K. When the same calorific value of the obtained syngas is used at thermodynamic equilibrium and efficiency of 80%, the thermal energy of gas from one module equals to $W_{\text{gas80\%}}$ = 9,269,846 GJ.

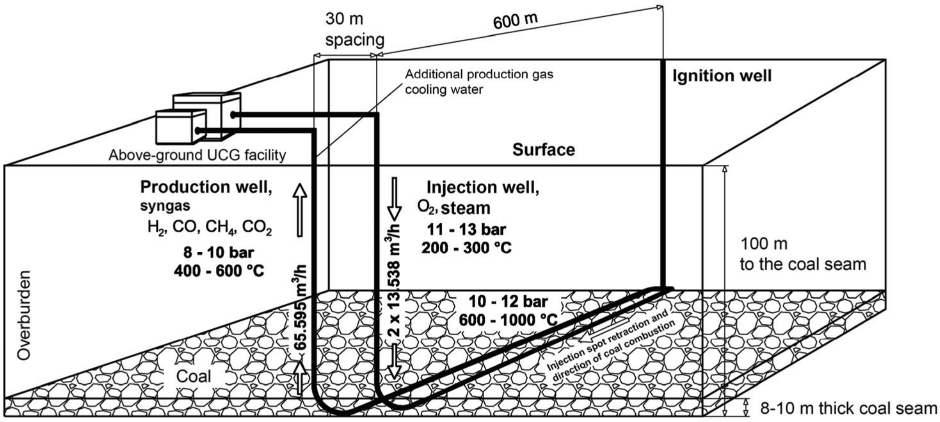

Figure 3. The technological scheme of the UCG process from Bloodwood Creek adapted for a module of coal in Velenje [16].

A summary of the analysis of energy parameters for underground coal gasification at the gasification efficiency of 80% is represented in Table 3.

Table 3. Energy analysis of UCG at the gasification efficiency of 80%

Parameter	Value
Quantity of syngas obtained from one module of coal	$K_{gas80\%}$ = 781,079,040 m^3
Thermal energy for one module	$W_{gas80\%}$ = 9,269,846 GJ
Quantity of syngas obtained from ten modules of coal	$K_{gasUCG80\%}$ = 7,810,790,400 m^3
Energy value of ten UCG modules	$W_{UCG80\%}$ = 92,698,460 GJ
Thermal power of dry gas	$P_{gas80\%}$ = 127.73 MW
Electric power of the UCG power plant	P_{el} = 76.6 MW
Thermal power of the UCG power plant	P_{ther} = 44.7 MW
UCG thermal power produced	$Q_{heatUCG}$ = 33,371,446 GJ
UCG electric power produced	$W_{electricityUCG}$ = 57,208,192 GJ

The value of the available thermal energy of gas at the efficiency of 80% from one module is calculated to $W_{module80\%}$ = 9,192,960 GJ, which coincides with the estimated value of the available thermal energy of $W_{gas80\%}$ = 9,269,846 GJ in the laboratory, as the difference between both values is insignificant. Consequently, the same applies for power, as the value of the available thermal power is calculated to $P_{UCG80\%}$ = 126.66 MW, which coincides with the estimated available thermal power of $P_{gas80\%}$ = 127.73 MW obtained in laboratory. This demonstrates that the estimates concerning the size class of the technological parameters for the dimensioning of the UCG facility are correct.

The efficiency of the electrical transformation in the above-ground facility or thermal power plant fuelled by syngas obtained from UCG that we took into account was $\eta_{powerplant-el}$ = 60%, which, for the future, is a more and more acceptable value of the transformation of gas energy into electric energy. The estimated electric power of a potential thermal power plant for one module within the UCG facility, while taking into account the efficiency of the transformation of $\eta_{powerplant}$ = 60% and the gasification efficiency of $\eta_{gasification}$ = 80%, is thus P_{el} = 76.6 MW. The estimated thermal power of a potential thermal power plant for one module within the UCG facility, while taking into account the efficiency of the thermal transformation of $\eta_{powerplant-thermalpower}$ = 35% and the gasification efficiency of $\eta_{gasification}$ = 80% is $P_{thermalpower}$ = 44.7MW.

UCG economic analysis

The economic period of the UCG project is $t_{UCGproject}$ = 28 years (4 years of investment and 24 years of operation) during which the operation of ten modules is envisaged (28 months for one module). The economic period was assessed on the basis of the gasification scheme proposed by Carbon Energy [8,16]. It has to be noted, however, that the exact time of operation will be deduced from the actual rate of the cavity increase of the Velenje lignite. In the literature, a 2-year-long realisation period (building UCG installation and producing electricity) and a 20-year-long exploitation period assessments can be found [20,21].

The total costs of the UCG project are represented in Table 4. These are all the costs from the beginning to the end of the project, and cover the construction and operation of the underground UCG facility (ten modules) and the entire above-ground UCG facility. Total costs of the UCG project including the implementation of investment (4 years) and a 24-year operation with no depreciation taken into account are $S_{UCGcosts}$ = 466,158,070 €. Total costs of the UCG project thus equal the sum of investment costs and operating costs. Total operating costs of the UCG project are: the manufacture and operation of modules, overheads, labour costs, financing costs in the total amount of $S_{\text{oper.costsUCG}}$ = 297,865,536 €, where a substantial part goes for the costs of manufacture and operation of modules S_{izdobr} = 248,422,379 €. The operation cost per year is therefore 10,638,055 €, which is comparable to the results of Nakaten et al. [20], who estimated these at 8,116,000 € per year.

Table 4. Total costs of UCG project

Cost type	Estimated cost, €
1. Investment costs	168,292,534
2. Operating costs	297,865,536
2.1. Manufacture and operation of modules	248,422,379
2.2. Overheads	9,600,000
2.3. Labour costs	16,254,956
2.4. Financing costs	23,588,201
Total costs	466,158,070
Different manners of coal exploitation	Estimate of revenues, €
Coal from 10 modules is sold to TEŠ (Thermal Power Plant Šoštanj)	287,280,000
Underground coal gasification	594,627,670
Underground coal gasification at 80% gasification efficiency	514,476,450

The more accurate value of investment or the estimated contract value of the Velenje UCG project is estimated to be $S_{\text{estimatedcontrvalue}}$ = 168,292,534 € and has been calculated on the basis of fixed prices *i.e.*, on the basis of the prices that are currently in force. It includes all the necessary investments, which are necessary for the initiation of regular production or operation of the UCG facility: costs related to the purchase of land, project dossier, implementation of research wells, electric and engineering equipment, surface infrastructure, the manufacture of the first module including the costs of drilling and piping and other costs and unforeseen works.

The technological UCG facility on the surface or the equipment of the thermal power plant fuelled by syngas obtained from coal is founded on the conceptual technological scheme of the facility shown in Figure 3 and on the data from Table 3.

As for the above-ground facility, the following elements generate the large part of costs: steam turbine, steam turbine generator, gas turbine, gas turbine generator, cleaning of syngas, combined cycle boiler, oxygen injection, CO_2 collector as well as special characteristics and requirements of the facility ensuing from the location of the future thermal power plant itself. The costs of the necessary infrastructure on the surface including the construction of roads, the establishment of links with electric power network and district heating network and reagent storage facilities, laboratory and management building, the installation for the production of chemicals and/or fuels or the entire thermal power plant for the production of electricity and thermal energy must not be forgoten.

A large part of the cost related to the underground facility is linked to the costs of drilling and installation of pipes or piping for the provision of reagents and for the extraction of the produced gas. Basically, the costs of the UCG process represent the costs of fuel and depend on the actual state of development of individual UCG methods.

By installing the UCG facility, the costs of preparing the reactor, *i.e.*, the drilling of the wells and the installation of the pipes represent the largest amount of costs. The price of the necessary equipment and of the work required is very high as the entire gasification process takes place underground. Thickness and depth of the coal deposit, the number of wells which need to be drilled, the multiple use of individual wells for the adjacent fields of coal - all of this plays an important role in estimating the costs. Consequently, the choice of the UCG method depends, to a large extent, on a minimization of costs related to drilling or to the length of wells, which need to be drilled, in order to reach the coal seam and to prepare the field to be gasified.

The costs of drilling and pipe instalation along the wells are highly variable, especially if we also take into account the costs of research wells and wells used for monitoring and control.

Since the sources of financing for the entire UCG project in Velenje are not yet known, the financing method was estimated. The following financial construction of investments is envisaged: 50% will be financed from own resources and 50% from a long-term bank loan.

The costs of the necessary installations for the underground coal gasification are estimated to be lower than the costs of the installations required for conventional mining at the same capacity. With the UCG method, there are also no costs of mining and coal transport compared to conventional procedures for producing electricity and thermal energy. It is also estimated, that the price of the electric and thermal energy obtained with the UCG method is lower than the price of energy obtained from conventional thermal power plants. However, the syngas obtained through the process of underground coal gasification cannot compete, in terms of price, against a conventionally obtained natural gas.

The choice of the reagent used (air, air enriched with oxygen, oxygen and/or addition of steam) has a huge impact on the economy of the process. This to a large extent defines the composition and calorific value of the obtained syngas, which can then be used in many different ways. The costs related to the reagent itself will be much higher if an air separation unit is needed which ensures a sufficient amount of oxygen.

The economy of the UCG process mostly depends on the geological properties of coal and on the use of land on the surface above the reactor cavity. From the economic point of view it is better to own a coal deposit where the project of underground coal gasification can be carried out. The depth itself and other geological and hydrological properties will have a direct impact on the costs of drilling and on the implementation of the underground link between the wells.

Table 4 contains the estimates of revenues for different cases of coal exploitation for the selling of thermal energy. In estimating the revenue, if the coal was sold to Thermal Power Plant Šoštanj, the revenue is estimated to be $P_{\mathrm{revenues10modulesTE}}$ = = 287,280,000 €. A selling energy value of coal of c_{coalTE} = 2.5 €/GJ and calorific value of the Velenje lignite of h_{lignite} = 10 GJ/t have been taken into account in our estimation. An estimate of the revenue in the event of underground coal gasification at both 100% and 80% efficiency of energy transformation was also made. In case all thermal energy, obtained from the underground part of UCG of all ten modules was sold on the market, the estimated revenue would be $P_{\mathrm{revenue10modules}}$ = 594,627,670 €. Taking into account the efficiency of gasification of 80% the estimated revenue from sales of all produced thermal energy from the underground UCG facility of all ten modules would be $P_{\mathrm{revenue10modules80\%}}$ = 514,476,450 €.

Continuing the calculations, if it is assumed that all the produced thermal and electric energy obtained from UCG at 80% gasification efficiency will be sold on the market; the use of energy needed for the operation of the UCG facility was considered and calculated as a cost. The fact that the facility operated continuously with constant production of thermal and electric energy every year was also taken into account. Once the operation of one module concludes, the operation of the next module continues.

The total anticipated revenue from sales of thermal energy obtained through the UCG process for the duration of the project is estimated to be $\mathrm{P}_{\mathrm{revenueheatUCG}}$ = 185,211,523 €. Total anticipated revenue from sales of electric energy of UCG for the duration of the project is estimated to be $P_{\mathrm{revenueelectricityUCG}}$ = 953,660,568 €. Total anticipated revenue from sales of thermal and electric energy on the market at 80% gasification efficiency for the entire duration of the UCG project is $P_{\mathrm{revenueUCG}}$ = 1,138,872,091 €. In our calculations of revenues from sales of thermal and electric energy the selling price with regard to the average selling price for 2009–2018 period in the HSE Group, namely the thermal energy price c_{heat} = 5.55 €/GJ = 20 €/MWh and the electric energy price $c_{\mathrm{electricity}}$ = 16.67 €/GJ = = 60 €/MWh were taken into account.

The UCG's performance per individual year with the review of revenues and expenditures with a default gasification efficiency of 80% are shown in Figure 4. During the entire operating period of UCG, the entire project will have revenues in the amount of

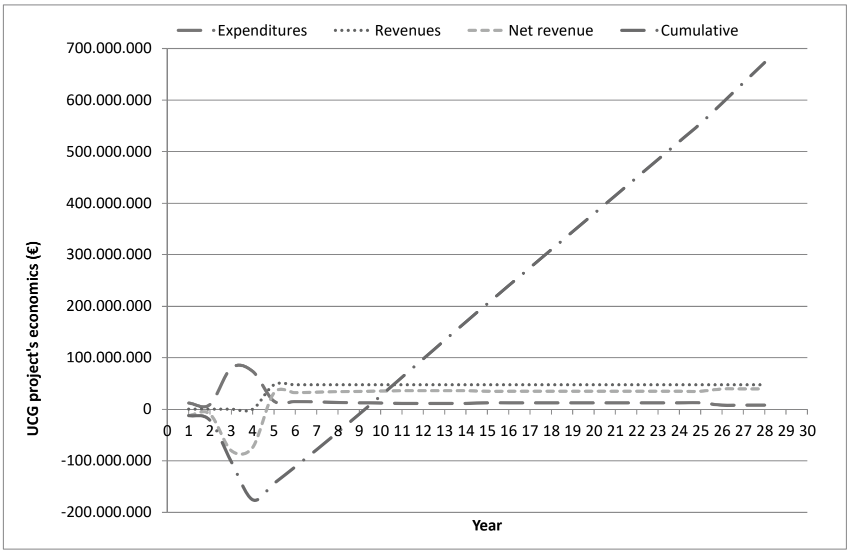

Figure 4. Financial flow of the entire UCG project.

$P_{\text{revenueUCG}}$ = 1,138,872,091 € and expenditures in the amount of S_{costsUCG} = 446,374,865 €. Total profit and loss or profit for the entire project for the entire duration of the operation of UCG is $D_{\text{profitUCG}}$ = = 692,497,231 €; however the cost of concession for the exploitation of coal and costs related to potential unforeseen incidents have to be taken into account. In calculating profit and cumulative of UCG performance, the remaining part of investment $S_{\text{remainvalue}}$ = = 19,783,210 €, which represents the difference between the investments made and depreciation, and defines the accounting value at the end of the UCG project, was taken into account.

The basis for the calculation of the financial performance of the UCG project is the financial flow of the project. The financial flow comprises a 4-year investment period and a 24-year operation period (economic period of the project). The basis for the calculation of the performance criteria is the financial flow of the investment and not the entire cash flow. The financial flow revenues are comprised of revenues from sales of thermal and electric energy and the remaining part of the project's value in the amount of non-depreciated value of fixed assets in the amount of $S_{\text{remainvalue}}$ = 19,783,210 €. The expenditures of financial flow are comprised of the value of investment (without financing costs) and operating costs (without depreciation). The financial flow of the entire UCG project is shown in Figure 4.

Statistical and financial indicators concerning the viability of the investment show that the investment is repaid after the operation of the third module, which is also shown in Figure 4. Here, a modular system of ten modules, where the envisaged operating period of one module extends over 28 months, was taken into account.

The basis for the estimate of the viability of the UCG investment is the financial flow. A discount rate of d = 7% is used. The present value of the covered project means, that when it is calculated according to the present money value, the investment would - after the costs of the entire investment have been covered - create further $P_{\text{netpresentvalue}}$ = 139.130.209 € of accumulation at the end of the project's period.

The intern rate of profitability is $f_{\text{internrateprof}}$ = = 16.08% and refers to the average annual rate of profitability of the investment during the life cycle of the project which is $t_{\text{projectUCG}}$ = 28 years.

Relative net present value of investment is $f_{\text{relativenetpresvalue}}$ = 0.901 and means that until the end of its economic period the investment will "gather" investment funds in the amount which will, at that given time, enable the investment of 90.1% share of an investment project of the same scale.

The period of repaying the costs of investment refers to the time required for the investment revenues to cover the entire amount of investment expenditures. In our case, the investment is repaid in year 10 of the economic period of the project.

The very different conditions in which individual tests took place must mean that any generalisation of the results is not acceptable and could even be dangerous; therefore, the results of each test can only be treated as specific to its own conditions. All the tests were small scale ones, and not one resulted in a commercially acceptable technology that would meet all environmental requirements. The site-specific techno-economic analyses have to be undertaken for each selected underground coal gasification study area individually, whereas results cannot be transferred from one target area to another [20]. The technical feasibility and economic success of a UCG project is highly site-specific [22].

Based on a life cycle costing analysis, Burchart-Korol *et al.* [21] concluded, that for cost effective production of electricity with UCG it is necessary to maximize the scale of an installation while optimizing the use of the produced electricity. The implementation of carbon capture and storage CCS causes an efficiency reduction of only 5–8% [20]. The costs consist of CO_2 separation, transportation, compression and injection, storage and monitoring costs. There are no transportation costs, since CO_2 is to be stored in the voids.

A techno-economic model for UCG was developed by Nakaten *et al.* [20], which combined UCG with a combined cycle gas turbine (CCGT) considering CO_2 capture and its subsequent storage (CCS) in the underground voids for a study area in Bulgaria. Their calculation results show that COE account to 48.56 €/MWh without CCS or emission charges, to 71.67 €/MWh considering 20.5% CCS costs and 79.5% emission charges and to 73.64 €/MWh with 100% emission charges [20]. The calculations in this work show that the cost of electricity can be as low as 20 €/MWh, which is the same value as is presented in the work by Pei *et al.* [22]. It has to be, however, considered that energy loss in a UCG process typically occurs due to water influx, underground cavity pressure drop, gas loss to the surrounding strata, and high temperature gasifying medium, which raises the cost of operation and lowers the product gas quality and profit [23]. It should also be considered that adaptations during the course of operation will be performed and that the syngas quality will vary from time to time.

Underground coal gasification has been gaining interest for the production of syngas due to the favourable economic outlook, for the use of coal in areas which are not suitable for conventional mining, for the production of electric and thermal energy and as a method of producing clean fuels. On the basis of comparison between the processes of gasification of different types of coal, and on the basis of understanding the strategies of management of individual processes, some companies have already developed key parameters for the planning or commercialisation of the UCG process.

The evolutions in the field of UCG show that the process is potentially very interesting, as preliminary research and studies about the possibilities of UCG have been performed in numerous countries. The UCG process is listed among potential possibilities for solving energy issues in the near future, as it is mentioned in long-term national development plans for exploiting natural resources.

This paper contains the presentation of the implementation of energy and economic analysis of the operation of one module and modular plant for a hypothetical case of gasification of the Velenje lignite according to the CEPL method. A new calculation procedure is also presented, which was, in the framework of energy and economic analysis, used to justify the use of lignite according to the used method. The conventional mining method, the ideal process of underground gasification and a default realistic efficiency of the underground gasification were compared. It was concluded, on the basis of energy and economic analysis, that the UCG project for the Velenje lignite at the location of Tičnica is feasible. This energy analysis presents real possibilities of exploiting the remaining lignite reserves in the Šaleška valley and also indicates the opportunity to exploit brown coal reserves in north-eastern Slovenia. Since very few UCG tests were made in the world, this represents an important energy, environmental, and business opportunity both in Slovenia and abroad.

CONCLUSION

The crucial decision concerning the UCG project, which also serves as the basis for the technical and economic viability of the project, is the choice of the appropriate location and its characterisation. The adequacy of individual fields of coal for the UCG method depends on many factors including physical and chemical characteristics of the coal itself, geological and hydrological properties of the field, environmental, energy and economic adequacy. There were very few tests performed around the globe on lignite and not one was performed on the thicker layers comparable to the one in Velenje, where the development of the combustion cavity differs from the one in thinner layers. The Velenje coal seam is one of the thickest individual coal seams or one of the thickest uniform layers of, especially lignite, in the world. Since the Velenje coal field is unique, there are no comparable studies available in the literature. Consequently, research is very important and at the same time also very difficult to perform. Based on the existing UCG method, a unique energy-economic analysis was executed, which has not been done so far. This energy-economic analysis is the only one in the world that applies to the exploitation of lignite at shallow depths and in the operating coal mine at the same time.

REFERENCES

[1] E. Shafirovich, A. Varma, Ind. Eng. Chem. Res. **48** (2009) 7865-7875

[2] M. Medved, D. Konovšek, Energetski viri - Course Notes, The Faculty of Energy Technology, University of Maribor, 2015

[3] C.W. Siemens, J. Chem. Soc. **21** (1868) 279-310

[4] E. Krause, A. Krzemień, A. Smolinski, J. Loss Prevent. Proc. **33** (2015) 173-182

[5] A.N. Khadse, Fuel **142** (2015) 121-128

[6] K. Kostúr, M. Laciak, M. Durdán, J. Kačur, P. Flegner, Measurement **63** (2015) 69-80

[7] A.W. Bhutto, A.A. Bazmi, G. Zahedi, Prog. Energ. Combust. **39** (2013) 189-214

[8] D. Konovšek, Master's thesis, Faculty of Electrical Engineering, Ljubljana, 2013

[9] R. Zhao, Y. Wang, Y. Bai, Y. Zuo, L. Yan, F. Li, Chem. Ind. Chem. Eng. Q. 21 (2015) 343-350

[10] H. Akbarzadeh, R.J. Chalaturnyk, Int. J. Coal Geol. **131** (2014) 126-146

[11] A. Khadse, M. Qayyumi, S. Mahajani, P. Aghalayam, Energy **32** (2007) 2061-2071

[12] S. Liu, S. Zhang, F. Chen, C. Wang, M. Liu, Energ. Fuels **28** (2014) 6869-6876

[13] F. Mueller-Langer, E. Tzimas, M. Kaltschmitt, S. Peteves, Int. J. Hydrogen Energ. **32** (2007) 3797-3810

[14] A. Zapušek, G. Berčič, S. Zavšek, I. Veber, L. Golob, D. Konovšek, J. Energ. Technol. JET **4** (2011) 61-76

[15] M. Medved, L. Golob, in Proceedings of Balkanmine, Ohrid, Republic of Macedonia, 2012

[16] Carbon Energy, http://www.carbonenergy.com.au/IRM/ /content/default.aspx (accessed 12 March 2014)

[17] A.W. Bhutto, A.A. Bazmi, G. Zahedi, Prog. Energy Combust. Sci. **39** (2013) 189-214

[18] B. Olateju, A. Kumar, Appl. Energy **111** (2013) 428-440

[19] G. Berčič, J. Energ. Technol. JET **7** (2014) 1-12

[20] N. Nakaten, R. Schlüter, R. Azzam, T. Kempka, Energy **66** (2014) 779-790

[21] D. Burchart-Korol, P. Krawczyk, K. Czaplicka-Kolarz, A. Smoliński, Fuel **173** (2016) 239-246

[22] P. Pei, J. Nasah, J. Solc, S.F. Korom, D. Laudal, K. Barse, Energ. Convers. Manage. **113** (2016) 95-103

[23] A. Shrivastava, V. Prabu, Energ. Convers. Manage. **110** (2016) 67-77.

DAMJAN KONOVŠEK[1]
ZDRAVKO PRAUNSEIS[1]
JURIJ AVSEC[1]
GORAZD BERČIČ[2]
ANDREJ POHAR[2]
SIMON ZAVŠEK[3]
MILAN MEDVED[1]

[1]Faculty of Energy Technology, University of Maribor, Slovenia
[2]National Institute of Chemistry, Ljubljana, Slovenia
[3]Velenje Coal Mine, Velenje, Slovenia

NAUČNI RAD

PODZEMNA GASIFIKACIJA UGLJA - ENERGETSKI I EKONOMSKI PRORAČUNI ZA RUDNIK UGLJA VELENJE

Podzemna gasifikacija uglja (PGU) je održiva mogućnost za eksploataciju ogromnih ležišta uglja koji su nedostupni konvencionalnom rudarstvu i može da zadovolji energetske, ekonomske i ekološke zahteve 21. veka. Zbog složenosti procesa, specifičnosti nalazišta i svojstva slojeva uglja, veoma je važno da se poznaju svi raspoloživi podaci i iskustva iz prošlosti, radi uspešnog obavljanja PGU operacije. Slovenija ima ogromne neiskopane rezerve uglja, i zato nudi mogućnost alternativnog korišćenja ovog domaćeg primarnog izvora energije. Prema dostupnoj tehnologiji za podzemnu gasifikaciju uglja, napravljena je energetska i ekonomska procena eksploatacije uglja za generisanje električne energije i toplote. Predložen je novi postupak za procenu energetske efikasnosti procesa gasifikacije uglja, koji je korišćen za uporednu analizu različitih primera eksploatacije uglja , kao i tehnološke šeme i način rada postrojenja u Velenju za proizvodnju sinteznog ugljenog gasa (singas). Pregledana je predložena lokacija za pilot demonstracioni eksperiment u rudniku uglja Velenje i utvrđena je održivost projekta PGU u Velenju.

Ključne reči: podzemna gasifikacija uglja, singas, čiste tehnologije za ugalj, energetska analiza, ekonomska analiza.

Available on line at
Association of the Chemical Engineers of Serbia *AChE*
www.ache.org.rs/CICEQ
Chemical Industry & Chemical Engineering Quarterly 23 (2) 291 (2017) CI&CEQ

ERRATUM NOTICE

Corrigendum: Marija Mihajlović, Marija Stanojević, Mirjana Stojanović, Jelena Petrović, Jelena Milojković, Marija Petrović, Zorica Lopičić. TO WHAT EXTENT DO SOFT MECHANICAL ACTIVATION AND PROCESS PARAMETERS INCREASE THE EFFICIENCY OF DIFFERENT ZEOLITE/PHOSPHATE ROCK FERTILIZER MIXTURES?. Chem. Ind. Chem. Eng. Q. **23**(1) (2017) 1–9. DOI: 10.2298/CICEQ150622047M

Page 2, left column, 4th line from above should read:
natural zeolites with nutrient elements such as NH_4^+ or K^+

Page 2, left column, 16th line from above should read:
However, some authors noted that the particle size

Page 7, 1st line from below should be replaced with the following lines:

Figure 6. PCA score plots obtained on the whole data set with samples labeled in accordance with: a) the zeolite/PR ratio (where 5 designates 5:1, 10 designates 10:1, and 15 designates 15:1 ratio) and b) the duration of mixing time (24, 48 and 72 h). Correlation loading plots of the PCA model for :c) the MACp/PR mixtures and d) the MANH_4–Cp/PR mixtures.

Corrigendum: Fatih Ilhan, Kaan Yetilmezsoy, Harun Akif Kabuk, Kubra Ulucan, Tamer Coskun, Busra Akoglu. EVALUATION OF OPERATIONAL PARAMETERS AND ITS RELATION ON THE STOICHIOMETRY OF FENTON'S OXIDATION TO TEXTILE WASTEWATER. Chem. Ind. Chem. Eng. Q. **23**(1) (2017) 11–19. DOI: 10.2298/CICEQ150907048I

The editorial team at the Chemical Industry and Chemical Engineering Quarterly takes many measures to ensure accuracy. However, we have been alerted to an unfortunate error in the footnote of the paper of Ilhan *et al.*, Chem. Ind. Chem. Eng. Q. **23**(1) (2017) 11–19 located on page 11, where the e-mail addresses of the corresponding author should be yetilmez@yildiz.edu.tr and kyetilmezsoy@gmail.com (K. Yetilmezsoy). Apologies are offered to readers of the Chem. Ind. Chem. Eng. Q. that this abuse was not detected during the editing process.

---

https://doi.org/10.2298/CICEQ170425016E